UNIVERSITY OF EXETER

Far-infrared & Sub-millimeter Studies of Circumstellar Disks

by

Joanna Mary Bulger

Submitted by Joanna Mary Bulger to the University of Exeter as a thesis for the degree of Doctor of Philosophy in Physics, November 2013.

I certify that all material in this thesis which is not my own work has been identified and that no material has previously been submitted and approved for the award of a degree by this or any other University.

Signature:
Joanna Mary Bulger

Abstract

Circumstellar disks are critical structures in the star and planet formation processes, as they provide a conduit to channel material onto the central object and supply a reservoir of dust and gas to form planets. This thesis focuses on the far-infrared, and sub-millimeter observations of circumstellar disks at two key evolutionary phases; primordial proto-planetary disks, and evolved debris disks – remnants of a system that has undergone a degree of planet formation. Four individual studies of circumstellar disks are presented in this thesis.

The results of a 97% complete census of far-infrared emission measured with the *Herschel* Space Observatory, targeting stars of spectral types M4 and later, in the Taurus molecular cloud are presented. This census is the first large-scale survey sensitive to emission across the stellar and sub-stellar boundary. Results from an initial test grid of model spectral energy distributions, generated with the radiative transfer code MCFOST, show that 73% of the observed Class II population are constrained by canonical disks that are viewed from face-on to edge-on inclinations.

Sub-millimeter observations with the Caltech Sub-millimeter Observatory are presented for an association of young T-Tauri stars in the Aquila star-forming region. The results of disk frequency and disk mass of this complete census are investigated in this extremely low stellar density environment.

A sub-millimeter investigation for two populations of candidate debris disk; warm and cold excess disks is presented. None of the candidate disks were detected in the sub-millimeter despite upper-limits below that expected, based on blackbody model fits to excesses at shorter wavelengths. Several scenarios are investigated in order to identify the null detection rate, such as stellar multiplicity and background-source contamination.

Finally, a partially resolved sub-millimeter map of the debris disk around the HR 8799 multiple planetary system is presented. The planet formation history of the system is investigated through the witnessed morphology of the emission.

Declaration

The work presented in Chapters 2, 3, 4, and 5 of this thesis was enabled through collaborations with multiple colleagues. The contributions of all those involved is detailed below:

Chapter 2 – *The Taurus Boundary of Stellar/Substellar (T-BOSS) objects: far-IR disk emission measured with Herschel*:

- J. Bulger was the lead investigator responsible for data reduction and analysis of the *Herschel* observations, compilation of literature studies, and performing SED model fits to the data,
- J. Patience, F. Ménard, H. Bouy, and J.-L. Monin provided guidance and assisted in the interpretation of the results,
- C. Pinte provided guidance on the implementation of the radiative transfer code MCFOST,
- K. Ward-Duong assisted in literature searches of companion studies.

Chapter 3 – *A sub-mm census of T-Tauri stars in the Aquila star-forming region*

- J. Bulger was the lead investigator, primary observer of the dataset obtained in 2012, and responsible for the data reduction and analysis of the results presented,
- J. Patience was the primary observer of the dataset obtained 2007,
- C. D. Dowell is the principle investigator of the instrument that was used for the data presented.

Chapter 4 – *Sub-mm observations of IRAS and WISE debris disk candidates]Sub-millimeter observations of IRAS and WISE debris disk candidates*

- J. Bulger was the lead investigator, primary observer of the datasets obtained at the CSO and MMT, and responsible for the data reduction and analysis of the results presented,
- T. Hufford and A. Schneider generated the model SED fits presented,
- J. Patience and I. Song provided guidance and assisted in the interpretation of the results,
- R. J. De Rosa and A. Rajan were co-observers in the data that was obtained at the CSO and MMT,
- C. D. Dowell, D. McCarthy, and C. Kulesa are the principle investigators of the instruments that were used for the data presented.

Chapter 5 – *The HR 8799 debris disk system*

- J. Bulger pursued follow-up observations at the CSO in 2010-2011, was responsible for the data reduction and analysis of the results, generated the model ray tracing images, and assisted in interpretation of the results presented,
- J. Patience was the lead investigator and primary observer of the dataset obtained at the CSO in 2007,
- B. Ayliffe and M. R. Bate were responsible for the N-body numerical simulation presented,
- C. Pinte generated the three-disk component SED fit presented,
- R. R. King, I. Song and J. Koda were co-observers whom pursued follow-up observations at the CSO between 2007-2010. The datasets of these observations were subsequently not used due to poor observing conditions,
- C. D. Dowell is the principle investigator of the instrument that was used for the data presented.
- A. Kovács assisted in discussions of the best-suited implementation of the CRUSH data reduction software for spatially extended targets.

Contents

List of Figures

List of Tables

Acknowledgements

First and foremost I would like to thank my supervisor Jenny Patience, for the guidance and encouragement that she has given me. I am sure that I would not be where I am today without her support, and I am extremely grateful for the experiences and opportunities that she has provide me with.

Numerous collaborations have gone into the research that I have undertaken over the course of my PhD, and I wish to extend my gratitude to all those involved. I gratefully acknowledge the financial support that I have received, which has enabled the research presented here. I thank the Science and Technology Facilities Council, the College of Engineering, Mathematics and Physical Sciences at the University of Exeter, and my collaborations at the School of Earth and Space Exploration at Arizona State University. I am forever indebted to all the observatory staff, whom I have been fortunate enough to come into contact with, for their contagious enthusiasm and willingness to pass on their expertise.

My thanks go to Rob, Kim and Abhi for our team observing runs at 14,000 feet to the roof top of PSF. Experiencing the clear skies and clouds together, and for always providing a ray of sunshine in the office when needed most. A big thank you goes to Freddie, Sabby, Lizzy and Barbara for holding up the fort during all the times that I've been away.

I thank my brothers, whom I can always rely on, where ever in the world each of us may be. Finally I wish to thank my parents, whom have been a complete inspiration through out my life, for their undying love and their continual support in the choices that I make.

Chapter 1

Introduction

Far-infrared (far-IR) and millimeter (mm) observations have long established that stars form in molecular clouds (e.g., Strom et al., 1975; Wilking, 1989; Lada, 1992). Theoretical considerations suggest that a natural consequence of the collapse of a rotating cloud core is the formation of a proto-star with a surrounding disk (e.g., Shu et al., 1987, 1993). These disks accrete material onto the central object and are also the host sites, providing the reservoirs of gas and dust, in which planet formation may occur. In order to understand the mechanisms in which circumstellar disks evolve and subsequently the physical processes of stellar evolution and planet formation requires knowledge of basic disk properties, such that can be obtained through direct observations and constrained through modelling procedures.

This thesis uses far-IR and sub-millimeter (submm) observations to investigate circumstellar disks properties across a range of evolutionary stages. The two key stages addressed in this thesis are:

1. proto-planetary disks – gas, rich young disks, from which material is being accreted onto a central object, and are the sites in which planets may form. Studies of these disks are presented in Chapters 2 and 3.
2. debris disks – gas poor, optically thin disks in which dust is second generation, produced by the collisional grinding of planetessimals. Studies of these disks are presented in Chapters 4 and 5.

1.0.1 Star formation and disk evolution

The most widely accepted paradigm of star formation occurs through the collapse of gravitationally bound cores within molecular clouds (e.g., McKee & Ostriker, 2007). The physical mechanisms for initiating core collapse remains unclear, though it is likely to be triggered through highly supersonic turbulent flows within molecular clouds (i.e. shock compression from convergent molecular gas streams), that give rise to local density enhancements with typical mean densities of n$\approx 10^4$-10^3 cm^{-3}, and sizes of $\sim$0.1 pc (e.g., Elmegreen & Lada, 1977; McKee & Ostriker, 2007; Williams et al., 2000). Once self-gravity of a core overcomes the resistive forces of pressure, internal turbulence and magnetic forces, collapse ensues on a free-fall timescale (Shu et al., 1987):

$$t_{\rm ff} = \sqrt{\frac{3\pi}{32G\rho}} \tag{1.1}$$

, where G is the Gravitational constant, ρ is the mean core density, and $t_{\rm ff}$ is on the order of $\sim 10^5$ years. A natural consequence of the gravitational collapse of core are flattened, disk structures due to the increase of rotational forces during the collapse and the consequence of conservation of angular momentum (e.g., Terebey et al., 1984). The subsequent evolution and lifetime of a star is dependent on its mass, and star formation is therefore traditionally divided into two regimes of low-mass and high-mass stars.

Protostellar objects are gaseous, pre-hydrogen burning objects in hydrostatic equilibrium, and as shown in Figure 1.1 appear on the Hertzsprung-Russell (HR) diagram (a plot of luminosity v.s. effective temperature), once a certain mass and size are obtained. The birth-line represents the initial conditions for pre-mainsequence contraction and the star evolves on the Kelvin-Helmholtz timescale (Kahn, 1974):

$$t_{\rm KH} = \frac{GM_\star^2}{R_\star L_\star} \tag{1.2}$$

, where G is the Gravitational constant, and $M_\star$, $R_\star$, $L_\star$ are the mass, radius and luminosity of the star respectively. The point at which hydrogen burning commences is the stage when the star enters onto the zero-age main-sequence (ZAMS), and once hydrogen burning occurs in the centre the star has entered onto its main-sequence phase. Theoretical evolutionary tracks are shown on Figure 1.1 and enable the age of a star to be estimated through its position on the HR diagram.

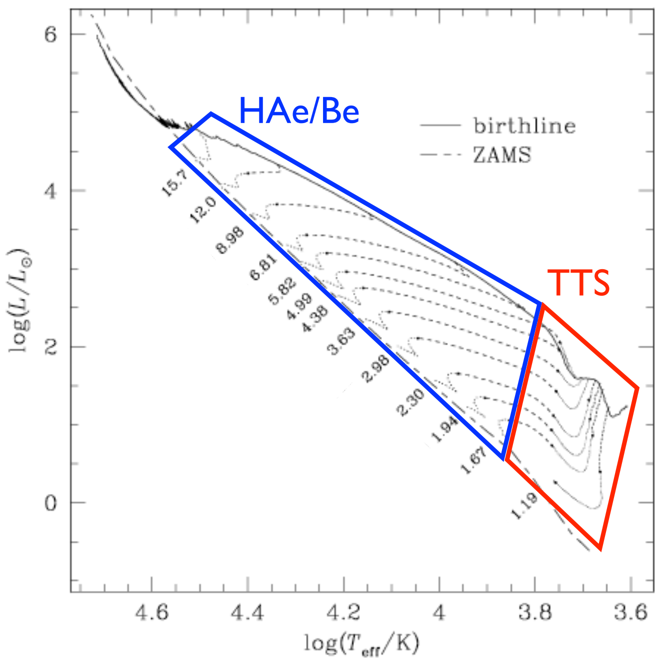

FIGURE 1.1: HR diagram, displayed by stellar effective temperature and luminosity, showing the pre-mainsequence theoretical evolutionary tracks for objects beginning at the birth-line and evolving onto the zero-age mainsequence (ZAMS). The numbers indicate the object mass ($M_\odot$) on the ZAMS. The blue zone indicates the region where Herbig Ae/Be stars are situated, and the red zone indicates the region where T-Tauri stars are situated. The plot has been adapted from Behrend & Maeder (2001).

For high-mass stars ($\gtrsim$8 $M_\odot$) the Kelvin-Helmholtz timescale is $\approx10^4$ years, therefore as $t_{\rm KH}<t_{\rm ff}$ high-mass stars reach the ZAMS before the termination of the collapse phase of protostellar evolution.

Pre-mainsequence stars have an evolutionary phase that lasts $\sim10^4 - 10^7$ years (i.e., $t_{\rm KH}\gtrsim t_{\rm ff}$), and are further classified into two categories based on their mass (as indicated in Figure 1.1). T-Tauri stars (TTS; Joy, 1945) are low-mass, pre-mainsequence stars ($M_\star\lesssim$2 $M_\odot$) of spectral types F-M, corresponding to stellar effective temperatures of ~7000-3000 K. Herbig Ae/Be stars are intermediate-mass, pre-mainsequence stars ($M_\star\sim$2-8 $M_\odot$; Herbig, 1960) of spectral type A-B, corresponding to stellar effective temperatures of ~8000-30000 K. Low-mass stars undergo an extensive pre-mainsequence evolution on the HR diagram and are the subject of Chapters 2 and 3. For low-mass stars it is generally accepted that material is transported onto the central object through an accretion disk (Shu et al., 1987), via the involvement of magnetic fields (Blanford, 1982), accretion columns (Koenigl, 1991), and X-ray winds (Shu et al., 1994). Pre-mainsequence stars are commonly referred to as young stellar objects (YSOs; Strom, 1972), and the observational characteristics and theoretical evolutionary status of these objects are further described in the following section (Section 1.0.2).

1.0.2 Young stellar objects and proto-planetary disks

The observational characteristics of YSOs are intimately linked to the association of the natal gas and dust from which they are formed. This circumstellar material absorbs and reprocesses radiation emitted by the embedded star which in turn significantly alters the spectral shape. In broad terms, the shape of the spectral energy distributions (SEDs) of YSOs depends on the nature and distribution of the surrounding material, and is therefore related to the state of evolution of the object. YSOs are typically classified based on the shape of the broad-band IR spectrum, according to the spectral index:

$$\alpha = -\frac{\mathrm{d}log(\nu F_\nu)}{\mathrm{d}log(\nu)} \tag{1.3}$$

, between ∼2-20 μm, where ν is the frequency of observation and F_ν is the observed flux (Lada, 1987). The classifications are frequently grouped into four classes, as shown in Figure 1.2 (Lada, 1987; Andre et al., 1993):

- **Class 0** objects are protostars that are not detected in the visible and IR wavelengths, as emission is blocked by a thick infalling, spherical envelope. These objects are the most deeply embedded and characterised by SEDs that peak at submm wavelengths, produced by the emission from the cold envelope with temperatures of T∼20 K. Lifetimes are on the order of $\sim 10^4$ years.
- **Class I** objects ($\alpha > 0$) have SEDs with increasing IR emission, and are protostars that are surrounded by both circumstellar disks and envelopes. These objects are often associated with bipolar outflows, that further disperse the envelope material that is accreting onto the accretion disk. Lifetimes are on the order of 1-5×10^5 years.
- **Class II** objects ($-2 < \alpha < 0$) have flat or negative slopes that correspond to excesses from dust in a disk around a pre-mainsequence star.
- **Class III** objects ($\alpha < -2$) are pre-mainsequence stars from which surrounding disk material has dissipated, and the shape of the SED is essentially photospheric with no significant excess emission at IR wavelengths.

Class II and Class III objects are visible at optical and near-IR wavelengths. Due to the youth of these objects (t $\approx 1-10$ Myrs), the circumstellar disks of gas and dust surrounding these stars are typically referred to as proto-planetary disks, since planet formation is believed to occur within the disk and within the timeframe of $\sim 3-10$ Myrs.

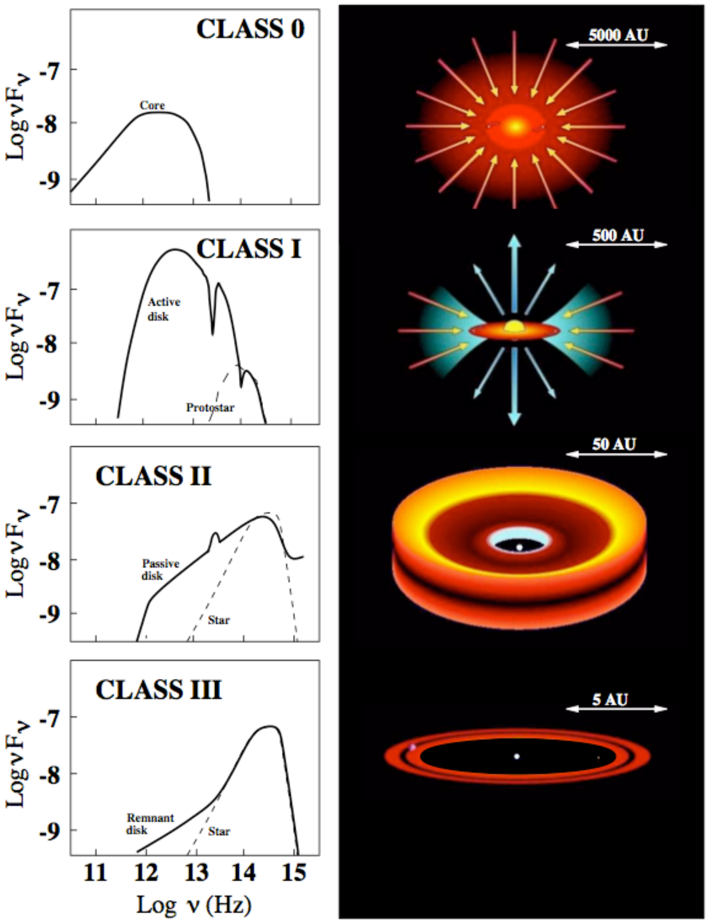

FIGURE 1.2: Empirical evolutionary stages showing different classes of young stellar objects. The lefthand panel shows the characteristic SED shapes of the corresponding object class depicted in the righthand panel. Class 0 represents the earliest stages of star formation in which the proto-star is deeply embedded with in a massive envelope of accreting material. Class III objects are the most evolved objects around which the proto-planetary disk has dispersed. Figure credit: M. McCaughrean.

1.0.3 Disk structure and SED modelling

SED modelling of proto-planetary disks provides an indirect means to determine characteristic global properties of disks. In addition to the constraints set from multi-wavelength observations of large-scale surveys of YSOs across a range of evolutionary stages, SED modelling plays a critical role in determining the physical evolution of disk structure and the material within them, which in turn may subsequently form planets. Proto-planetary disks have a rich structure with different physical mechanisms dominating in different regions of the disk. This section outlines the various disk models that have been used and developed upon through constraints of direct observations.

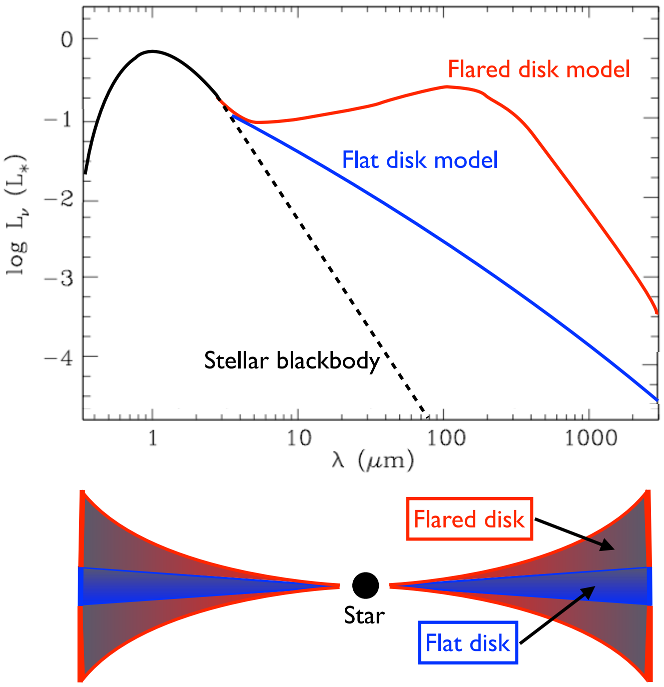

FIGURE 1.3: The top plot represents the characteristic SEDs shapes of flat disks (blue line) and flared disks (red line). The dashed line shows the contribution of emission from the stellar photosphere. The bottom cartoon diagram represents the flat disk (blue region) and flared disk (combined blue and red regions) geometric shapes, as viewed edge-on. The flared disk intercepts a larger fraction of the stellar radiation at larger radii, and correspondingly excesses are greater than that of a flat disk at far-IR and mm wavelengths. The SED has been adapted from Chiang & Goldreich (1997).

Adams et al. (1987) showed that a flat, opaque dust disk will absorb and re-radiate a significant fraction of stellar emission that produces a sizeable excess in the IR, as demonstrated in Figure 1.3. Models in which the disk heating mechanism is solely due to irradiation from the central source are referred to as irradiated or passive disk models. Furthermore from observation and theory it is known that young pre-mainsequence stars continue to accrete material from their circumstellar disks. The accretion rates for T-Tauri stars are typically observed to be in range of $10^{-10} - 10^{-7}$ M$_\odot$/yr (Gullbring et al., 1998). Due to the frictional forces that cause net inward motion, gravitational energy is converted into heat (e.g., Lynden-Bell & Pringle, 1974). Disk models that account for this viscous/accretion heating are referred to as active disk models.

The radial temperature distribution of a disk is determined by the energy balance between heating and cooling of disk material. In the simple case of a flat, passive disk model the luminosity of the star is:

$$L_\star = 4\pi R_\star^2 \sigma_{\rm SB} T_{\rm eff}^4 \qquad (1.4)$$

, where $R_\star$ is the radius of the star, $\sigma_{\rm SB}$ is the Stefan-Boltzmann constant, and $T_{\rm eff}$ is the stellar effective temperature. Assuming that the thickness (h) of the disk is negligible ($h \ll R_\star$), the incident flux to a unit area of the disk is:

$$F_{\star\ \rm irr} = \frac{L sin\theta}{4\pi r^2} \tag{1.5}$$

, where θ is the mean incident angle of irradiation, approximated as $\frac{0.4R_\star}{r}$. The radiative cooling flux from a unit area of the disk is:

$$F_{\rm cool} = \sigma_{\rm SB} T_{\rm eff}^4 \tag{1.6}$$

, and the temperature profile of the disk is therefore:

$$T = T_{\rm eff} \left(\frac{r}{R_\star} \right)^{-\frac{3}{4}} \tag{1.7}$$

In the case of active disk models, where accreting material acts as an additional source of heating, at large distances from the star ($r \gg R_\star$), the accretion luminosity is:

$$L_{\rm acc} = \frac{G M_\star \dot{M}_{\rm acc}}{R_\star} \tag{1.8}$$

, where G is the gravitational constant, and $\dot{M}_{\rm acc}$ is the mass accretion rate. The temperature profile of the disk then follows:

$$T \propto \left[\dot{M}_{\rm acc} + \frac{L_\star}{r^2} \right]^{\frac{1}{4}} \tag{1.9}$$

, and shows that the disk temperature is dominated by stellar irradiation at large distances, whilst at small distances accretion is the dominant heating mechanism.

It was shown that the observed SEDs of young stars fall less steeply than the $\lambda F_\lambda \propto \lambda^{-\frac{4}{3}}$ decline expected from the temperature distribution of flat, active disk models. Subsequent disk models incorporating flared surfaces (see Figure 1.3) were shown to provide better fits to the observed SEDs (e.g., Kenyon & Hartmann, 1987). Flared disks are expected to be in vertical hydrostatic equilibrium, where the gravity of the central star is balanced by the gas pressure. Assuming that a disk axisymmetric and the force balance is for $z \ll r$:

$$-\frac{G M_\star}{r^3} z - \frac{1}{\rho} \frac{{\rm d}P}{{\rm d}z} = 0 \tag{1.10}$$

, where ρ is the gas density, P is the gas pressure, and therefore assuming that the disk is vertically isothermal, the density of the disk that solves Equation 1.10 is given by:

$$\rho(z) = \rho_0 e^{\left(-\frac{z^2}{2H^2}\right)} \tag{1.11}$$

, where ρ_0 is the density at the mid-plane of the disk and H is the disk scale-height defined as:

$$H = \left(\frac{R_\star c_\mathrm{s}^2}{GM_\star}\right)^{\frac{1}{2}} \tag{1.12}$$

, where c_s is the isothermal sound speed.

Existing flared disk models show that $H \propto r^{\frac{9}{7}}$ and therefore $T \propto r^{-\frac{3}{7}}$, a temperature gradient that is much less steep than the temperature profile of $T \propto r^{-\frac{3}{4}}$ for flat disk models, since flared disks can capture more radiation from the star.

The work in this thesis uses the 3D Monte Carlo radiative transfer code MCFOST (Pinte et al., 2006, 2009) to model SEDs of proto-planetary disks (Chapter 2) and the HR 8799 debris disk system (Chapter 5). MCFOST determines the temperature distribution of circumstellar dust self-consistently and uses Mie theory to account for the absorption and scattering events between the modelled photons and particles. The input parameters for modelling with MCFOST are:

- properties of the central star; $R_\star$, T_eff, and $M_\star$,
- dust grain properties; a_min, a_max, and the grain size distribution which is typically set to follow the power-law $n(a) \propto a^{-3.5}$, where the power-law index follows that observed in the inter-stellar medium (Mathis et al., 1977),
- geometry of the circumstellar disk; R_in, R_out, disk inclination, H, and disk surface density, which is the vertically integrated column density defined as: $\Sigma(z) = \int_{-\infty}^{+\infty} \rho \, \mathrm{dz}$. Assuming axial symmetry the of the disk Σ and H are parameterised following the power-laws: $\Sigma(r) = \Sigma_0 \left(\frac{r}{r_0}\right)^{-p}$ and $H = H_0 \left(\frac{r}{r_0}\right)^{\beta}$. The power-law indices p and β are constrained through imaging observations of circumstellar disks.

1.0.4 Disks around young brown dwarfs

Both theories and observations of brown dwarfs have highlighted the importance of searching for disks around these low mass objects. Formation scenarios for brown dwarfs include ejection of stellar embryos (e.g., Bate et al., 2003; Reipurth & Clarke, 2001), disk fragmentation (e.g., Stamatellos & Whitworth, 2009), and erosion of star-forming clouds by radiation from massive stars (Hollenbach et al., 1994). It is still an open question whether disks around stars of different masses evolve alike. Based on near-IR and mm observations, proto-planetary disk fractions around brown dwarfs are either roughly equal to those around more massive stars (e.g., Luhman et al., 2005), or higher (Scholz et al., 2007; Luhman et al., 2008). SED modelling hints at similar dust processing and disk clearing phases for brown dwarfs and their higher mass counterparts (Pascucci et al., 2011), but disks around brown dwarfs may be flatter (Szűcs et al., 2010) or similar (Mulders & Dominik, 2012) compared to those around their more massive counterparts.

Brown dwarfs also greatly outnumber the more massive solar type stars and are an attractive target for exoplanet searches because of their proximity and low mass. Brown dwarf proto-planetary disks offer a physically different environment (compared to disks around more massive stars) to study disk structure and evolution because of the lower stellar heating and ionizing flux. The observation of a brown dwarf with a directly-imaged planetary mass companion indicate that at least some substellar objects support disks with masses, sizes, and lifetimes sufficient for planet formation early in their history (Chauvin et al., 2004; Song et al., 2006). Alternatively, this pair may have formed in a manner analogous to binary stars. Observations of young brown dwarfs are essential to understand the potential for planet formation around brown dwarfs. Furthermore, the population of exoplanets orbiting low mass stars shows suggestive differences to the corresponding exoplanet population around more massive stars, yet the exoplanet frequency remains unclear around brown dwarfs (e.g., Johnson et al., 2010). By detecting and investigating the disk properties around young late M-stars and brown dwarfs, it is possible to investigate the origins of the exoplanet populations. With the sensitivity and resolution offered from observations with the *Herschel* Space Observatory (Pilbratt et al., 2010) it is possible to quantitatively study disks around brown dwarfs at far-IR wavelengths. In Chapter 2 of this thesis, far-IR observations obtained with *Herschel* are presented, providing a 97% complete census of low-mass stars and brown dwarfs in the Taurus star-forming region.

1.0.5 Multi-wavelength observations

Circumstellar disks exhibit a large range in spatial scale, density and temperature, and therefore different observational techniques have to be applied that probe the various different regions of the disk. As demonstrated in Figure 1.4; optical and near-IR wavelengths revel light scattered from the disk surface, mid-IR wavelengths probe the hot inner (∼1-10 AU), disk surface layers, where emission is optically thick, with far-IR observations extending further radially outward, and observations in the submm-mm wavelengths ($\gtrsim$10 AU) are sensitive to the cool dust grains in the outer disk region. With the unprecedented resolution and sensitivity obtained with *Herschel* across the far-IR - submm, full wavelength coverage can be achieved for large scale surveys of proto-planetary disks. Wide range, multi-wavelength coverage is essential in deriving disk properties through SED modelling procedures. The large number of free parameters prescribed in disk structure, such as scale height, inner and outer disk radius, flaring index, disk mass, inclination and grain properties leads to a high degree of degeneracy between model fits if unconstrained by observations (e.g., Wood et al., 2002).

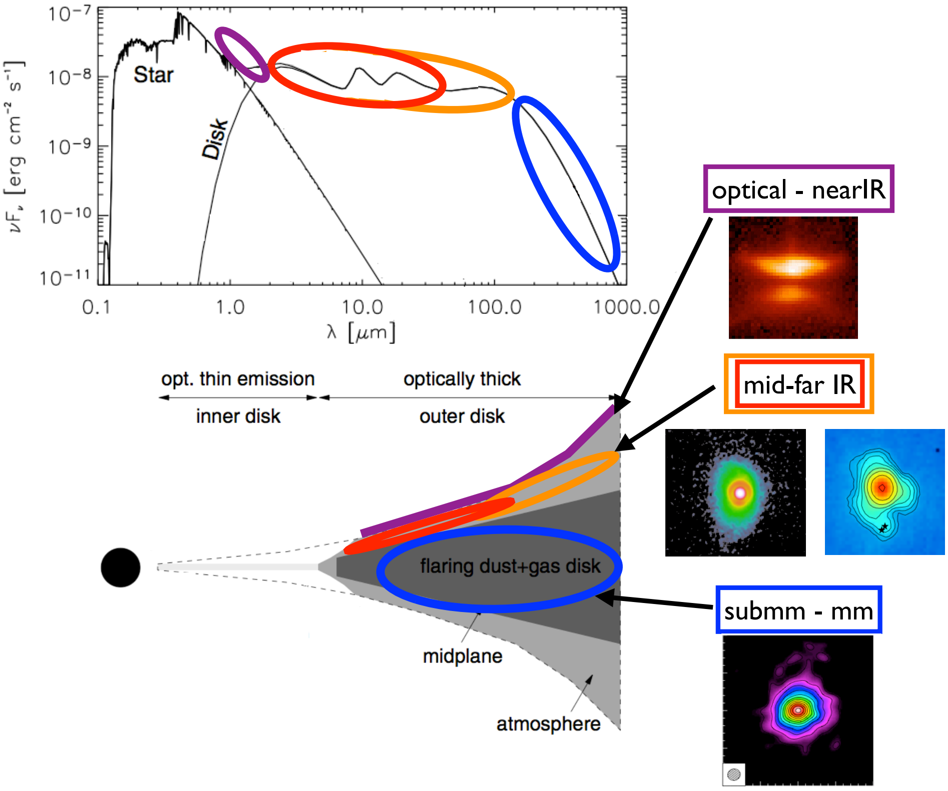

FIGURE 1.4: Schematic view showing the disk regions probed with observations at optical-mm wavelengths. Optical and near-IR observations reveal light scattered from the disk surface. Mid- and far-IR observations trace emission from the optical thick surface layers of the disk. Emission at submm-mm wavelengths is optically thin and probe cool dust grains in the mid-plane and outer disk regions. SED and disk cross-section schematic are adapted from Dullemond et al. (2006) and Ratzka et al. (2007). Optical-submm images are extracted from Burrows et al. (1996); Okamoto et al. (2009); Howard et al. (2013) and Isella et al. (2010)

Observations of disks at submm-mm wavelengths are of particular interest since in this wavelength regime the observed flux provides a direct estimate of the disk mass, allowing constraints on the timescales and mechanisms of planet formation to be made. Assuming that the dust particles within a disk emit as blackbody radiators, the observed flux at any given frequency is given by:

$$F_\nu = 2\pi \frac{\cos\theta}{D^2} \int_{\mathrm{R_{in}}}^{\mathrm{R_{out}}} B_\nu(T_\mathrm{d})(1 - \mathrm{e}^{-\tau_\nu}) r \ \mathrm{dr} \tag{1.13}$$

, where θ is the disk inclination (typically defined as θ=0° for a face-on disk), D is the distance to the source, $\mathrm{R_{in}}$ and $\mathrm{R_{out}}$ are in inner and outer disk radii, B_ν is the Planck function, T_d is the characteristic dust grain temperature, and the optical depth τ_ν is defined as:

$$\tau_\nu = \frac{\kappa_\nu \Sigma(r)}{\cos\theta} \tag{1.14}$$

, where κ_ν is the dust opacity, $\Sigma(r)$ is the vertical column density and directly corresponds to the disk mass as: $M_\mathrm{d} = 2\pi \int_{\mathrm{R_{in}}}^{\mathrm{R_{out}}} \Sigma(r) r \ \mathrm{dr}$. Assuming emission at the observed frequency is optically thin ($\tau_\nu \ll 1$) therefore $(1 - \mathrm{e}^{-\tau_\nu}) \rightarrow \tau_\nu$, for a face-on disk, Equation 1.13 reduce to:

$$F_\nu = \frac{2\pi}{D^2} \int_{\mathrm{R_{in}}}^{\mathrm{R_{out}}} B_\nu(T_\mathrm{d}) \kappa_\nu \Sigma(r) r \ \mathrm{dr} \tag{1.15}$$

In the Rayleigh-Jeans limit ($h\nu \ll \mathrm{k_B}T$) $B_\nu(T_\mathrm{d}) = \frac{2\nu^2 \mathrm{k_B} T_\mathrm{d}}{c^2}$, where $\mathrm{k_B}$ is the Boltzmann constant and c is the speed of light, Equation 1.15 further reduces to:

$$F_\nu = \frac{2\pi}{D^2} \frac{2\nu^2 \mathrm{k_B} T_\mathrm{d}}{c^2} \kappa_\nu \int_{\mathrm{R_{in}}}^{\mathrm{R_{out}}} \Sigma(r) r \ \mathrm{dr} \tag{1.16}$$

The disk mass is therefore calculated as:

$$M_\mathrm{disk} = \frac{F_\nu D^2 c^2}{2\nu^2 \mathrm{k_B} T_\mathrm{d} \kappa_\nu} \tag{1.17}$$

The dust opacity in disks at submm and mm wavelengths is typically characterised as:

$$\kappa_\nu = \kappa_0 \left(\frac{\nu}{\nu_0}\right)^\beta \tag{1.18}$$

, where $\kappa_0 = 0.1$ cm^2 g^{-1} at $\nu_0 = 10^{12}$ Hz (Beckwith et al., 1990). This normalisation implicitly includes a gas-to-dust ratio of 100:1, and is estimated from compositional measurements of the interstellar medium (Pollack et al., 1994). Results of SED modelling conducted over IR-mm wavelengths by Andrews & Williams (2005) for large sample of proto-planetary disks in the Taurus star-forming region show that the derived disk mass in Equation 1.17 is reasonably accurate with $T_{\rm dust}$ = 20 K (Williams & Cieza, 2011). In Chapter 3 a complete census of submm observations for an association of T-Tauri stars in the Aquila star-forming region are presented. The results of which are used to investigate disk frequency and disk mass across a range of different stellar density environments.

1.0.6 Debris disks

Debris disk were first identified through IR excess observed with the Infrared Astronomical Satellite (*IRAS*). The SEDs of main-sequence stars with circumstellar material shows IR excess above ∼10 μm, from which it is possible to constrain the dust size, spatial distribution, and total mass of the disk (Backman & Paresce, 1993). Given the timescale for the dust to spiral into the star or be ejected from the system, due to scattering, Poynting-Roberston drag, or radiation pressure, these disks of dust must be sustained by an ongoing process such as the collisional grinding of planetesimals into smaller particles or an event such as a catastrophic collision of planets (Cameron, 1997). Debris disk systems represent an important phase of the planet formation process and their detailed study can provide key insights into the evolution of planetary systems.

The majority of information about debris disk systems is derived from the SED of the star. Given the limited number of broadband photometric observations, excesses are typically modelled with a single temperature blackbody fit, where the peak wavelength of emission corresponds to the orbital distance at which the dust grains lie. Mid-IR wavelengths probe temperatures of ∼200 K, where the grains reside at a few AU, equivalent to the distance of the Asteroid belt. Far-IR and submm wavelengths probe temperatures $\lesssim$50 K from tens to hundreds of AU, and corresponding to distances equivalent to that of the Kuiper belt. Submm observations of debris disks are especially critical as the emission is close to the Rayleigh-Jeans limit, providing a direct measurement of the disk mass.

It is important to understand the distribution and mass of dust present in these warm and cold debris disk systems since they may exhibit important similarities to the early Solar System. In our Solar System, zodiacal particles are warm ($\gtrsim$ 160 K) dust grains found within ∼3 AU of the Sun. Slow, persistent collisions between asteroids, augmented by material released from comets, continue to replenish these particles. Lunar surface cratering statistics bear witness to a much more violent collisional history - when the Solar System was $\lesssim$ 600 Myr old, the impact rate of bodies in the region of the terrestrial planets was as large as 1000 times the current rate. The dust production rate in the young zodiacal may have therefore been orders of magnitude larger than the current value. Collisions between solid bodies around youthful Sun-like stars are manifested as strong excess emission at mid-IR wavelengths and would point toward ongoing formation and evolution of planets in the terrestrial planet zone. The dust grains in warm excess debris disks are quickly removed on a timescale much shorter than the age of stars. Two leading theories that explain the abundance of dust in these systems are (1) a large influx of small scale collisions or (2) giant collision involving planetary bodies.

1. Numerous small-scale catastrophic collisions among a large population of solid bodies, analogous to the late heavy bombardment (LHB) in the Solar System, can create the observed amounts of dust grains detected in the warm excess. LHB, also known as Lunar Cataclysm is a posited event that happened in the inner Solar System about 3.9 Gyr ago (Cohen et al., 2000). In one model of the LHB, migrating giant planets and on-set of Jupiter and Saturns orbital resonance stirred up planetesimals, sending them into the inner planetary system (e.g., Gomes et al., 2005). This abrupt increase of impactor influx at the inner planetary region created abundant dust grains orders of magnitude higher than in quiescent stage.
2. The abnormally large specific angular momentum of the Earth-Moon system provides another possible source for high dust levels since it can be easily explained by an oblique collision between the young Earth and a body with comparable mass (Hartmann et al., 1975). In this picture, the young Earth was thought to have collided with a Mars sized planet when our Earth was about 30-50 Myr old (Kleine et al., 2005). Large quantities of dust ($\lesssim$90% of the impactor) were ejected onto circum-terrestrial and solar orbits (Cameron, 1997; Canup, 2007). The Moon was rapidly accreted from the circum-terrestrial disk while the solar-orbiting material would have temporarily caused our Sun to appear as an extreme mid-IR excess star.

By combining of mid-IR and submm observations of debris disks it is possible to understand if the dust is confined to the inner regions around the star and more likely to be caused by a giant impact on a planet rather than a LHB event producing dust throughout the system and causing a submm excess. In Chapter 4 the results of submm observations for a set of warm and cold debris disk candidates is presented.

In addition to broadband photometry, for a small fraction of debris disks it is possible to resolve the disk through direct imaging. These images are produced by the scattered

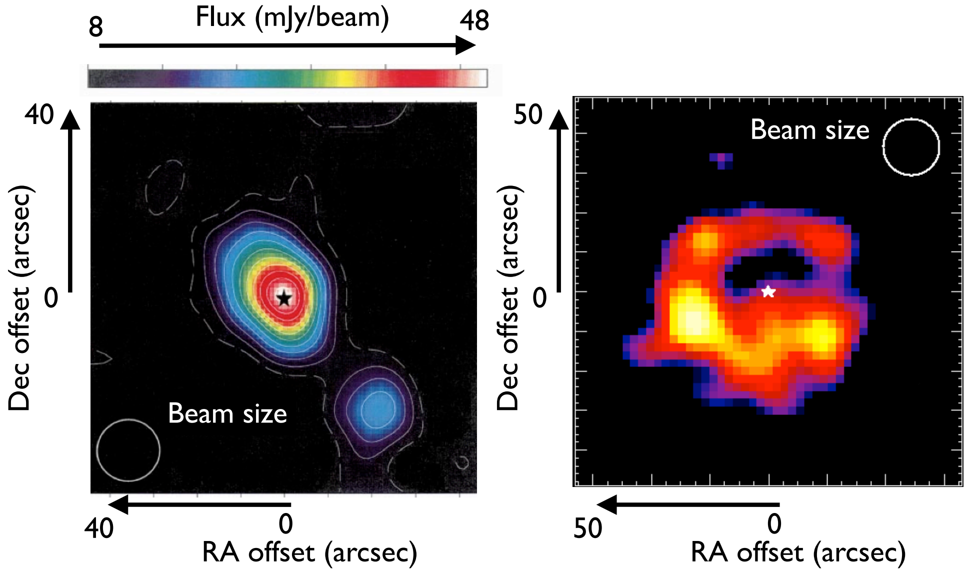

FIGURE 1.5: Resolved submm (850 μm) maps of debris disks around β Pic (**left**) and ϵ Eridani (**right**). Different morphologies are witnessed in each map, brightness asymmetry and clumpy disk structure. Such structures are interpreted to be due to the presence of a perturbing planetary body. Figures extracted from Holland et al. (1998) and Greaves (2005).

light at optical wavelengths, or through thermal emission that trace warm inner disk regions in the mid-IR, or the cold outer disk regions in the submm. Due to the limited sensitivity and resolution of ground based submm observatories, only a handful of debris disk systems have been resolved at submm wavelengths. Resolved observation of debris disk are critical since they provide a direct measure of the disk size, and dynamical interactions of planets may sculpt the disk structure (e.g., Wyatt, 2006; Reche et al., 2008). A broad range in disk morphologies witnessed in the emission and can indicate the presence of a perturbing planetary body. As shown in Figure 1.5 the brightness symmetry seen in the 850 μm map of β Pic is believed to caused by the confirmed planetary companion β Pic b (Holland et al., 1998), and the clumpy disk morphology witnessed in the 850 μm map of ϵ Eridani map be due to the emission of dust grains associated with material that is trapped in resonance with a planet orbiting interior to the disk (Greaves et al., 1998).

Observations at submm wavelengths are ideal for studying the interaction of the disk and planets, since the large grains are expected to remain in resonances with the planets, while the smaller grains evolve into axisymmetric structures due to scattering or radiation pressure as demonstrated in Figure 1.6. The HR 8799 debris disk system is currently the only system in which multiple planets have been directly imaged (Marois et al., 2008, 2010), and is a rare case in which it is possible to explore the dynamical effects on disk structure of planets with known locations, further providing insight into the planet formation and stability of the system (e.g., Dodson-Robinson et al., 2009; Currie et al., 2011; Goździewski & Migaszewski, 2009). In Chapter 5, the results of a partially resolved submm map, and numerical planet-disk interactions of the HR 8799 debris disk system are presented.

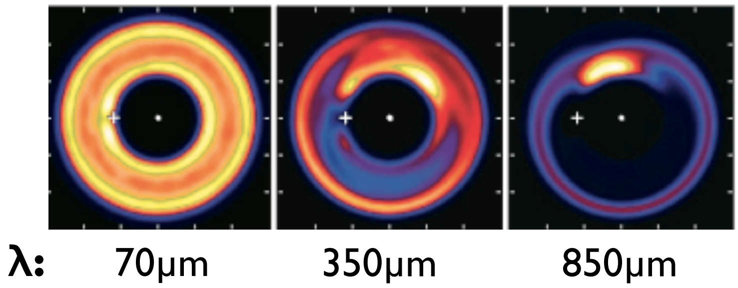

Figure 1.6: Simulations showing the distributions of dust grains in a debris disk (viewed face-on) as observed at far-IR to submm wavelengths. The dust grains within the debris disk are generated through the collisional grindings of planetessimals trapped in a 2:1 resonance with that of a planet. Dust grains of different sizes are subject to radiation and gravitational forces that cause the grains to either evolve out into axisymmetric structures or remain in resonance with the planet. Figure adapted from Wyatt (2006).

1.0.7 Open questions

As discussed in the previous sections it is known that stars form in collapsing interstellar clouds, that young stars are surrounded by dense, gas- and dust-rich proto-planetary disks in which planets can form, and that debris disks is what remains around the star after the dispersal of the primordial material at ages of $\lesssim$10 Myr. The existence of debris disks around mainsequence stars provides evidence that planetessimal formation in protoplanetary disks is efficient. However, it is not known how these planetessimals, and subsequently planets typically form. Therefore key questions that can be asked in the study of circumstellar disks are: what is the geometry and structure of proto-planetary disks around low-mass stars and brown-dwarfs? Are all proto-planetary disks massive enough for planet formation to occur? How do environmental factors such as stellar density effect the properties of proto-planetary disks? Are warm and cold debris disk components typical around mainsequence stars? Do planets effect the observed debris disk morphology through gravitational perturbations? These questions are addressed throughout this thesis with observations primarily focusing at far-IR and submm wavelengths of both proto-planetary disks and debris disks, and are discussed in the subsequent chapters.

Chapter 2

The Taurus Boundary of Stellar/Substellar (T-BOSS) objects: far-IR disk emission measured with *Herschel*

From Bulger, J., Patience, J., Ward-Duong, K., et al., submitted to A&A

Abstract

With the PACS instrument on *Herschel*, 134 low mass members of the Taurus star-forming region, spanning the M4-L0 spectral type range and covering the transition from low mass stars to brown dwarfs were observed. Combining the new *Herschel* results with other *Herschel* programs, a total of 150 of the 154 M4-L0 Taurus members members have observations, and we have performed a 97% complete study of the TBOSS (Taurus Boundary of Stellar/Substellar) sample. Among the 150 targets, 70 μm fluxes were measured for 7 of the Class I objects, 48 of the 67 Class II members, and 3 of the 76 Class III targets. For the detected Class II objects, the median 70 μm flux level declines with spectral type, however the distribution of excess relative to central object flux does not change across the stellar/substellar boundary in the M4-L0 range. Connecting the 70 μm TBOSS values with the results from K0-M3 Class II members results in the first comprehensive census of far-IR emission across the full mass spectrum of the stellar and substellar population of a star-forming region, and the median flux declines with spectral type in a trend analogous to the flux decline expected for the central objects. Spectral energy distributions (SEDs) were constructed for all TBOSS targets covering the optical to far-IR range and extending to the submm/mm for a subset of sources. Based on an initial exploration of the impact of different physical parameters on the *Herschel* fluxes, geometrical factors such as inclination and structural parameters such as scale height and flaring have the largest influence on the fluxes in the PACS bands. From an initial test grid of model SEDs generated with the radiative transfer code MCFOST, 73% of the observed Class II population are constrained by face-on to edge-on disk inclinations. From the 24 μm to 70 μm spectral index of the SEDs, 5 new candidate transition disks were identified. Considering the previously known and new candidate transition disks, the spectral indices over longer wavelengths are not distinct to those of the full Class II population, suggesting that the outer regions of the transition disks are similar to Class II disks. The steep 24 μm to 70 μm slope for a subset of 8 TBOSS targets may be an indication of truncated disks in these systems, however additional measurements are required to establish the outer radii of these disks conclusively. Given the limited number of high angular resolution companion search observations of the TBOSS sample, it is not possible to determine the frequency of disks in low mass multiple systems, although interesting individual systems including a ~5 AU pair with disk emission and two examples of mixed pairs including secondaries with disks were measured in the *Herschel* data. Finally, comparing the TBOSS results with a *Herschel* study of Ophiuchus brown dwarfs reveals a higher fraction of disks around the Taurus substellar population.

2.1 Introduction

Disks are critical structures in the star and planet formation process, as they provide a conduit to channel material onto the central object (e.g. Hartmann, 1997) and supply a reservoir of dust and gas to form planets (e.g. Pollack et al., 1996; Boss, 1997). Variations in the frequency, lifetimes, and structure of disks as a function of central object mass have important implications for formation models (e.g. Bate et al., 2003; Reipurth & Clarke, 2001) and the viability of future planet formation. Infrared and mid-infrared observations of young brown dwarfs (e.g. Luhman, 2006; Luhman et al., 2010; Guieu et al., 2007) have enabled the identification of inner disks. This common presence of disks around stellar and substellar objects has been used to argue for a common formation mechanism (Scholz & Jayawardhana, 2008; Haisch et al., 2010), while other observations hint at possible differences in the dynamical history of low mass stars/brown dwarfs compared to higher mass stars (Thies & Kroupa, 2007). Formation scenarios for brown dwarfs also have implications for the properties of brown dwarf disks, and a number of possible mechanisms have been proposed, including ejection of stellar embryos (e.g.

Bate et al., 2003; Reipurth & Clarke, 2001), erosion of star-forming clouds by radiation from massive stars (Whitworth & Zinnecker, 2004), gravitational instabilities in the early stages of disks (e.g. Stamatellos & Whitworth, 2011; Basu & Vorobyov, 2012), and gravitational collapse of clouds analogous to the formation of stars (e.g. Padoan et al., 2005; Hennebelle & Chabrier, 2008).

Trends in the population of exoplanets orbiting low mass stars have suggested intriguing differences compared to the planetary systems around more massive stars and observations of protoplanetary disks around low mass objects are required to investigate possible origins of the distinct populations. Analysis of the Kepler planet candidate statistics shows a steep increase in the occurrence of planets with the smallest radii as host star mass declines (Howard et al., 2012). By contrast, the frequency of Hot Jupiters around M-stars is lower than for higher mass stars (e.g. Johnson et al., 2010). The detection of brown dwarfs with directly-imaged planetary mass companions (Chauvin et al., 2004; Song et al., 2006) indicate that at least some substellar objects are associated with planet formation early in their history. The overall exoplanet population frequency remains unclear around brown dwarfs. By detecting and characterizing the disks around young M-stars and brown dwarfs, it is possible to investigate the origins of the exoplanet populations.

As one of the nearest regions of star-formation (∼140 pc; Kenyon et al., 1994; Bertout et al., 1999; Torres et al., 2009), Taurus represents an important population of young stars and brown dwarfs for which detailed investigations of disk frequencies and properties are possible. The stellar density of the Taurus region is uniquely low (4-30 stars/pc^3, Gomez et al., 1993), which enables isolating the individual objects and avoiding confusion within the beam of longer wavelength observations. Large scale surveys of Taurus members have identified the presence of disks based on excess emission above the photosphere out to 24 μm with sensitive *Spitzer* measurements (e.g. Luhman et al., 2010), but these wavelengths do not probe the cooler material in the disk that covers the portions of the spectral energy distributions over which the emission transitions from optically thick to optically thin, and is strongly influenced by factors such as flaring, scale height, and settling. The *Spitzer* survey of Taurus at 70 μm (Rebull et al., 2010) detected a large population of the earlier spectral type members, but did not have the sensitivity to measure disk emission from the lowest mass stars and brown dwarfs. In Taurus, ∼50% of all members have spectral types later than M3 (Luhman et al., 2010), making the existing far-IR measurements fundamentally incomplete and resulting in a biased view of the early stages of star and planet formation. As pre-mainsequence stars contract onto the mainsequence (e.g. Chabrier et al., 2000), their effective temperatures increase and a spectral type of M4 in a star-forming region corresponds to ∼M2 at an age of 1Gyr, comparable to the ages of the stars in the Solar Neighbourhood. Among the nearest stars, the majority are M-dwarfs (e.g. Reid & Gizis, 1997; Henry, 1998), again highlighting the importance of understanding the environments of low mass stars to develop a comprehensive disk population study.

To obtain a nearly complete census of far-IR emission across the full population of Taurus, we have performed a large-scale survey of low mass stars and brown dwarfs with *Herschel*, targeting the M4-L0 members to extend the exploration of disk mass and structure into the substellar regime with a sensitivity that was not possible prior to *Herschel*. The nearly complete sample for this study is defined in Section 2.2, followed by the new *Herschel* PACS observations in Section 2.3. The data analysis including the measurement of far-IR fluxes and construction of the SEDs for each target in the full sample is described in Section 2.4. The results for the members of each evolutionary class, a comparison with *Spitzer* data, the detection rates, and spatially extended and multiple sources are reported in Section 2.5. In Section 2.6, the discussion covers a number of topics including the dependence of the results on spectral type and companions, the SEDs for different types of targets such as transition disks, and a comparison of the Taurus substellar disks with the population in Ophiuchus. Finally, Section 2.7 summarizes the conclusions.

2.2 Sample

The target sample was selected to provide a comprehensive census of far-IR disk emission from Taurus members spanning both sides of the stellar/substellar boundary. The demarcation of the substellar boundary occurs at a spectral type of M6.25 at the age of Taurus (e.g. Luhman et al., 2005), and the spectral type range of the TBOSS (Taurus Boundary Of Stellar/Substellar) sample is M4-L0. From a *Spitzer* 3-24 μm study of the Taurus population (Luhman et al., 2010), 152 M4-L0 members were included, which represented 99% of the membership, with the remaining 1% of the Taurus population comprised of objects with spectral types earlier than M4. Of the new Taurus members identified in a *Spitzer* study including 70 μm data (Rebull et al., 2010), all but 2 with spectral types of M4 and later were included in the Luhman et al. (2010) study. Of the 154 M4-L0 members listed in the combination of the *Spitzer* studies, *Herschel* Photodetector Array Camera and Spectrometer (PACS; Poglitsch et al., 2010) 70 μm or 100 μm and 160 μm fluxes or detection limits are reported for 150 objects - a 97% complete census of the low mass stars and brown dwarfs in Taurus.

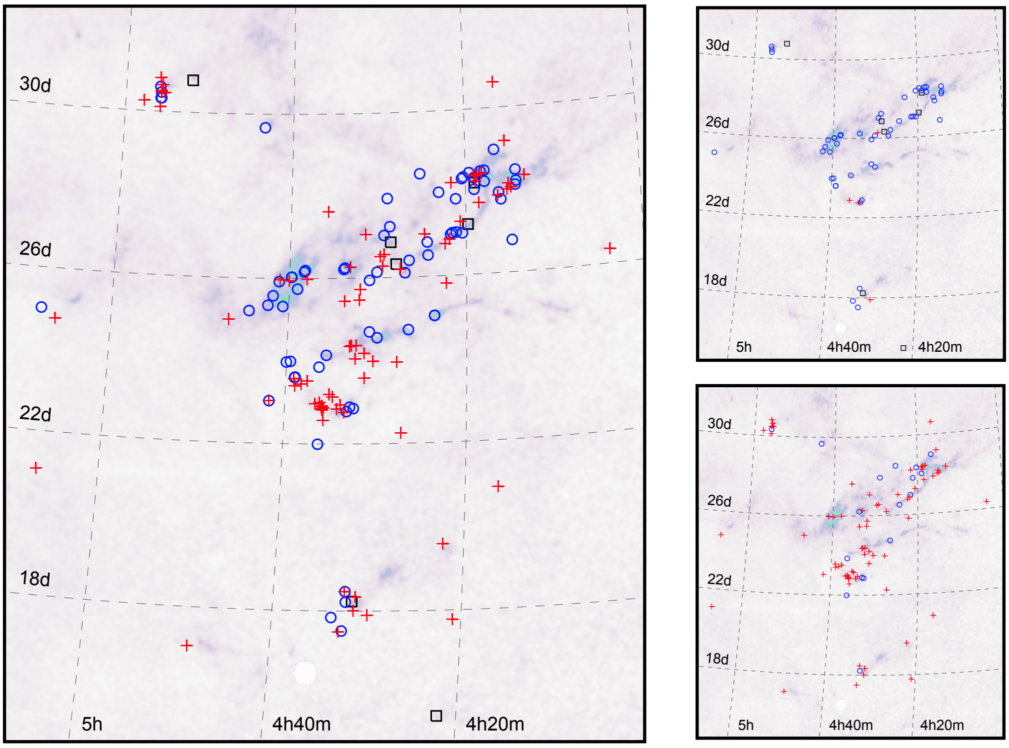

Figure 2.1: The spatial distribution of the TBOSS sample across the Taurus molecular cloud (shown in the map of extinction from Dobashi et al., 2005) is shown on the left. Black squares indicate Class I objects, blue circles indicate Class II objects, and red crosses indicate Class III objects. The distribution of the TBOSS sample with *Herschel* PACS detections are shown in the top, right map and the distribution of the TBOSS sample with *Herschel* PACS upper limits are shown in the bottom, right map.

The large majority of the *Herschel* observations, covering 134 targets, were performed as part of our program (OT1_patienc_1). The results for 12 targets were drawn from the literature - 4 targets from Harvey et al. (2012) from the program GT1_pharve01_2, and 8 targets from Howard et al. (2013) from the program KPOT_bdent_1 as part of the Gas Survey of Protoplanetary Systems (GASPS; Dent et al., 2013). Another 4 targets were observed as part of the Guaranteed Time Key Programme, KPGT_pandre_1 and the level 2.5 processed archive maps were analyzed. For the 4 targets not observed by *Herschel*, far-IR *Spitzer* measurements exist for J04251550+2829275, J04355760+2253574, IRAS S04414+2506 (Rebull et al., 2010), but no measurements exist for XEST 26-052. Table 2.1 reports the 2MASS name, alternate name, evolutionary class and spectral type of each of the 154 M4-L0 Taurus members with either *Herschel* or *Spitzer* far-IR photometry. The 154-object TBOSS sample includes 7 Class I, 69 Class II, and 78 Class III members, and 63 of the targets are brown dwarfs (M6.25-L0). The spectral types have been compiled from the original reference (noted in Table 2.1) and, for the targets with more than one spectral type measurement reported, the most recent result was adopted for this study.

Figure 2.1 shows the distribution of the TBOSS sample across the Taurus molecular cloud.

Table 2.1: TBOSS sample properties, ordered by evolutionary class and spectral type.

2MASS	Other name	SED class[1]	SpTy.	Ref.	Notes
J04520668+3047175	IRAS 04489+3042	I	M4 ± 1	5	
J04275730+2619183	IRAS 04248+2612	I	M4.5 ± 0.25	5	
J04185813+2812234	IRAS 04158+2805	I	M5.25 ± 0.25	5	
J04313613+1813432	LkHa 358	I	M5.5 ± 1	16	
J04220007+1530248	IRAS 04191+1523 B	I	M6-M8	2	g
...	L1521F-IRS	I	M6-M8	2	g
J04194657+2712552	[GKH94] 41	I	M7.5 ± 1.5	3	
J04144730+2646264	FP Tau	II	M4 ± 1	16	
J04174965+2829362	V410 X-ray 1	II	M4 ± 0.5	17	
J04202583+2819237	IRAS 04173+2812	II	mid-M	3	f
J04334171+1750402	...	II	M4 ± 0.5	3	
J04555605+3036209	XEST 26-062	II	M4 ± 0.25	3	
J05075496+2500156	CIDA 12	II	M4 ± 1	16	
J04324938+2253082	JH 112 B	II	M4.25 ± 0.25	3	
J04385859+2336351	...	II	M4.25 ± 0.25	4	
J04190110+2819420	V410 X-ray 6	II	M4.5 ± 2	14	
J04322415+2251083	...	II	M4.5 ± 0.25	3	
J04161210+2756385	...	II	M4.75 ± 0.25	8	
J04322210+1827426	MHO 6	II	M4.75 ± 0.25	11	
J04334465+2615005	...	II	M4.75 ± 0.25	3	
J04422101+2520343	CIDA 7	II	M4.75 ± 0.25	5	
J04554535+3019389	...	II	M4.75 ± 0.25	8	
J04141458+2827580	FN Tau	II	M5 ± 1	16	
J04155799+2746175	...	II	M5 ± 0.25	3	
J04251550+2829275	...	II	M5 ± 1	1	d, h
J04265732+2606284	KPNO 13	II	M5 ± 0.25	9	
J04393364+2359212	...	II	M5 ± 0.25	6	
J04394488+2601527	ITG 15	II	M5 ± 0.25	6	
J04432023+2940060	CIDA 14	II	M5 ± 0.5	13	
J04193545+2827218	FR Tau	II	M5.25 ± 0.25	3	
J04202555+2700355	...	II	M5.25 ± 0.25	8	
J04210795+2702204	CFHT 19	II	M5.25 ± 0.5	7	
J04210934+2750368	...	II	M5.25 ± 0.25	3	
J04284263+2714039	...	II	M5.25 ± 0.25	8	
J04305171+2441475	ZZ Tau IRS	II	M5.25 ± 0.5	7	
J04362151+2351165	...	II	M5.25 ± 0.25	6	
J04403979+2519061	...	II	M5.25 ± 0.25	8	
J04141760+2806096	CIDA 1	II	M5.5 ± 0.5	10	
J04163911+2858491	...	II	M5.5 ± 0.25	5	
J04174955+2813318	KPNO 10	II	M5.5 ± 0.5	7	
J04213459+2701388	...	II	M5.5 ± 0.25	8	
J04295950+2433078	CFHT 20	II	M5.5 ± 0.5	7	
J04554801+3028050	...	II	M5.6 ± 0.25	8	
J04181710+2828419	V410 Anon 13	II	M5.75 ± 0.25	11	
J04230607+2801194	...	II	M6 ± 0.25	6	
J04262939+2624137	KPNO 3	II	M6 ± 0.25	11	
J04292165+2701259	IRAS 04263+2654	II	M6 ± 0.5	7	
J04323028+1731303	GG Tau Ba+Bb (Ba)	II	M6 ± 0.5	10	b
	GG Tau Ba+Bb (Bb)	II	M7.5 ± 0.5	10	b
J04390163+2336029	...	II	M6 ± 0.25	4	

Table 2.1: continued.

2MASS	Other name	SED class[1]	SpTy.	Ref.	Notes
J04400067+2358211	...	II	M6 ± 0.25	6	
J04554969+3019400	...	II	M6 ± 0.25	8	
J04141188+2811535	...	II	M6.25 ± 0.5	8	
J04214631+2659296	CFHT 10	II	M6.25 ± 0.5	7	
J04242646+2649503	CFHT 9	II	M6.25 ± 0.5	7	c
J04201611+2821325	...	II	M6.5 ± 0.25	3	
J04242090+2630511	...	II	M6.4 ± 0.25	6	
J04330945+2246487	CFHT 12	II	M6.2 ± 0.5	7	c
J04382134+2609137	GM Tau	II	M6.5 ± 0.5	10	
J04411078+2555116	ITG 34	II	M6.1 ± 0.5	7	
J04321606+1812464	MHO 5	II	M7 ± 0.5	10	
J04353536+2408266	IRAS 04325+2402 C	II	M6-M8	2	a, g
J04394748+2601407	CFHT 4	II	M7 ± 0.5	12	
J04233539+2503026	FU Tau A	II	M7.25 ± 0.25	3	a
J04381486+2611399	...	II	M7.25 ± 0.25	8	
J04390396+2544264	CFHT 6	II	M7.25 ± 0.5	7	
J04442713+2512164	IRAS S04414+2506	II	M7.25 ± 0.25	8	d
J04414825+2534304	...	II	M7.75 ± 0.25	8	
J04290068+2755033	...	II	M8.25 ± 0.25	5	
J04305718+2556394	KPNO 7	II	M8.25 ± 0.25	11	c
J04335245+2612548	...	II	M8.5 ± 0.25	6	
J04361030+2159364	...	II	M8.7 ± 0.25	5	
J04414489+2301513	...	II	M8.5 ± 0.25	5	
J04263055+2443558	...	II	M8.75 ± 0.25	5	
J04190126+2802487	KPNO 12	II	M9 ± 0.25	9	
J04300724+2608207	KPNO 6	II	M9 ± 0.5	7	c
J04233573+2502596	FU Tau B	II	M9.25 ± 0.25	3	a
J04131414+2819108	LkCa 1	III	M4 ± 1	16	b
J04184023+2824245	V410 X-ray 4	III	M4 ± 1	14	
J04292071+2633406	J1-507	III	M4 ± 1	16	b
J04292971+2616532	FW Tau A+B+C	III	M4 ± 1	16	b
J04295422+1754041	...	III	M4 ± 0.25	5	
J04332621+2245293	XEST 17-036	III	M4 ± 0.25	3	
J04464260+2459034	RXJ 04467+2459	III	M4 ± 0.5	13	
J05061674+2446102	CIDA 10	III	M4 ± 1	16	
J04355286+2250585	XEST 08-049	III	M4.25 ± 0.25	3	
J04150515+2808462	CIDA 2	III	M4.5 ± 1	16	b
J04163048+3037053	...	III	M4.5 ± 0.25	8	
J04203918+2717317	XEST 16-045	III	M4.5 ± 0.25	3	
J04355209+2255039	XEST 08-047	III	M4.5 ± 0.25	3	
J04414565+2301580	...	III	M4.5 ± 0.5	3	
J04554820+3030160	XEST 26-052	III	M4.5 ± 0.25	3	e
J04222404+2646258	XEST 11-087	III	M4.75 ± 0.25	3	
J04354203+2252226	XEST 08-033	III	M4.75 ± 0.25	3	
J04381630+2326402	...	III	M4.75 ± 0.25	4	
J04554757+3028077	...	III	M4.75 ± 0.25	8	
J04162725+2053091	...	III	M5 ± 0.25	4	
J04244506+2701447	J1-4423	III	M5 ± 1	16	
J04311578+1820072	MHO 9	III	M5 ± 0.5	10	
J04315844+2543299	J1-665	III	M5 ± 1	16	b
J04410424+2557561	Haro 6-32	III	M5 ± 0.25	8	
J04555636+3049374	...	III	M5 ± 0.25	8	
J04034997+2620382	XEST 06-006	III	M5.25 ± 0.25	3	
J04144739+2803055	XEST 20-066	III	M5.25 ± 0.25	3	

Table 2.1: continued.

2MASS	Other name	SED class^1	SpTy.	Ref.	Notes
J04322627+1827521	MHO 7	III	M5.25 ± 0.25	11	
J04344544+2308027	...	III	M5.25 ± 0.25	4	
J04554046+3039057	...	III	M5.25 ± 0.25	8	
J04555288+3006523	...	III	M5.25 ± 0.25	8	
J05064662+2104296	...	III	M5.25 ± 0.25	4	
J04183030+2743208	KPNO 11	III	M5.5 ± 0.25	9	
J04190197+2822332	V410 X-ray 5a	III	M5.5 ± 0.5	15	
J04205273+1746415	J2-157	III	M5.5 ± 1	16	
J04312382+2410529	V927 Tau A+B	III	M5.5 ± 1	16	b
J04214013+2814224	XEST 21-026	III	M5.75 ± 0.25	3	
J04335252+2256269	XEST 17-059	III	M5.75 ± 0.25	3	
J04354183+2234115	KPNO 8	III	M5.75 ± 0.25	11	
J04400174+2556292	CFHT 17	III	M5.75 ± 0.5	7	
J04330197+2421000	MHO 8	III	M6 ± 0.25	11	
J04330781+2616066	KPNO 14	III	M6 ± 0.25	9	
J04355760+2253574	...	III	M6 ± 1	1	d, h
J04161885+2752155	...	III	M6.25 ± 0.25	5	
J04320329+2528078	...	III	M6.25 ± 0.25	5	
J04552333+3027366	...	III	M6.25 ± 0.25	8	
J04180796+2826036	V410 X-ray 3	III	M6.5 ± 0.5	10	
J04321786+2422149	CFHT 7	III	M6.3 ± 0.5	7	a
J04385871+2323595	...	III	M6.5 ± 0.25	4	
J04185115+2814332	KPNO 2	III	M6.75 ± 0.5	7	
J04270739+2215037	...	III	M6.75 ± 0.25	4	
J04350850+2311398	CFHT 11	III	M6.75 ± 0.5	7	
J04152409+2910434	...	III	M7 ± 0.25	5	
J04312405+1800215	MHO 4	III	M7 ± 0.5	10	
J04341527+2250309	CFHT 1	III	M7 ± 0.5	12	
J04484189+1703374	...	III	M7 ± 0.25	5	
J04312669+2703188	CFHT 13	III	M7.25 ± 0.5	7	
J04380083+2558572	ITG 2	III	M7.25 ± 0.25	8	
J04294568+2630468	KPNO 5	III	M7.5 ± 0.25	11	
J04325026+2422115	...	III	M7.5 ± 0.5	7	
J04361038+2259560	CFHT 2	III	M7.5 ± 0.25	11	
J04390637+2334179	...	III	M7.5 ± 0.25	4	
J04221644+2549118	CFHT 14	III	M7.75 ± 0.5	7	
J04311907+2335047	...	III	M7.75 ± 0.25	5	
J04322329+2403013	...	III	M7.75 ± 0.25	5	
J04363893+2258119	CFHT 3	III	M7.75 ± 0.25	11	
J04221332+1934392	...	III	M8 ± 0.25	5	
J04274538+2357243	CFHT 15	III	M8.25 ± 0.5	7	
J04325119+1730092	LH 0429+17	III	M8.25 ± 0.25	3	
J04215450+2652315	...	III	M8.5 ± 0.25	5	
J04302365+2359129	CFHT 16	III	M8.6 ± 0.5	7	
J04355143+2249119	KPNO 9	III	M8.5 ± 0.25	11	
J04334291+2526470	...	III	M8.75 ± 0.25	5	
J04151471+2800096	KPNO 1	III	M9 ± 0.5	7	
J04354526+2737130	...	III	M9.25 ± 0.25	5	
J04574903+3015195	...	III	M9.25 ± 0.25	8	
J04272799+2612052	KPNO 4	III	M9.5 ± 0.5	7	
J04373705+2331080	...	III	L0 ± 0.5	3	

Notes. [1] SED classes for all targets are those reported in Luhman et al. (2010), excluding the additional two new members reported in Rebull et al. (2010), as indicated in the Notes column.

a-c. For those targets not observed with *Herschel* PACS under our program (OT1_jpatienc_1), observations were performed under the following program IDs: a. KPGT_pandre_1, b. KPOT_bdent_1, c. GT1_pharve01_2.

d. Observed in the far-IR with *Spitzer* MIPS only.

e. No far-IR observations exist for this target.

f. For the mid-M classification reported in Luhman et al. (2010) we adopt a spectral type of M4.

g. For the M6-M8 classification reported in Luhman et al. (2010) we adopt a spectral type of M7.

h. SED class from Rebull et al. (2010).

References. The spectral types and uncertainties have been extracted from the following references: (1) Rebull et al. (2010); (2) Luhman et al. (2010); (3) Luhman et al. (2009a); (4) Slesnick et al. (2006); (5) Luhman (2006); (6) Luhman et al. (2006); (7) Guieu et al. (2006); (8) Luhman (2004); (9) Luhman et al. (2003a); (10) White & Basri (2003); (11) Briceño et al. (2002); (12) Martín et al. (2001); (13) Briceño et al. (1999); (14) Luhman & Rieke (1998); (15) Briceño et al. (1998); (16) Kenyon & Hartmann (1995); (17) Strom & Strom (1994).

2.3 Observations

Of the 154 targets in the TBOSS sample, 150 were observed with the *Herschel* PACS instrument. PACS records two wavelengths simultaneously, and the observations of 146 include both 70 μm data from the Blue channel and 160 μm data from the Red channel, while 12 targets include 100 μm and 160 μm maps. For majority of the sample, the 134 targets observed for our *Herschel* PACS program (OT1_patienc_1), the mapping strategy involved obtaining two scan maps per target, with each map at a different orientation (70° and 110°). The cross scans are designed to reduce the stripping effect of the $1/f$ noise and, consequently, to provide more homogeneous and higher redundancy coverage of the map area. The medium mapping scan speed ($20''$/s) was employed with scan leg lengths of $3'.0$, cross scan steps of $4''.0$, and a total of 8 scan legs per orientation. Each map was centered on the target and the field-of-view was typically $3' \times 7'$. The pointing accuracy of *Herschel* is $0''.8$[1], and the beam size is $5''.6$ in the 70 μm maps, $6''.8$ in the 100 μm maps and $11''.3$ in the 160 μm maps. The total on-source integration time was 180s for all but 5 targets for which the integration time was 240s. Table A.1 reports the *Herschel* scan and cross scan ID numbers along with the observation date, observation duration and total on-source integration time for each target in the OT1_patienc_1 program. The integration time is the same for each wavelength map. Table A.2 summarizes the program ID, scan ID numbers, observation date, and observation duration per target for the 16 targets not observed in the OT1_patienc_1 program. For the 4 targets with *Spitzer* Multiband Imaging Photometer (MIPS; Rieke et al., 2004) measurements only, the observation details are reported in Rebull et al. (2010).

---

[1] http://herschel.esac.esa.int/twiki/bin/view/Public/SummaryPointing

2.4 Data Analysis

2.4.1 Measurement of PACs fluxes

The *Herschel* program OT1_jpatienc_1 data were reduced using the *Herschel* Interactive Processing Environment (HIPE; Ott, 2010) software version 9.0.0. For each target, the scan and corresponding cross scan were pre-processed using the standardized routines given in the PACS Data Reduction Guide (version 7, June 2011) were followed, and the calibration employed the PACS calibration file set v48. The initial map was used to identify any bright sources that needed to be masked prior to performing the Multi-resolution Median Transform (MMT) de-glitching routine and applying a high pass filter to each data set. The location of any point source with a signal greater than three times the standard deviation of the initial map was masked.

Depending on the brightness and size of the source in the initial map, a different number of frames were used in the high pass filtering, as suggested in the Data Reduction Guide. For the 9 brightest and/or resolved targets, the high pass filter radius corresponding to 51 frames in the Blue channel and 71 frames in the Red channel was used; for the 125 fainter, point sources, increments of 31 frames in the Blue channel and 51 frames in the Red channel were used to filter the thousands of frames involved in the scans of each target. After filtering, each scan and cross-scan was re-processed and the final map for each target was formed by a co-addition using the `photProject()` task.

The target fluxes were measured using aperture photometry, with the aperture size determined by the observation wavelength and object size. Among the 146 targets observed at 70 μm and 160 μm, 141 are unresolved point sources and 5 are spatially resolved. For the point sources, the aperture radii of $5''.5$ at 70 μm and $10''.5$ at 160 μm recommended by the *Herschel* Science Center[2] were used to measure the target fluxes. For the extended sources, the fluxes were measured within a 3σ contour, derived from three times the standard deviation of the map noise. The source flux error was calculated as the standard deviation of the flux in nine comparison apertures of the same size as the target aperture and distributed in the high coverage area of each map. Upper limits were determined by three times the standard deviation of the nine comparison apertures. Finally, aperture corrections defined in the *Herschel* Science Center technical note[2], were applied to the source fluxes and upper limits. Additional absolute flux calibration uncertainties of 2.6% at 70 μm and 4.2% at 160 μm reported in the technical note[2] are not included in the

---

[2] Technical note: PICC-ME-TN-037

reported uncertainties. For the 4 targets observed as part of the KPGT_pandre_1 program, 3 targets were unresolved point source and 1 target was spatially resolved. For the point sources, fluxes were measured from aperture photometry of the level 2.5 processed maps; an aperture of $5\farcs6$ was used for the 100 μm data. For the resolved target, the flux was measured within a 3σ contour from the level 2.5 processed map. For the 12 targets observed as part of the GT1_pharve01_2 and KPOT_bdent_1 programs, the fluxes were obtained from the literature (Harvey et al., 2012; Howard et al., 2013).

2.4.2 Construction of SEDs

Compilation of photometry.
Spectral energy distributions (SEDs) were constructed for all targets of the TBOSS sample. In addition to the *Herschel* PACS photometry, the SEDs include photometry from optical to millimeter wavelengths.

The optical photometry measurements consist of R_C and I_C band measurements compiled from the following studies: Guieu et al., 2006; Luhman, 2004; Luhman et al., 2003a; Briceño et al., 2002; Martín et al., 2001; Luhman, 2000 and Briceño et al., 1999. For targets where more that one measurement is reported, the median value was calculated and uncertainties of 0.8 mag at R_C and 0.3 mag at I_C were adopted, in order to account for source variability and uncertainties in the photometric transformation to the Cousins system (e.g. Briceño et al., 2002; Mayne et al., 2012. Magnitudes were converted to flux densities using zero-points of 3080 Jy and 2550 Jy for R_C and I_C, respectively (Bessell, 1979). In the near-infrared, *JHK* magnitudes for all targets were extracted from the Two Micron All Sky Survey (2MASS) point source catalog (Skrutskie et al., 2006) and were converted into flux densities using zero-points of 1594 ± 28 Jy, 1024 ± 20 Jy and 667 ± 13 Jy (Cohen et al., 2003). The combined R_C and I_C and 2MASS *JHK* fluxes, uncertainties, and references are listed in Table A.4.

In the mid-IR, with the *Spitzer* Infrared Array Camera (IRAC: 3.6 μm, 4.5 μm, 5.8 μm and 8.0 μm; Fazio et al., 2004), and at 24 μm with the Multiband Imaging Photometer for *Spitzer* (MIPS; Rieke et al., 2004), magnitudes were compiled from Luhman et al. (2010) and Rebull et al. (2010) and converted into flux densities using the zero-points of 281 ± 4 Jy, 180 ± 3 Jy, 115 ± 2 Jy and 65 ± 1 Jy at 3.6 μm, 4.5 μm, 5.8 μm and 8.0 μm respectively (Reach et al., 2005), and 7.2 ± 0.1 Jy at 24 μm (Engelbracht et al., 2007). Additionally, the Wide-field Infrared Survey Explorer (*WISE*) All-Sky Data Release (Cutri & et al., 2012) was used to extract photometry for all targets measured in the *W*1, *W*2, *W*3 and *W*4 channels (3.4 μm, 4.6 μm, 12 μm and 22 μm). *WISE* magnitudes were converted into flux densities using the zero-points of 310 ± 5 Jy, 172 ± 3 Jy, 31.7 ± 0.5 Jy and 8.4 ± 0.1 Jy in the *W*1, *W*2, *W*3 and *W*4 channels respectively (Wright et al., 2010). IRAC 3.6 μm and *WISE W*1 fluxes and uncertainties are given in Table A.4. *WISE W*2-*W*4 and IRAC 4.5 μm, 5.8 μm and 8.0 μm fluxes and uncertainties are given in Table A.5.

In the far-IR, *Spitzer* MIPS 70 μm measurements were compiled from Rebull et al. (2010), using the zero-point of 0.78 ± 0.01 Jy (Engelbracht et al., 2007). In addition to the new *Herschel* PACS observations presented here, for a subset of the TBOSS sample PACS 70 μm, 100 μm and 160 μm measurements were compiled from Harvey et al. (2012) and Howard et al. (2013). All far-IR fluxes and uncertainties are given in Table A.6.

The sub-millimeter and millimeter measurements consist of observations at 350 - 1200 μm and were compiled from from the following studies: Klein et al. (2003); Young et al. (2003); Andrews & Williams (2005); Bourke et al. (2006); Andrews et al. (2008); Bouy et al. (2008); Francesco et al. (2008); Harris et al. (2012), and Mohanty et al. (2013). At 1.3 mm and 2.6 mm, measurements were compiled from the following studies: Beckwith et al. (1990); Osterloh & Beckwith (1995); Motte & André (2001); Scholz et al. (2006); Schaefer et al. (2009); Phan-Bao et al. (2011); Ricci et al. (2013) and Andrews et al. (2013). All fluxes and uncertainties for the sub-millimeter and millimeter data are given in Table A.7.

The SEDs also show the best-fit stellar atmospheric models to the optical and near-IR photometry. The atmospheric models were fixed based on the adopted spectral type of each target, and using the temperature conversion from Luhman et al. (2003b). The stellar radius and log(g) were estimated from the effective stellar temperature ($T_{\rm eff}$) of each target and from the 1 Myr evolutionary models of Baraffe et al. (1998) for targets with $T_{\rm eff}$ >2700 K (≤M8) and those from Chabrier et al. (2000) for targets with $T_{\rm eff}$ <2700 K. The SEDs show the PHOENIX-based (Hauschildt et al., 1999), "BT-settl" models (Allard et al., 2003, 2011) for targets with $T_{\rm eff}$ >2700 K and the "AMES-Dusty" models (Allard et al., 2001) for targets with $T_{\rm eff}$ <2700 K. The redding law from Mathis (1990) for $R_v = 3.1$ was applied to the stellar atmospheric models, and extinction measurements for each target were taken from the literature and correspond to the same reference as that of the target spectral type. Unless otherwise reported, the extinction measurements for each target were scaled to A_V following the extinction law of Mathis (1990). For targets with no reported extinction, A_V was estimated using A_V = 9.44 × *E(J-H)*, derived from the extinction law of Mathis (1990), where $E(J-H) = (J-H) - (J-H)_0$ and is the excess with respect to the expected stellar photosphere. The intrinsic $(J\text{-}H)_0$ colors were taken from Luhman et al. (2010). The

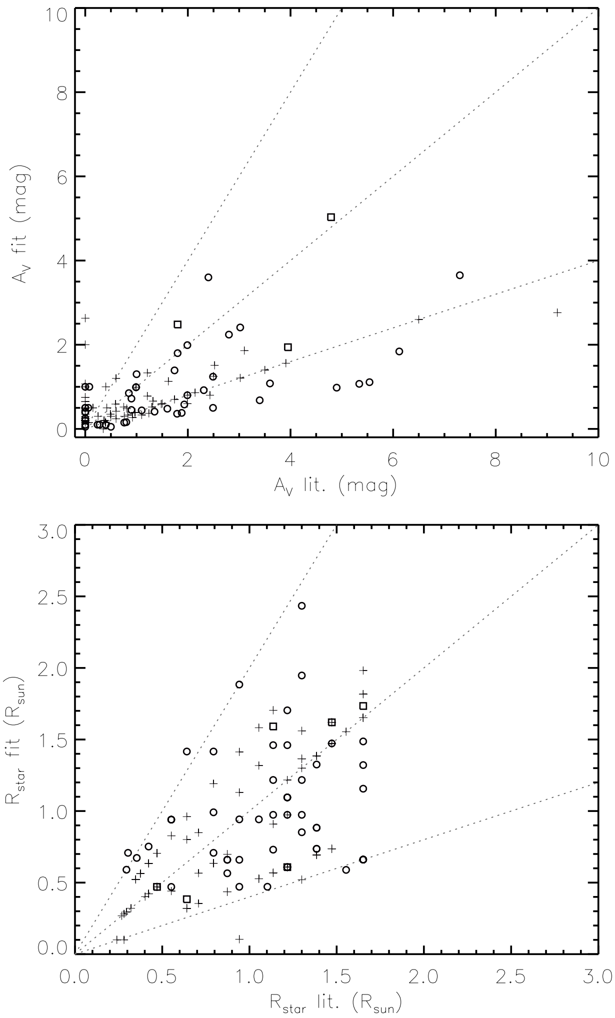

Figure 2.2: Comparison plots of the SED best-fit values of A_V **(top)** and $R_{\rm star}$ **(bottom)** against those reported in the literature. Literature A_V values are compiled from the references listed in Table 2.2. $R_{\rm star}$ values are derived from the spectral types reported in the literature, using the temperature conversion of Luhman et al. (2003b) and the 1 Myr evolutionary models of Baraffe et al. (1998) and Chabrier et al. (2000). Squares indicate Class I objects, circles indicate Class II objects, and crosses indicate Class III objects. The dotted lines represent fits that are 0.4, 1 and 2 times that of the literature values.

visual extinctions compiled from the literature and those derived in this paper are given in Table 2.2.

The best-fit model for each target was obtained by minimizing the χ^2 value, summed over the I_C and 2MASS *JHK* bands, where detections are reported. Visual extinction (A_V) and stellar radius ($R_{\rm star}$) were used as free parameters in the fitting process, since the atmospheric models, set by target spectral type, resulted in poor fits for some cases. A_V and $R_{\rm star}$ were typically constrained to vary from no extinction to twice the reported A_V values and from 0.4 to 2 times the derived stellar radii values. The reported A_V and derived R_{star} values for each target and the corresponding best-fit SED values are listed in Table 2.2 and shown in Figure 2.2.

For the multiple systems with angular separations in the range ∼5-11″ – FU Tau A+B, IRAS 04191+1523 A+B, and IRAS 04325+2402 AB+C – emission long-ward of the mid-IR is unresolved. For these systems, the combined system photometry were compiled and the underlying best-fit spectra displayed in the SEDs were combined from the spectral types of both the primary and secondary components. Additionally, for GG Tau Ba+Bb, with an angular separation of 10.″75 from the primary system Aa+Ab (Kraus & Hillenbrand, 2009), emission is resolved with both *Herschel* PACS at 70 μm (Howard et al., 2013) and the SMA at 1.3 mm (Harris et al., 2012). The SED for GG Tau Ba+Bb was constructed with photometry from the secondary system, and the underlying best-fit spectrum was combined from both the spectral types of the Ba and Bb components. The best-fit extinctions and stellar radii for these four multiples systems are given in Table 2.2.

Table 2.2: TBOSS stellar properties derived from the literature and evolutionary models in comparison with the best fit values from our SED fitting.

2MASS	Other name	SpTy.	Lit. A_V	T_{eff}	$R_\star$ model	A_V fit	$R_\star$ fit	Ref.
J04034997+2620382	XEST 06-006	M5.25	0.0	3091	1.217	2.0	0.608	12
J04131414+2819108	LkCa 1	M4	0.0	3270	1.652	0.2	1.817	6
J04141188+2811535	...	M6.25	1.0	2963	0.873	2.5	0.873	9
J04141458+2827580	FN Tau	M5	1.4	3125	1.300	0.0	2.600	6
J04141760+2806096	CIDA 1	M5.5	5.5	3058	1.136	1.7	1.420	4
J04144730+2646264	FP Tau	M4	0.2	3270	1.652	0.7	1.734	6
J04144739+2803055	XEST 20-066	M5.25	0.0	3091	1.217	0.2	0.973	12
J04150515+2808462	CIDA 2	M4.5	0.8	3198	1.472	0.3	1.620	6
J04151471+2800096	KPNO 1	M9	0.4	2400	0.295	0.2	0.295	5
J04152409+2910434	...	M7	2.4	2880	0.641	0.8	0.320	10
J04155799+2746175	...	M5	0.0	3125	1.300	1.0	1.300	12
J04161210+2756385	...	M4.75	2.0	3161	1.385	2.0	1.385	9
J04161885+2752155	...	M6.25	1.2	2963	0.873	0.8	0.436	10
J04162725+2053091	...	M5	0.2	3125	1.300	0.5	1.365	4
J04163048+3037053	...	M4.5	0.7	3198	1.472	0.5	0.736	9
J04163911+2858491	...	M5.5	3.4	3058	1.136	0.3	0.455	10
J04174955+2813318	KPNO 10	M5.5	0.0	3058	1.136	1.3	1.136	5
J04174965+2829362	V410 X-ray 1	M4	1.0	3270	1.652	2.5	2.065	15
J04180796+2826036	V410 X-ray 3	M6.5	1.5	2935	0.794	0.6	0.635	4
J04181710+2828419	V410 Anon 13	M5.75	2.8	3024	1.054	2.8	0.422	3
J04183030+2743208	KPNO 11	M5.5	0.0	3058	1.136	0.5	0.568	8
J04184023+2824245	V410 X-ray 4	M4	18.9	3270	1.652	3.8	1.982	7
J04185115+2814332	KPNO 2	M6.75	0.4	2908	0.708	1.0	0.354	5
J04185813+2812234	IRAS 04158+2805	M5.25	1.8	3091	1.217	2.5	0.608	10
J04190110+2819420	V410 X-ray 6	M4.5	0.9	3198	1.472	1.1	0.589	7
J04190126+2802487	KPNO 12	M9	0.5	2400	0.295	0.7	0.413	8
J04190197+2822332	V410 X-ray 5a	M5.5	2.5	3058	1.136	1.5	0.909	1
J04193545+2827218	FR Tau	M5.25	0.0	3091	1.217	0.0	1.217	12
J04194657+2712552	[GKH94] 41	M7.5	27.0	2795	0.470	4.0	0.470	12
J04201611+2821325	...	M6.5	0.0	2935	0.794	1.0	0.397	12
J04202555+2700355	...	M5.25	2.0	3091	1.217	1.6	0.487	9
J04202583+2819237	IRAS 04173+2812	mid-M	12.0	3270	1.652	6.0	1.734	4
J04203918+2717317	XEST 16-045	M4.5	0.0	3198	1.472	0.8	1.620	12
J04205273+1746415	J2-157	M5.5	0.0	3058	1.136	0.5	0.568	6
J04210795+2702204	CFHT 19	M5.25	7.3	3091	1.217	5.1	1.521	5
J04210934+2750368	...	M5.25	0.0	3091	1.217	0.5	1.217	12
J04213459+2701388	...	M5.5	1.7	3058	1.136	0.9	1.136	9
J04214013+2814224	XEST 21-026	M5.75	0.0	3024	1.054	0.2	0.527	12
J04214631+2659296	CFHT 10	M6.25	3.6	2963	0.873	1.8	0.349	5
J04215450+2652315	...	M8.5	1.2	2555	0.348	1.3	0.522	10
J04221332+1934392	...	M8	0.0	2710	0.402	0.4	0.402	10
J04221644+2549118	CFHT 14	M7.75	0.6	2753	0.422	1.2	0.422	5
J04222404+2646258	XEST 11-087	M4.75	1.1	3161	1.385	0.3	1.385	12

Table 2.2: continued.

2MASS	Other name	SpTy.	Lit. A_V	$T_{\rm eff}$	$R_\star$ model	A_V fit	$R_\star$ fit	Ref.
J04230607+2801194	...	M6	0.0	2990	0.942	1.5	0.942	11
J04242090+2630511	...	M6.5	0.0	2935	0.794	0.5	0.397	11
J04242646+2649503	CFHT 9	M6.25	0.9	2963	0.873	0.9	0.349	5
J04244506+2701447	J1-4423	M5	1.0	3125	1.300	0.4	1.365	6
J04251550+2829275		M5	3.4	3125	1.300	0.3	1.300	14
J04262939+2624137	KPNO 3	M6	1.6	2990	0.942	1.6	0.377	3
J04263055+2443558	...	M8.75	0.0	2478	0.321	0.9	0.321	10
J04265732+2606284	KPNO 13	M5	2.5	3125	1.300	1.7	2.600	8
J04270739+2215037	...	M6.75	0.4	2908	0.708	0.5	0.849	4
J04272799+2612052	KPNO 4	M9.5	2.5	2245	0.268	1.3	0.268	5
J04274538+2357243	CFHT 15	M8.25	1.3	2633	0.375	0.5	0.563	5
J04275730+2619183	IRAS 04248+2612	M4.5	3.9	3198	1.472	1.9	1.620	10
...	L1521F-IRS	M6-M8	...[a]	2880	0.641	0.5	0.384	4
J04284263+2714039	...	M5.25	0.5	3091	1.217	1.3	1.217	9
J04290068+2755033	...	M8.25	0.0	2633	0.375	0.6	0.375	10
J04292071+2633406	J1-507	M4	0.8	3270	1.652	0.3	1.817	6
J04292165+2701259	IRAS 04263+2654	M6	4.9	2990	0.942	0.4	1.884	5
J04292971+2616532	FW Tau A+B+C	M4	0.4	3270	1.652	0.0	1.652	6
J04294568+2630468	KPNO 5	M7.5	0.0	2795	0.470	0.3	0.470	3
J04295422+1754041	...	M4	0.0	3270	1.652	2.6	1.652	10
J04295950+2433078	CFHT 20	M5.5	3.6	3058	1.136	2.5	2.273	5
J04300724+2608207	KPNO 6	M9	0.9	2400	0.295	1.4	0.295	5
J04302365+2359129	CFHT 16	M8.5	1.5	2555	0.348	0.6	0.522	5
J04305171+2441475	ZZ Tau IRS	M5.25	2.4	3091	1.217	3.1	1.278	5
J04305718+2556394	KPNO 7	M8.25	0.0	2633	0.375	1.5	0.375	3
J04311578+1820072	MHO 9	M5	0.9	3125	1.300	0.3	1.300	4
J04311907+2335047	...	M7.75	0.6	2753	0.422	0.6	0.634	10
J04312382+2410529	V927 Tau A+B	M5.5	0.4	3058	1.136	0.2	1.704	6
J04312405+1800215	MHO 4	M7	1.3	2880	0.641	0.7	0.961	4
J04312669+2703188	CFHT 13	M7.25	3.5	2838	0.552	1.4	0.441	5
J04313613+1813432	LkHa 358	M5.5	13.6	3058	1.136	2.7	1.591	6
J04315844+2543299	J1-665	M5	1.0	3125	1.300	0.4	1.560	6
J04320329+2528078	...	M6.25	0.0	2963	0.873	0.5	0.698	10
J04321606+1812464	MHO 5	M7	1.2	2880	0.641	0.1	0.961	4
J04321786+2422149	CFHT 7	M6.5	0.0	2935	0.794	0.3	1.191	5
J04322210+1827426	MHO 6	M4.75	1.1	3161	1.385	1.4	1.385	3
J04322329+2403013	...	M7.75	0.0	2753	0.422	0.2	0.422	10
J04322415+2251083	...	M4.5	1.7	3198	1.472	0.9	0.589	12
J04322627+1827521	MHO 7	M5.25	0.1	3091	1.217	0.2	1.217	3
J04324938+2253082	JH 112 B	M4.25	3.1	3234	1.554	2.2	1.865	12
J04325026+2422115	...	M7.5	9.2	2795	0.470	2.8	0.705	5
J04325119+1730092	LH 0429+17	M8.25	0.0	2633	0.375	0.2	0.563	12
J04330197+2421000	MHO 8	M6	1.0	2990	0.942	1.0	1.413	3
J04330781+2616066	KPNO 14	M6	3.0	2990	0.942	1.2	1.130	8
J04330945+2246487	CFHT 12	M6.5	3.4	2935	0.794	1.7	0.794	5
J04332621+2245293	XEST 17-036	M4	3.9	3270	1.652	1.6	1.652	12
J04334171+1750402	...	M4	0.3	3270	1.652	1.3	1.652	12
J04334291+2526470	...	M8.75	0.0	2478	0.321	1.1	0.321	10
J04334465+2615005	...	M4.75	3.0	3161	1.385	3.0	0.554	12
J04335245+2612548	...	M8.5	5.0	2555	0.348	0.5	0.522	4
J04335252+2256269	XEST 17-059	M5.75	0.0	3024	1.054	0.2	1.582	12
J04341527+2250309	CFHT 1	M7	3.1	2880	0.641	1.9	0.801	13
J04344544+2308027	...	M5.25	2.1	3091	1.217	0.9	0.608	4
J04350850+2311398	CFHT 11	M6.75	0.0	2908	0.708	0.2	0.566	5
J04354183+2234115	KPNO 8	M5.75	0.5	3024	1.054	0.3	0.527	3
J04354203+2252226	XEST 08-033	M4.75	1.7	3161	1.385	0.7	1.385	12
J04354526+2737130	...	M9.25	0.0	2323	0.281	0.2	0.281	10
J04355143+2249119	KPNO 9	M8.5	0.0	2555	0.348	0.7	0.522	3
J04355209+2255039	XEST 08-047	M4.5	2.0	3198	1.472	0.6	1.472	12
J04355286+2250585	XEST 08-049	M4.25	1.2	3234	1.554	0.4	1.554	12
J04355760+2253574		M6	0.0	2990	0.942	1.0	0.104	14
J04361030+2159364	...	M8.5	0.0	2555	0.348	0.1	0.522	10
J04361038+2259560	CFHT 2	M7.5	2.0	2795	0.470	0.8	0.705	3
J04362151+2351165	...	M5.25	1.5	3091	1.217	1.0	0.487	11
J04363893+2258119	CFHT 3	M7.75	1.0	2753	0.422	1.0	0.634	3
J04373705+2331080	...	L0	0.0	2090	0.240	0.7	0.100	12
J04380083+2558572	ITG 2	M7.25	0.6	2838	0.552	0.2	0.827	9
J04381486+2611399	...	M7.25	0.0	2838	0.552	1.0	0.579	9
J04381630+2326402	...	M4.75	...[b]	3161	1.385	0.3	0.693	4
J04382134+2609137	GM Tau	M6.5	6.1	2935	0.794	0.6	0.794	4
J04385859+2336351	...	M4.25	0.0	3234	1.554	1.5	0.622	4
J04385871+2323595	...	M6.5	...[b]	2935	0.794	0.2	0.635	4
J04390163+2336029	...	M6	1.8	2990	0.942	0.5	1.130	4
J04390396+2544264	CFHT 6	M7.25	0.4	2838	0.552	0.5	0.552	5

Table 2.2: continued.

2MASS	Other name	SpTy.	Lit. A_V	T_{eff}	$R_\star$ model	A_V fit	$R_\star$ fit	Ref.
J04390637+2334179	...	M7.5	...[b]	2795	0.470	0.2	0.470	4
J04393364+2359212	...	M5	0.0	3125	1.300	1.0	1.300	11
J04394488+2601527	ITG 15	M5	2.7	3125	1.300	0.5	2.600	11
J04394748+2601407	CFHT 4	M7	10.7	2880	0.641	0.0	0.641	13
J04400067+2358211	...	M6	0.0	2990	0.942	0.5	0.377	11
J04400174+2556292	...	M5.75	6.5	3024	1.054	2.6	1.318	5
J04403979+2519061	...	M5.25	2.5	3091	1.217	1.2	1.217	9
J04410424+2557561	Haro 6-32	M5	0.6	3125	1.300	0.4	0.520	9
J04411078+2555116	ITG 34	M6.5	1.8	2935	0.794	1.8	1.191	5
J04414489+2301513	...	M8.5	0.0	2555	0.348	0.9	0.348	10
J04414565+2301580	...	M4.5	0.4	3198	1.472	0.2	1.472	12
J04414825+2534304	...	M7.75	1.0	2753	0.422	1.3	0.634	9
J04422101+2520343	CIDA 7	M4.75	1.2	3161	1.385	1.2	1.385	10
J04432023+2940060	CIDA 14	M5	0.3	3125	1.300	0.4	1.560	2
J04442713+2512164	IRAS S04414+2506	M7.25	0.0	2838	0.552	0.1	0.552	9
J04464260+2459034	RXJ 04467+2459	M4	1.6	3270	1.652	1.1	1.652	2
J04484189+1703374	...	M7	0.0	2880	0.641	0.8	0.320	10
J04520668+3047175	IRAS 04489+3042	M4	4.8	3270	1.652	5.0	1.734	10
J04552333+3027366	...	M6.25	0.0	2963	0.873	1.0	0.436	9
J04554046+3039057	...	M5.25	0.2	3091	1.217	0.3	0.608	9
J04554535+3019389	...	M4.75	0.0	3161	1.385	1.3	1.385	9
J04554757+3028077	...	M4.75	0.0	3161	1.385	0.4	0.693	9
J04554801+3028050	...	M5.6	0.0	3044	1.103	1.0	0.441	9
J04554820+3030160	XEST 26-052	M4.5	0.0	3198	1.472	0.3	0.736	12
J04554969+3019400	...	M6	0.0	2990	0.942	1.1	0.377	9
J04555288+3006523	...	M5.25	0.0	3091	1.217	0.2	0.608	9
J04555605+3036209	XEST 26-062	M4	1.9	3270	1.652	0.0	1.652	12
J04555636+3049374	...	M5	0.4	3125	1.300	0.2	1.365	9
J04574903+3015195	...	M9.25	0.0	2323	0.281	0.2	0.100	9
J05061674+2446102	CIDA 10	M4	0.5	3270	1.652	0.4	1.652	6
J05064662+2104296	...	M5.25	0.8	3091	1.217	0.5	0.608	4
J05075496+2500156	CIDA 12	M4	0.8	3270	1.652	1.2	1.652	6
Multiple systems with combined SEDs								
J04220043+1530212	IRAS 04191+1523 A	K6-M3.5	33.3	3705	2.544			4
J04220007+1530248	IRAS 04191+1523 B	M6-M8	34.4	2880	0.641			4
	IRAS 04191+1523 AB + C					2.7	3.312	
J04353539+2408194	IRAS 04325+2402 AB	K6-M3.5	36.9	3705	2.544			4
J04353536+2408266	IRAS 04325+2402 C	M6-M8	38.0	2880	0.641			4
	IRAS 04325+2402 AB + C				3.185	3.7	4.457	
	GG Tau Ba	M6	...	2990	0.942			
	GG Tau Ba	M7.5	...	2795	0.470			
J04323028+1731303	**GG Tau Ba + Bb**		1.1			0.3	0.847	4
J04233539+2503026	FU Tau A	M7.25	2.0	2838	0.552			12
J04233573+2502596	FU Tau B	M9.25	0.0	2323	0.276			12
	FU Tau A+B					0.0	9.113[c]	

Notes. References refer to the extinctions compiled from the literature, as listed in the A_V column. [a] For L1521F-IRS upper limits are reported in 2MASS at *JHK*. [b] For these systems the calculated the excesses between the 2MASS *JH* and the intrinsic colors (Luhman et al., 2010) are negative. [c] The best-fit spectrum of FU Tau A+B resulted in an extreme fit to the stellar radius. The system is noted to be an over luminous source in Luhman et al. (2009b).

References. Extinction values have been compiled from the following references: (1) Briceño et al. (1998); (2) Briceño et al. (1999); (3) Briceño et al. (2002); (4) This work; (5) Guieu et al. (2006); (6) Kenyon & Hartmann (1995); (7) Luhman & Rieke (1998); (8) Luhman et al. (2003a); (9) Luhman (2004); (10) Luhman (2006); (11) Luhman et al. (2006); (13) Luhman et al. (2009a); (14) Martín et al. (2001); (15) Rebull et al. (2010); (16) Strom & Strom (1994).

2.5 Results

Of the 150 TBOSS targets observed with *Herschel*, 58 were detected, 2 have unresolved emission from earlier spectral type companions, and 90 have upper limits. The spatial distribution of the full TBOSS sample is shown in Figure 2.1 along with the corresponding subset of detections and upper limits. The *Herschel* results for each evolutionary class are reported in Section 2.5.1 (Class I), 2.5.2 (Class II), and 2.5.3 (Class III). After the summary of *Herschel* results, the PACS fluxes are compared with *Spitzer* MIPS fluxes in Section 2.5.4. Combining the *Herschel* and *Spitzer* results, the overall TBOSS far-IR detection rates are calculated in Section 2.5.5. Although the *Herschel* beam size corresponds to >750 AU in Taurus, several TBOSS targets are spatially extended, and these cases are reported in Section 2.5.6. Finally, the results of multiplicity surveys are compiled along with *Herschel* measurements in Section 2.5.7.

2.5.1 Class I population

All of the seven Class I Taurus members with M4 and later (M4+) spectral types are detected in both PACS channels, and the fluxes are listed in Table 2.3. The Class I targets include the brightest of the TBOSS sample, although the two brightest Class I sources are unresolved binaries, as noted in Table 2.3. Binary sources are discussed in more detail in Section 2.5.7. The fluxes of the isolated Class I substellar objects range from ∼270 mJy to >4 Jy, larger than nearly all of the Class II sources and indicating that a substantial amount of dust is present around brown dwarfs in the early stage of evolution. The maps at each wavelength for the Class I targets are given Figure 2.5 and in Figure A.1 of Appendix A and the SEDs combining the *Herschel* fluxes with shorter and longer wavelength data are compiled in Figures A.8 and A.9 - of Appendix A.

2.5.2 Class II population

The majority of the M4+ Class II Taurus members are detected at 70 μm with a large range of fluxes spanning three orders of magnitude. Approximately half of the Class II TBOSS sample also have PACS 160 μm fluxes. The fluxes of detected Class II TBOSS members are reported in Table 2.3, and several Class II sources have fluxes comparable to the Class I members. Upper limits for the few Class II targets without detections at either wavelength are listed in Table 2.4. The angular resolution degrades at longer wavelengths, and the source JH 112 B, is undetected at 70 μm, but a long wavelength detection is due to contamination from emission associated with an earlier spectral type primary. Additionally, the 100 μm emission witnessed for IRAS 04325+2402 C (shown in Figure 2.5) is unresolved from an earlier spectral type primary, and is further discussed in Section 2.5.7. Maps of the detected Class II sources are given in Figures A.2 - A.6 in Appendix A. In Appendix A, the SEDs of the detections are given in Figures A.9-A.11 and the *Herschel* non-detections in Figure A.12. Furthermore a subset of the Class II objects are reported in the literature possessing transitional disks. Based on our *Herschel* PACS data we report additional candidate transition disks, discussed in Section 2.6.3. The SEDs for these transition disks and candidates are shown in Figure 2.15.

2.5.3 Class III population

Only a small subset of Class III TBOSS targets are detected at one or more wavelengths in the *Herschel* data, and the Class III fluxes reported in Table 2.3 are not the faintest measured fluxes; the Class III emission is larger than some Class II members. The larger number of Class III upper limits are given in Table 2.4. Among the Class III targets is the only source with a non-detection at 70 μm and a longer wavelength detection uncontaminated by a more massive primary – XEST 08-033. The 160 μm map for XEST 08-033 shows two sources unlike most of the detected targets, although the source at the coordinates of XEST 08-033 is unresolved as expected for a circumstellar disk. All the Class III maps are shown in Figure A.7 of Appendix A, and the corresponding SEDs are plotted in Figure 2.15. The SEDs involving *Herschel* upper limits for Class III targets are given in Figures A.13 - A.16 of Appendix A.

2.5.4 Comparison with *Spitzer* MIPS

Among the TBOSS targets detected at 70 μm with the *Herschel* PACS maps, 21 sources have existing 70 μm detections with *Spitzer* MIPS data (Rebull et al., 2010). A plot of the PACS 70 μm fluxes as a function of the corresponding MIPS 70 μm fluxes for these 21 sources are shown in Figure 2.3. For the sources with fluxes <1 Jy, the agreement between the two values is typically within the MIPS absolute flux calibration uncertainty (<10%). For the six sources brighter than 1 Jy, the discrepancy between the PACS and MIPS fluxes range from 25-40%, and the *Herschel* PACS flux is systematically higher. As noted in the *Herschel* Science Center technical note[3], the processed PACS data are affected by the high pass filter width, source masking, drizzling, and aperture sizes used in the photometry. The contribution of these factors is expected to impact the final flux by only a few per-cent and cannot explain the full discrepancy between the larger systematic offset. The most likely cause is due to the impact of non-linearity for MIPS data compared to PACS; the PACS detector is linear up to flux levels well above the brightest TBOSS target, while the MIPS detector is non-linear for fluxes above ∼1 Jy[4].

---

[3] Technical note: PICC-ME-TN-037

[4] https://nhscsci.ipac.caltech.edu/sc/index.php/Pacs/AbsoluteCalibration

TABLE 2.3: *Herschel* PACS Detections, ordered by evolutionary class and spectral type.

2MASS	Other name	Class	SpTy.	70 μm (mJy)	100 μm (mJy)	160 μm (mJy)	Ref.	Notes
J04520668+3047175	IRAS 04489+3042	I	M4	2151 ± 5		2103 ± 34		
J04275730+2619183	IRAS 04248+2612	I	M4.5	4531 ± 17		10093 ± 141		
J04185813+2812234	IRAS 04158+2805	I	M5.25	1089 ± 3		2953 ± 25		
J04313613+1813432	LkHa 358	I	M5.5	1300 ± 200	1320 ± 200	1530 ± 300	2	
J04220007+1530248	IRAS 04191+1523 B	I	M6-M8	(7002 ± 13)		(8884 ± 232)		
...	L1521F-IRS	I	M6-M8	522 ± 4		3712 ± 52		
J04194657+2712552	[GKH94] 41	I	M7.5	269 ± 5		279 ± 66		
J04144730+2646264	FP Tau	II	M4	307 ± 3		351 ± 11		
J04174965+2829362	V410 X-ray 1	II	M4	36 ± 3		<122		
J04202583+2819237	IRAS 04173+2812	II	mid-M	172 ± 3		72 ± 6		
J04334171+1750402	...	II	M4	17 ± 3		<28		
J04555605+3036209	XEST 26-062	II	M4	330 ± 4		639 ± 39		
J05075496+2500156	CIDA 12	II	M4	51 ± 3		44 ± 6		
J04324938+2253082	JH 112 B	II	M4.25	<318		(284 ± 26)		
J04385859+2336351	...	II	M4.25	38 ± 3		76 ± 13		
J04190110+2819420	V410 X-ray 6	II	M4.5	445 ± 4		342 ± 36		
J04161210+2756385	...	II	M4.75	201 ± 3		228 ± 8		
J04322210+1827426	MHO 6	II	M4.75	107 ± 2		188 ± 7		
J04334465+2615005	...	II	M4.75	149 ± 2		178 ± 22		
J04422101+2520343	CIDA 7	II	M4.75	330 ± 2		342 ± 19		
J04554535+3019389	...	II	M4.75	22 ± 3		<30		
J04141458+2827580	FN Tau	II	M5	1755 ± 4		816 ± 16		
J04155799+2746175	...	II	M5	25 ± 3		<48		
J04265732+2606284	KPNO 13	II	M5	28 ± 4		<182		
J04393364+2359212	...	II	M5	70 ± 1		44 ± 15		
J04394488+2601527	ITG 15	II	M5	272 ± 3		114 ± 28		
J04193545+2827218	FR Tau	II	M5.25	46 ± 3		<33		
J04202555+2700355	...	II	M5.25	107 ± 3		100 ± 15		
J04210795+2702204	CFHT 19	II	M5.25	3277 ± 8		3076 ± 61		
J04284263+2714039	...	II	M5.25	20 ± 2		51 ± 12		
J04305171+2441475	ZZ Tau IRS	II	M5.25	2901 ± 5		2922 ± 26		
J04403979+2519061	...	II	M5.25	72 ± 2		61 ± 20		
J04141760+2806096	CIDA 1	II	M5.5	266 ± 2		212 ± 21		
J04174955+2813318	KPNO 10	II	M5.5	160 ± 2		82 ± 26		
J04213459+2701388	...	II	M5.5	37 ± 2		101 ± 19		
J04295950+2433078	CFHT 20	II	M5.5	128 ± 4		91 ± 23		
J04554801+3028050	...	II	M5.6	11 ± 3		<63		
J04181710+2828419	V410 Anon 13	II	M5.75	35 ± 2		<113		
J04230607+2801194	...	II	M6	41 ± 3		38 ± 9		
J04262939+2624137	KPNO 3	II	M6	23 ± 4		33 ± 12		
J04292165+2701259	IRAS 04263+2654	II	M6	329 ± 3		176 ± 14		
J04323028+1731303	GG Tau Ba+Bb	II	M6+M7.5	210 ± 20	...	...	2	a
J04390163+2336029	...	II	M6	15 ± 3		<24		
J04400067+2358211	...	II	M6	55 ± 2		52 ± 5		
J04141188+2811535	...	II	M6.25	17 ± 5		<293		
J04242646+2649503	CFHT 9	II	M6.25	10 ± 1		<6	1	
J04330945+2246487	CFHT 12	II	M6.5	2 ± 1		<8	1	
J04382134+2609137	GM Tau	II	M6.5	36 ± 2		<35		
J04411078+2555116	ITG 34	II	M6.5	21 ± 4		<38		
J04353536+2408266	IRAS 04325+2402 C	II	M6-M8		(16906 ± 26)			b, c
J04394748+2601407	CFHT 4	II	M7	109 ± 5		<150		
J04381486+2611399	...	II	M7.25	95 ± 2		67 ± 24		
J04390396+2544264	CFHT 6	II	M7.25	23 ± 3		<56		
J04414825+2534304	...	II	M7.75	37 ± 3		<122		
J04305718+2556394	KPNO 7	II	M8.25	4 ± 1		<7	1	
J04414489+2301513	...	II	M8.5	11 ± 2		<18		
J04300724+2608207	KPNO 6	II	M9	2 ± 1		<5	1	
J04292971+2616532	FW Tau A+B+C	III	M4	30 ± 4	33 ± 4	70 ± 40	2	
J04295422+1754041	...	III	M4	89 ± 3		86 ± 8		
J04332621+2245293	XEST 17-036	III	M4	82 ± 4		181 ± 27		
J04354203+2252226	XEST 08-033	III	M4.75	<16		104 ± 28		

Notes. Fluxes in reported in parenthesis are unresolved from a companion of earlier spectral type (>M4), not included in the TBOSS sample. Upper limits are reported at a 3σ level. The errors listed are the 1σ statistical measurement error. Uncertainties in the absolute flux calibration at 70 μm, 100 μm and 160 μm are 2.64%, 2.75% and 4.15% respectively.

a. GG Tau Ba+Bb unresolved from the primary systems at 100 μm and 160 μm (Howard et al., 2013).

b. Fluxes measured from the level 2.5 processed maps observed under the program KPGT_pandre_1.

c. IRAS 04325+2402 falls outside of the coverage region from the KPGT_pandre_1 processed map at 160 μm.

References. (1) Harvey et al. (2012); (1) Howard et al. (2013).

Table 2.4: *Herschel* PACS upper limits, ordered by evolutionary class and spectral type.

2MASS	Other name	Class	SpTy.	70 μm (mJy)	100 μm (mJy)	160 μm (mJy)	Ref.	Notes
J04322415+2251083	...	II	M4.5	<9		<77		
J04432023+2940060	CIDA 14	II	M5	<13		<25		
J04210934+2750368	...	II	M5.25	<13		<47		
J04362151+2351165	...	II	M5.25	<15		<64		
J04163911+2858491	...	II	M5.5	<9		<55		
J04554969+3019400	...	II	M6	<5		<17		
J04214631+2659296	CFHT 10	II	M6.25	<10		<84		

Table 2.4: continued.

2MASS	Other name	Class	SpTy.	70 μm (mJy)	100 μm (mJy)	160 μm (mJy)	Ref.	Notes
J04201611+2821325	...	II	M6.5	<7		<26		
J04242090+2630511	...	II	M6.5	<9		<58		
J04321606+1812464	MHO 5	II	M7	<11		<82		
J04233539+2503026	FU Tau A	II	M7.25		<39	<247		a
J04290068+2755033	...	II	M8.25	<8		<36		
J04335245+2612548	...	II	M8.5	<11		<47		
J04361030+2159364	...	II	M8.5	<7		<22		
J04263055+2443558	...	II	M8.75	<12		<51		
J04190126+2802487	KPNO 12	II	M9	<6		<88		
J04233573+2502596	FU Tau B	II	M9.25		<39	<247		a
J04131414+2819108	LkCa 1	III	M4	<9	<9	<21	1	
J04184023+2824245	V410 X-ray 4	III	M4	<23		<88		
J04292071+2633406	J1-507	III	M4	<8	<8	<21	1	
J04464260+2459034	RXJ 04467+2459	III	M4	<10		<35		
J05061674+2446102	CIDA 10	III	M4	<6		<42		
J04355286+2250585	XEST 08-049	III	M4.25	<6		<109		
J04150515+2808462	CIDA 2	III	M4.5	<9	<9	<22	1	
J04163048+3037053	...	III	M4.5	<11		<28		
J04203918+2717317	XEST 16-045	III	M4.5	<5		<45		
J04355209+2255039	XEST 08-047	III	M4.5	<11		<1657		
J04414565+2301580	...	III	M4.5	<5		<18		
J04222404+2646258	XEST 11-087	III	M4.75	<6		<44		
J04381630+2326402	...	III	M4.75	<6		<26		
J04554757+3028077	...	III	M4.75	<7		<63		
J04162725+2053091	...	III	M5	<9		<39		
J04244506+2701447	J1-4423	III	M5	<5		<41		
J04311578+1820072	MHO 9	III	M5	<8		<76		
J04315844+2543299	J1-665	III	M5	<9	<9	<25	1	
J04410424+2557561	Haro 6-32	III	M5	<8		<48		
J04555636+3049374	...	III	M5	<5		<35		
J04034997+2620382	XEST 06-006	III	M5.25	<5		<20		
J04144739+2803055	XEST 20-066	III	M5.25	<6		<67		
J04322627+1827521	MHO 7	III	M5.25	<8		<23		
J04344544+2308027	...	III	M5.25	<10		<48		
J04554046+3039057	...	III	M5.25	<10		<73		
J04555288+3006523	...	III	M5.25	<7		<16		
J05064662+2104296	...	III	M5.25	<6		<22		
J04183030+2743208	KPNO 11	III	M5.5	<6		<55		
J04190197+2822332	V410 X-ray 5a	III	M5.5	<5		<75		
J04205273+1746415	J2-157	III	M5.5	<5		<27		
J04312382+2410529	V927 Tau A+B	III	M5.5	<9	<9	<32	1	
J04214013+2814224	XEST 21-026	III	M5.75	<8		<31		
J04335252+2256269	XEST 17-059	III	M5.75	<12		<27		
J04354183+2234115	KPNO 8	III	M5.75	<3		<31		
J04400174+2556292	CFHT 17	III	M5.75	<11		<159		
J04330197+2421000	MHO 8	III	M6	<4		<48		
J04330781+2616066	KPNO 14	III	M6	<6		<79		
J04161885+2752155	...	III	M6.25	<6		<50		
J04320329+2528078	...	III	M6.25	<9		<33		
J04552333+3027366	...	III	M6.25	<7		<34		
J04180796+2826036	V410 X-ray 3	III	M6.5	<7		<86		
J04321786+2422149	CFHT 7	III	M6.5		<39	<322		a
J04385871+2323595	...	III	M6.5	<4		<30		
J04185115+2814332	KPNO 2	III	M6.75	<7		<74		
J04270739+2215037	...	III	M6.75	<8		<27		
J04350850+2311398	CFHT 11	III	M6.75	<7		<56		
J04152409+2910434	...	III	M7	<7		<29		
J04312405+1800215	MHO 4	III	M7	<11		<38		
J04341527+2250309	CFHT 1	III	M7	<7		<67		
J04484189+1703374	...	III	M7	<6		<25		
J04312669+2703188	CFHT 13	III	M7.25	<8		<54		
J04380083+2558572	ITG 2	III	M7.25	<6		<69		
J04294568+2630468	KPNO 5	III	M7.5	<7		<37		
J04325026+2422115	...	III	M7.5	<10		<82		
J04361038+2259560	CFHT 2	III	M7.5	<7		<82		
J04390637+2334179	...	III	M7.5	<5		<44		
J04221644+2549118	CFHT 14	III	M7.75	<5		<26		
J04311907+2335047	...	III	M7.75	<7		<24		
J04322329+2403013	...	III	M7.75	<9		<35		
J04363893+2258119	CFHT 3	III	M7.75	<5		<50		
J04221332+1934392	...	III	M8	<5		<45		
J04274538+2357243	CFHT 15	III	M8.25	<6		<47		
J04325119+1730092	LH 0429+17	III	M8.25	<7		<33		

Table 2.4: continued.

2MASS	Other name	Class	SpTy.	70 μm (mJy)	100 μm (mJy)	160 μm (mJy)	Ref.	Notes
J04215450+2652315	...	III	M8.5	<5		<35		
J04302365+2359129	CFHT 16	III	M8.5	<6		<51		
J04355143+2249119	KPNO 9	III	M8.5	<7		<102		
J04334291+2526470	...	III	M8.75	<6		<32		
J04151471+2800096	KPNO 1	III	M9	<3		<41		
J04354526+2737130	...	III	M9.25	<8		<30		
J04574903+3015195	...	III	M9.25	<9		<15		
J04272799+2612052	KPNO 4	III	M9.5	<7		<21		
J04373705+2331080	...	III	L0	<5		<27		

Notes. Upper limits are reported at a 3σ level. The errors listed are the 1σ statistical measurement error. Uncertainties in the absolute flux calibration at 70 μm, 100 μm and 160 μm are 2.64%, 2.75% and 4.15% respectively.

a. Flux measured from the level 2.5 processed map observed under the program KPGT_pandre_1.

References. (1) Howard et al. (2013).

2.5.5 Far-IR Detection rates for Taurus members

Histograms of the TBOSS sample observed with *Herschel* PACS and detections are plotted in Figure 2.4. By combining results from the TBOSS far-IR observations with similar *Herschel* PACS (Howard et al., 2013) and *Spitzer* MIPS (Rebull et al., 2010) measurements of the earlier spectral type Taurus members, a comprehensive accounting of the detection rates above and below the stellar/substellar boundary is given in Table 2.6. 73% of Class I targets of any spectral type were detected at both 70 μm and 160 μm, and 52% of observed Class II K-stars were similarly detected at both wavelengths. The detection rate declines for later spectral types, however even the substellar Class II members exhibit disk emission at 70 μm in the majority of systems. For the Class III members, the detection rate is systematically low ranging from 5% for K-stars to 0% for brown dwarfs. Direct comparisons of the far-IR emission among the substellar members of Taurus and other star-forming regions are not possible, since the TBOSS survey represents a uniquely sensitive and complete study.

2.5.6 Spatially extended targets

Although the *Herschel* PACS beam sizes are $5\farcs6$ and $11\farcs3$ which translate into spatial scales of >750 AU at the distance of Taurus, five TBOSS targets exhibit extended structure in the PACS maps shown in Figure 2.5. Three of the resolved sources are binary systems, for which the components for two of these systems are separated by an angle larger than the 70 μm beam size. IRAS 04191+1523 is extended along the binary axis and two peaks are visible in the map. IRAS 04325+2402 also extended along the binary axis and only one peak is present in the map. In these systems, the TBOSS target is the secondary component. For the remaining resolved binary IRAS 04248+2612, both

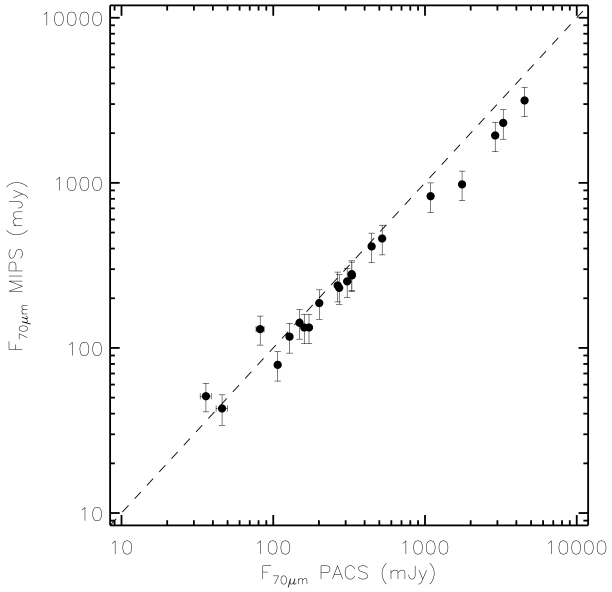

FIGURE 2.3: Plot showing the relation of PACS 70 μm and corresponding MIPS 70 μm fluxes for the TBOSS targets detected with both instruments. Non-linearity of the MIPS detector at ∼1 Jy is the likely cause of the 25-40% flux discrepancy seen for the targets >1 Jy, measured with PACS.

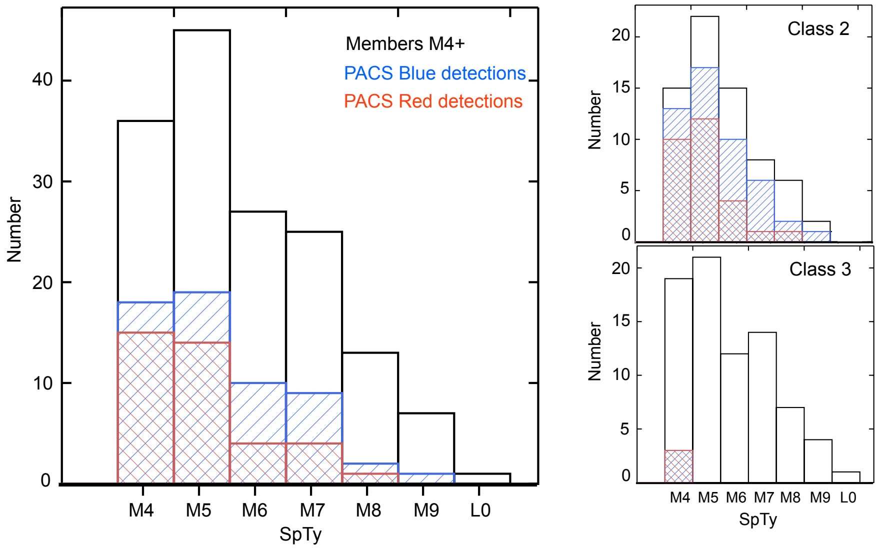

FIGURE 2.4: Histogram of spectral type for the TBOSS sample observed with *Herschel* PACS. The full observed sample and the number of PACS Blue channel (70 μm) detections and Red channel (160 μm) detections are shown on the left. The Class II and Class III observed sample, and PACS Blue and Red detections are shown in the top and bottom plots on the right respectively.

components are M4+, only one peak is present, and a larger extension to the Northwest direction ∼45° to the binary axis is evident. In addition to the binaries, two isolated objects are spatially extended - the Class I target L1521F-IRS and the Class III target

XEST 17-036. In both systems, the emission is largely symmetric. The Class I emission may result from an envelope of dust, however the origin of extended emission in the Class III source is difficult to explain.

Within the 70 μm map of the faintly detected brown dwarf J04141188+2811535 is the earlier spectral type object V773 Tau which also appears to be spatially extended, as shown in Figure 2.7. The FWHM of V773 Tau is $6\farcs5$, while the FWHM of ten targets with similar brightness is $5\farcs5 \pm 0\farcs2$. Follow-up interferometric imaging should be able to resolve the disk structure and determine which component or components harbour the disk. In addition to the wide separation TBOSS brown dwarf companion to V773 Tau, the primary source which includes many components, within an $0\farcs3$ radius, there are at least four stars (Boden et al., 2007, 2012). The spatially extended *Herschel* emission indicates that there may be a circumbinary distribution to the dust.

2.5.6.1 Hubble Space Telescope archival data

High-angular resolution imaging observations of YSOs at optical and near-IR wavelengths are sensitive to emission that is scattered by the surface layers of the surrounding material, and can therefore reveal significant information about the circumstellar morphology and subsequently the evolutionary status of the observed target. For the five targets that are spatially resolved with *Herschel* PACS two targets – IRAS 04248+2612 (IRAS 04248) and IRAS 04325+2402 (IRAS 04325) – have been observed with the Hubble Space Telescope (HST) using the Near Infra-red Camera and Multi-Object Spectrometer (NICMOS; Thompson et al., 1998). The imaging observations were observed with the broadband filters F110W (1.1 μm), F160W (1.6 μm), and F205W (2.05 μm) and the data for IRAS 04248 and IRAS 04325 are reported in Padgett et al. (1999) and Hartmann et al. (1999) respectively. The color-composite images are shown in Figure 2.6. The angular resolution with HST in the near-IR is $\sim$40 times better than that of *Herschel* PACS at 70 μm, revealing to greater detail the distribution, and structure of material surrounding the targets.

The image of IRAS 04248 shows a complex bipolar reflection nebula that extends for $\sim 10''$ along a north-west to south-east direction. The orientation is consistent with that witnessed in the PACS 70 μm, and 160 μm images. A dark absorption lane is seen to extend at least 450 AU in diameter, perpendicular to the direction of the nebula, and is consistent that the disk of this system is viewed at approximately edge-on (Whitney et al., 1997).

IRAS 04325 is a known binary with a projected separation of $\sim 8''$ (Duchêne et al., 2004).

As revealed in the NICMOS observations a large-scale nebulosity is witnessed around the primary component IRAS 04325AB (spectral type K3-M3.5; Luhman et al., 2010), at a position angle of ∼180° from the secondary component IRAS 04325C (spectral type M6-M8; Luhman et al., 2010). The emission around IRAS 04325C is consistent with that of existing HST observations of YSOs with material in the form of a disk and envelope (e.g., Burrows et al., 1996). Modelled fits performed by Hartmann et al. (1999) find that the best-fit disk radius is 30 AU, at a near edge-on inclination of 83°. These HST observations of IRAS 04248 and IRAS 04325 provide additional broadband photometry points, and direct constraints on the morphology of the surrounding material (i.e., distributed in a disk and/or envelope) that can be used in future SED modelling procedures.

2.5.7 Binary and single star population

Taurus has been the subject of many companion search programs (e.g. early results in Ghez et al. (1993) and Leinert et al. (1993), although most surveys have targeted the earlier spectral type members. Of the 154 M4+ TBOSS sample, only 38 have been observed by infrared direct imaging from the ground (Duchêne et al., 2004; Luhman et al., 2009a), high resolution imaging employing space-based measurements with HST/WFPC3 (White & Ghez, 2001), ground-based speckle imaging (Kohler & Leinert, 1998; Konopacky et al., 2007), and aperture masking or AO imaging (Kraus & Hillenbrand, 2009; Kraus et al., 2011). Among the subset of 38 TBOSS targets with information on the presence of companions, 23 are members of multiple systems, 12 are isolated single objects, and 3 are single objects with neighbouring stars categorized as unassociated with the TBOSS targets. For the majority of the TBOSS multiples, the target is the primary, however 9 of the targets are the secondary components in the systems. Details of each of the multiple systems are given in Table 2.5, along with an indication of which systems were detected and which involve possible contamination from an earlier spectral type primary. The separations of the components range from $0\farcs04$ to $26\farcs21$, and approximately half of the systems are unresolvable with *Herschel* and half are sufficiently wide to measure independent fluxes or limits for each component.

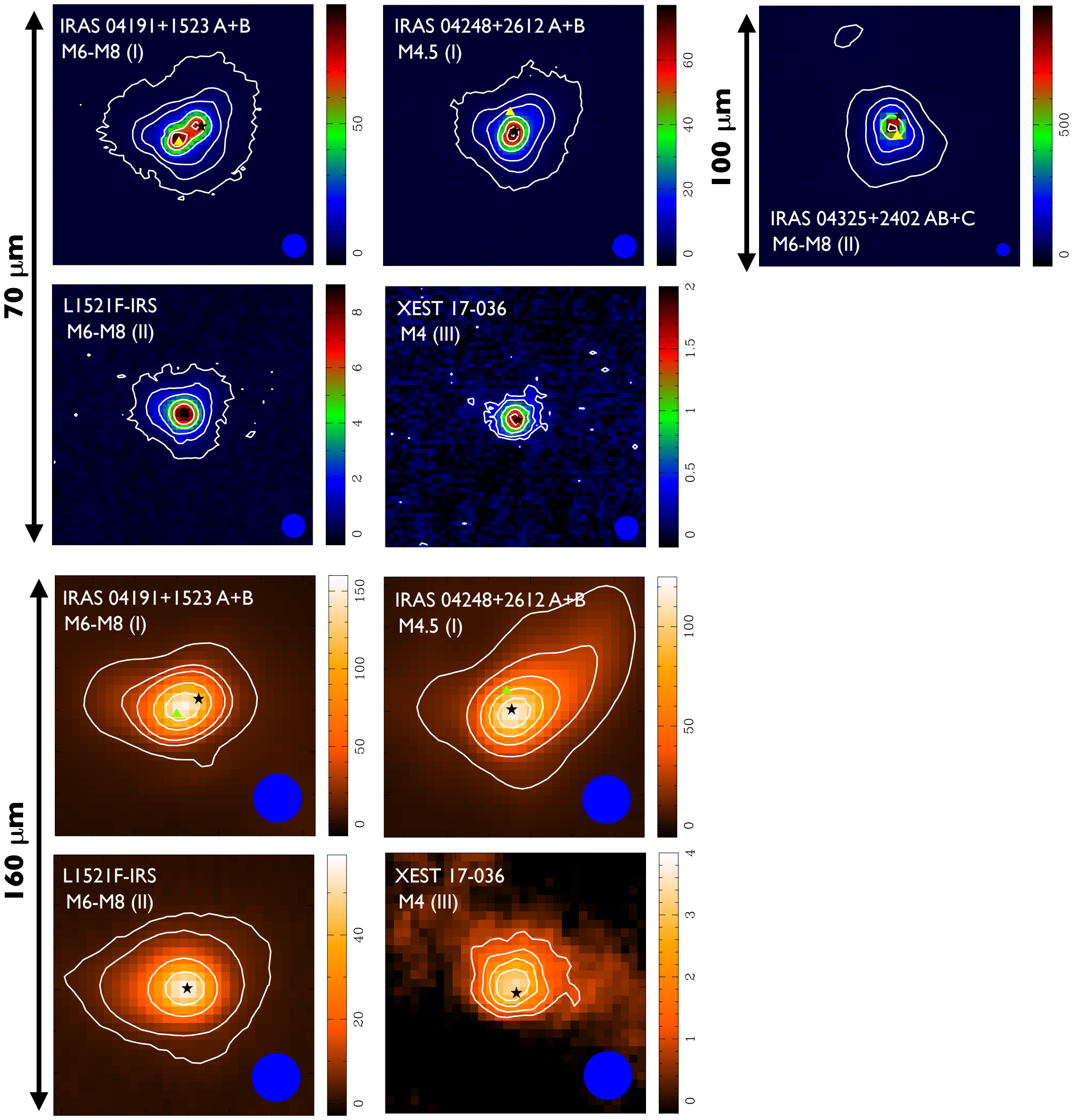

FIGURE 2.5: PACS Blue channel (70 μm and 100 μm) and Red channel (160 μm) maps of the five spatially extended TBOSS targets. Target name, spectral type and evolutionary class are labelled in the top, lefthand corner of each map. The 70 μm and 160 μm maps are 60″ in size along each axis, and the 100 μm maps is 120″ in size along each axis. Beam sizes are represented by the blue circles in the bottom, right hand corner of each map. The scale bar shows the intensity of each map in units of mJy/pixel. 2MASS coordinates of the TBOSS targets are represented by the black stars. For binary systems, the position of the companion star are indicted with yellow triangles in the 70 μm and 100 μm maps, and by green triangles in the 160 μm maps. Contours levels begin at 3σ in all maps and extend up to 500σ, 400σ, 150σ, 40σ and 300σ in the Blue channel maps of IRAS 04191+1523 B, IRAS 04248+2612, L1521F-IRS, XEST 17-036 and IRAS 04325+2402 C respectively, and up to 50σ, 60σ, 70σ and 10σ in the Red channel maps of IRAS 04191+1523 B, IRAS 04248+2612, L1521F-IRS and XEST 17-036 respectively.

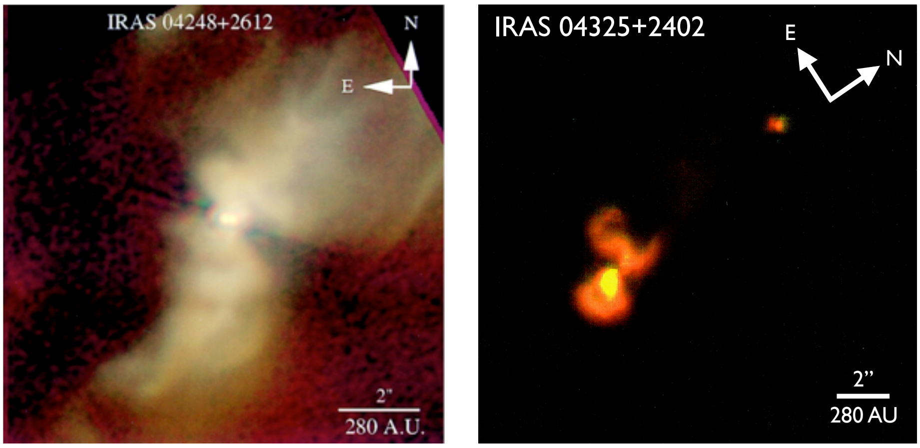

FIGURE 2.6: Images of the PACS spatially resolved targets that have been observed with HST – IRAS 04248+2612 (**left**; Padgett et al., 1999), and IRAS 04325+2402 (**right**; Hartmann et al., 1999). The color composites images shown are NICMOS broadband observations of F110W (1.1 μm), F160W (1.6 μm), and F205W (2.05 μm) for IRAS 04248 and F160W, and F205W for IRAS 04325.

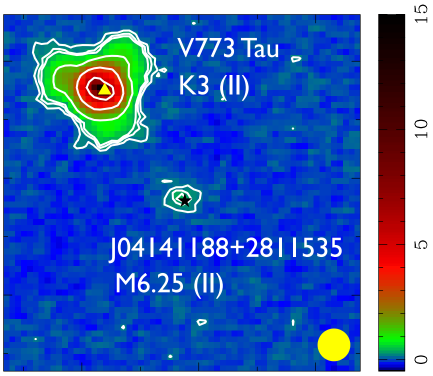

FIGURE 2.7: PACS Blue channel (70 μm) map of the faintly detected brown dwarf J04141188+2811535 (black star). The earlier type companion V773 Tau (yellow triangle) is also seen within the map and is spatially extended. Target name, spectral type and evolutionary class for each component of the system are indicated on the map. The map is $60''$ in size along each axis. The beam size is represented by the yellow circle in the bottom, right hand corner. Contour levels are plotted at 3, 5, 7, 20, 50 and 100σ. The scale bar shows the intensity of the map in mJy/pixel.

2.6 Discussion

2.6.1 Far-IR emission as a function of SpTy.

The large number of PACS 70 μm detections in the TBOSS Class II sample defines the lower boundary of far-IR emission. Connecting the TBOSS fluxes with previous measurements of earlier spectral type Class II Taurus members reported in the literature (Howard et al., 2013; Rebull et al., 2010), provides the first complete census of this

Table 2.5: Multiplicity of the TBOSS sample, ordered by evolutionary class and companion separation.

2MASS (1)	Other name (2)	Class (3)	SpTy. (4)	Companion name (5)	ρ ($''$) (6)	PACS Blue Det. (7)	Ref. (8)
J04275730+2619183	IRAS 04248+2612	I	M4.5	...	4.55	y-contam	3
J04220007+1530248	IRAS 04191+1523 B	I	M6-M8	IRAS 04191+1523 A	6.09	y-contam*	3
J04403979+2519061	...	II	M5.25	...	0.04	y	5
J04292165+2701259	IRAS 04263+2654	II	M6	...	0.22	y	5
J04284263+2714039	...	II	M5.25	...	0.62	y	5
J04323028+1731303	GG Tau Ba+Bb	II	M6	GG Tau Ba - Bb	1.47	y^a	10
				GG Tau A - B	10.75		6
				GG Tau Aa - Ab	0.25		10
J04233539+2503026	FU Tau A	II	M7.25	FU Tau B	5.70	n	9
J04233573+2502596	FU Tau B	II	M9.25	FU Tau A	5.70	n	9
J04554801+3028050	...	II	M5.6	J04554757+3028077	6.54	y	6
J04324938+2253082	JH 112 B	II	M4.25	JH 112 A	6.80	n	6
				JH 112 Aa -Ab	1.57		7
J04353536+2408266	IRAS 04325+2402 C	II	M6-M8	IRAS 04325+2402 AB^b	8.15	y-contam*	3
J04414489+2301513	...	II	M8.5	J04414565+2301580	12.81	y	6
				J04414565+2301580 Aa - Ab	0.23	n	7
J04141188+2811535	...	II	M6.25	V773 Tau	26.21	y	6
				V773 Tau A(ab)	SB^c		1
				V773 Tau A - B	0.12		2
				V773 Tau A - C	0.26		2
J04464260+2459034	RXJ 04467+2459	III	M4	...	0.05	n	7
J04292971+2616532	FW Tau A+B+C	III	M4	FW Tau A - B	0.08	y-contam	10
				FW Tau A - C	2.30	y-contam	10
J04292071+2633406	J1-507	III	M4	...	0.08	n	7
J05061674+2446102	CIDA 10	III	M4	...	0.08	n	7
J04312382+2410529	V927 Tau A+B	III	M5.5	...	0.27	n	10
J04400174+2556292	CFHT 17	III	M5.75	...	0.58	n	5
J04414565+2301580	...	III	M4.5	J04414565+2301580 Aa - Ab	0.23	n	7
				J04414489+2301513	12.81	n	6
J04554757+3028077	...	III	M4.75	J04554801+3028050	6.54	n	6
J04312405+1800215	MHO 4	III	M7	...	10.42	n	4
J04321786+2422149	CFHT 7	III	M6.5	V928 Tau	18.90	n	6
				V928 Tau A - B	0.21		7
Observed Single							
J04313613+1813432	LkHa 358	I	M5.5			y	5
J04161210+2756385	...	II	M4.75			y	5
J04210795+2702204	CFHT 19	II	M5.25			y	5
J04213459+2701388	...	II	M5.5			y	5
J04295950+2433078	CFHT 20	II	M5.5			y	5
J04442713+2512164	IRAS 04414+2506	II	M7.25			y	5
J04554535+3019389	...	II	M4.75			y	8
J04144730+2646264	FP Tau	II	M4			y	8
J04174965+2829362	V410 X-ray 1	II	M4			y	8
J05075496+2500156	CIDA 12	II	M4			y	5
J04380083+2558572	ITG 2	III	M7.25			n	8
J04131414+2819108	LkCa 1	III	M4			n	5

Notes. Col. (1) 2MASS identifier. Col. (2) Other name. Col. (3) Spectral evolutionary class. Col. (4) Spectral type. Col. (5) Companion name. Col. (6) Projected companion separations. Col. (7) Targets with PACS Blue channel (70 μm or 100 μm) detections are designated "y", and targets with upper limits are designated "n". "y-contam" indicates detected emission that is contaminated due the companion listed, and "y-contam*" indicates contamination due to the listed companion that is of a spectral type earlier than that of the TBOSS sample (¡M4). Col. (8) Reference of companion separation.

a. Emission of GG Tau Ba+Bb is resolved from GG Tau Aa+Ab with PACS at 70 μm (Howard et al., 2013).

b. IRAS 04325+2402 AB is a speculated binary (Hartmann et al., 1999).

c. Spectroscopic binary (SB).

References. (1) Boden et al. (2007); (2) Boden et al. (2012); (3) Duchêne et al. (2004); (4) Kohler & Leinert (1998); (5) Konopacky et al. (2007); (6) Kraus & Hillenbrand (2009); (7) Kraus et al. (2011); (8) Kraus et al. (2012); (9) Luhman et al. (2009b); (10) White & Ghez (2001).

emission for a full population of a star-forming region. Figure 2.8 plots the 70 μm fluxes and upper limits as a function of spectral type spanning K0-M9 for 159 Taurus Class II members, representing 89% of all objects of this evolutionary class. Although the *Spitzer* and *Herschel* GASPS programs had shallower detection limits than the TBOSS observations, the detection rates for the early spectral types is nearly 100% as shown in Figure 2.9, indicating that the trends seen in the flux as a function of spectral type are not due to an observational bias.

The overall shape of the flux distribution in Figure 2.8 exhibits a systematic decline

Table 2.6: Detection rates

Class / SpTy	Total	70 μm Observed	70 μm Detection Rate	160 μm Observed	160 μm Detection Rate
Class I	33	26	92% (24)	21	71% (15)
Class I	33	27	93^{+2}_{-8}% (25)	22	73^{+7}_{-11}% (16)
K0-K7	18	13	100^{+0}_{-12}% (13)	10	80^{+7}_{-17}% (8)
M0-M3	8	8	75^{+9}_{-20}% (6)	6	33^{+22}_{-13}% (2)
M4-M6	4	4	100^{+0}_{-31}% (4)	4	100^{+0}_{-31}% (4)
M6.25-L0	3	2	100^{+0}_{-46}% (2)	2	100^{+0}_{-46}% (2)
Class II	178	156	84^{+3}_{-3}% (131)	138	52^{+4}_{-4}% (72)
K0-K7	37	32	97^{+1}_{-7}% (31)	26	81^{+5}_{-10}% (21)
M0-M3	72	60	87^{+3}_{-6}% (52)	48	50^{+7}_{-7}% (24)
M4-M6	44	43	84^{+4}_{-7}% (36)	41	63^{+7}_{-8}% (26)
M6.25-L0	25	21	57^{+11}_{-10}% (12)	23	4^{+9}_{-1}% (1)
Class III	128	117	4^{+3}_{-1}% (5)	114	4^{+3}_{-1}% (5)
K0-K7	24	22	5^{+9}_{-1}% (1)	20	5^{+10}_{-2}% (1)
M0-M3	26	20	5^{+10}_{-2}% (1)	18	6^{+10}_{-2}% (1)
M4-M6	43	41	7^{+6}_{-2}% (3)	41	7^{+6}_{-2}% (3)
M6.25-L0	35	34	0^{+5}_{-0}% (0)	35	0^{+5}_{-0}% (0)

Notes. The detection rates for the K0-K7, and M0-M3 bins have been tabulated from the *Spitzer* MIPS observations reported in Rebull et al. (2010) and the *Herschel* PACS observations reported in Howard et al. (2013). The detection rates for the M4-M6, and M6.25-L0 bins have been tabulated from the *Herschel* PACS 70 μm and 160 μm observations reported here and are supplemented with results from the literature (Harvey et al., 2012; Howard et al., 2013).

with later spectral types, and the slope of the decline is shallower for K- and early-M stars than for mid- to late-M dwarfs. For comparison with the disk flux trend, the stellar bolometric luminosity predicted from the 1 Myr evolutionary models of Baraffe et al. (1998), that span the spectral types K7 to ~M8 (i.e. $T_{\rm eff}$ ~4100-2300 K), either side of the inflection point is displayed in Figure 2.8. For the TBOSS Class II objects detected at 70 μm, bolometric luminosities were calculated from the best-fit stellar radii derived in the SED fitting procedure and for the Taurus Class II population outside the TBOSS sample (<M4) bolometric luminosities were supplemented from those reported in Andrews et al. (2013). The similarity in the shapes of the stellar bolometric luminosity and the disk flux data suggests that the excess flux fraction from the disk is common across the full population of Taurus. For the TBOSS sample, the disk excess fraction is plotted as a function of spectral type in Figure 2.10. There is no distinction across the stellar/substellar boundary and a KS test indicates that the stellar and substellar TBOSS samples are drawn from the same parent distribution.

At any given spectral type, there is a significant spread in the far-IR emission, typically over an order of magnitude, as seen in Figure 2.8. To investigate possible origins of the large dispersion in disk flux, we generated a series of model SEDs with the radiative transfer code MCFOST (Pinte et al., 2006, 2009) and considered the range of 70 μm fluxes in the model SEDs. Rather than creating an exhaustive multi-parameter grid search on any given target, we varied individual disk parameters about a reference disk defined by: inner and outer radius ($R_{\rm in}$, $R_{\rm out}$), minimum and maximum grain size ($a_{\rm min}$, $a_{\rm max}$), surface density exponent (p), scale height (H_0), flaring exponent (β) and disk mass ($M_{\rm disk}$). As shown in Figure 2.11, disk properties such as $R_{\rm in}$, $R_{\rm out}$, $a_{\rm min}$, $a_{\rm max}$, p, and $M_{\rm disk}$ do not have a large impact on the 70 μm flux relative to other wavelength regimes, and the PACS data do not constrain these parameters. In contrast, variations in geometrical and structural factors such as disk inclination, H_0 (equivalent to disk opening angle), and β, can individually account for variations up to nearly an order of magnitude.

The flaring geometry of disks i.e., H_0 and β, are seen to have the most dominant impact on the SED shape at far-IR wavelengths. As seen in Figure 2.11 large values of disk scale height and flaring index correspond to greater levels of excess. This is due to the greater fraction of stellar radiation that is intercepted and reprocessed by the circumstellar dust (e.g., Dullemond & Dominik, 2004b).

Following on from this assessment, properties for a canonical disk model were used to generate a grid of model SEDs, across spectral types ranging from K0-M9, in order to investigate the effect that disk inclination alone can have in the spread of 70 μm flux for objects with the same spectral type. The input stellar properties ($T_{\rm eff}$, $R_{\rm star}$, and $M_{\rm star}$) were set based on the 1 Myr evolutionary models of Palla & Stahler (1999) for spectral types <K7, Baraffe et al. (1998) for spectral types K7-M8, and those from Chabrier et al. (2000) for spectral types $\geq$M8. Six of the eight input disk parameters were fixed in accordance to typical values reported in the literature; $a_{\rm min}$ = 0.03 μm, $a_{\rm max}$ = 1000 μm, H_0 = 10 AU at a reference radius of 100 AU, β = 1.125, p = -1.0 and $R_{\rm out}$ = 100 AU. The surface density power index p = -1.0 is adopted as it is found to be the median best-fit value of existing protoplanetary disks studies around low-mass stars reported in the literature (i.e., $p\sim$0-2; Kitamura et al., 2002; Andrews & Williams, 2007; Baillié & Charnoz, 2014).

The two remaining disk parameters were scaled in accordance to the properties of the central object; $M_{\rm disk}$ was set at 1% of the stellar mass (e.g Scholz et al., 2006; Andrews et al., 2013) with a standard gas to dust ratio of 100:1, and $R_{\rm in}$ was set at the sublimation radius for dust grains at $T_{\rm sub}$ = 1500 K. The SED models were generated for disk inclinations at; face-on (0°), 60°, and edge-on (90°), from which the 70 μm fluxes were extracted and are shown in Figure 2.8. Between the face- and edge-on disk inclinations, over an order of magnitude spread in flux is seen across the majority of the spectral range, and 73% of the observed population is bounded between these two models. Direct observations of disks around brown dwarfs, and constraints from SED modelling results reported in the literature, suggest that the outer disk radius is typically in the range ∼10-40 AU for these low mass objects (e.g. Scholz et al., 2006; Luhman et al., 2007; Ricci et al., 2013). In order to ensure that the canonical value $R_{\rm out}$ = 100 AU does not bias the model results for objects in the brown dwarf regime, a second grid of SEDs were generated in which $R_{\rm out}$ was scaled as $M_{\rm star}^{\frac{1}{2}}$ (keeping the density across the area of the disk constant across the spectral range) and bound at 10 AU for an object of spectral type M9. No significant change in the 70 μm flux was witnessed between the these two grid of models. Whilst the disk model 70 μm fluxes from face- to edge-on exhibit a spread of over a magnitude, and encompass the majority of the observed population, an equivalent trend and spread is seen in the observed bolometric luminosities. In addition to the 1 Myr isochrone shown in Figure 2.8, the isochrones for 0.4 and 2 times that of the model stellar radii are also displayed, and selected based on the results of the SED fitting of the TBOSS sample. To distinguish whether or not the stellar properties alone are the underlying cause of the observed trend and spread in disk fluxes; for the TBOSS sample the data in Figure 2.8 are display corresponding to the size of the best-fit stellar radii. The random scatter of large (>1.5 times the stellar evolutionary model radii) and small (<0.5 times the stellar evolutionary model radii) best-fit model radii throughout the population, indicates that the spread witnessed in the 70 μm disk excess is not solely explained due to the emission of the central source. This further re-enforces the requirement for detailed modelling of the disk properties across the full population, and is the subject of a forthcoming paper.

2.6.2 SEDs of the TBOSS sample

By combining the TBOSS sample *Herschel* far-IR photometry with literature and catalog measurements from the optical, IR, mid-IR, and submm/mm, SEDs were constructed for each target, and the median SED for each spectral type was constructed for the Class II sources. The Class I SEDs are given in Figure A.8 of Appendix A, and the PACS fluxes are at or near the peak power point for these embedded sources. Due to the difficulty in interpreting the SEDs for targets with unresolved companions, SEDs for that category of target are plotted separately in Figure A.9 of Appendix A. As shown in Table 2.6 of detection rates, 75% of the Class II targets are detected with at least one *Herschel* band, and the SEDs for these detected sources are compiled in Figures 2.15 and 2.18 and Figures A.9-A.11. To compare the shapes of the SEDs for different spectral types, the median SED for detected Class II targets of each type is plotted on Figure 2.12, with the medians

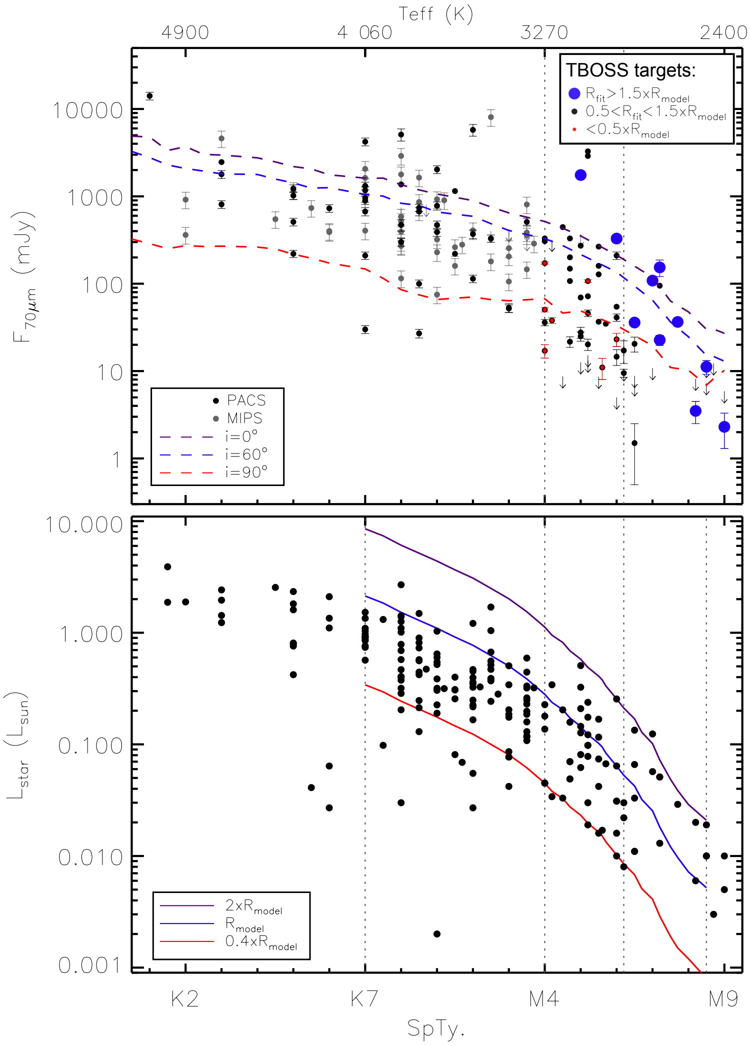

FIGURE 2.8: (**top**) 70 μm flux shown as a function of spectral type for the Taurus Class II population, with spectral types spanning early K to late M. The vertical dotted lines mark the boundaries of the TBOSS sample (targets of spectral types M4+) and the stellar/substellar limit (M6.25). Fluxes measured from PACS and MIPS are represented by the black and grey points respectively. Additionally, for the detected TBOSS targets, the large, blue points correspond to best-fit stellar radii of >1.5 times that of the evolutionary model values, and the small red points correspond to best-fit stellar radii of <0.5 times that of the evolutionary model values. Downwards arrows represent the 3σ upper limits. The dashed lines represent the 70 μm fluxes extracted from a test grid of model SEDs, generated with the radiative transfer code MCFOST and represent the fluxes for disk inclinations of face-on (0°; purple dashed-line), 60° (blue dashed-line) and edge-on (90°; red dashed-line). (**bottom**) Bolometric luminosities of the Taurus Class II population, with spectral types spanning early K to late M. The luminosities of the TBOSS sample are derived from the best-fit stellar radii. The luminosities for targets of spectral type <M4 are from those reported in Andrews et al. (2013). The 1 Myr isochrone from Baraffe et al. (1998) is represented with the blue solid line and the corresponding isochrones are shown for values of 2 and 0.4 times that of the model stellar radii (purple and red solid lines respectively).

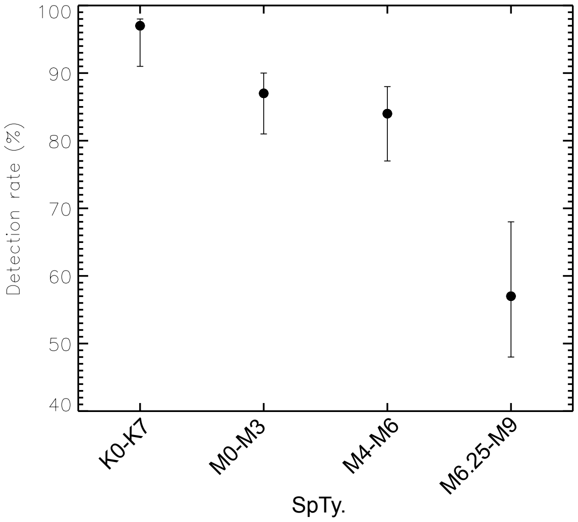

FIGURE 2.9: Taurus Class II, 70 μm detection rates for objects spanning the spectral types K0-M9. The M4-M6 and M6.25-M9 detections rates are compiled from the TBOSS sample observed with *Herschel* PACS. The K0-K7 and M0-M3 detections rates are compiled form the *Herschel* PACS observations reported in Howard et al. (2013) and the *Spitzer* MIPS observations reported in Rebull et al. (2010).

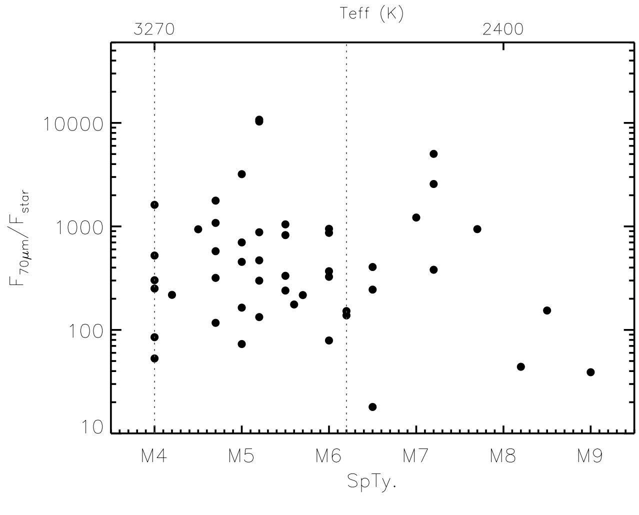

FIGURE 2.10: 70 μm disk excess fraction shown as a function of spectral type for the detected Class II TBOSS objects.

scaled by the *J*-band flux. Due to the characteristic SED shape of Class II objects with edge-on disks (similar in appearance to Class I objects), targets with known edge-on disks – IRAS 04248+2612 , IRAS 04248+2612, J04381486+2611399, J04442713+2512164, and ZZ Tau-IRS (Padgett et al., 1999; Andrews et al., 2008; Luhman et al., 2007; Bouy et al., 2008; White & Hillenbrand, 2004) – are not included in the median SED, calculated per spectral type. Overall, the relative flux at longer wavelengths declines as a function of spectral types, though there is no discontinuity at the stellar/substellar boundary. The

SEDs of the smaller number of undetected Class II targets are shown in Figure A.12 of Appendix A. Only 4 Class III targets have *Herschel* detections, and the SEDs for these four sources are given in Figure 2.15. Finally, the Class III TBOSS targets with far-IR upper limits are plotted in Figures A.13-A.16.

2.6.2.1 Effects on A_V from circumstellar dust

Best-fit stellar photospheric models are displayed on the SEDs for each target of the TBOSS sample. The fits were obtained by allowing the stellar radius ($R_{\rm star}$) and extinction along the line-of-sight (A_V) to vary as free parameters. In order to investigate the effects that circumstellar dust has on A_V an investigation has been carried out for three targets under which best-fit extinctions fall into three categories: 1. no extinction (A_V=0 mag – XEST 26-052), 2. median extinction ($A_V \sim 1$ mag – FP Tau), and 3. high extinction ($A_V \sim 4$ mag – V410 Xray 4). These targets were modelled with the online SED fitting tool developed by Robitaille et al. (2006), which consists of a grid of 200,000 radiation transfer models of axisymmetric YSOs, that span a range of stellar masses and evolutionary stages, and are characterised by stellar, disk and envelope parameters.
We obtain best-fit stellar radii of $R_{\rm star}$=1.7 $\mathrm{R}_\odot$ for XEST 26-052, FP Tau, and V410 Xray 4, which is consistent with the predicted stellar radius derived from the 1 Myr evolutionary models based on the spectral types of the targets (i.e. Baraffe et al., 1998; Luhman et al., 2003a). From the Robitaille fitting tool, the best-fit extinctions obtained for XEST 26-052, FP Tau, and V410 Xray 4 are 0.3 mag, 0 mag, and 15.7 mag respectively, and the corresponding best-fit stellar radii are 0.8 $R_{\rm star}$, 2 $R_{\rm star}$, and 2.4 $R_{\rm star}$ respectively. Across these three targets representative of the range of extinctions levels amongst the sample, ∼60% and up to 100% difference in extinction is witnessed between the two best-fit methods, and correspondingly a difference of ∼10-40% is seen in the best-fit stellar radii. This preliminary investigation indicates the degeneracy that exists between extinction due to foreground material along the line-of-sight and extinction due to that of circumstellar material. SED modelling procedures that can derive best-fit vales of A_V, and disk properties self-consistently will be pursued in future investigations for the full TBOSS sample.

2.6.3 Candidate transition disks

Transition disks represent a more advanced stage of disk evolution in which material in the disk has dissipated, either marked by an inner hole (e.g. Calvet et al., 2005), or a

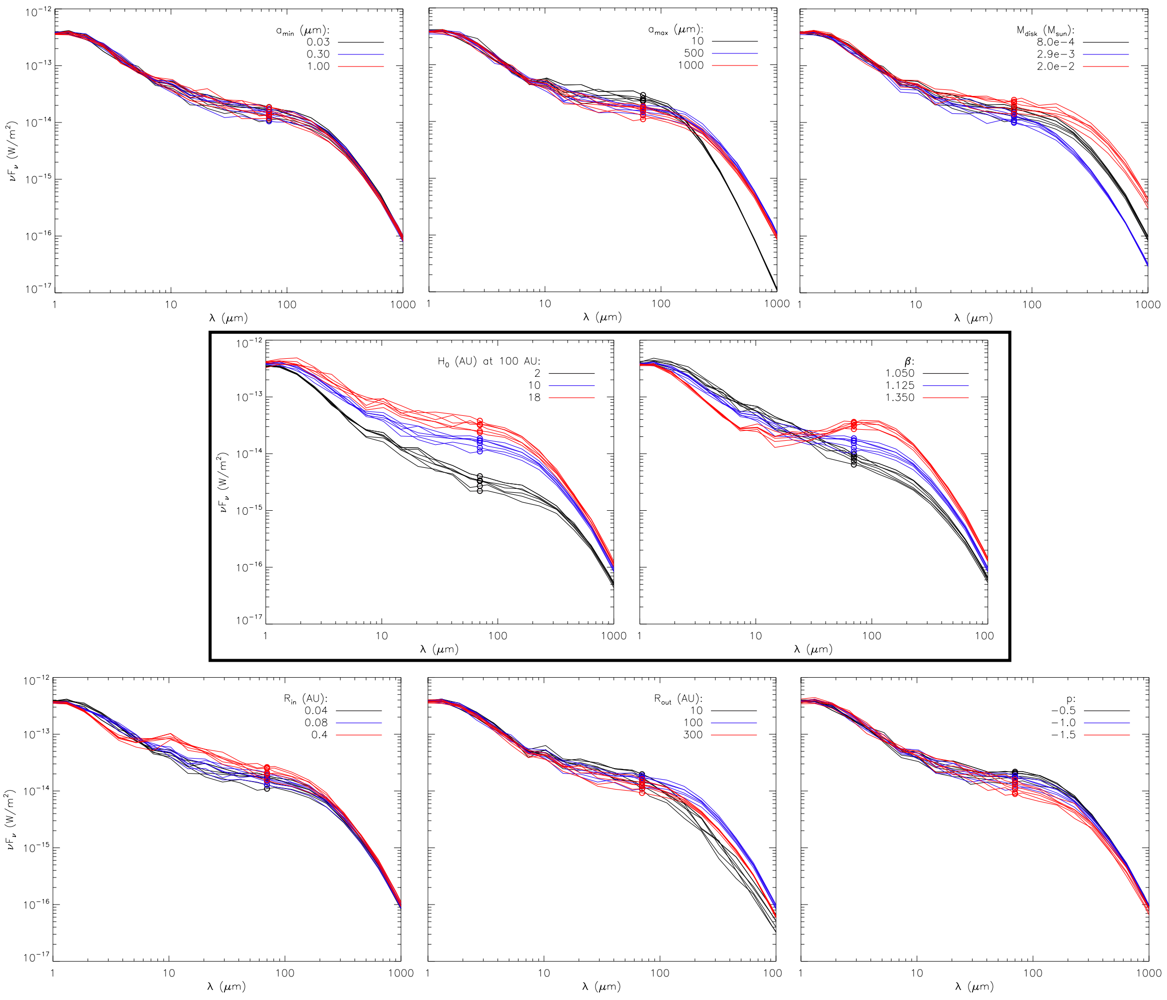

FIGURE 2.11: SED visualisation showing the impact that individual disk parameters have on excesses at 70 μm, the wavelength of which is highlighted on the SEDs with the open circle symbols. The SEDs were generated with the 3D radiative transfer code MCFOST (Pinte et al., 2006, 2009). In each individual panel, 3 models of SEDs were generated (black, blue and red lines), by varying one of the the eight disk parameters with values that are displayed in each panel. From left to right and top to bottom, the disk parameters are: minimum grain size ($a_{\rm min}$), maximum grain size ($a_{\rm max}$), disk mass ($M_{\rm disk}$), scale height (H_0) at a reference disk radius of 100 AU, disk flaring exponent (β), inner radius ($R_{\rm in}$), outer radius ($R_{\rm out}$), and surface density exponent (p). The SEDs were generated for a star of spectral type M4, and the stellar properties were set based on the temperature conversion of Luhman et al. (2003b) and the 1 Myr evolutionary models of Baraffe et al. (1998), i.e. $T_{\rm eff}$=3300 K, $R_{\rm star}$=1.65 $R_\odot$, $M_{\rm star}$=0.29 $M_\odot$. The model SEDs are shown at disk inclinations of 18°, 32°, 41°, 49°, 57° and 63° (where 0° is for a face-on disk inclination), for each value of the varied disk parameters. Disk geometry; inclination, H_0 and β are seen to impact the emission at 70 μm the most.

homologous depletion (Currie et al., 2009). A number of physical processes have been suggested to clear disk material, including photoevaporation (Alexander et al., 2006), disruption from companions (Artymowicz & Lubow, 1994), and grain growth (Dullemond

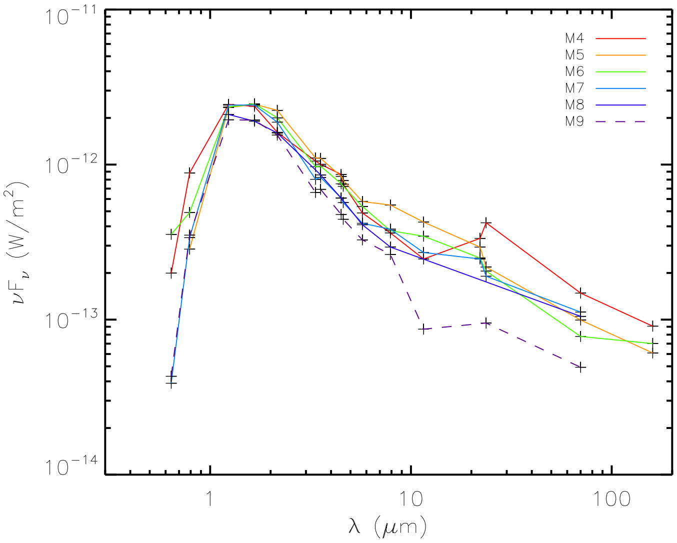

FIGURE 2.12: Median SEDs of the Class II TBOSS targets detected with *Herschel* PACS. The median SEDs are normalized by the *J*-band flux, and shown per spectral type for M4-M8. The normalised SED of the one, M9 detected target (KPNO 6; Harvey et al., 2012) is shown and represented by the purple, dashed line.

& Dominik, 2004a). The shape of the SED – specifically spectral indices between pairs of wavelengths – or spectral line features, or the absence of gas have been used to identify transition disks and later stage debris disks (Muzerolle et al., 2010; Kim et al., 2013). Within the TBOSS sample, 4 transition disks are known (Currie et al., 2011; Cieza et al., 2012), along with 2 debris/photoevaporative disks (Currie et al., 2011). Details of the previously known TBOSS transition and debris disks are listed in Table 2.7.

TABLE 2.7: Transition disks within the TBOSS sample

2MASS	Other name	Class	SpTy.	TD type	Ref.
J04144730+2646264	FP Tau	II	M4	Homologously depleted	1
J04190110+2819420	V410 X-ray 6	II	M4.5	Inner Hole	2
J04322210+1827426	MHO 6	II	M4.75	Candidate	3
J04161210+2756385	...	II	M4.75	Candidate	3
J04403979+2519061	...	II	M5.25	Debris	2
J04202555+2700355	...	II	M5.25	Candidate	1
J04210934+2750368	...	II	M5.25	Homologously depleted	2
J04284263+2714039	...	II	M5.25	Homologously depleted	2
J04213459+2701388	...	II	M5.5	Candidate	3
J04332621+2245293	XEST 17-036	III	M4	Candidate /Debris	3
J04295422+1754041		III	M4	Candidate	3
J04292971+2616532	FW Tau A+B+C	III	M4	Photevap.	2
J04354203+2252226	XEST 08-033	III	M4.75	Candidate/Debris	3

References. Cieza et al. (2012); (2) Currie et al. (2011); (3) This work.

A series of spectral indices ($\alpha = -\frac{d \log(\nu F_\nu)}{d \log(\nu)}$) over wavelength ranges from the 3.6 - 8.0 μm IRAC bands to the 160 - 1300 μm bands as a function of effective temperature

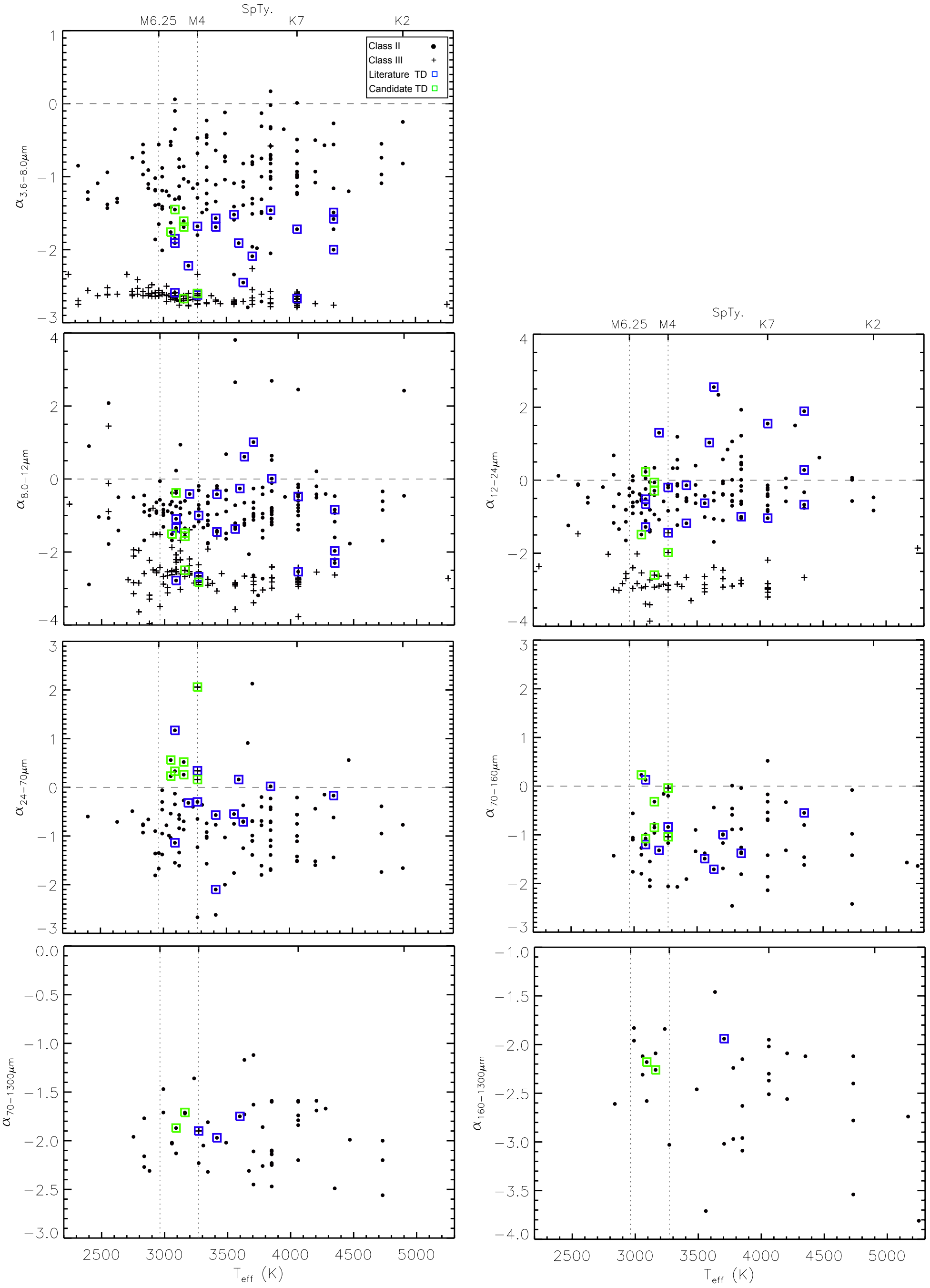

FIGURE 2.13: Series of spectral index plots shown as a function of stellar effective temperature, merging all Taurus Class II (filled circles) and Class III (crosses) populations with; mid-IR emission (IRAC, MIPS and *WISE*), far-IR emission (PACS and MIPS), and 1.3 mm emission (for those targets not with no reported 1.3 mm observations, the nearest submm/mm observation was scaled to 1.3 mm assuming $F_\nu \propto \nu^2$). Blue squares enclose the targets identified in the literature with transition disks and and green squares enclose targets the candidate transition disks objects identified in this paper.

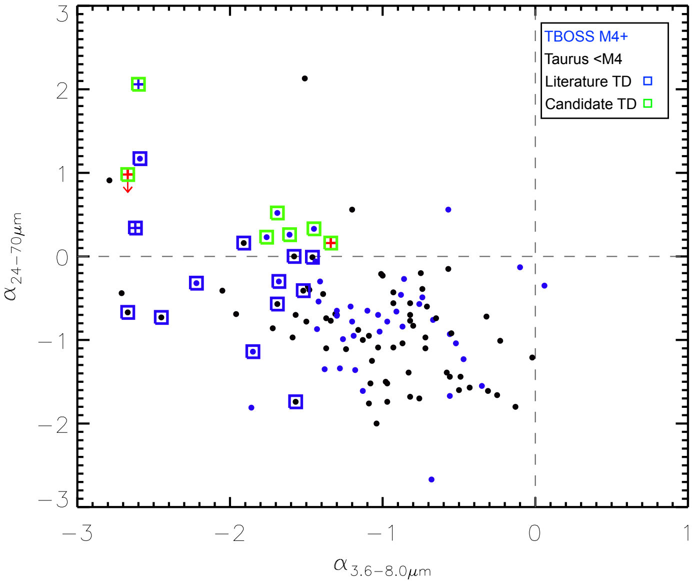

FIGURE 2.14: Spectral index plot showing that Taurus Class II (filled circles) and Class III (crosses) populations with mid-IR and far-IR excess. The spectral indices; $\alpha_{3.6-8.0\mu m}$ and $\alpha_{24-70\mu m}$ are used to identify candidate targets with transition disks (TDs) and debris disk. Targets identified in the literature with TDs, and the candidate TDs reported here, are enclosed by blue and green squares respectively. J04295422+1754041 (red cross) was unobserved with IRAC and MIPS, and the spectral indices are calculated from the *WISE* 3.4 μm and 12 μm fluxes and the *WISE* 22 μm and PACS 70 μm fluxes. XEST 08-033 (red cross with downward arrow) was only detected with PACS at 160 μm, and the 24-70 spectral index shown is calculated from the 70 μm upper limit.

are plotted in 7 panels in Figure 2.13 for the full Taurus Class II and Class III population with detections. Over the shortest 3.6 - 8.0 μm wavelength range, the transition disk SEDs have steeply declining slopes and occupy the region at the extreme of the Class II distribution and overlapping with Class III members. The transition disks again have a distinct distribution in the SED power law index over the 24 - 70 μm range; the majority of the slopes are flat to rising. Based on the 24 - 70 μm spectral index, we identified a new population of 7 additional transition disk candidates with rising slopes, and these new systems are noted in Table 2.7. Amongst these 7 transition disk candidates, J04202555+2700355 was previously investigated in Currie et al. (2011) who report an inconclusive evolutionary status (primordial or transition disk with inner hole) based on SED modelling results. XEST 17-036 and XEST 08-033 are considered to be debris disks based on their $\alpha_{3.6-8.0\mu m}$ values that are consistent with those of previously reported debris/photoevaporative disks in the literature. Furthermore, XEST 17-036 – is remarkable in that it is among the few spatially resolved targets. Our selection criteria and classification for the targets that we identify to be candidate transition/debris disks is highlighted in the spectral index plot shown in Figure 2.14, and follows that $\alpha_{24-70\mu m}$ >0, with -2$\lesssim$ $\alpha_{3.6-8.0\mu m}$ $\lesssim$-1 are candidate transition disks, and those with $\alpha_{3.6-8.0\mu m}$ $\lesssim$-2.5 are candidate debris disks. The SEDs of the known and candidate transition disks are shown in Figure 2.15. The 5 new transition disk candidates have spectral types ranging from M4-M5.5. Currently, none of the candidate transition/debris disks have high resolution imaging data (and only 3 of the known M4+ transition disks have such data), making it impossible to assess the likelihood of a dynamically cleared inner region for these disks.

From the total number of transition disks it is possible to determine the typical statistical lifetime for this evolutionary stage. Following the procedure of Luhman et al. (2010), in which the estimated transition disk lifetime is ~0.45 Myr for K5-M5 spectral types – calculated from the ratio of the number of transition disks to that of primordial disks and assuming that the average primordial disk lifetime is ~3 Myr – we obtain a ratio of 9/52 (accounting for the 4 Class III objects that are detected at 70 and/or 160 μm), and an estimated lifetime of ~0.52 Myr for spectral types M4-M9.

2.6.3.1 SED modelling of the TD targets

Transition disks have been characterised observationally as having little excesses above the photosphere in the near-IR to mid-IR wavelengths. This characteristic SED can be understood in terms of an outer disk that has been truncated at some radius, with or without a small amount of dust remaining in the inner disk region inside the truncation radius. SED models estimate that these cavities range from ~1-100 AU (e.g., Andrews et al., 2011; Brown et al., 2007; Espaillat et al., 2011). The sample of TBOSS targets consists of 6 TDs that have been previously reported in the literature, and 7 new additional candidates presented here. In order to obtain a preliminary estimate of the range of cavity sizes for these 13 TDs, initial "Chi-by-eye" best-fit SED modelling was performed, and the resulting models are shown in Figure 2.16. The radiative transfer code MCFOST was used to generate the SED models, consisting of two disk zones that bound a cavity devoid of material, that is defined by the inner and outer disk radii (R_{in}, R_{out}) of each zone. The initial disk input parameters were set to those described in Section 2.6.1. The inner and outer disk radii of the inner disk (zone 1) was set to R_{in}=R_{sub}, where R_{sub} is the dust sublimation radius, and R_{out}=100 AU. The outer disk (zone 2) was set with initial disk radii values of R_{in}=150 AU, and R_{out}=200 AU. The disk mass was initially distributed between the two disk zones such that 0.01% was input into zone 1, and the remaining mass into zone 2. These parameters and the remaining disk parameters (i.e.,

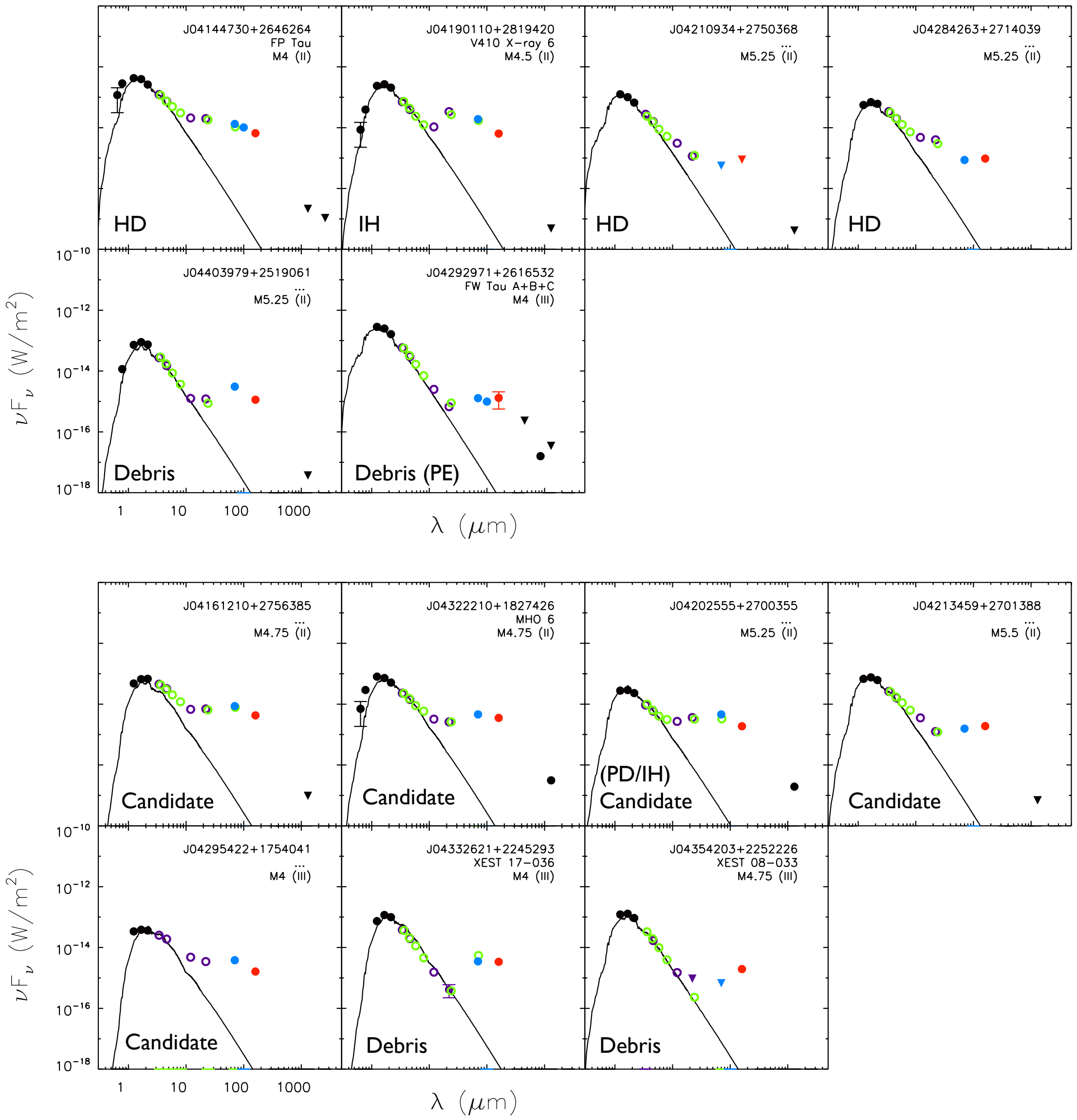

FIGURE 2.15: Spectral energy distributions showing the targets with transition disks (TD) previously reported in the literature (**top panel**) and the candidate targets with TD identified in this work (**bottom panel**). For those targets identified in the literature, the TD types; homologous depletion (HD), inner disk hole (IH), debris, and photo-evaporated (PE) are displayed on each SED. The candidate TDs are identified by the rising spectral index from 24-70 μ ($\alpha_{24-70\mu m}$¿0). In addition to the positive $\alpha_{24-70\mu m}$ indices for XEST 17-036 and XEST 08-033, the $\alpha_{3.6-8.0\mu m}$ indices are typical for those of Class III (debris disk) objects. The target name, spectral type, and spectral class are labelled in each SED. The observed broadband photometry is compiled from optical (R_C, I_C), and near-IR (2MASS; *JHK*) wavelengths (black points), the mid-IR (IRAC and *WISE*; green and purple open circles respectively), the far-IR (MIPS, PACS Blue and Red channels; green open circles, blue and red points respectively) and submm-mm wavelengths (black points). 3σ upper limits are represented by the downwards triangles. The best-fit atmospheric model are displayed for each target.

Literature transition disks

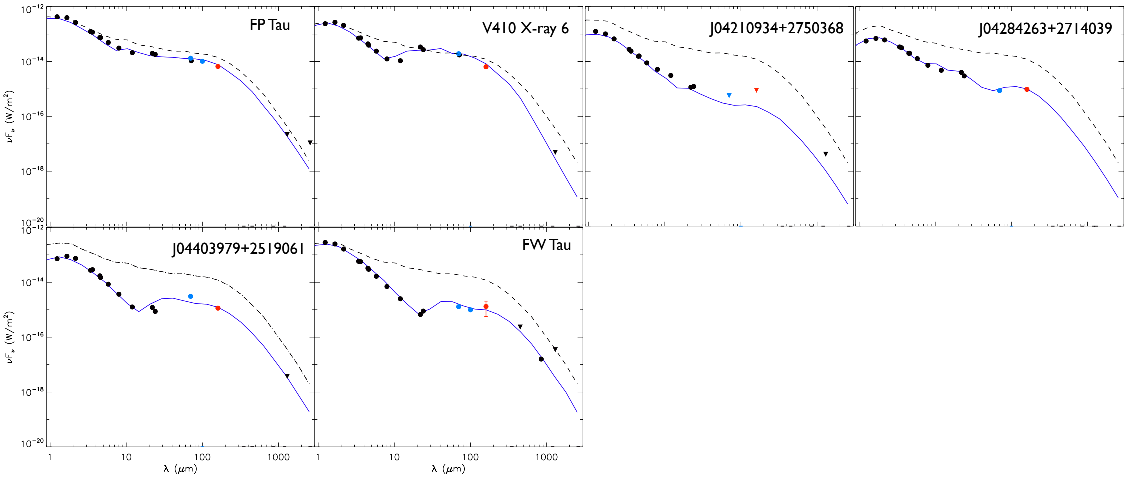

TBOSS candidate transition disks

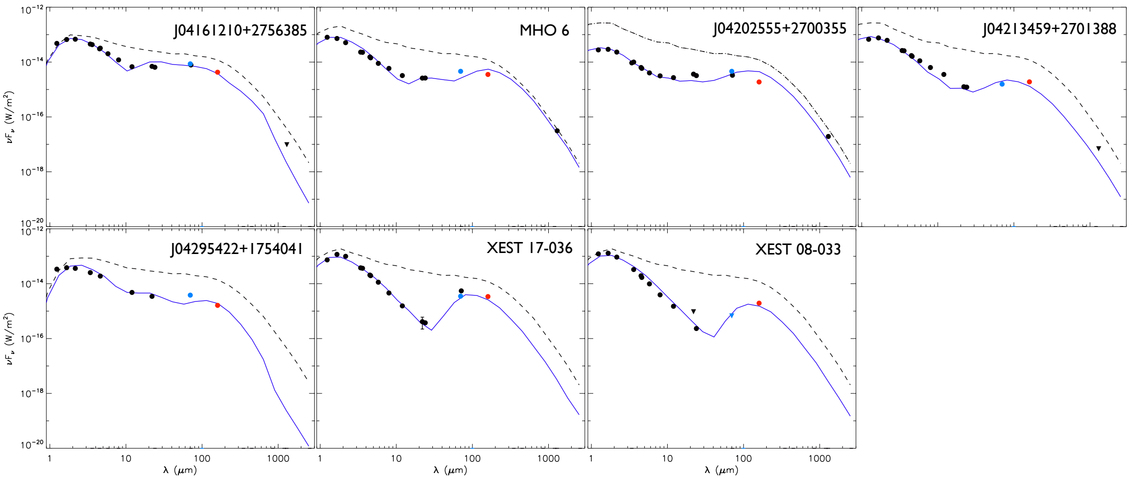

Figure 2.16: Spectral energy distributions showing the targets with transition disks (TD) previously reported in the literature (**top panel**) and the candidate targets with TD identified in this work (**bottom panel**). The blue points represent the PACS 70 μm and/or 100 μm fluxes, and the red point represents the PACS 160 μm fluxes. "Chi-by-eye" best fit disk models are display on each plot (blue line). For comparison, a fiducial Class II object disk model is over-plotted (dashed line) with model parameters set to those described in Section 2.6.1, and stellar parameters corresponding to those of the TD target.

$a_{\rm min}$, $a_{\rm max}$, β, p, and H_0 at a reference radius of 100 AU) were varied freely in order to obtain the best-fit model by adopting a "Chi-by-eye" method (e.g., Robitaille et al., 2007). The stellar parameters were fixed to the spectral type of each target, and the best-fit models reported are for those with a disk inclination of 60° from face-on.

Table A.3 lists the best-fit parameters of both disk zones 1 and 2 for each target. The outer disk radii of zone 1, i.e., the disk truncation radius, range from 5-120 AU, consistent with existing values reported in the literature, and the width of the cavities range from 5-90 AU. As can be seen in Figure 2.16, the TD targets exhibit a wide variety

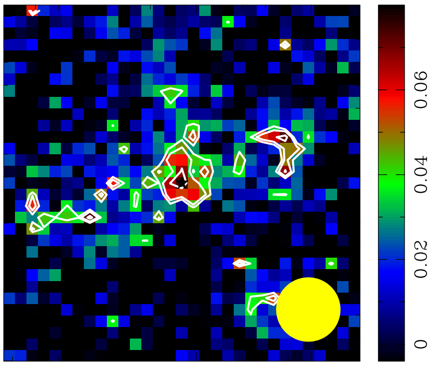

FIGURE 2.17: PACS Blue channel (70 μm) combined map of the undetected Class II objects. The map is 30″ in size along each axis. The beam size is represented by the yellow circle in the bottom, right hand corner and the black star marks the peak position in the map. Contour levels are plotted at 4, 5 and 6σ. The scale bar shows the intensity of the map in mJy/pixel.

of SED shapes, which may be indicative of the dispersion mechanisms that give rise to the modelled cavities within the disk. The inner and outer disk zone radii, reported in Table A.3, provide a preliminary estimate of the range of cavity sizes, however due to the large number of free parameters involved in the modelling procedure, a large degree of degeneracy exists between model fits. Whilst it is beyond the scope of the work presented here, future endeavours include detailed SED modelling of the TD targets and additionally the remaining targets of the TBOSS sample, will be carried out by generating a comprehensive grid of models and using Bayesian statistics to determine the best-fits.

2.6.4 Candidate truncated disks

A total of 15 Class II targets with 24 μm fluxes were not detected with the *Herschel* 70 μm PACS maps, one target of which was unobserved with *Herschel*, and is undetected at 70 μm with *Spitzer* MIPS. The upper limits for each source are reported in Table 2.4. The non-detections are not simply the latest spectral type targets, but include examples extending to M4.25. To estimate the average flux for this small subset of undetected Class II members, all the maps were combined to form a single submm map in Figure 2.17, and the flux of the faint combination source was measured as 3.0 ± 0.5 mJy. Both the individual detection limit and this estimate of the average flux is plotted on the SEDs for the 17 non-detected Class II targets. For 3 of the these targets – CIDA 14, MHO 5 and J04322415+2251083 – the individual limit alone indicates that the slope of the SED has a power law index ($\alpha_{24-70\mu m}$) of -2.0 or steeper. Considering the lower value of the combined flux from all the non-detected targets, 5 of the Class II targets with 24 μm detections and 70 μm upper limits have slopes steeper than -2.0.

One possible explanation for the shape of the Class II targets with exceptionally steep far-IR SED slopes is truncation of their disks. An example of a likely truncated disk in the ϵ Cha moving group around ET Cha was identified from a similarly steep SED index ($\alpha_{24-70\mu m}$ = -1.4) over wavelengths extending to the PACS bands combined with a non-detection of the CO(3-2) line (Woitke et al., 2011). In addition to the 3 Class II non-detected sources, there are 5 Class II targets with 70 μm detections that also define a slope as steep as that of ET Cha – CFHT 12, FR Tau, KPNO 13, J04141188+2811535, and V410 Xray 1 – resulting in a total of 8 candidate truncated disks (the SEDs of which are shown in Figure 2.18). Follow-up high sensitivity CO spectral line observations of these steep slope SED targets could provide further evidence of truncated disks around these 8 Taurus targets. While a stellar companion can gravitationally truncate a disk, all of the candidate truncated disk systems lack high resolution imaging data so it is not possible to assess this scenario.

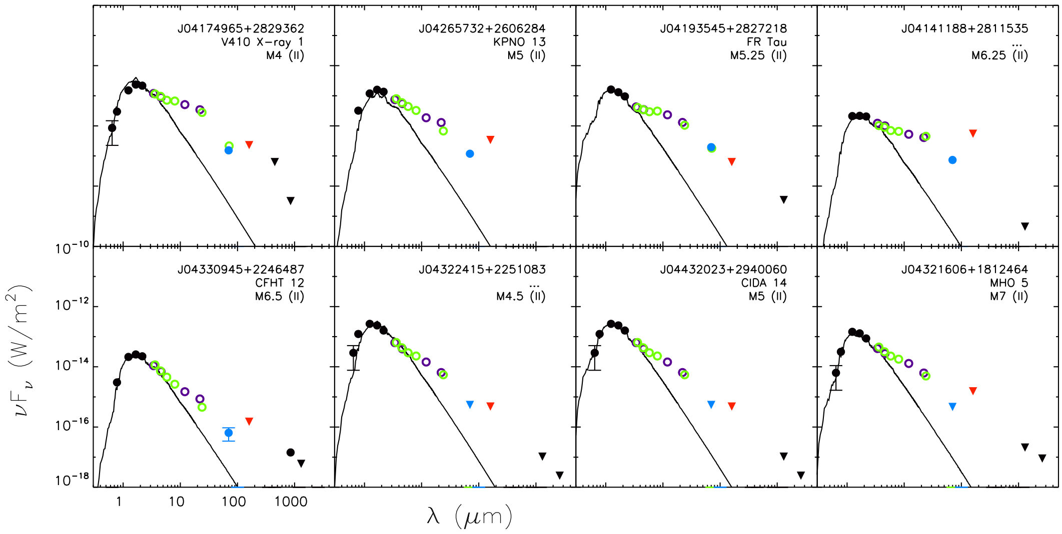

FIGURE 2.18: SEDs of the eight candidate targets with truncated disks, identified from the steeply declining spectral index from 24-70 μm ($\alpha_{24-70\mu m}$<-1.4). The target name, spectral type, and spectral class are labelled in each SED. The observed broadband photometry is compiled from optical (R_C, I_C), and near-IR (2MASS; *JHK*) wavelengths (black points), the mid-IR (IRAC and *WISE*; green and purple open circles respectively), the far-IR (MIPS, PACS Blue and Red channels; green open circles, blue and red points respectively) and submm-mm wavelengths (black points). 3σ upper limits are represented by the downwards triangles. The best-fit atmospheric model are displayed for each target.

2.6.5 Impact of companions

In previous studies of single dish submm emission from Taurus single and binary stars, the submm flux of binary stars with separations $\lesssim$50 AU was measured to be significantly lower than single stars (e.g. Jensen et al., 1994; Andrews & Williams, 2005). These investigations targeted the earlier spectral type member of Taurus. Results for wider systems have suggested submm binary system fluxes compared to singles that are similar (Andrews & Williams, 2005) or reduced by a factor of $\sim$3 (Mohanty et al., 2013) . Spatially resolved submm/mm interferometry maps of Class II Taurus K- and early-M star binaries have noted a lower frequency of circumsecondary disks compared to circumprimary disks (Jensen & Akeson, 2003) and a $\sim$50% lower detection rate for components of binaries relative to single stars (Harris et al., 2012).

For the TBOSS M4+ sample, only 35 target have high resolution imaging companion search data listed in Table 2.5, and 13 of the 35 are Class III objects for which there are few PACS detections and an additional 3 cannot be considered due to likely contamination from an earlier spectral type primary. Given the limited number of known binaries and singles among the TBOSS sample, it is not yet possible to assess the similarity or difference in the frequency or typical flux level of disks for targets with and without companions, only to identify interesting examples of disks in multiple systems. Both the closest known TBOSS pair J04403979+2519061 separated by only $0\farcs04$ or $\sim$5.5 AU and the widest known TBOSS pair J04141188+2811535 separated by $26\farcs21$ or >3600 AU have detected disk emission. The two brightest 70 μm detections are both Class I binary systems. In the brightest case – IRAS 04191+1523 – the TBOSS target is the secondary with a primary that has a spectral type earlier than M4, and, in the next brightest case – IRAS 04248+2612 – the primary is the TBOSS target. For the faintest TBOSS detection of $\sim$1.5 mJy, the object (CFHT 12) does not have high resolution imaging data, so its binary/single status is unknown. The next two faintest targets – J04414489+2301513 and J04554801+3028050 – each have a flux of $\sim$11 mJy and are the secondary components of unusual Class II/Class III mixed pair systems discussed further in Section 2.6.6. Among the interesting subsets of Class II targets without detections and the Class III targets with detections, only two have observations related to companions, and each of those cases – the Class II target JH 112 B and FW Tau – is a triple system. The FW Tau Class III system is a compact arrangement of three M4+ stars within $2\farcs3$ or 322 AU and detections in the *Herschel* PACS bands. Additional high resolution imaging data on the TBOSS targets are required to further investigate the impact of companions on the disks around low mass stars and brown dwarfs.

2.6.6 Mixed pair systems

Mixed pairs form an interesting subset of multiple systems comprised of a component with a disk and a component without a disk. Based on inner disk signatures such as $H\alpha$ emission and IR excess, a compilation of properties of spatially resolved binaries has documented a difference in the mixed pair frequency between star-forming regions, and Taurus mixed pair systems represent ∼20% of the mixed pair population (Monin et al., 2007). Considering these inner disk diagnostics, the component with the disk is equally likely to be the primary or secondary (Monin et al., 2007; Daemgen et al., 2012). With interferometric submm/mm observations sensitive to the bulk of the disks in Class II binaries in Taurus and Ophiuchus (Jensen & Akeson, 2003; Patience et al., 2008; Harris et al., 2012), 19 pairs have been spatially resolved consisting of 14 systems with only a circumprimary disk, 3 systems of both circumprimary and circumecondary disks, and 2 systems with only a circumsecondary disk. In each of the systems with only a circumsecondary disk in the submm/mm, the primaries are actually close binary pairs with separations of ∼5-45 AU (Kraus et al., 2011). Among the TBOSS sample, two examples of Class II/Class III mixed systems are identified - J04414565+2301580/J04414489+2301513 and J04554757+3028077/J04554801+3028050. In each case, the secondary is the disk-bearing component, based on both with the inner disk diagnostics resulting in different evolutionary classes and in the far-IR emission from the *Herschel* data. The primary of the J04414565/J04414489 system is a close pair, while the J04554757/J04554801 primary has no close companion based on high resolution imaging (Kraus et al., 2011). In the J04414565/J04414489 system, the host of the secondary disk is a very low mass M8.5 (∼20 $M_{\rm Jup}$) brown dwarf approaching the planetary mass regime.

2.6.7 Proto-brown dwarfs in Taurus

The earliest stages of brown dwarf evolution are important to characterize for comparison with formation models and to gauge the capacity for the development of planetary systems. The evolutionary sequence from starless core to proto-brown dwarf is likely to be subject to the environment in which the core forms (Ward-Thompson et al., 2007), i.e. the first discovery of a pre-brown dwarf core made by André et al. (2012) - a self-gravitating starless core of dust and gas, with a resulting mass in the brown-dwarf regime - is witnessed in the dense Ophiuchus L1688 cloud. Three sources within the TBOSS sample may be considered as proto-brown dwarf candidates – [GKH94] 41, IRAS 04191+1523 B, and L1521F-IRS. First classified by Pound & Blitz (1993), these

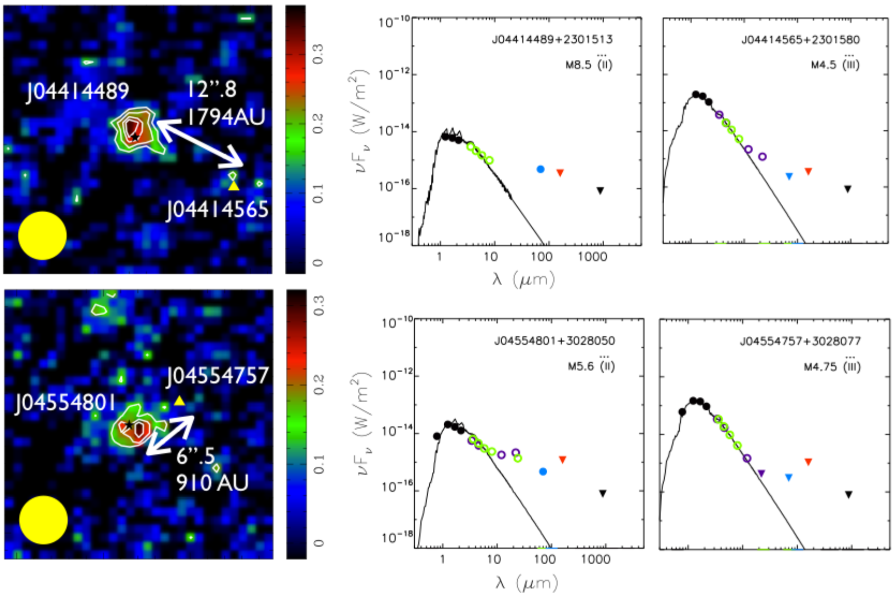

FIGURE 2.19: PACS Blue channel (70 μm) maps (**left**) for the two mixed pair systems identified in the TBOSS sample; J0441489+2301513 / J04414565+2301580 and J04554801+3028050 / J04554757+3028077, and the corresponding SEDs (**right**). The black stars in the maps show the 2MASS positions of the detected Class II secondaries (J0441489 and J04554801), and the yellow triangles mark the 2MASS positions of the undetected Class III primaries (J04414565 and J04554757). Contours are plotted at 3, 4, 5 and 6σ and the PACS 70 μm beam size is represented by the yellow circle in the bottom, left corner of each map. Target name, spectral type, and spectral class are displayed in the SEDs. Broadband photometry, compiled from optical-mm wavelengths and the underlying best-fit atmospheric models are displayed in the SEDs.

objects are cores of substellar mass, and are undergoing gravitational collapse (Adams et al., 1987; Andre et al., 1993).

[GKH94] 41 has been identified to be a disk-dominated source based on IRS spectra (Furlan et al., 2011), and is therefore at a more evolved stage than the Class I classification that has been adopted here (Luhman et al., 2010). The accretion rate for L1521F-IRS is expected to be low and likely towards the end of its main accretion phase (Bourke et al., 2006). IRAS 04191+1523 B is the secondary component of a 6.″1 binary (Duchêne et al., 2004), making the data at wavelengths longer than 8 μm contaminated by the primary emission. Given the quiescent phase of accretion and the bolometric temperature consistent with M6-M8 (Luhman et al., 2010), L1521F-IRS and IRAS 04191+1523 B will remain substellar unless a large amount of material is added to the central source. From the SED of L1521F-IRS, this candidate proto-brown dwarf appears heavily embedded and the slope over the 160 μm to 1.3 mm range is α=-1.8 which is markedly shallower than the other isolated Class I TBOSS targets with slopes of α=-2.7 to -3.4. The SED slope of L1521F-IRS is similar to ISM grains and may indicate that this target is in the earliest phase of the formation of an isolated brown dwarf.

2.6.8 Comparison with other star-forming regions

Comparison of the results of large-scale disk population studies performed in different star-forming regions and young clusters can provide an indication of the impact of environmental factors and evolutionary trends. From IR observations over the *J*- to *L*-band of young populations spanning the 0.3-5 Myr age range, a typical disk lifetime of $\lesssim$3 Myr was inferred from the decline in IR excess frequency (Haisch et al., 2001b). Based on longer wavelength *Spitzer* observations of Taurus extending to 24 μm, the disk fraction (defined by the ratio of Class II to Class II and Class III members) as a function of central object mass was found to be similar to Chameleon I, but higher than IC 348, and the lower stellar density of Taurus and Chameleon was suggested as an explanation for the observed difference (Luhman et al., 2010). The longest wavelength disk population comparison of Taurus and another region is drawn from submm surveys of Taurus and Ophiuchus, and the disk fractions and average disk masses were similar (Andrews & Williams, 2005, 2007). These existing IR to submm population studies mainly focus on the earlier spectral type members outside the TBOSS sample range.

Given the unique sensitivity and scope of the TBOSS survey, it is difficult to compare the Taurus M4+ far-IR disk results with those of other star-forming regions. The most analogous study is a recent *Herschel* investigation of 42 brown dwarfs (taken as objects with M6+ spectral types) in the L1688 cloud of Ophiuchus which reported a disk fraction of $\sim$0.3 (de Oliveira et al., 2013). Considering the M6+ targets in the TBOSS sample, the detected disk fraction is also $\sim$0.3 (22 of 67 targets), however the sensitivity of the TBOSS observations is much deeper. Restricting the TBOSS M6+ disks to those that could have been detected in the Ophiuchus study ($\gtrsim$25 mJy) yields a lower disk fraction of $\sim$0.15, suggesting that the average disk flux for a Taurus member at or below the stellar/substellar boundary is lower than for an equivalent object in Ophiuchus.

2.7 Summary

Of the 154 total M4-L0 members of the Taurus star-forming region, we report new 70 μm and 160 μm fluxes or upper limits for 134 targets and combine the results with other *Herschel* programs to compile the PACS measurements for 150 targets comprising the

TBOSS sample. For the 148 TBOSS targets not contaminated by fluxes from unresolved earlier spectral type primaries, the detection rates counting any *Herschel* band were calculated for the different evolutionary classes and spectral type ranges. Considering all M4-L0 spectral types, 100% of Class I, 75% of Class II, and 4% of Class III TBOSS targets were detected. Dividing the Class II targets into M4-M6 members above the substellar limit and M6.25+ brown dwarfs, the far-IR detection rate is significantly higher for the lowest mass stars relative to brown dwarfs. Although the disk frequencies are different, the distributions of disk-to-central-object far-IR flux are indistinguishable above and below the substellar limit, based on a K-S test.

To obtain a benchmark first census of far-IR disk emission across the full stellar and substellar population of any star-forming region, the TBOSS results were combined with *Spitzer* and *Herschel* surveys of the earlier spectral type members. The 70 μm flux as a function of spectral type declines with a trend similar to the decline in flux of the central object, and the range of flux at a given spectral type span at least an order of magnitude. Using the radiative transfer code MCFOST to model the range of *Herschel* fluxes, the dominant parameters influencing the PACS bands was found to be the disk inclination, scale height, and flaring index. The majority of the detected Taurus Class II population can be constrained with flared disks ($\beta = 1.125$), with scale heights of 10 AU at a reference disk radius of 100 AU (equivalent to an opening angle of 5°), and with disk inclinations from face- to edge-on.

For all TBOSS targets, the SEDs were constructed by joining the far-IR data with results from optical to mid-IR surveys and submm/mm fluxes when available. Based on the spectral indices over the 24 μm to 70 μm range, 5 new candidate transition disks were identified. While the new and known transition disks have a distinct distribution in the slope over the 24 μm to 70 μm range, the spectral indices for these objects at longer wavelengths are indistinguishable from the values for the general Class II population. Another set of 8 targets have very steep SED slopes over the 24 μm to 70 μm range, possibly indicating truncated disks such as has been suggested for the disk around ET Cha (Woitke et al., 2011). Two other unusual targets are disk-bearing secondary components of mixed systems. Finally, the overall Taurus substellar disk frequency is similar to that of the brown dwarfs in Ophiuchus, but the average disk flux for a Taurus M6+ target is lower than for a comparable object in Ophiuchus.

Chapter 3

A sub-mm census of T-Tauri stars in the Aquila star-forming region

3.1 Introduction

Star-formation occurs within giant molecular clouds with the largest of these entities possessing masses of 10^4-10^6 $M_\odot$ and sizes spanning 50-200 pc (Dame et al., 2001). A natural consequence of the collapse of rotating molecular cloud cores leads to the formation of protoplanetary disks, which are the reservoirs of gas and dust from which planets may form (Shu et al., 1993). As there may be fundamental differences in the physics of low mass star-forming regions compared to higher mass and/or denser regions, knowledge of disk frequency and disk properties across a range of different stellar environments are necessary in order to constrain the timescales and mechanisms of both stellar evolution and planet formation. Numerical simulations indicate that disk lifetimes may be significantly shortened in dense regions (Clarke & Pringle, 1991), such as that of the Orion Nebula Cluster (ONC) compared to that of more isolated, low density regions of the Taurus molecular cloud. Infra-red and millimeter studies of low mass ($\sim$1 $M_\odot$), pre-mainsequence stars indicate that protoplanetary disks disperse by $\lesssim$10 Myr (e.g., Haisch et al., 2001b; Carpenter et al., 2005; Hernández et al., 2007). Cold disk material ($\sim$10K) is probed outside $\sim$10 AU at sub-millimeter (submm) and millimeter (mm) wavelengths. In this wavelength regime emission is optically thin and the observed flux provides a direct measure on the disk mass. Such observations are critical since disk mass is related to the mass of the planets that may potentially form.

This chapter presents a complete submm census of an association of young T-Tauri stars in an extremely low density environment of the Aquila star-forming region. These observations enable a comparison between other young ($\lesssim$3 Myr) star-forming regions, placing constraints on the disk frequencies, and provides a comparison of disk masses in stellar density environments that span ~6 orders of magnitude. The Aquila region and association of T-Tauri stars are described in Section 3.2. The observation details are given in Section 3.3, and the results are given in Section 3.4. Finally, in Section 3.5 comparisons of this submm census of Aquila with that of existing submm and mm surveys that target other star-forming regions – the Taurus and Ophiuchus molecular clouds, IC 348, NGC 2024 and the ONC – is discussed in order to compare the impact that stellar density has on the frequency and properties of cold disks.

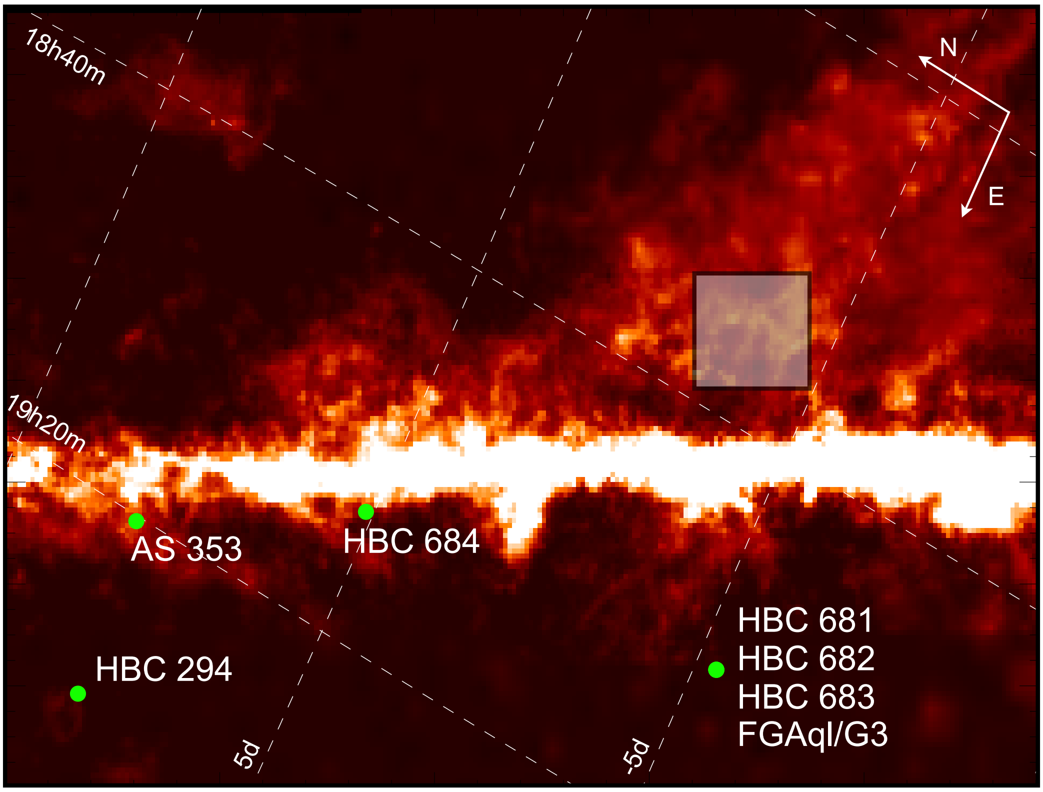

FIGURE 3.1: ^{12}CO map of the Aquila Rift (Dame et al., 2001). The locations for the association of Aquila members identified in Rice et al. (2006) are represented by the green points and lie in the lower extreme region of the cloud. The grey box indicates the region that was surveyed with *Herschel* (Könyves et al., 2010).

3.2 Aquila association

The Aquila Rift cloud structure spans a region ∼20°×10° in size, as shown in the CO map given in Figure 3.1, and has an estimated mass of ∼1-3×10^5 $M_\odot$ (Dame et al., 2001). Rice et al. (2006) have identified 7 systems located in the Aquila region, that are associated based on radial velocity measurements. The location of these 7 systems are shown in Figure 3.1, and adopting the distance of 200 ± 30 pc as used in Rice et al. (2006), cover a region ∼60×30 pc in size. Properties of the 7 systems, that comprise of ∼13 stars, are given in Table 3.1. As discussed in Rice et al. (2006) each member possess a range of intriguing and interesting characteristics. This chapter presents the first submm observations of these members. A 3°×3° region of the Aquila rift was observed with the PACS and SPIRE instruments on board the *Herschel* satellite (Könyves et al., 2010), however all members of the Aquila association lie outside of the observed region, as indicated by the grey box in Figure 3.1.

TABLE 3.1: Members of the Aquila association.

Name	RA (J2000)	Dec (J2000)	SpTy.	Multiplicity	Separation ($''$)	A_V (mag)
HBC 681	19 02 22.20	-05:36:20.38	K5	A B	1.2	0.1
FG Aql/G3	19 02 22.60	-05 36 22.03	M0	A		2.7
HBC 682	19 02 22.83	-05 36 15.33	K5	Ab B	SB^a, 1.0	1.6
HBC 683	19 02 23.21	-05 36 37.35	K7	A		0.7
HBC 684	19 07 09.87	+05 13 10.76	K5	A		1.6
AS353 A+B	19 20 31.00	+11 01 54.65	K5	A Bb	5.6, 0.2	3.5
HBC 294	19 38 57.42	+10 30 16.12	K7	A B	0.5	1.1

Notes. Spectral types, multiplicity properties, and A_V are from those reported in (Rice et al., 2006). The multiplicity column indicates the number of observed companions and the corresponding projected separations are listed in the separation column. ^{a} Spectroscopic binary (SB).

3.3 Observations and Data reduction

Submillimeter observations, at 350 μm of the Aquila association were acquired with the 10.4 m Caltech Sub-millimeter Observatory (CSO), with the SHARC-II bolometer array (Dowell et al., 2003). SHARC-II is a background limited instrument with a 12 × 32 element array. Observations were obtained in three nights, carried out in 2007-Aug-06, 2012-June-10, and 2012-June-12. A Lissajous scanning pattern was employed for the observations, resulting in a map size of $\sim3\overset{\prime}{.}3 \times 2\overset{\prime}{.}0$. The seven Aquila systems were observed in four individual sweep maps. All observations were performed with the Dish Surface Optimization System (DSOS; Leong et al., 2006) which corrects for dish surface figure changes as a function of telescope elevation, and results in a stable beam size of ∼8.″5 at 350 μm. Target observations were conducted with scan lengths of 620s in stable weather, and 320s in variable weather conditions. The telescope pointing was checked every hour, with 120s integration scans of the primary flux calibrators; Uranus and Neptune, and the bright pointing calibrator Arp220. The data acquired in 2007 were obtained with excellent opacity conditions ($\tau_{225\mathrm{GHz}}$ = 0.03-0.04), and those acquired in 2012 were obtained in good to poor conditions ($\tau_{225\mathrm{GHz}}$ = 0.05-0.07). Since the noise equivalent flux density is dependent on the exponential of the atmospheric opacity, the conditions impacted the amount of time required for detections.

The analysis of the CSO 350 μm data included four main steps: application of a pointing model[1], reduction of the raw data with the Comprehensive Reduction Utility for SHARC-II (CRUSH) pipeline, measurement of aperture photometry, and calibration of fluxes. As an initial step, the pointing drifts of the telescope were estimated for each observation with a pointing model that accounts for both static effects, measured with many pointing sources at different positions throughout the run, and for time variable effects, measured with pointing sources observed before and after the target. The calculated pointing offsets and the contemporaneous measurement of the atmospheric opacity are then incorporated into the data processing, implemented with the CRUSH 2.11-2 software (Kovács, 2006, 2008). The CRUSH data reduction pipeline employs an iterative approach to separate the source signal from the larger, variable, and correlated noise of the background. The target observations were flux calibrated and tied to the source signal measured within aperture radii of 5.″0 from the primary flux calibrator maps of Neptune and Uranus. The absolute fluxes of the planets are based on the distance from the Earth and the Sun. Both Neptune and Uranus have uncertainties of ∼6%. The uncertainty on the flux calibration is combined with the uncertainty on the source signal. The total uncertainty on the 350 μm fluxes of the science targets range from ∼15-25%.

3.4 Results

The measured 350 μm fluxes for all 7 systems of the Aquila association are given in Table 3.2. Detections were obtained for two systems – HBC 684 and HBC 294 – and are each further described in Section 3.4.1. Furthermore emission was detected at a 4σ level, peaked at a position approximately equidistant between the systems: HBC 681, HBC 682, and FG Aql/G3. These 3 systems are separated by $\lesssim$10″, and since this is

---

[1] www.submm.caltech.edu/ sharc/analysis/pmodel

comparable to the CSO beam size at 350 μm ($\sim$9$''$), it is not possible to associate the detected emission with any particular system. Upperlimits are set for these 3 systems based on the total emission measured within the 3σ contour and is listed in Table 3.2. The 350 μm maps of HBC 684, HBC 294 and HBC 681, HBC 682, FG Aql/G3 and HBC 683 are shown in Figures 3.2 and 3.3 respectively.

HBC 683 and AS 353 were undetected and Table 3.2 lists the 3σ upperlimits, derived from 3 times the rms map noise. Flux calibration uncertainties are included in the fluxes and upper limits reported in Table 3.2.

TABLE 3.2: Observed and derived disk properties.

Name	SED class	$F_{350\mu m}$ (mJy)	M_{disk} $M_\odot$
HBC 681	II	<74	<0.0004
FG Aql/G3	II	<74	<0.0004
HBC 682	III	<74	<0.0004
HBC 683	II	<74	<0.0004
HBC 684	FS	5492 ± 1248	0.0334 ± 0.0076
AS353 A+B	II	<87	<0.0005
HBC 294	FS	294 ± 46	0.0018 ± 0.0003

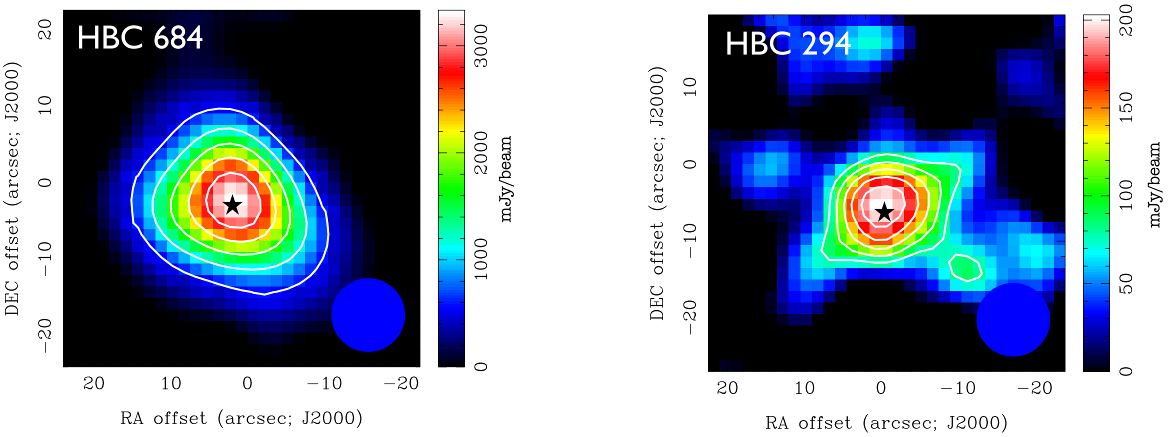

FIGURE 3.2: CSO 350 μm maps for the two detected Aquila members; **(left)** HBC 684 - contours are plotted at 5, 10, 15, 20, 25 and 30 σ, **(right)** HBC 294 - contours are plotted at 3, 4, 5 and 6 σ. In both maps the black star represents the 2MASS coordinates of the source and the blue circle shown in the lower right corner represents the beam size.

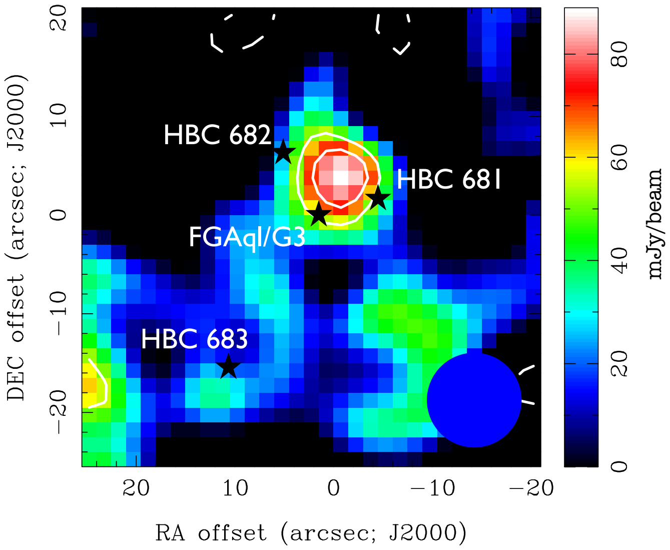

FIGURE 3.3: CSO 350 μm map showing the observed region of the Aquila members HBC 681, HBC 682, FG Aql/G3 and HBC 683. The black stars show the 2MASS coordinates for each member, and the blue circle shown in the lower right corner represents the beam size. Contours are plotted at -3 (dashed lines), 3 and 4 σ. Emission at a 4σ level is seen between the members HBC 681, HBC 682 and FG Aql/G3. Due the $\sim 9''$ beam size of the observation, it is not possible to associate the detected emission to either of the members. HBC 683, shown in the lower left of the map is undetected.

3.4.1 Detected systems

3.4.1.1 HBC 684

The 350 μm emission for HBC 684, measured within the 3σ contour, is 5.5 ± 1.2 Jy, as listed in Table 3.2. This is comparable to the high end of emission measured around Class I Taurus objects of similar spectral types (Andrews & Williams, 2005). In addition to the exceptionally large flux measured, the emission is also resolved and the best fit gaussian is $15''.2 \times 14''.6$ along the major and minor axes at a position angle of 13° from the North. HBC 684 is a particularly interesting object as noted in Rice et al. (2006) since it manifests all its spectral lines in emission, both at visible and near-IR wavelengths. This may indicate a disk that is just occulting the star, revealing only an inverted layer above that of the stellar photosphere.

3.4.1.2 HBC 294

The 350 μm flux density for HBC 294, measured within the 3σ contour, is 294 ± 46 mJy, as listed in Table 3.2. This system is a sub-arcsecond binary with a projected separation of $0\farcs52$, corresponding to ~100 AU (Ageorges et al., 1994). This system shows signs of ongoing accretion as identified in Rice et al. (2006). The emission detected may indicate that the material is in a circumbinary structure. Higher resolution follow-up observations are required to confirm the true distribution of the material.

3.4.2 Disk mass

Assuming that the observed 350 μm dust emission is optically thin, the total disk mass and mass limits have been estimated through the relation (Beckwith et al., 1990):

$$M_{\rm disk} = \frac{F_\nu d^2}{\kappa_\nu B_\nu(T_{\rm dust})} \tag{3.1}$$

, where F_ν is the observed flux, d is the distance to the source, $T_{\rm dust}$ is the dust temperature, B_ν is the Planck function, and κ_ν is the dust opacity. In this wavelength regime κ_ν follows the power law approximation (Beckwith et al., 1990):

$$\kappa_\nu = \kappa_0 \left(\frac{\nu}{\nu_0}\right)^\beta \tag{3.2}$$

For consistency with existing submm and mm studies (e.g., Beckwith et al., 1990; Carpenter, 2002; Eisner & Carpenter, 2003; Eisner et al., 2008), disk masses and limits have been calculated using $T_{\rm dust}$=20 K, β=1.0 and κ_0 = 0.002 cm^2 g^{-1} at 1300 μm, where the standard gas to dust ratio of 100:1 is incorporated into the value of κ_0 (Beckwith et al., 1990). The disk masses and upper limits for all systems of the Aquila association are given in Table 3.2.

3.4.3 Construction of spectral energy distributions

Spectral energy distributions (SEDs) have been constructed for all systems of the Aquila association. In addition to the 350 μm observations presented in this chapter, the SEDs include photometry extracted from the Two Micron All Sky Survey point source catalog (2MASS; Skrutskie et al., 2006) and the Wide-field Infrared Survey Explorer All-Sky Data Release (*WISE*; Cutri & et al., 2012). The magnitudes were converted to flux densities (Jy) using zero-points of 1594 ± 28 Jy, 1024 ± 20 Jy and 667 ± 13 Jy (Cohen et al., 2003) for the 2MASS *JHK* bands respectively, and zero-points of 310 ± 5 Jy, 172 ± 3 Jy, 31.7 ± 0.5 Jy and 8.4 ± 0.1 Jy were used for the *WISE* *W*1, *W*2, *W*3, and *W*4 channels respectively (Wright et al., 2010).

In addition to the observed broadband photometry, the best-fit stellar atmospheric models to the near-IR photometry are also shown in each SED. The atmospheric models displayed in the SEDs are the PHOENIX-based (Hauschildt et al., 1999), "BT-settl" models (Allard et al., 2003, 2011), and were set based on the spectral type of each system with the temperature conversion from Luhman et al. (2003b). The stellar radius and log(g) were estimated from the effective stellar temperature (T_{eff}) of each system, and from the 1 Myr evolutionary models of Baraffe et al. (1998). The redding law from Mathis (1990) for $R_v = 3.1$ was applied to the stellar atmospheric models, and the extinction measurements for each system were extracted from those reported in (Rice et al., 2006), as listed Table 3.1. The best-fit model for each system was obtained by minimizing the χ^2 value, summed over the 2MASS *JHK* bands. Visual extinction (A_V) and stellar radius (R_{star}) were used as free parameters in the fitting process. The SEDs of the two systems detected at 350 μm; HBC 684 and HBC 294, are shown in Figure 3.4. The SEDs of the remaining systems of the association undetected at 350 μm; HBC 681, 682, 683, FG Aql/G3 and AS 353, are shown in Figure 3.5.

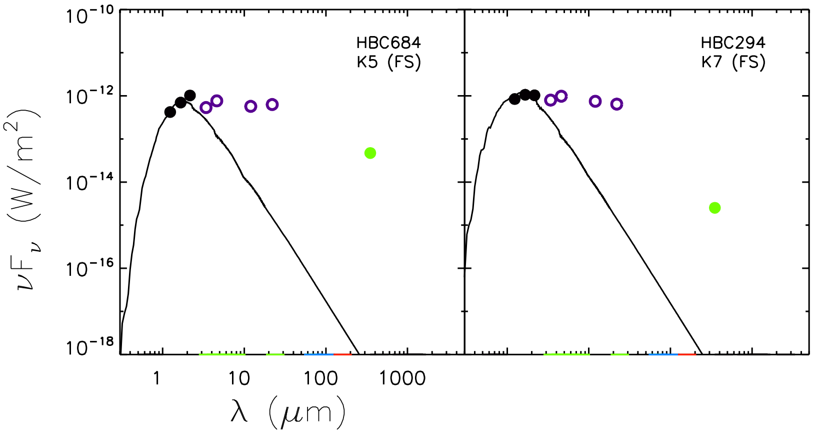

FIGURE 3.4: SEDs of the two detected members HBC 684 **(left)** and HBC 294 **(right)**. The green point shows the CSO 350 μm detection. Additional broadband photometry points are compiled from 2MASS (*JHK* - black points) and *WISE* (3.4-22 μm - purple circles). The best fit "BT-settl" atmospheric models are displayed and correspond to the stellar effective temperatures of each spectral type. The best fit, free parameters R$_{star}$ and A_V for HBC 684 are 6.0 R$_\odot$ and 0.5 mag, and for HBC 294 are 5.8 R$_\odot$ and 0.3 mag.

For all members of the Aquila association the 350 μm fluxes and upper limits presented in this chapter are the only observations beyond the mid-IR (*WISE* at 22 μm), that are sensitive to emission from cold dust located in the outer regions of a disk. Due to the vicinity of the association within the Galactic plane, all members of the association are not included in the *IRAS* Faint Source Catalog (Moshir et al., 1992), and were unobserved with both the *Spitzer* and *Herschel* satellites. The sparsity of broadband photometry observations for these members is witnessed in the SEDs, shown in Figures 3.4 and 3.5, and future follow-up observations particularly at submm and mm wavelengths is warranted. For HBC 684 and HBC 294 an additional observation unique of 350 μm will provide a submm spectral index which can be used to identify the presence of grain growth within the detected disks and provide constraints on the disk properties through SED modelling procedures. The resolution of ALMA is capable of resolving the detected emission between the systems; HBC 681, HBC 682 and FG Aql/G3. Furthermore with the sensitivity of ALMA, follow-up observations will provide deeper constraints on the additional undetected sources HBC 683 and AS 353.

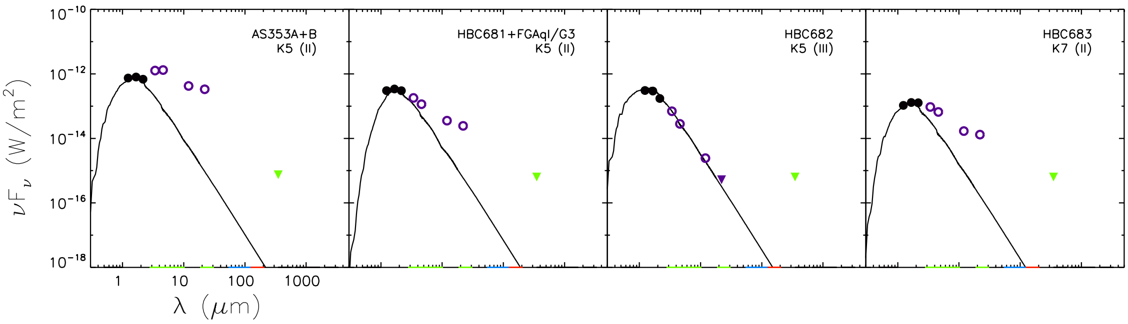

FIGURE 3.5: SEDs of the undetected members of the Aquila association. The members, spectral types and SED evolutionary classes are labelled on each SED. The green downward triangle shows the CSO 350 μm upper limit. Additional broadband photometry points are compiled from 2MASS (*JHK* - black points) and *WISE* (3.4-22 μm - purple circles). A combined SED for HBC 681 and FQ Aql/G3 is shown for these two members, since the angular separation between the two systems is less than the angular resolution of *WISE* ($\theta \sim$6-7$''$). The best fit "BT-settl" atmospheric models are displayed and correspond to the stellar effective temperatures of the spectral types listed. The best fit, free parameters $R_{\rm star}$ and A_V are: AS 353 - 4 R$_\odot$ and 0.7 mag, HBC 681+FG Aql/G3 - 3.1 R$_\odot$ and 0.7 mag, HBC 682 - 1.6 R$_\odot$ and 0.7 mag, and HBC 683 - 0.9 R$_\odot$ and 0.7 mag.

3.4.4 Spectral evolutionary status

Spectral indices have been calculated using the *WISE W1* and *W3* bands (from 3.4-8.0 μm) with the relation:

$$\alpha = -\frac{\mathrm{d}log(\nu F_\nu)}{\mathrm{d}log(\nu)} \tag{3.3}$$

, where ν is the frequency of observation and F_ν is the observed flux density (Lada, 1987). In order to quantify the evolutionary status of the Aquila systems, the classification of Greene & Meyer (1995) has been adopted. The two detected systems at 350 μm – HBC 684 and HBC 294 – are classified as flat spectrum (FS; $-0.3<\alpha<0.3$) objects. AS 353 and HBC 683 are classified as Class II objects ($-1.6<\alpha<-0.3$), consistent with the spectral line observations that are indicative of disk accretion for Classical T-Tauri stars (CTTs) presented in Rice et al. (2006). The angular separation of HBC 681 and FG Aql/G3 is $\sim6''$ and emission from the two systems is unresolved with *WISE* across all bands. The combined spectral classification for these two systems is that of a Class II object. Finally, HBC 683 is a Class III object ($\alpha<-1.6$) and is classified as a weak lined T-Tauri star, based on the equivalent width of $H\alpha$ absorption in Rice et al. (2006).

3.5 Comparisons with other star-forming regions

The submm census of the Aquila association presented in this chapter provides a measure of the disk frequency and disk mass in an extremely low density environment. The stellar density of the Aquila association, listed in Table 3.3, has been estimated by calculating the volume of a rectangular cube, where the length and height are bounded by the distances of the outermost members of the association. The volume of cylinder, where the radius and length are again bounded by the outermost members, has been used in order to gauge a measure of the uncertainty on the estimated stellar density.

Results of analogous submm and mm surveys that target the Taurus (Andrews & Williams, 2005; Andrews et al., 2013), Ophiuchus (Andrews & Williams, 2007) molecular clouds, IC 348 (Carpenter, 2002), NGC 2024 (Eisner & Carpenter, 2003) and the ONC (Eisner et al., 2008), have been compiled in order to provide a comparison of disk frequency and disk mass across stellar density environments that range from ∼6-800 stars/pc^3. Stellar densities computed within a half number radius from the region center have been adopted for IC 348, the ONC and NGC 2024 (King et al., 2012; Lada et al., 1991). For the Ophiuchus molecular cloud, the stellar density computed for the main cloud L1688 has been adopted from King et al. (2012). Finally, the stellar density for the Taurus molecular cloud, calculated within a radius of 1 pc from the main northern cloud filament - L1495 has been adopted from King et al. (2012). The stellar densities, cluster distances (adopted from the corresponding stellar density reference), and mean cluster ages are listed in Table 3.3. All regions are young ($\lesssim$3 Myr) and provide good comparison with that of the Aquila association, estimated to be ∼1 Myr (Rice et al., 2006).

TABLE 3.3: Properties of several star-forming regions.

Region	Distance (pc)	Stellar density (stars/pc^3)	Age (Myr)	Ref.
Aquila	200	0.0009 ± 0.0008	~1	c, 6
IC3 48	320	326 ± 73	2-3	a, 3
NGC 2024	400	778 ± 225	~0.5	b, 1
ONC	400	425 ± 33	1-3	a, 5
Ophiuchus	130	236 ± 27	~1	a, 2
Taurus	140	6 ± 1	1-3	a, 4

References. Stellar density references are those from: (a) King et al. (2012); (b) Lada et al. (1991); (c) This work. Mean cluster age estimates are those from: (1) Ali et al. (1998); (2) Greene & Meyer (1995); (3) Haisch et al. (2001a); (4) Hartmann et al. (2001); (5) Hillenbrand (1997); (6) Rice et al. (2006).

The submm and mm surveys of the comparison star-forming regions, have been undertaking at wavelengths ranging from 350 μm - 3 mm. The reported flux densities have therefore been extrapolated to 350 μm (to match the observations presented here), following the power law relation in continuum emission at submm and mm wavelengths; $F_\nu \propto \nu^{2+\beta}$ (Beckwith et al., 1990). Studies of circumstellar material have suggested that dust emissivity at submm wavelengths varies with β ~1 (e.g., Beckwith et al., 1990; Beckwith & Sargent, 1991) rather than β ~2 as found from observations of interstellar dust grains (e.g., Goldsmith et al., 1997; Hunter, 1998; Friesen et al., 2005). However measurements of β are uncertain and measured values range from 0 - 2 due to uncertainties in the true distribution of the material (e.g., Beckwith & Sargent, 1991; Andrews & Williams, 2007; Natta et al., 2007). A flux scaling with β=0 has been adopted here to provide an absolute lower limit on the extrapolated fluxes. The extrapolated 350 μm fluxes are further scaled to the distance of Aquila (200 pc Rice et al., 2006) using the adopted distances to each region as listed in Table 3.3. Figure 3.6 shows the scaled flux distributions for the Taurus, Ophiuchus, NGC 2024, and ONC star-forming regions. IC 348 is omitted since no emission was detected within the sensitivity limits of the survey (Carpenter, 2002). The measured fluxes of the two detected Aquila systems are shown (red lines) in the flux distributions in Figure 3.6 for comparison.

3.5.1 Disk frequency

The disk frequency of the Aquila association and analogous submm/mm studies of other star-forming regions; Taurus, Ophiuchus, IC 348, ONC and NGC 2024, have been calculated from the 3σ sensitivity limits of the 3 mm NGC 2024 survey (Eisner & Carpenter, 2003) and the 350 μm Aquila observations presented in this chapter.

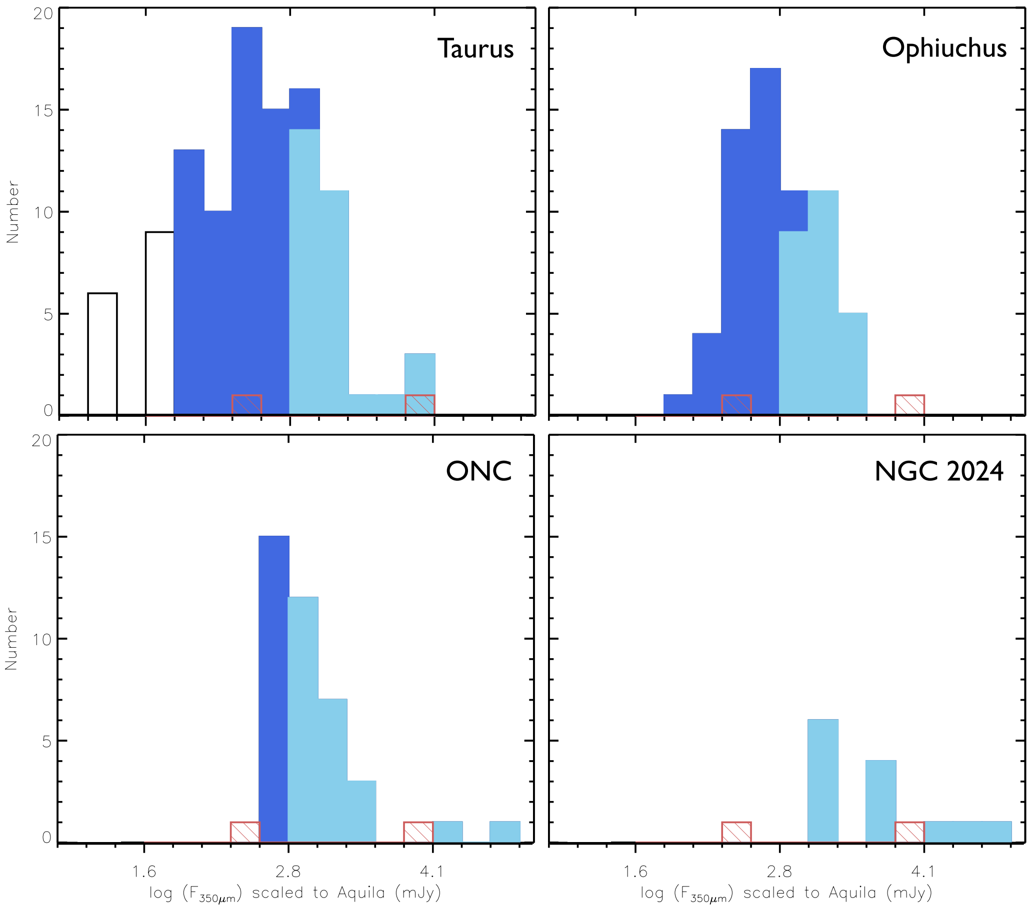

FIGURE 3.6: Flux distributions of the sources detected in the Taurus, Ophiuchus, ONC and NGC 2024 star-forming regions. The survey fluxes for each region have been scaled to a wavelength of 350 μm following the power-law approximation $F_\nu \propto \nu^2$, and each region has been scaled to the distance of Aquila (d=200 pc). The open histogram (black line) represents the full population of detected sources within each survey. Sources detected at the 3σ sensitivity limits the Aquila census and NGC 2024 survey are represented by the dark blue and light blue filled histograms respectively. The fluxes of the two detected Aquila sources (red lines) are shown for comparison in each of the plots.

The sensitivity limits obtained in the NGC 2024 survey, 0.75 mJy/beam and corresponding to ≈240 mJy/beam scaled to 350 μm at the distance of Aquila, are the most restrictive limits of the six surveys under comparison. The distribution of the sources that the NGC 2024 and Aquila 3σ limits are sensitive to in the comparison surveys are shown in Figure 3.6. Both limits are deeper that the sensitivity of the IC 348 survey, in which no detections were obtained.

There are no clear trends are witnessed in the plots of disk frequency as a function of stellar density, shown in Figure 3.7. It is interesting to note that at the Aquila 3σ sensitivity limit, the disk frequencies across the stellar densities that range from

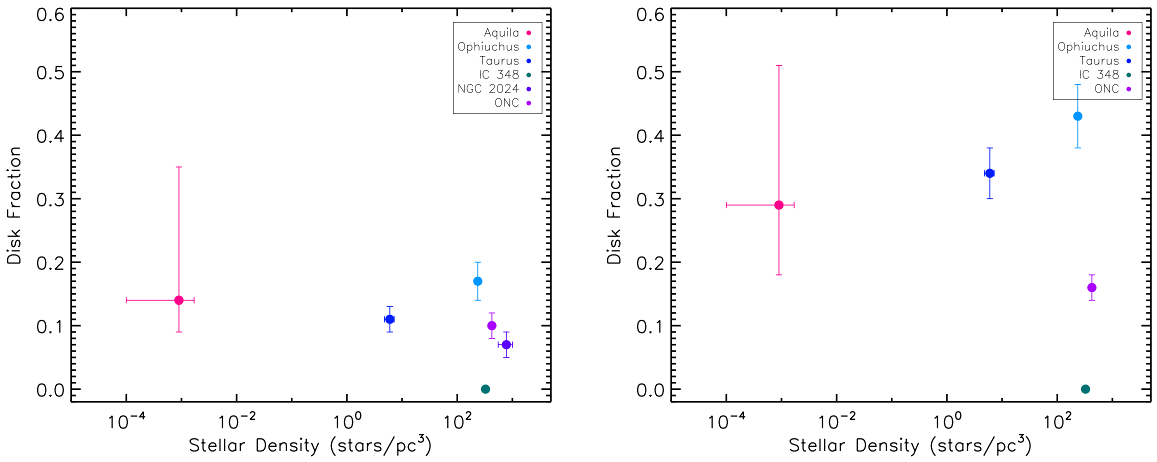

FIGURE 3.7: Disk fraction shown as a function of stellar density for the Aquila association (pink point), Ophiuchus (light-blue point), Taurus (dark-blue point), IC 348 (green point), NGC 2024 (dark-purple point), and the ONC (light-purple point) star-forming regions. (**left**) Disk fractions are calculated at the 3σ sensitivity limit of the NGC 2024 survey (Eisner & Carpenter, 2003). (**right**) Disk fractions are calculated at the 3σ sensitivity limit of the Aquila census.

9e^{-4} stars/pc^3 (Aquila) to ∼800 stars/pc^3 (ONC) is less than 50%. This indicates that even in benign, low density environments, the presence of a disk is not guaranteed, and other environmental factors such as multiplicity must be taken into account. The environmental effects on disk in dense regions, such as those of the Ophiuchus, NGC 2024 and IC 348, may tidally truncate disks to smaller radii due to close stellar encounters (Scally & Clarke, 2001), resulting in a lower fraction of disks. Furthermore in the dense and massive star-forming region of the ONC, the large amounts of ionising radiation from massive stars may photo-evaporate the outer disks of surrounding stars (Hollenbach et al., 2000), that will also result in a lower disk frequency. It is harder to explain the low disk frequency witnessed in the Aquila region. The multiplicity fraction of the association is high, with at least 13 stars in 7 systems (Rice et al., 2006). Binary systems with separations in the range of 1-100 AU are expected to have disks truncated at $0.2-0.5$ times the binary separation (Mathieu et al., 2000). Since only one system – HBC 294 – has a projected separation ≤100 AU, and is one of the two source for which a detection was obtained, binarity of the association does not readily explain the low disk frequency in the region. Another possible explanation may be the effect of disk dispersal over the age of the systems. Whilst the mean cluster age is estimated to be ∼1 Myr, and five of the seven systems exhibit signs of youth associated with CTTs (Rice et al., 2006), the estimated ages for HBC 682 and FG Aql/G3 are ∼ 6-12 Myr. This age range is consistent with the time scale in which protoplanetary disks have dispersed the majority of their material (Haisch et al., 2001b).

3.5.2 Disk Mass

The derived disk masses of the detected Aquila systems – HBC 684 and HBC 294 – are compared to the median disk masses of that of higher density environments of the Taurus and Ophiuchus star-forming regions. HBC 684 and HBC 294 were identified as FS sources in Section 3.4.4 based on the spectral indices across the *WISE* 3.4 μm and 8.0 μm bands. Following this procedure the median disk mass was calculated from all FS sources, above the 3σ Aquila detection limit, in both Taurus and Ophiuchus and are shown in Figure 3.8.

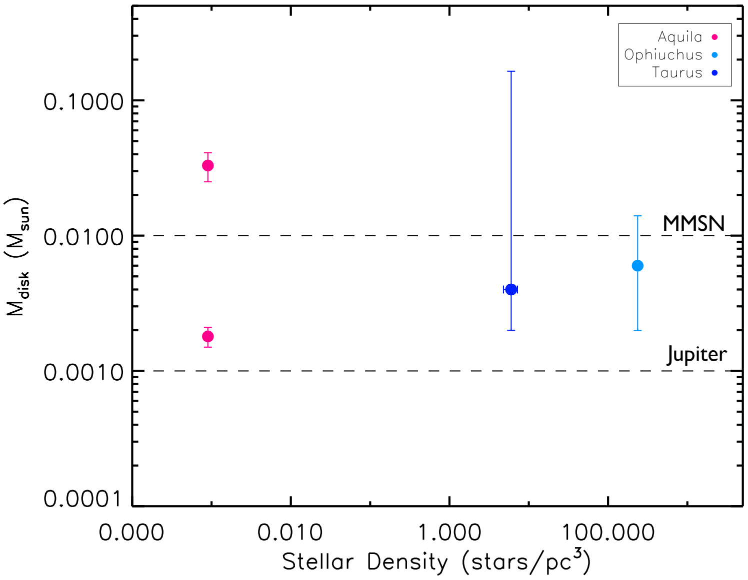

FIGURE 3.8: Estimated disk masses shown as a function of stellar density. The Aquila systems (HBC 684 and HBC 294) are represented with pink points. The median disk masses, and distribution quartiles for the flat spectrum sources in the Taurus and Ophiuchus star forming regions are represented with the dark-blue and light-blue point respectively, and have been calculated at the 3σ sensitivity limit of the Aquila census. Masses of the minimum mass of the solar nebula (MMSN) and that of Jupiter are indicated by the dashed lines.

The median disk masses are also compared to the minimum mass of the solar nebula (MMSN; $\sim$0.01 $M_\odot$ Weidenschilling, 1977), and to that of a Jupiter mass (0.001 $M_\odot$). It is seen that HBC 294 is typical to that of the disk masses in Taurus and Ophiuchus, and with masses <MMSN implies that these disks do not posses the mass required to produce a planetary system equivalent to that of out own, but do have the potential to form at least one giant mass planet. Comparatively, the estimated disk mass around HBC 684 is massive, and is approximately 3 times greater than that of the MMSN.

3.6 Summary

This chapter presents the first submm observations, carried out at 350 μm of an association of young T-Tauri stars in the Aquila star-forming region. Detections have been obtained for two of the seven systems – HBC 684 and HBC 294. Additionally, emission at 4σ level is seen in the region of the three systems; HBC 681, HBC 682 and FG Aql/G3. However due to the angular separation of these systems and the beam size of the CSO at 350 μm is it not possible to associate the emission to any one particular source. These systems are presented to be prime candidates for higher-resolution follow up observations with ALMA. For the remaining undetected systems – AS 353 and HBC 683, deeper follow up observations are required in order to rule out the presence of a cold disk.

Spectral evolutionary classifications for each system of the association have been estimated from the spectral indices calculated over the *WISE* 3.4-12 μm wavelength range, and consist of flat-spectrum sources to Class III objects. SEDs of the systems have been constructed and exhibit shapes characteristic to their evolutionary classification.

The stellar density of the association has been estimated, and is uniquely low (0.0009 ± 0.0008 stars/pc^3), which is over an order of magnitude less than the well known low stellar density environment of the Taurus star-forming region. The disk frequency of the Aquila association is 29 $^{+22}_{-11}$%. Comparisons of this frequency to that of five other star-forming regions (Taurus, Ophiuchus, IC 348, NGC 2024 and the ONC), with stellar densities ranging from ~10-1000 stars/pc^3, show that there is no clear trend between disk fraction and stellar density. Given the sensitivity limit of this census, this result suggests that other environmental factors should be taken into account, such as multiplicity, age, and properties of nearby surrounding stars for future assessments of the disk fractions across different star-forming regions.

Finally, the disk masses of the two detected flat-spectrum sources (HBC 684 and HBC 294) have been estimated and compared to the median values of the higher density environments of Taurus and Ophiuchus. A large spread is masses seen across these three regions and all posses masses required for the formation of at least one Jupiter mass planet.

Chapter 4

Sub-millimeter observations of *IRAS* and *WISE* debris disk candidates

From Bulger, J., Hufford, T., Schneider, A., et al., 2013, A&A, 556, 119

Abstract

A set of six debris disk candidates identified with *IRAS* or *WISE* excesses were observed at either 350 μm or 450 μm with the Caltech Submillimeter Observatory. Five of the targets – HIP 51658, HIP 68160, HIP 73512, HIP 76375, and HIP 112460 – have among the largest measured excess emission from cold dust from *IRAS* in the 25-100 μm bands. Single temperature blackbody fits to the excess dust emission of these sources predict 350-450 μm fluxes above 240 mJy. The final target – HIP 73165 – exhibits weak excess emission above the stellar photosphere from *WISE* measurements at 22 μm, indicative of a population of warm circumstellar dust. None of the six targets were detected, with 3σ upper limits ranging from 51-239 mJy. These limits are significantly below the expected fluxes from SED fitting. Two potential causes of the null detections were explored – companion stars and contamination. To investigate the possible influence of companion stars, imaging data were analyzed from new adaptive optics data from the ARIES instrument on the 6.5m MMT and archival *HST*, Gemini NIRI, and POSS/2MASS data. The images are sensitive to all stellar companions beyond a radius of 1-94 AU, with the inner limit depending on the distance and brightness of each target. One target is identified as a binary system, but with a separation too large to impact the disk. While the gravitational effects of a companion do not appear to provide an explanation for the submm upper limits, the majority of the *IRAS* excess targets show evidence for contaminating sources, based on investigation of higher resolution *WISE* and archival *Spitzer*

and *Herschel* images. Finally, the exploratory submm measurements of the *WISE* excess source suggest that the hot dust present around these targets is not matched by a comparable population of colder, outer dust. More extensive and more sensitive *Herschel* observations of *WISE* excess sources will build upon this initial example to further define the characteristics of warm debris disks sources.

4.1 Introduction

Debris disks were first identified with the *Infrared Astronomical Satellite* (*IRAS*), from the observation that the far-IR flux of Vega (Aumann et al., 1984) was significantly brighter than expected from the stellar photosphere. Excess emission above the level of a stellar photosphere at wavelengths from the mid-IR to the millimeter provides evidence of reprocessed starlight emitted by a circumstellar debris disk of dust (c.f. reviews by Zuckerman, 2001; Wyatt, 2008). The disk origin of these excesses has been confirmed with spatially resolved imaging (e.g., Smith & Terrile, 1984; Holland et al., 1998). Given the timescale for the dust to spiral into the star or be ejected from the system, these dust disks must be sustained by an ongoing process such as the collisional grinding of planetesimals into smaller particles (Backman & Paresce, 1993) or an event such as a catastrophic collision of planets (Cameron, 1997).

While *IRAS* provided an all-sky survey for debris disks with a typical sensitivity of $(\mathrm{L}_{\mathrm{dust}}/L_{\star}) \sim 10^{-5}$, subsequent pointed observations from the *Spitzer* Space Telescope (Werner et al. 2004), achieved an order of magnitude greater sensitivity. The combined results of the all-sky and pointed observations have identified over 200 debris disks among field stars (e.g., Mannings & Barlow, 1998; Moór et al., 2006; Rhee et al., 2007; Habing et al., 1999; Silverstone, 2000; Rieke et al., 2005; Su et al., 2006; Bryden et al., 2006; Beichman et al., 2006; Hillenbrand et al., 2008; Carpenter et al., 2009). Assuming a single temperature blackbody model for the excess emission in the spectral energy distribution, it is possible to classify debris disks as warm (equivalent to that of our Asteroid belt), with $\mathrm{T}_{\mathrm{dust}}$ ≈100-250 K, that lie at distances $\lesssim$10 AU, and cold debris disks (equivalent to that of our Kuiper belt), with $\mathrm{T}_{\mathrm{dust}}$ $\lesssim$50 K, typical distances of several hundred AU.

With the more recent *Herschel* and Wide-field Infrared Survey Explorer *(WISE)* missions, it is possible to conduct pointed searches for cold debris disks down to the Kuiper belt level $(\mathrm{L}_{\mathrm{dust}}$ / $\mathrm{L}_{\star}) \sim 10^{-7}$ to 10^{-6} (Stern, 1996) and all-sky surveys for warm debris disks at a sensitivity level that was previously only obtained with *Spitzer* pointed observations. In addition to the sensitivity offered by both *Herschel* and *WISE*, the significant improvement of spatial resolution is important to identify possible sources of contamination. Examples of debris disks identified through *IRAS* excesses (e.g., Moór et al., 2006; Rhee et al., 2007) that are actually due to confusion from background source contamination have been revealed by higher resolution ground-based observations carried out in the IR and submm (e.g., Song et al., 2002; Jayawardhana et al., 2002; Lisse et al., 2002; Sheret et al., 2004).

Mid-IR to far-IR observations have been critical in identifying the current population of debris disks, however measurements at longer wavelengths in the submm/mm wavelength range provide the best means to estimate one of the most important properties of a disk, the dust mass. For disks that are spatially resolved in the submm, it is also possible to determine additional disk characteristics such as size and inclination which are degenerate with other disk parameters in a spectral energy distribution (SED) fit. For disks that have imaged asymmetries, these structures can encode the effects of gravitational interactions (e.g., Liou & Zook, 1999; Kuchner & Holman, 2003; Wyatt, 2006; Quillen & Faber, 2006). The submm/mm wavelength range is ideal for studying the interaction of the disk and planets, i.e., in the case of the multiple planet, debris disk system around HR 8799 (e.g., Patience et al., 2011; Hughes et al., 2011), since the large grains are expected to remain in resonances with the planets, while the smaller grains evolve into axisymmetric structures due to scattering or radiation pressure (Wyatt, 2006).

In this paper, we present the results of a submm and IR imaging study of several *IRAS* excess stars and one *WISE* excess star. This sample includes previously known systems with cold dust (Moór et al., 2006; Rhee et al., 2007) and newly identified debris disk candidates with evidence of either cold or warm dust. The properties of the sample are summarized in Section 4.2. The single-dish submm observations, infrared imaging and archival searches are described in Section 4.3. In Section 4.4, the data reduction and analysis of our submm and IR observations is presented. The results and implications of the IR image analysis is given in Section 4.5. In Section 4.6, we draw comparisons of our investigation to previous submm studies of debris disks. Finally, the conclusions of our study are given Section 4.7.

4.2 The sample

The target sample for this investigation of cold and warm excess debris disks is drawn from two main sources – the *IRAS* Faint Source Catalog (FSC v.2; Moshir et al., 1992) and results from the *WISE* All-Sky Data Release (Cutri & et al., 2012). We selected a sample of cold excess disk candidates from the literature (Lestrade et al., 2006; Moór et al., 2006; Rhee et al., 2007) that satisfy three criteria: (1) a large *IRAS* excesses at 60 μm or 100 μm, (2) a distance within 100 pc, and (3) a declination above -30°. SEDs were constructed, and a single temperature blackbody model was fit to the *IRAS* excesses. Targets with an expected 350 μm flux greater than 100 mJy were considered for this study, and the SEDs of the targets are shown in Figures 4.1 and 4.2. Due to weather considerations, we focused our observations on sources with the greatest predicted 350 μm flux and with nearby distances (<40 pc), in order to obtain meaningful limits and have the capacity to resolve the disks of the nearest systems. A total of 5 cold debris disks candidates were observed in this study, and are listed in Table 4.1, along with a summary of the modelled dust properties from the literature. The second type of target with evidence for warmer dust was drawn from the *WISE* (3.4 μm, 4.6 μm, 12 μm, and 22 μm) All-Sky Data Release. The identification of a *WISE* W3 (12 μm) and/or W4 (22 μm) band excess was based on a careful cross-correlation of the *WISE* and *Hipparcos* catalogues (Perryman & ESA, 1997; van Leeuwen, 2007) with a distance cut of 100 pc and an estimate of the photospheric flux from theoretical atmosphere models (Hauschildt et al., 1999). Due to the limited clear weather windows during the observing runs, it was only possible to observe one warm excess source – HIP 73615. HIP 73615 has an excess only in the *WISE* W4 band, and the excess above the photosphere is 34 times the uncertainty in the photometry. The properties of this target is listed in Table 4.1, and the SED for this warm debris disk candidate is plotted in Figure 4.3.

TABLE 4.1: Observed sample

Name	RA (J2000)	Dec (J2000)	Prop. mot. ($''$/yr)	D (pc)	SpTy	Age (Myr)	Excess source	T_{dust} (K)	$L_{dust} / L_\star$	Ref.
HIP 51658	10:33:13.88	+40:25:31.65	-0.142, 0.008	34.6 ± 0.6	A7	200	*IRAS*	40	1.06×10^{-4}	1
HIP 68160	13:57:16.13	+23:21:44.37	-0.330, -0.158	38 ± 1	K0	230	*IRAS*		1.49×10^{-3}	2
HIP 73165	14:57:11.01	-04:20:47.32	-0.097, -0.153	26.9 ± 0.2	F0		*WISE*			
HIP 73512	15:01:29.96	+15:52:08.45	0.102, -0.238	30 ± 1	K2	3000?	*IRAS*	85	1.17×10^{-3}	1
HIP 76375^{a}	15:35:56.61	+40:25:31.65	-0.448, 0.051	22 ± 0.3	K3	5000?	*IRAS*	29	7.86×10^{-4}	1
HIP 112460	22:46:49.81	+44:20:03.10	-0.705, -0.461	5.12 ± 0.05	M3.5	500	*IRAS*	19		3

Notes. a. Known binary reported in the literature.
References. (1) Rhee et al. (2007); (2) Moór et al. (2006); (3) Lestrade et al. (2006)

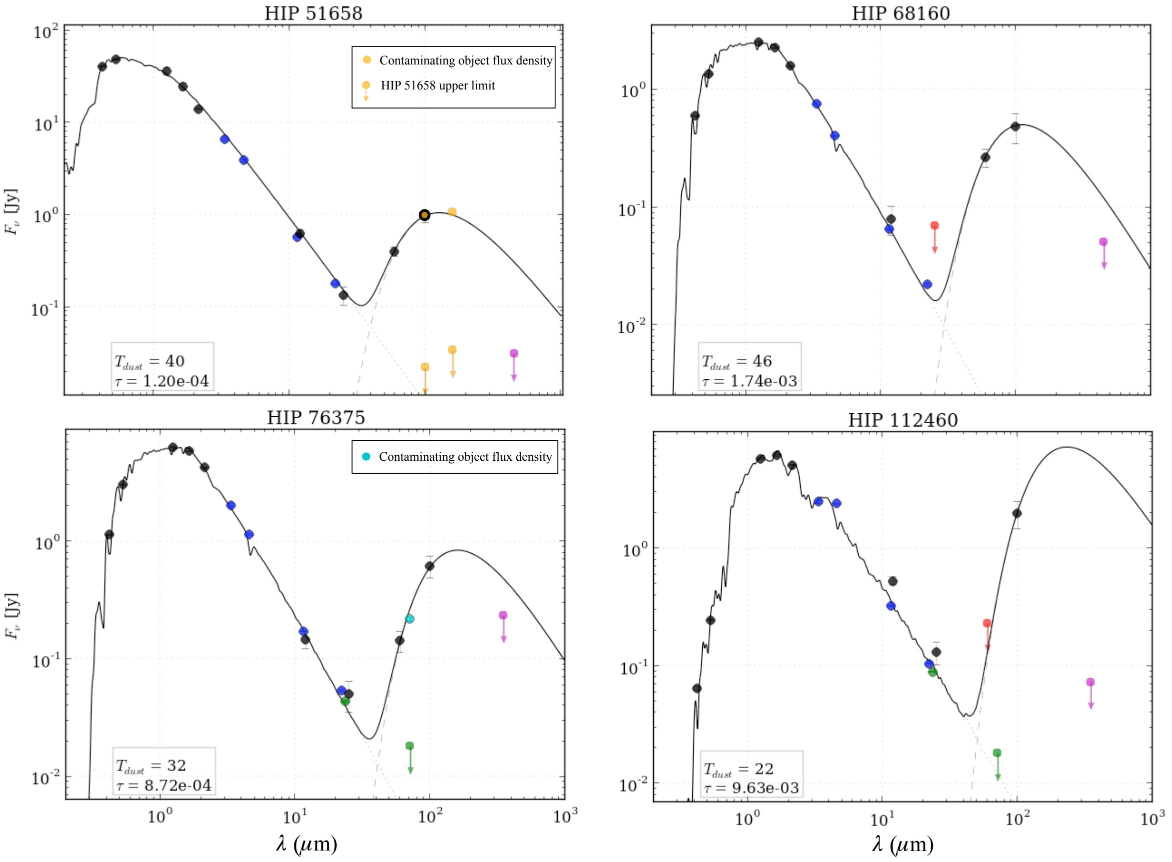

FIGURE 4.1: SEDs of the cold debris disk source candidates for which the submm flux limits are substantially below the extension of the single temperature blackbody fit to the *IRAS* excesses – HIP 51658, HIP 68160, HIP 76375 and HIP 112460. The NextGen atmospheric models corresponding to the best-fit stellar photosphere and the blackbody fit are plotted. The optical-near IR photometric points (black points) have been compiled from Tycho2 and 2MASS. The mid-IR photometric points have been drawn from *WISE* (dark blue points). For HIP 51568, with *Herschel* PACS photometry, the orange points with downward arrows correspond to the source 3σ upper limits. The orange points represent the cumulative flux density of three nearby contaminating objects. For HIP 76375 and HIP 112460, with *Spitzer* MIPS photometry, the green points represent the source flux density and green points with downward arrows represent the source 3σ upper limits. The flux density of the contaminating object measured in the MIPS 70 μm image for HIP 76375 is represented by the light-blue point. The CSO submm flux upper limit at 350 or 450 μm are represented by the pink points with downward arrows.

4.3 Observations

4.3.1 Sub-mm Observations

Observations of the six sources were made with the SHARCII bolometer array (Dowell et al., 2003) on the 10.4m Caltech Sub-millimeter Observatory (CSO) on Mauna Kea.

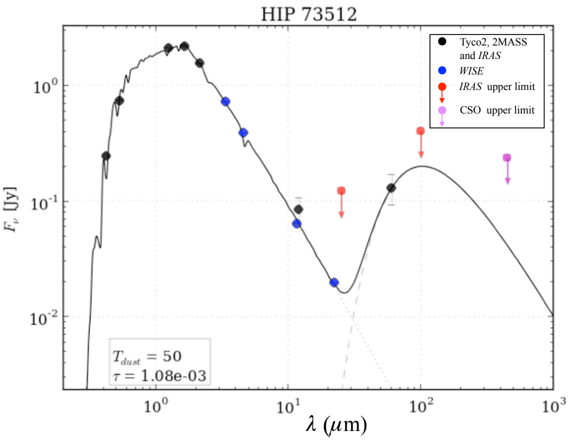

Figure 4.2: SED of the cold debris disk candidate - HIP 73512 for which the submm flux limit lies above the extension of the single temperature blackbody fit to the *IRAS* excesses. The NextGen atmospheric model corresponding to the best-fit stellar photosphere and the blackbody fit are plotted. Deeper submm observations for are required to further assess this source as a cold debris disk candidate.

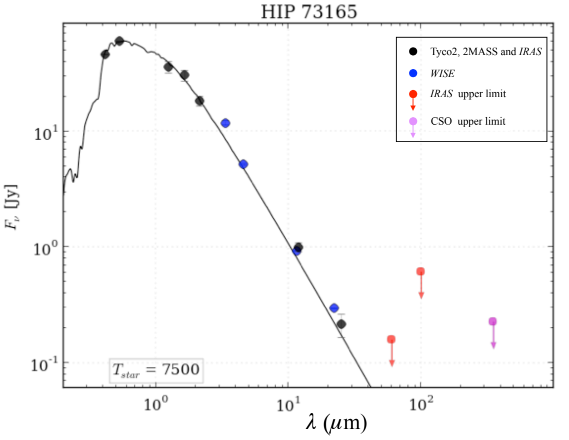

Figure 4.3: SED of our *WISE* excess source - HIP 73165. The NextGen atmospheric model corresponding to the best-fit stellar photosphere is plotted. Excess is seen in the W4 band above the photosphere, and is 34 times the uncertainty in the photometry. The CSO 450 μm 3σ upper limit (pink point and downwards arrow) shows the level to which the lack of submm excess emission is seen.

SHARCII contains a 12 × 32 array of pop-up bolometers with a >90 % filling factor over the field and provides background-limited 350 μm and 450 μm maps. For the closest systems, we obtained 350 μm maps to potentially resolve the disks. For the remaining targets we measured 450 μm maps to measure longer wavelength fluxes distinct from the *Herschel* bands. Table 4.2 lists the wavelengths that were observed for each source along with the corresponding exposure times. The field-of-view of the SHARCII maps was $\sim 2' \times 0'.6$, and the beam sizes at 350 μm and 450 μm are $\sim 8''.5$ and $\sim 10''.0$, respectively. The beam shape was stabilized by the active primary surface correction (Leong et al., 2006), which corrects for dish surface imperfections and changes in the gravity vector as a function of elevation.

The data were acquired during two observing runs: February 14-22 2012 and June 6-14 2012. There were no significant changes to the instrument over the course of the observations. The conditions during the observations ranged from excellent $\tau_{225\mathrm{GHz}} = 0.03$ to marginal $\tau_{225\mathrm{GHz}} = 0.07$. The observing sequence consisted of a series of target scans bracketed by scans of planets and nearby secondary calibrators, serving as both absolute flux calibration and pointing calibration measurements. The calibrators that were observed for each science target are listed in Table 4.2. Pointing calibration measurements were taken at least once per hour during the observing period and focus corrections were monitored throughout the night. Typical individual target scan times were 620s, while 120s was sufficient for the calibrators. A total of 1 to 11 scans were taken on the science targets.

TABLE 4.2: Sub-millimeter observations

Name	UT Date	λ (μm)	Exp. Time	$\tau_{225\mathrm{GHz}}$ range	Secondary Calibrators	Flux Calibrators
HIP 51658	2012 02 16	450	6×10 min	0.04-0.06	3C273, OH231.8, OJ287	CRL618, OH231.8
HIP 68160	2012 02 16	450	5×10 min	0.03-0.06	3C273, OJ287	CRL618, OH231.8
HIP 73165	2012 06 10	350	5×10 min	0.06-0.07	Arp220	Neptune, Uranus
HIP 73512	2012 06 10	450	6×10 min	0.06-0.07	Arp220	Arp220, Mars
HIP 76375	2012 06 10	350	8×5 min	0.05-0.06	Arp220	Neptune, Uranus
HIP 112460	2012 06 13	350	8×10 min	0.06-0.07	Arp220	Neptune, Uranus

4.3.2 Imaging Observations

High angular resolution observations were used to search for the presence of a stellar binary companion to each member of the sample, since a companion can impact the stability of debris disk material. Dedicated observations were obtained for four targets with the Arizona Infrared Imager and Echelle Spectrograph (ARIES; McCarthy et al., 1998) at the 6.5m AO-equipped MMT on December 23 2012. The observing strategy was the same for each target, with a series of short unsaturated exposures taken first to calibrate the photometry of the observing sequence, followed by deep exposures in which the core of the PSF of the target was saturated, increasing the sensitivity to faint stellar companions. For both sets of exposures, images were obtained at a series of offset positions to measure the sky background and mitigate the effects of bad pixels. Additionally, the CFHT and *HST* archives were searched for previous high angular resolution observations of each sample member. Collectively, the new and archival observations include all the targets. Details of the high angular resolution observations of the sample are given in Table 4.3.

To increase the range of separations at which a stellar binary companion can be detected to a limit of 10,000 AU, digitized photographic plates were obtained from the SuperCosmos Sky Survey Science Archive (Hambly et al., 2001) for each target within the sample. For the targets within 30 pc, several of the 15′× 15′digitized plates were combined to ensure the angular coverage was sufficient to detect co-moving companions with separations up to the 10,000 AU outer boundary considered for this study. The large time baseline between the first and last photographic observation, combined with the high proper motion of the sample members, allowed for an identification of wide common proper motion (CPM) companions. An example of one of the wide-field images is shown in Figure 4.4.

Table 4.3: High-resolution imaging observations

	This Work				Archival Data			
Name	UT Date	Filter	Instrument/ Telescope	Exp. Time (s)	UT Date	Filter	Instrument/ Telescope	Exp. Time (s)
HIP 51658	2012 12 23	K_s	ARIES/MMT	600	2010 02 04	K_p	AOBIR/CFHT	440
HIP 68160	2012 12 23	K_s	ARIES/MMT	620	2008 03 21	F606W	WFPC2/*HST*	500
HIP 73165	-	-	-	-	2005 08 15	F160W	NICMOS/*HST*	1663
HIP 73512	2012 12 23	K_s	ARIES/MMT	450	2008 03 09	F160W	NICMOS/*HST*	1120
HIP 76375	-	-	-	-	2008 03 13	F160W	NICMOS/*HST*	1120
HIP 112460	-	-	-	-	2002 07 24	FeII	AOBIR/CFHT	64

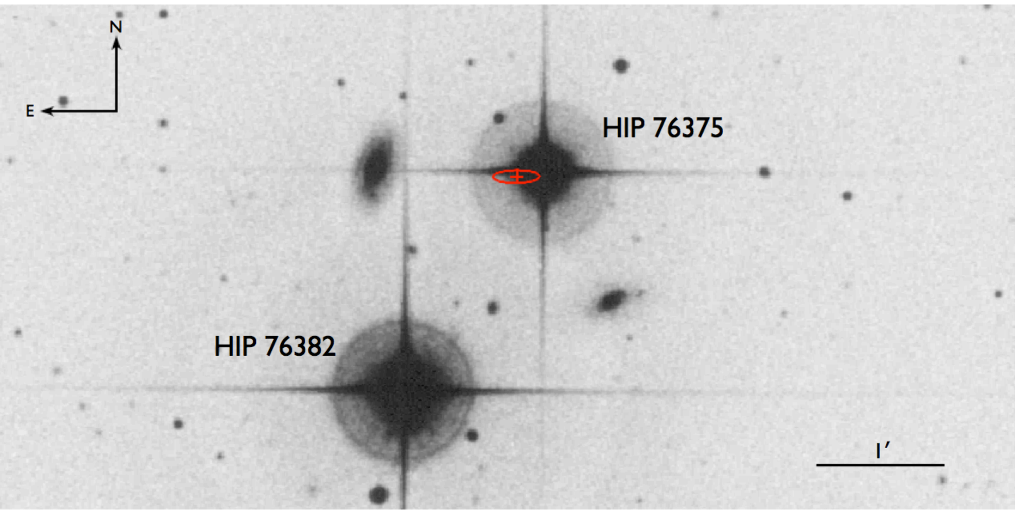

Figure 4.4: Field plate image of HIP 76375, the only source in our sample with a known companion. The orientation is indicated with the arrows, along with a scale bar for this 8′ × 4′ image. The companion - HIP 76382, identified from CPM (Shaya & Olling, 2011) is labeled on the image and lies 148° from the primary, with a separation of 121″.8. The *IRAS* FSC positional uncertainty for HIP 76375 is displayed on the image (red ellipse).

4.3.3 Archival mid-IR/far-IR images

For each target, images from the all-sky surveys of *IRAS* and *WISE* were obtained for this program. Figure 4.5 shows the region centered on each target for each of the four bands of *WISE* (left) and four bands of *IRAS* (right). Overplotted on each image is the approximate size of the 100 μm *IRAS* beam; the beam is estimated as circular using the average of the elliptical major and minor axis as the radius. We searched the *Spitzer* Heritage Archive and the *Herschel* Science Archive for higher resolution, pointed far-IR observations for each target, and three of the targets have additional higher resolution data. Level 2 MIPS data at 24 μm and 70 μm were retrieved for HIP 76375 and HIP 112460, and level 2.5 PACS data at 100 μm and 160 μm was retrieved for HIP 51658. The pointed observations with *Spitzer* and *Herschel* are shown in Figure 4.6.

4.4 Data Analysis

4.4.1 Submm maps and fluxes

The analysis of the CSO 350 μm and 450 μm data included four main steps: application of a pointing model[1], reduction of the raw data with the CRUSH pipeline (Kovács, 2006, 2008), measurement of aperture photometry, and calibration of fluxes. As an initial step, the pointing drifts of the telescope were estimated for each observation with a pointing model that accounts for both static effects, measured with many pointing sources at different positions throughout the run, and for time variable effects, measured with pointing sources observed before and after the science target. These offsets and the contemporaneous measurement of the atmospheric opacity are then incorporated into the data processing, implemented with the CRUSH (version 2.11-2) software (Kovács, 2006, 2008). The output of CRUSH includes an intensity map and signal-to-noise ratio map. The image processing algorithm is optimized depending on source brightness. We utilized the data reduction settings appropriate to the flux levels for the planets, pointing sources and science targets. Circular apertures with a radius of $9\farcs5$ at 350 μm and $10\farcs6$ at 450 μm were used for the target photometry; the aperture sizes are based on the measured FWHM of the point source calibrators at each wavelength.

---

[1] http://www.submm.caltech.edu/~sharc/analysis/pmodel

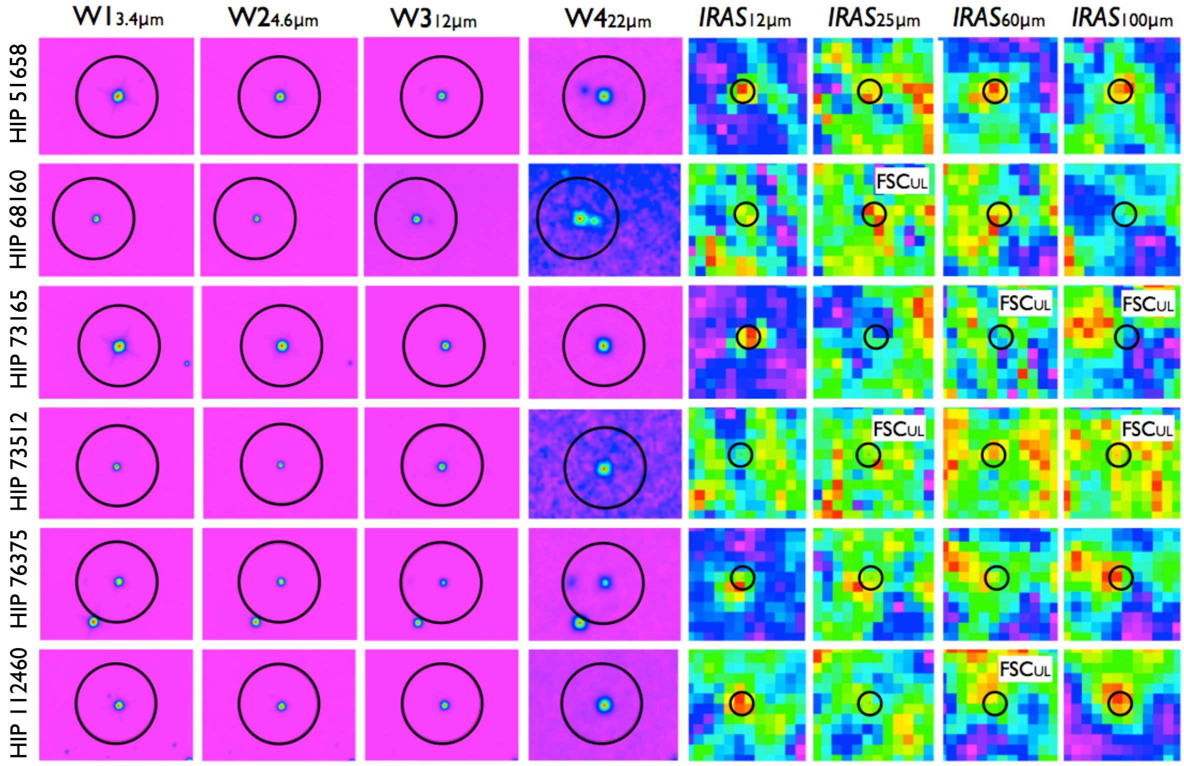

Figure 4.5: The *WISE* All-Sky Survey Atlas images and *IRAS* Sky Survey Atlas (ISSA) for all the sources of our sample. The images are displayed per source (represented by the row heading) in order of survey, and the wavelength of observation from left to right (indicated by the column heading). Orientation for all images are North, up and East, left. The *WISE* images are 400″× 300″in size. The spatial resolution of the ISSA images at each wavelength are smoothed to the *IRAS* 100 μm beam size and are 900″× 900″in size. The black circles represent the *IRAS* 100 μm beam centered over the source positions. The sources and the wavelengths for which *IRAS* FSC upper limits are reported are indicted in the images. The four cold debris disks candidates with submm limits well below the corresponding SED fits are HIP 51658, HIP 61680 and HIP 76357 and HIP 112460, and are investigated for the possibility of contaminating sources within the *IRAS* beam. For HIP 51658, HIP 61680 and HIP 76357 nearby objects are visible in the higher resolution *WISE* images (also see Figure 4.6). Additionally, for HIP 76357 the secondary companion (HIP 76382) is seen dominant in all *WISE* images and is noticeably seen in the 12 μm and 25 μm ISSA images. No contaminating sources are visible in either the *WISE* or ISSA images for HIP 112460.

Absolute fluxes of the planets are based on the distance from the Earth and the Sun, calculated at the time of observation and determined using the planetary brightness temperatures measured by Griffin & Orton (1993). The planets Mars, Neptune and Uranus were used for primary flux calibration and have absolute calibration uncertainties of ∼5-10% (Griffin & Orton, 1993). For nights without a planet observation, the calibration is tied to the secondary calibrators Arp 220, CRL 618 and OH231.8. For observations at 350 μm, we use a flux density of 23.3 ± 4.2 Jy for CRL 618 (derived by C. D. Dowell and listed on the SHARCII website[2]). The uncertainty is based on the long term variability of evolved stars (Sandell, 2003; Jenness et al., 2002). At 450 μm, we use a flux density of 6.3 ± 0.8 mJy for Arp220 (Dunne & Eales, 2001), 12.1 ± 2.2 mJy for CLR 618 and 12.7 ± 2.2 mJy for OH231.8 (Jenness et al., 2002). The uncertainty of the flux calibration is combined with the uncertainty of the source signal which is measured from the CRUSH source maps. The total uncertainty on the submm fluxes of the science targets ranges from ∼15-30%.

None of the six targets were detected in the CSO 350 μm or 450 μm maps. We have therefore pursued two types of analysis in order to investigate the causes for these null detections, presented in Section 4.5. With infrared imaging, we investigate the possible disruptive effects caused by companion stars and with an analysis of available mid-IR to far-IR maps, we explore the possibility of source contamination in the *IRAS* catalogue resulting in a misidentification of the target as a debris disk system.

4.4.2 High resolution and wide-field, near-IR/optical companion search images

For the ground-based AO images from the MMT and CFHT, we performed standard image processing steps to account for sky background and detector dark current, non-linearity, bad pixels, and quantum efficiency variations. The individual science images were aligned, and median combined. For the *HST* archive data, the images were already reduced and flux calibrated, so no additional processing was required. Each final target image was searched for stellar companions, and detection limits were calculated as a function of separation. For each target, the minimum separation at which a stellar companion at the bottom of the Main Sequence (0.08 $M_\odot$) could be detected was determined. The variance of the pixel values within the science images was measured as a function of separation, scaled by the flux and apparent magnitude of the central target, and compared to the expected apparent magnitude of a 0.08 $M_\odot$ stellar companion obtained from theoretical models (Baraffe et al., 1998).

Three of the sample members have also been searched for binary companions with speckle interferometry (HIP 51658, HIP 76375, and HIP 112460; Miura et al., 1995; Hartkopf & Mason, 2009; Balega et al., 2007), and none of which were found to have a binary companion. While these techniques would be sensitive to a high mass ratio binary companion at close separations, their sensitivity does not extend to the bottom of the

---

[2] http://www.submm.caltech.edu/∼sharc/

Main Sequence. Future observations with increased sensitivity are required in order to rule out the presence of any stellar companion interior to the detection limits given in Table 4.4.

To search for companions beyond the field-of-view of the high angular resolution instruments, the digitized photographic plates for each target were blinked to reveal the presence of any wide co-moving companions. To ensure wide CPM companions were not missed during the visual inspection, the PPMXL (Roeser et al., 2010) and the UCAC4 (Zacharias et al., 2012) catalogues were also searched for stars with proper motions consistent with the object being physically bound to the primary.

Table 4.4: Companion search results

Target	Radius to reach bottom of MS (AU)	Detected Companion	Companion Separation (AU)	Position Angle (°)	Δmag (mag)	Technique
HIP 51658	39	N	-	-	-	-
HIP 68160	94	N	-	-	-	-
HIP 73165	45	N	-	-	-	-
HIP 73512	41	N	-	-	-	-
HIP 76375	35	Y	2725	148	ΔK=0.79	CPM
HIP 112460	1	N	-	-	-	-

4.4.3 *IRAS* data

We visually inspected each image in order to assess the quality and association of *IRAS* Faint Source Catalogue fluxes that have been extracted for the targets. The synthesized beam sizes of the Faint Source Survey images are approximately $1' \times 4'$ at 12 μm and 25 μm, $2' \times 4'$ and $4' \times 5'$ at 60 μm and 100 μm, respectively. The positional uncertainties of *IRAS* detections for our sample is $\sim 3''$ in the in-scan direction and $\sim 18''$ in the cross-scan direction. In addition, we have reassessed the quality of the FSC extracted flux densities for our targets, with the use of the online Scan Processing and Integration (*SCANPI*) tool[3]. *SCANPI* combines the signal for all (in-scan) survey scans that correspond to the target position and provides fluxes of faint sources, estimates of true local upper limits and deviation of the signal peak to that of the source position. Despite the stringent processing of the survey scans and catalog criteria that have been implemented for source extraction and identification, the large angular resolution of the *IRAS* beams is one of the primary factors of possible source contamination.

---

[3] http://irsa.ipac.caltech.edu/applications/Scanpi/

4.4.4 Higher resolution mid-far IR *WISE*, *Spitzer* and *Herschel* images

WISE provides a factor of 10 higher resolution images in the mid-IR than *IRAS*. The *WISE* beam sizes are $6''\!.1$, $6''\!.4$, $6''\!.5$ and $12''$ at 3.4 μm (W1), 4.6 μm (W2), 12 μm (W3) and 22 μm (W4) respectively. To utilize this significant improvement of resolution, we performed visual cross inspection of the four *WISE* bands, to identify any contaminating objects that are contained within the *IRAS* beam sizes. Additionally, we investigated the available *Spitzer* MIPS and *Herschel* PACS (Poglitsch et al., 2010) processed images from the archive for the targets HIP 76375, HIP 112460, and HIP 51658. HIP 68160 was not observed by either *Spitzer* or *Herschel*. The *Spitzer* FWHM beam size with MIPS at 24 μm is $6''$, a factor two greater than the *WISE* W4 band, and pointed observations further increase the sensitivity beyond that achieved with the *WISE* survey. The far-IR MIPS channels at 70 μm and 160 μm, with corresponding beam sizes of $20''$ and $40''$, and the *Herschel* PACS channels at 70 μm , 100 μm and 160 μm, with FWHM beam sizes of $5''\!.6$, $6''\!.8$ and $11''\!.4$ respectively, provide the far-IR wavelength coverage with significantly greater resolution than that of *IRAS*, enabling the identification of contaminating objects such as background galaxies that become increasingly brighter across the mid-far IR regime.

4.5 Results

None of the six debris disk targets were detected in the CSO SHARCII maps. The 3σ upper limits range from 31 mJy for HIP 51658 to 239 mJy for HIP 73512 at 450 μm, and all the limits are reported in Table 4.5. For four of the five cold debris disks targets, the submm flux limits are substantially below the extension of the blackbody fit to the *IRAS* excesses, as shown in Figure 4.1. The CSO limit for the cold debris disk candidate HIP 73512 is above the blackbody fit, as shown in Figure 4.2, and the CSO data do not constrain the disk in this case. The *WISE* excess source HIP 73165 also shows a lack of submm emission at a level reported in Table 4.5 and plotted on the SED in Figure 4.3.

4.5.1 CSO flux limits

The flux limits were converted into dust mass limits following previous submm studies (e.g., Zuckerman & Becklin, 1993) using the expression $M_{\rm d} = (F_\nu D^2)/B_\nu(T)\kappa_\nu$, where the blackbody function $B_\nu(T)$ is equal to $2kT/\lambda^2$ in the Rayleigh-Jeans limit. The dust opacity at the frequency of observation κ_ν assumes a functional form $\kappa_\nu = \kappa_0(\nu/\nu_0)^\beta$ at submm wavelengths. We use a normalization value $\kappa_0 = 0.17$ m^2 kg^{-1} at 850 μm and scale with β=1 (Zuckerman & Becklin, 1993; Pollack et al., 1994). Existing submm studies find that β=1 is a representative value of debris disks (Dent et al., 2000) and the normalization value for dust opacity is adopted for direct comparison with previous studies (e.g., Sylvester et al., 2001; Wyatt et al., 2003; Liu et al., 2004; Sheret et al., 2004; Najita & Williams, 2005; Williams & Andrews, 2006). Assuming an average dust temperature of 30 K for the submm-emitting dust, the submm flux limits correspond to dust mass limits of 0.001 to 0.261 M$_\oplus$, as reported in Table 4.5. These dust mass limits are comparable to the detections of other nearby debris disks based on either submm fluxes or fits to *IRAS* fluxes over a large wavelength range (e.g., compilation in Rhee et al., 2007).

The submm upper limits are plotted along with previous measurements at shorter wavelengths to construct the SEDs of the *IRAS* cold excess debris disks with limits below the blackbody fit in Figure 4.1 and with a limit above the blackbody fit in Figure 4.2. The *WISE* warm excess debris disk SED is plotted in Figure 4.3. For the cold excess sources, the fits to the 60-100 μm emission, assuming a single temperature blackbody, are also shown for comparison with the measured CSO limits. For the targets HIP 51658, HIP 68160, HIP 76375 and HIP 112460, the submm limits are all well below the expected flux level at these wavelengths, making these limits more restrictive than previous submm measurements of some debris disks candidates Williams & Andrews (2006). For the *WISE* source, there is not a large enough wavelength coverage for the excess emission to perform a fit, and the exploratory measurement at the longer wavelength is shown in comparison to the newly reported mid-IR excess in the *WISE* W4 band. With only an excess in the longest wavelength *WISE* band, it is not possible to fit a blackbody to estimate an expected flux level for the CSO measurement, but the non-detection is consistent with a spatially confined distribution of hot dust for this source. Larger scale studies with more sensitive limits from *Herschel* will provide more definitive constraints on the origin of *WISE* excesses for sources such as HIP 73165.

4.5.2 Companion systems

Since a companion star will gravitationally truncate the outer portion of a disk and reduce the amount of submm-emitting dust, all targets were searched for stellar companions. A visual inspection of the high-resolution data did not reveal any companion candidates.

Table 4.5: Sub-millimeter detection limits

Target	λ (μm)	Map noise rms (mJy/beam)	Flux limit[a] (mJy)	Dust mass limit[b] ($M_\oplus$)
HIP 51658	450	8	<31	<0.046
HIP 68160	450	13	<51	<0.089
HIP 73165	350	66	<227	<0.094
HIP 73512	450	66	<239	<0.262
HIP 76375	350	68	<234	<0.065
HIP 112460	350	22	<73	<0.001

Notes. a. Flux calibration uncertainties are included in the 3σ limits reported.
b. Calculated assuming an average dust temperature of 30 K.

Separately, a visual inspection of each of the blinked image pairs combined with a search of the astrometric catalogues, identified one co-moving object – the known wide common proper motion (CPM) companion to HIP 76375 (Shaya & Olling, 2011). The HIP 76375 system is shown in Figure 4.4. The binary separation is $121\farcs8$, which corresponds to a projected physical separation of ~2700 AU – too large to impact the disk size unless the orbit is very eccentric and periastron passage occurs at a much smaller separation. Table 4.4 lists the details of the HIP 76375 binary system and the closest separation at which the data become sensitive to companions at the bottom of the Main Sequence for each of the targets. The minimum separation ranges from only 1 AU for the M-star HIP 112460 at ~5 pc to 94 AU for the more massive and more distant A-star HIP 51658 at ~30 pc. In addition to the companion search we performed, five targets were included in the interferometric (van Belle et al., 2008; van Belle, 2010) and speckle (Hartkopf & McAlister, 1984; Miura et al., 1995; Hartkopf & Mason, 2009; Balega et al., 2007) searches, and no companions were discovered for these targets, although the detection limits were not deep enough to include all possible stellar companions.

4.5.3 *IRAS* source contamination

For the four cold debris disk candidates with submm limits well below the SED fit (shown in Figure 4.1), we investigated the possibility of contaminating sources within the *IRAS* beam. All targets have *WISE* images in four bands with higher resolution than *IRAS*, and three of the four targets have *Spitzer* data in at least one bandpass. Three of the four objects – HIP 51658, HIP 61680, and HIP 76375 – show contaminating sources in the higher resolution mid-IR/far-IR images shown in Figure 4.6. Only one candidate disk target – HIP 112460 – shows a single object in the higher resolution *WISE* and *Spitzer* maps shown in Figure 4.7. The results of the contamination analysis for these sources is discussed in the following subsections.

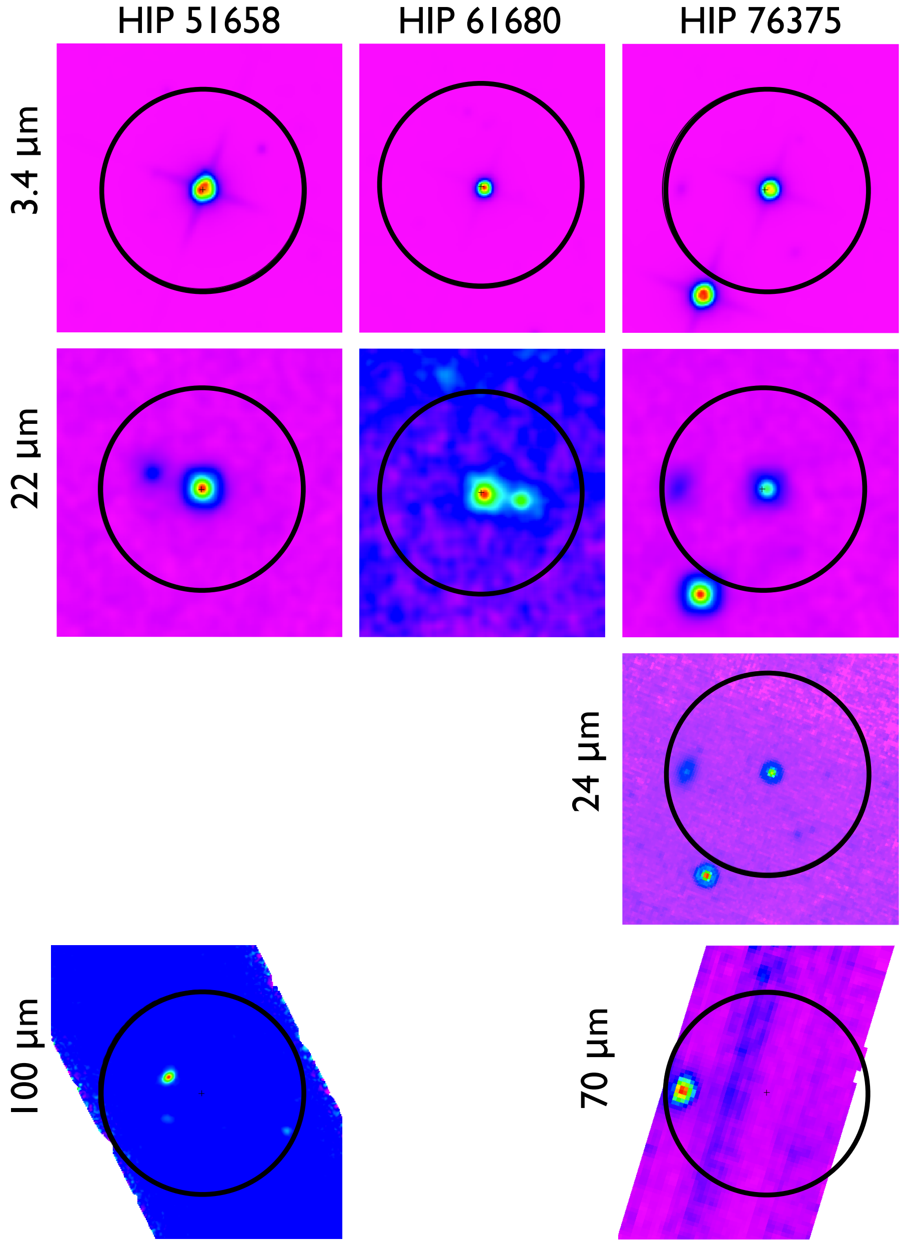

FIGURE 4.6: Higher resolution IR images for the sources – HIP 51568, HIP 61680 and HIP 76375, in which nearby contaminating objects are seen in the *WISE* and when available *Spitzer* MIPS and *Herschel* PACS images. The orientation for all images are North, up and East, left and the images are 300″ in size along each axis. The black circles represent the *IRAS* 100 μm beam centered over the source positions. For HIP 51658 a nearby object (~55″ to the NE) is seen to become increasingly brighter at increasing wavelengths, as shown in the *WISE* 22 μm (W4) and *Herschel* PACS 100 μm images. For HIP 68160, a nearby object (~35″ to the west) is seen in the W4 image. For HIP 76375 and the binary companion - HIP 76382 (121″ to the SE) are both visible in the *WISE* 3.4 μm (W1), W4 and *Spitzer* MIPS 24 μm images. Neither component of the system are seen in the *Spitzer* MIPS 70 μm image. The galaxy IC 4563 (~80″ to the East), is visible in the W4 and MIPS images, and lies within the *IRAS* beam area.

4.5.3.1 HIP 51658

From the sequence of *WISE* images for HIP 51658 in Figures 4.5 and 4.6, a nearby object $\sim 55''$ to the NE of HIP 51658 is seen and becomes increasingly brighter with wavelength. Also shown in Figure 4.6 is the *Herschel* PACS 100 μm map centered on the target which reveals the offset source, but not the target. In both the *WISE* and *Herschel* maps there are additional fainter sources within the *IRAS* beam (not visible with the scaling of Figure 4.6). Three distinct sources are detected in the *Herschel* 100 μm map. From our *SCANPI* analysis of this source, we find that signals are significant in all IRAS bands ($>5\sigma$) and the deviation from source position to the signal peak is $<0.5'$.

To determine the flux of the contaminating objects, we have measured the flux densities of the nearby three objects that fall within the *IRAS* beam centered over the source position, and find that the cumulative flux density at 100 μm is consistent with the *IRAS* FSC 100 μm flux. Furthermore, the 160 μm cumulative flux density fits well to the single temperature blackbody, modelled excess fit. The PACS fluxes, along with our 450 μm upper limit that lies significantly below the fit, are shown in Figure 4.1. This analysis indicates that the associated *IRAS* 60 μm and 100 μm fluxes of this source are contaminated and that HIP 51658 is not a bona fide debris disk system. To determine more accurate flux upper limits for HIP 51658, we have extracted level 2.5 processed PACS 100 μm and 160 μm images from the *Herschel* archive and measured 3σ flux upper limits of 22 mJy at 100 μm and 34 mJy at 160 μm, following the point source photometry guidelines recommended by the *Herschel* team[4].

4.5.3.2 HIP 68160

As shown in Figure 4.6, a nearby object $\sim 35''$ to the west of HIP 68160 is visible in the W4 22 μm image, and lies within the *IRAS* beam. The *IRAS* 25 μm flux for this source is reported as an upper limit in the FSC. As there are no higher resolution far-IR observations available from *Spitzer* or *Herschel* for this source, we are unable to quantify the level of flux contamination within the *IRAS* 60 μm and 100 μm bands, unlike the case of HIP 51658. The presence of the additional source in the *WISE* W4 image does, however, suggest that the *IRAS* fluxes are heavily influenced by this red object. Based on this second source in the field, HIP 68160 is also a probable case of a misclassified debris disk system.

---

[4] Technical Note PICC-ME-TN-037 in http://herschel.esac.esa.int

4.5.3.3 HIP 76375

This target is the only known binary in our sample. Both the target and binary companion (separation of $121\overset{''}{.}8$) are visible in all four *WISE* images (see Figure 4.5) and the MIPS 24 μm image (see Figure 4.6). From our *SCANPI* analysis we note that there is a large positional offset ($1.9'$) from the source to signal peak in the *IRAS* 12 μm band, with a SNR of 8. Figure 4.5 shows the *IRAS* scans at 12 μm, 60 μm and 100 μm. In the 12 μm scan, the position of the binary companion falls on the peak emission pixel, indicating that the *IRAS* 12 μm flux reported for this source contaminated is from emission of the secondary.

To investigate the longer wavelength measurements, we have extracted the archival MIPS images at 24 μm and 70 μm for this source, shown in Figure 4.6. In all the *WISE* images and in the MIPS 24 μm image, both the target and companion are visible. The galaxy, IC 45634[5] ($\sim80''$ to the E) is seen to become increasingly brighter with longer wavelengths, as seen in Figures 4.5 and 4.6. In the MIPS 70 μm image, neither the source or companion are visible, yet the galaxy is clearly seen and lies within the *IRAS* 100 μm beam, centered over the source position. The SNR of the signal, returned with *SCANPI* at 60 μm is marginal at 2.9σ and the positional offset from the source to signal peak is $0.33'$. Whilst this offset is below the FSC criteria to flag the source as an upper limit, it is significantly greater than that of other 60 μm source detections (as determined through comparison of our sources and those of a similar study i.e. Williams & Andrews, 2006 – as is discussed in Section 4.6).

From the MIPS images we have measured the source flux at 24 μm, the 3σ upper limit at 70 μm, and the flux of the galaxy (light blue point); included on the SED shown in Figure 4.1. We find that the source 24 μm flux lies on the modelled photosphere of this object and that the 70 μm upper limit lies significantly below the single blackbody, model excess fit. Furthermore, we find that the 70 μm flux of the galaxy matches well to the excess fit. In visual inspection of the *IRAS* scans it can be seen that at the position of the galaxy, the corresponding pixel becomes increasingly brighter at longer wavelengths. From this analysis, we conclude that both the *IRAS* 60 μm and 100 μm flux is contaminated due to the emission from the galaxy.

---

[5] Identified in the NASA/IPAC Extragalactic Database - http://ned.ipac.caltech.edu/

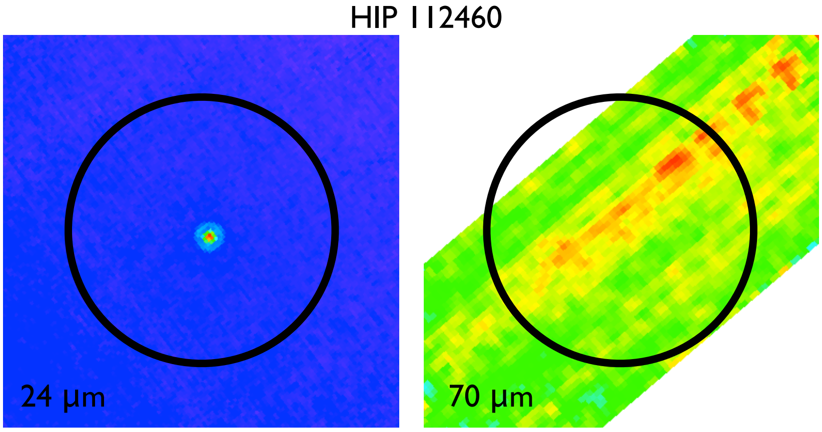

Figure 4.7: Higher resolution *Spitzer* MIPS images for HIP 112460. The orientation of both images are North, up and East, left and the images are 300″ in size along each axis. The black circles represent the *IRAS* 100 μm beam centered over the source position. The source is clearly detected in the 24 μm image, with no visible nearby contaminating objects. The 3σ upper limit of the source measured in the 70 μm image lies well below the modelled, single blackbody excess fit. Whilst stripping artefacts are seen in the 70 μm image, no nearby contaminating objects are visible.

4.5.3.4 HIP 112460

Although HIP 112460, the M-star cold debris disk candidate has the largest discrepancy between the predicted submm flux from the SED and the measured CSO limit (a factor of ∼100), no additional source was identified within the *IRAS* beam. From inspection of the higher resolution *WISE* and MIPS images, no contaminating object is detected in the surrounding field of this source, as shown in Figure 4.7. Due to the low latitude of the source (b = -13°), it is possible that the associated 100 μm *IRAS* flux is contaminated from Galactic cirrus emission. Another possibility for this nearby source is a dilution of the flux from a disk due to a spatially resolved disk. To assess the impact of a spatially resolved disk, we searched for the largest reported spatially resolved disks around M-stars (AU Mic – MacGregor et al., 2013 and GJ 581 – Lestrade et al., 2012), scaled the disk size based on the distance to HIP 112460, and determined the number of beams across which the flux would be distributed in a uniform disk. Even for the larger of the two resolved M-star disks, the resulting size at the distance of HIP 112460 would spread the flux across ∼9 beams, diluting the flux by a factor too small to account for the large discrepancy.

Another possible explanation for the submm non-detection is a variable source. Some support for this hypothesis comes from the conflicting flux measurements at different epochs, since the fluxes obtained from later observations with *WISE* at 12 μm and 22 μm and *Spitzer* MIPS at 24 μm fall on the photosphere of the star, compared to the excesses obtained from the earlier *IRAS* at 12 and 25 μm scans, and seen at high significance at 12 μm and 100 μm in Figure 4.5. From the *Spitzer* MIPS images of this source, we measured the 24 μm flux and the 70 μm upper limit. As shown in Figure 4.1, the *Spitzer* 24 μm flux lies on the modelled stellar photosphere for this source and both the 3σ upper limits at 70 μm and our 350 μm observation, lie well below the modelled, single blackbody excess fit (unlike the *IRAS* values). A large scale *IRAS* variability investigation of blazars (Impey & Neugebauer, 1988) did find sources with variability up to an order of magnitude at 100 μm, however such a large amplitude change was very rare. Another example of a large degree of variability intrinsic to a debris disk at somewhat shorter wavelengths in the mid-IR was reported for the debris disk – TYC 8241 2652 1, which exhibited a remarkable change of a factor of ∼30 over a timescale of less than two years (Melis et al., 2012). More observations are required to provide further understanding into the nature of this unusual, possibly variable, system.

4.6 Investigation of other debris disks with upper limits

The high rate of source contamination of the *IRAS* FSC fluxes found amongst our cold debris disk sample prompted us to conduct the same contamination analysis for a previous submm study, at 850 μm of eight debris disks (Williams & Andrews, 2006), to further assess the likelihood of additional examples of misidentified debris disks. In the Williams & Andrews (2006) study, the sources were selected through *IRAS* FSC excesses, similar to our program. Upper-limits were obtained for two of the eight sources – HD 56099 and HD 78702, yielding an non-detection rate of 25%. From inspection of the higher resolution *WISE* and *Spitzer* MIPS images of these two sources, we find that a nearby object lies within the *IRAS* beam size for HD 56099. No nearby contaminating objects are visible in either the *WISE* or *Spitzer* images for HD 78702. For HD 56099, the nearby object is visible in the *WISE* W3 and W4 images and in the MIPS 24 μm, 70 μm and 160 μm images, and becomes increasingly brighter with wavelength. Moór et al. (2006) identify this source to be a misclassified debris disk system, due to the nearby object contamination as identified, and Moór et al. (2011) have further analysed the *Spitzer* observations for this target and find a low significance level of excess above that of the stellar photosphere. One out of eight sources, in the study carried out by Williams & Andrews (2006), was misidentified of possessing a cold debris disk. Accounting for the misidentified cold debris disk source, the non-detection rate within the Williams & Andrews (2006) study is ∼29%. Comparatively, for the cold debris disk sample presented within this chapter, three out of the five sources show evidence of nearby object contamination of the associated *IRAS* FSC fluxes and the non-detection rate of the cold debris disk candidates is 100%.

4.7 Conclusions

We have presented new submm observations at either 350 μm or 450 μm, searching for dust emission around a sample of cold and warm nearby (< 40pc) debris disk candidates, that have been identified from *IRAS* or *WISE* excesses.

Upper-limits were obtained for all six targets, and four of the limits are well below the expected submm flux, based on a single temperature blackbody model fit to previous shorter wavelength photometry. Of the four cold excess sources with very discrepant submm limits compared to the SED fit, we found that three targets have clearly identified contaminating objects in the *IRAS* beam, and therefore are likely misidentified debris disk candidates. Quantitive measurements of the contaminating objects were obtained for two targets – HIP 51658 and HIP 76375 – from higher resolution, pointed *Herschel* PACS and *Spitzer* MIPS observations at wavelengths comparable to the *IRAS* excess fluxes. From visual inspection of the *WISE* all-sky survey images, we find that HIP 61680 is also like to suffer from *IRAS* contamination, in which we identify a nearby, background object that becomes increasingly brighter over the *WISE* bands as the likely true source of the *IRAS* FSC measurement.

The rate of *IRAS* contamination has likely lead to a greater number of sources in being identified as possessing cold debris disks than the actual number. Considering the high level of source contamination in this study and comparable results from an analysis of other debris disks candidates with submm non-detections (Williams & Andrews, 2006), lower detection rates than anticipated for large scale debris disks surveys that are currently being pursued with *Herschel* and SCUBA2 may be found.

It is important to highlight the need for careful examination of source contamination for observations in the far-IR and submm wavelengths, where the probability of detecting a nearby background source can be as high as 36% (Booth et al., 2013; Berta et al., 2011). In this study we find 4-5 examples of contamination either from identified objects or possible background variability, giving a contamination rate of 31-38% similar to the probability reported in Booth et al. (2013).

Finally, we note that it is only now that it is possible to assess systematically the *IRAS* associations of debris disk candidates by using the complementary mid-IR to far-IR wavelength coverage and higher resolution and sensitivity provided by *WISE*, *Spitzer* and *Herschel*.

Chapter 5

The HR 8799 debris disk dystem

Adapted from Patience, J., Bulger, J., King, R., et al., 2011, A&A, 531, L17

Abstract

Dynamical interactions between planets and debris disks may sculpt the disk structure and impact planetary orbits, but only a few systems with both imaged planets and spatially resolved debris disks are known. With the Caltech Submm Observatory (CSO), we have observed the HR 8799 debris disk at 350 μm. The 350 μm map is the first spatially resolved measurement of the debris disk encircling the HR 8799 planetary system at this wavelength. Both the flux and size of the emission are consistent with a Kuiper belt of dust extending from ~100-300 AU. Although the resolution of the current map is limited, the map shows an indication of offset asymmetric emission, and several scenarios for this possibility are explored with radiative transfer calculations of a star-disk system and N-body numerical simulations of planet-disk interactions with parameters representative of the HR 8799 system.

5.1 Introduction

Planets and debris disks are intimately linked, as planets can scatter or trap planetesimals in a disk (Mouillet et al., 1997), and planetesimals may drive planet migration (Kirsh et al., 2009). Three planetary systems have been imaged orbiting dusty A-stars (Marois et al., 2008; Kalas et al., 2008; Lagrange et al., 2010) with remnant debris disks (Smith & Terrile, 1984; Holland et al., 1998; Zuckerman & Song, 2004) sustained by the collisional grinding of planetesimals into smaller particles (Backman & Paresce, 1993). These systems present rare cases in which it is possible to explore the dynamical effects on disk structure of planets with known locations. Structures such as asymmetries and clumps can encode the effects of gravitational interactions (e.g., Liou & Zook, 1999; Kuchner & Holman, 2003; Wyatt, 2006; Quillen & Faber, 2006). The submm/mm wavelength range is ideal for studying the interaction of the disk and planets, since the large grains are expected to remain in resonances with the planets, while the smaller grains evolve into axisymmetric structures due to scattering or radiation pressure (Wyatt, 2006).

From *IRAS* photometry, HR 8799 was identified as a debris disk system with excess emission above the stellar photosphere at 60 μm, consistent with cool dust (Zuckerman & Song, 2004). With sensitive *Spitzer* measurements over the 5.5-35 μm range, the disk was further estimated to contain two components: a hotter inner ring of dust analogous to the asteroid belt with an inner radius of 6 AU and a cooler outer disk (Chen et al., 2006). The presence of dust, combined with a young age estimated from the colour-magnitude diagram, made HR 8799 a target for high-contrast imaging which revealed a system of four giant planets at projected separations ranging from ∼14-70 AU (Marois et al., 2008, 2010). The planets are located between the two dust populations. Subsequent *Spitzer* images at 70 μm resolved a distribution of dust at very large radii from HR 8799, and this emission may probe smaller blown out grains (Su et al., 2009). This chapter reports the first observations of the disk at 350 μm, including a spatially resolved map and a comparison with numerical models.

5.2 Observations

Submillimeter observations of HR 8799 were acquired with the 10m Caltech Submillimeter Observatory (CSO) with the SHARCII instrument (Dowell et al., 2003) which includes a 12 × 32 bolometer array with a >90% filling factor. At the observation wavelength of 350 μm, the beam size is $\sim 8\farcs5$ and the shape is stabilised by the Dish Surface Optimization System (DSOS) which corrects for dish figure changes as a function of telescope elevation. The Lissajous scanning pattern employed for the observations resulted in a map size of $\sim 3\farcm3 \times 2\farcm0$. The data were acquired over two nights with excellent tau conditions (τ_{225GHz} = 0.03-0.04) on 6 & 7 Aug 2007. Follow-up telescope time allocated to obtain deeper maps did not have sufficient tau conditions. For the observing sequence, a series of 4-6 scans of 300s to 620s each were obtained on the target and were preceded and followed by 120s scans of a bright pointing and flux calibrator, Uranus, Neptune, or the quasar 3C454.3. In total, 20 scans were taken on the science target for a total of

2.75 hours of data. Given the importance of calibration, a similar number of 23 scans of calibrators were recorded over the time period of the observations. The target and calibrators sampled a similar range of temperature, elevation, and opacity.

5.3 Data analysis

The construction of the CSO map required two main steps – calculating pointing offsets and extracting the signal from the background. For each scan, a pointing correction was first calculated by first computing and then applying pointing corrections that account for both static and time variable pointing drifts, using calibrator scans, a pointing model[1] and software. The calibration scans were used in conjunction with the pointing model to calculate the pointing offset applicable at the time and sky position of each target observation. The pointing corrections, along with the measurements of the atmospheric opacity at the time of observation, were then included in the data processing using the software CRUSH, version 2.01-4 (Kovács, 2008). In the final map, the total flux was measured within the 3σ contour using the MIRIAD (Sault et al., 1995) software. The absolute flux calibration was based on the scans of the planet Uranus and the planet flux at the observation date from the JPL Horizons model. The total uncertainty in the HR 8799 flux is 35%, a combination of the small (6%) variation in the Uranus flux measurements and the rms noise level in measured in the final source map.

To quantify the location of the emission peak, the distance from the host star position to the brightest part of the disk was measured. Since the photosphere of HR 8799 is not detectable at 350 μm, it was necessary to identify the location of the central source based on the telescope pointing. The bright calibration targets were used to empirically measure the pointing accuracy. For the pointing test, each calibrator scan was reduced in a manner analogous to the targets – i.e., by removing that calibrator scan (and others taken within a few minutes) from the pointing correction calculation and deriving a new pointing correction from the remaining calibrators and pointing model and then applying the pointing offset to the CRUSH reduction. This approach should be conservative in calculating the pointing offset to apply to the calibrator scan since the calibrators for the target are taken at most 30min before/after the targets, while this approach for the calibrators has mainly included calibrators ∼60min before/after each calibrator scan treated as a pointing test. The absolute value of the pointing error for each calibrator analysed with this procedure was measured from the difference of the position of the

---

[1] www.submm.caltech.edu/sharc/analysis/pmodel

calibrator in each map to its known coordinates. Since we are interested in the central position of the source, we calculated the standard deviation of the mean of the absolute offsets. Based on this empirical test, the position uncertainty is ±0″.6. Since the position of the emission peak is identified within a fraction of a pixel in the final map, the source position uncertainty dominates the uncertainty on distance measurements.

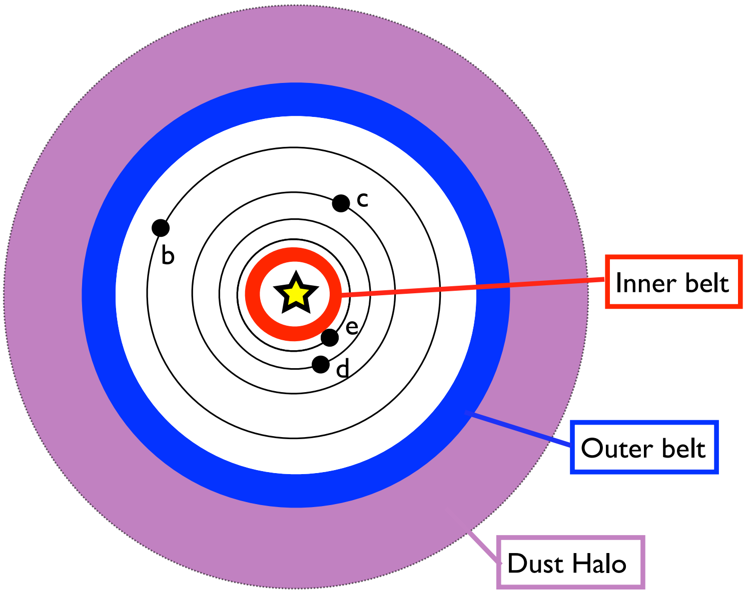

FIGURE 5.1: Schematic diagram of the HR 8799 debris disk system, showing the adapted 3-component model from Su et al. (2009) used to generate the SED models with the MCFOST radiative transfer code. The model includes two dust belts that are separated by the four directly imaged planets (b, c, d, and e; Marois et al., 2008, 2010). The warm inner disk extends from 6-8 AU, the cold outer belt extends from 100-300 AU, and an external halo of small grains extends to an outer radius of 1000 AU.

5.4 Numerical modelling

To interpret the debris disk map, the flux and morphology were compared with three numerical models – a radiative transfer model of a star surrounded by symmetric zones of dust, a simulation of massive planets migrating outwards and interacting with planetesimals and dust, and a simulation from the literature of a low mass planet interacting with planetesimals. The Monte Carlo 3D continuum radiative transfer code MCFOST (Pinte et al., 2006) was used to generate SED models and images at 350 μm. In the MCFOST routines, the photons from the central star with properties given in Reidemeister et al. (2009) were propagated through the disk with a model incorporating a combination of Mie theory scattering, absorption, and re-emission. The disk parameters used to construct the SED model are given in Table 5.1. The disk zones are based on the 3-component model described in Su et al. (2009). Minor modifications were included to account for the dynamically cleared chaotic zones around the innermost and outermost planet (Quillen & Faber, 2006; Moro-Martín et al., 2010; Fabrycky & Murray-Clay, 2010). A schematic diagram of the disk zones is shown in Figure 5.1. A series of simulated images were generated for a range of outer disk radii and inclinations, and Table 5.1 shows the values most consistent with the CSO map.

TABLE 5.1: MCFOST HR 8799 disk model parameters

Model Parameter[a]	Asteroid Belt	Kuiper Belt	Outer Halo
M_{dust} [$M_\odot$]	3.3×10^{-12}	3.6×10^{-7}	5.7×10^{-8}
r_{in} [AU]	6	100	300
r_{out} [AU]	8	300	1000
$H_0(r_{in})$ [AU]	0.6	9	30
$H(r)$	$\sim r^0$	$\sim r^0$	$\sim r^0$
$\Sigma(r)$	$\sim r^0$	$\sim r^0$	$\sim r^{-1}$
a_{min} [μm]	2.0	3.0	1.0
a_{max} [μm]	4.5	1000	10
dn/da	$\sim a^{-3.5}$	$\sim a^{-3.5}$	$\sim a^{-3.5}$

Notes. (a) Dust mass M_{dust}, inner radius r_{in}, outer radius r_{out}, scale height H_0 at a reference radius r_0, flaring profile exponent for the disk height $H(r)$, surface density profile $\Sigma(r)$, minimum grain size a_{min}, maximum grain size a_{max} and the differential grain size distribution dn/da.

The structure in the CSO map was also compared with numerical models performed using an N-body code. Our numerical model included the interaction of planets resembling HR 8799b (6 M_{Jup}) (Currie et al., 2011) and HR 8799c (8 M_{Jup}) (Currie et al., 2011) migrating outwards at the same rate through a disk of planetesimals. Since there was no significant difference in the results when two planets were included rather than one, the planets more distant planets from the debris disk should have no impact and were not added to the simulation. The initial planetesimal belt had a width of 5 AU and an inner radius of 91 AU, and the planets migrated 15 AU to their final orbits. Once the two planets had reached approximately their present day orbits (Marois et al., 2008), the orbits were circularised, and the planetesimal disk replaced by a dust disk. The stability of the planetesimals in a very similar configuration has already been shown in previous simulations (Moro-Martín et al., 2010).

The transformation of planetesimals to dust entailed the introduction of radiation pressure and Poynting-Robertson drag through the parameter β that quantifies the ratio of radiation to gravitational forces (Burns et al., 1979). The grains responsible for the 350 μm emission have a size distribution peaked near 350 μm, so the β value appropriate for the map is 0.0055. The model is designed to investigate the inner region of the Kuiper belt and does not include the entire disk structure or all three components of the SED model. Simulated surface density maps of the inner Kuiper belt were produced at a range of wavelengths. Finally, the CSO map structure was also considered in the context of results of dynamical simulations of a low mass planet interacting with a planetesimal belt (Reche et al., 2008).

5.5 Results

5.5.1 Disk flux and size

The CSO map is given in Figure 5.2, and the measured flux for the disk integrated over the 3σ contour is 89 ± 26 mJy. The 350 μm map of the HR 8799 debris disk reveals emission that is extended compared to the maps of the bright point source calibrators taken on the same night. Only spatially resolved images of dust with small β values are capable of distinguishing the location of the dust based on the structure, since the SED solution for the disk radius is degenerate with dust properties such as a_{min}. The inner disk is not resolved, but set at 100 AU, based on previous simulations of orbital stability (Moro-Martín et al., 2010) and the mass of the outermost planet.

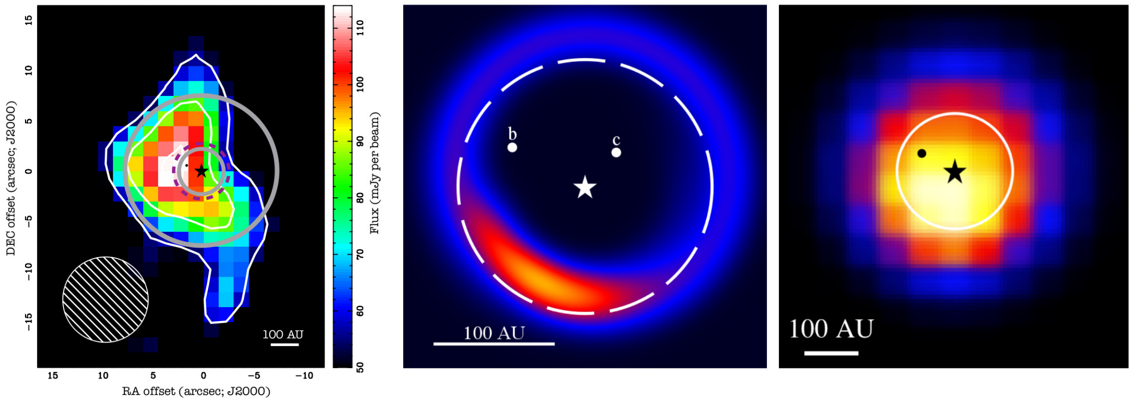

FIGURE 5.2: **(left)** The CSO 350 μm image with the positions of the star (black star) and outermost planet (dot) indicated. The solid circles trace the locations of the inner and outer edge of the Kuiper belt used in the SED model and the dashed line shows the expected position of the 2:1 resonance. **(middle)** The disk surface density map from the simulation. The semi-major axis centers around the 2:1 resonance with the outer planet (dashed line), and the moderate eccentricities (∼0.3) of the dust grains explain their displacement from the circular path. **(right)** The same numerical simulation convolved with an $8''.5$ Gaussian to compare with the brightness peak position in the CSO map of the same resolution. The 2:1 resonance is indicated by the white line.

To estimate the size of the dust belt, a series of MCFOST models were run with a range of outer disk radii. All models simultaneously matched the 350 μm flux and previously measured fluxes reported in Su et al. (2009) or compiled by Reidemeister et al. (2009), plotted in Figure 5.3. Although the map resolution and sensitivity are limited, the disk outer radius is consistent with ~300 AU, and this radius is marked on Figure map, along with the assumed inner radius. The 350 μm emission is largely confined within a radius of 300 AU. Further details on the set of simulated 350 μm images from MCFOST are given in Figure 5.4. A radius of 200 AU results in a more compact structure inconsistent with the data, though higher sensitivity maps will be required to rule out disks much larger than 300 AU, since the surface brightness of the most extended emission is beyond the dynamic range of the CSO data.

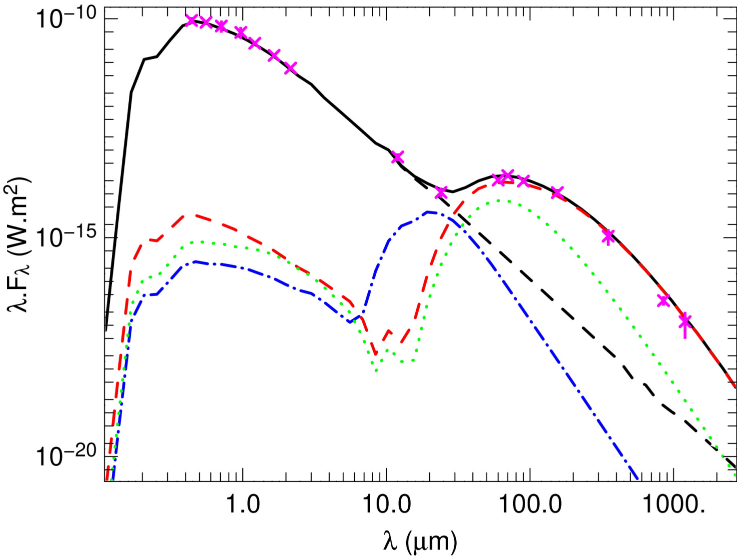

FIGURE 5.3: The fluxes of the HR 8799 star/disk system are plotted as a function of wavelength (purple crosses), along with the SED model with the parameters listed in Table 5.1 (solid black line). Contributions from the stellar flux (black dashed line) and scattered and emitted light from the asteroid belt (blue dash-dot line), the Kuiper belt (dashed red line), and outer halo (green dotted line).

5.5.2 Disk structure

The observed disk morphology is compared with two types of models of the disk structure – a symmetric dust distribution simulated with MCFOST and an asymmetric dust distribution governed by gravitational interactions and radiation pressure. Assuming a symmetric circular ring for the disk described in Table 5.1, the effect of changing the inclination is explored in Figure 5.4. As the emission is optically thin at 350 μm (unlike scattered light images at shorter wavelengths), the disk pattern remains symmetric as

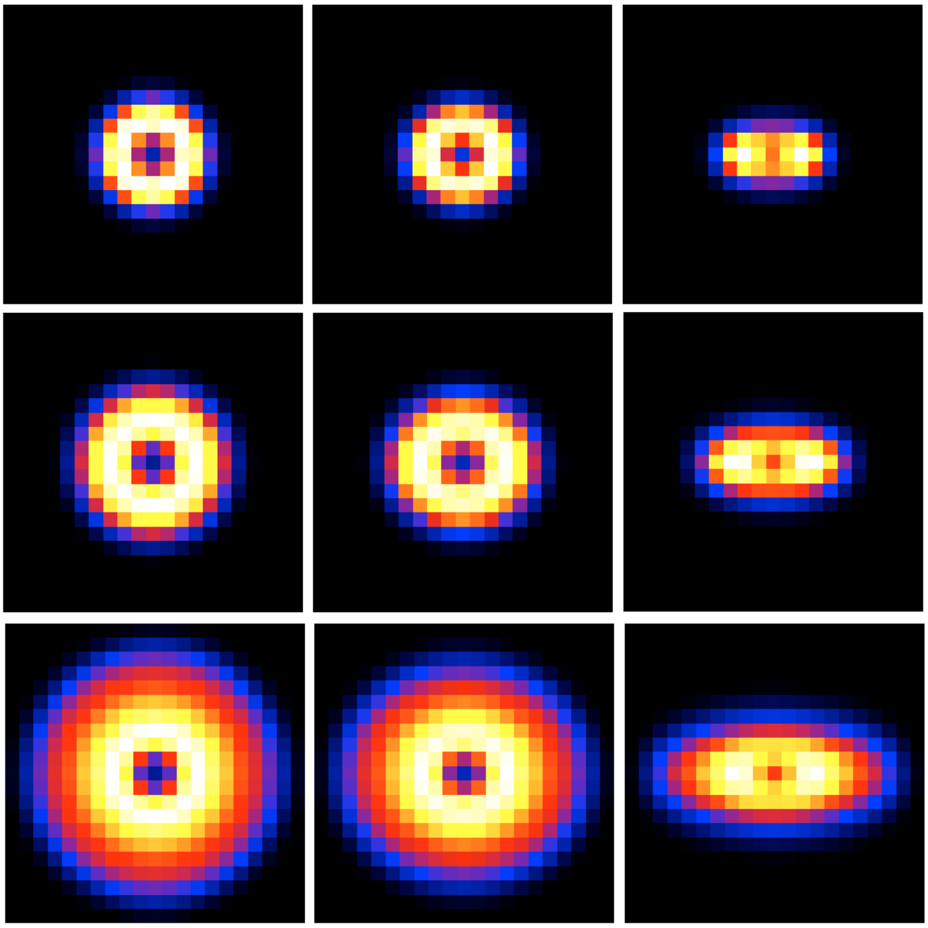

FIGURE 5.4: Model ray tracing images at a wavelength of 350 μm generated with the MCFOST code for combinations of three outer disk sizes and disk inclinations. **(top row, from left to right)** 200 AU outer disk with inclinations of 0°, 30°, and 60°. **(middle row)** 300 AU outer disk with same sequence of inclinations. **(bottom row)** 500 AU outer disk with same sequence of inclinations. Each image has a size of 1200 AU × 1200 AU and the pixels match the size of the CSO map pixels. The dynamic range is a factor of 10.

the inclination increases. Since the observed map is not well matched by these symmetric patterns, it is not possible to place a strong constraint on the disk inclination to compare with estimates from planet astrometry (Lafrenière et al., 2009), 70 μm emission (Su et al., 2009), and stability (Moro-Martín et al., 2010).

The CSO map is also compared with numerical models resulting in an asymmetric dust distribution. In addition to the extended structure, the HR 8799 disk emission at 350 μm is slightly offset from the coordinates of the host star. The distance from the star to the brightest point in the disk is $2''.1 \pm 0''.7$, or 84 ± 28AU. While the uncertainty is too large to assign a specific value to the radius of the brightest region of the disk, an estimate can be compared with the distance to the peak in surface density of the numerical simulation in Figure 5.2. A dominant one-sided arc of higher surface density describes the distribution of grains with β values on the order of 0.005 or less, as they become trapped in the 2:1 mean motion resonance (Wyatt, 2006), based on previously published simulations of migrating planets with masses up to 1 $\mathrm{M_{Jup}}$ (Wyatt, 2006). Our simulation of a planetesimal belt is a test case extending to include two higher mass planets; a similar asymmetric pattern is evident in our dust surface density map in Figure 5.2. The CSO map of the debris disk shows a structure suggestive of a single bright clump like the pattern produced by dust grains trapped in the 2:1 mean motion resonance with a planet, while the map does not reveal two distinct clumps separated by 180 degrees, as expected for material trapped in the 3:2 resonance (Wyatt, 2006). Within the uncertainty of the measurement, the radius of the brightest region of the disk is consistent with the peak in the surface density image in our simulation; a convolution of the simulated map with the CSO beam showing a similar offset is given in Figure 5.2.

Based on previous simulations, resonant trapping cannot easily explain that the brightest clump leads rather than lags the planet position, since the libration point lagging position has a higher probability to be filled for an outward migration with a planet with eccentricity greater than 0.03 (Wyatt, 2006). In our simulation of a planetesimal belt surrounding two massive planets with slow outward migration, the azimuthal angle of the bulge is subject to large scale oscillations over the course of several orbits, moving between a leading and a trailing position in a continuous manner, without crossing in front of the planet. Such an oscillating structure can be produced if the orbits of the planets become eccentric as they migrate (due to mutual interactions) and, once formed, the structure can persist even if the eccentricities of the planetary orbits are later damped.

If dynamical interactions are governing the particle spatial distribution such that the 350 μm-emitting grains are trapped in a 2:1 mean motion resonance with the outermost planet, then there are important implications for the orbital history of HR 8799b. To enhance the population of planetesimals in the resonance, orbital migration is required, although the rate of migration cannot be too high, or the trapping probability will decrease (Reche et al., 2008). Planet migration may have strongly influenced the timing and mass flux of the Late Heavy Bombardment of the terrestrial planets in the Solar System (Gomes et al., 2005), so evidence of orbital migration may be an important factor for the conditions in the as-yet unexplored terrestrial planet region in the HR 8799 system. Theoretical arguments favouring Currie et al. (2011) and rejecting Dodson-Robinson et al. (2009) orbital migration for the HR 8799 system have also been proposed. For a resonant pattern to persist, the eccentricity of the orbit of the planet needs to be low, since the libration amplitude of the planetesimals in resonance is increased as eccentricity increases, causing the distribution to become smooth (Reche et al., 2008). Numerical simulations of the HR 8799 planet system (prior to the discovery of the innermost planet (Marois et al., 2010)), have identified a set of possible stable orbital solutions, including two with low eccentricities for HR 8799b of 0.008 or 0.014 (Goździewski & Migaszewski, 2009). The clumped structure of the CSO map favours these low eccentricity solutions. For comparison, the eccentricity of the orbit of Neptune is 0.0112 and the migration of Neptune may have caused the objects to move into the resonances (Malhotra, 1993).

An alternate, non-resonant mechanism for producing a single disk clump is the presence of an outer, low mass planet on an eccentric orbit (Reche et al., 2008), an interesting possibility for a system that already includes four giant planets. In this case, the planet mass would be very low, comparable to an Earth mass, the eccentricity would be large ($\sim$0.4-0.7) and the clump would appear at apastron. The lifetime for non-resonant structures is expected to be lower, on the order of 35 Myr (Reche et al., 2008), though the recent assessment of the HR 8799 age of 30 Myr (Zuckerman et al., 2011) is within the feature lifetime, and the system is old enough to have passed from the runaway growth to the oligarchic growth phase of terrestrial planet formation, with enough time for terrestrial planet formation (Chambers, 2001).

5.6 Discussion and future prospects

The HR 8799 debris disk was first resolved in the far-IR with *Spitzer* MIPS at 70 μm, and subsequent observations with *Herschel* in the far-IR have revealed resolved observations at 70 μm, 100 μm, 160 μm, and 250 μm, as shown in Figure 5.5 (Su et al., 2009; Matthews et al., 2013). The CSO map at 350 μm has shown possible indications of dynamical sculpting of the debris disk from the gravitational influence of the outermost planet. Comparisons with observations obtained in the far-IR is complicated, since shorter wavelength observations are sensitive to small dust particles, where as observations in the submm are sensitive to dust that is large enough to trace the planetesimal distribution. Simulations of the surface density distribution of dust particles emitting at 24 μm, 70 μm, 350 μm, and 850 μm are given in Figure 5.6. At the shortest wavelength of 24 μm, a symmetric ring is expected and may be resolvable with 8m-class telescopes, though below the limit of *Spitzer*, and the 70 μm emission is more distributed than the 350 μm map. Excepting the compact background source seen to the northwest of the *Herschel* images, axisymmetric emission from the disk is witnessed in the far-IR images shown in Figure 5.5. Given the limited resolution and dynamic range of the data, these

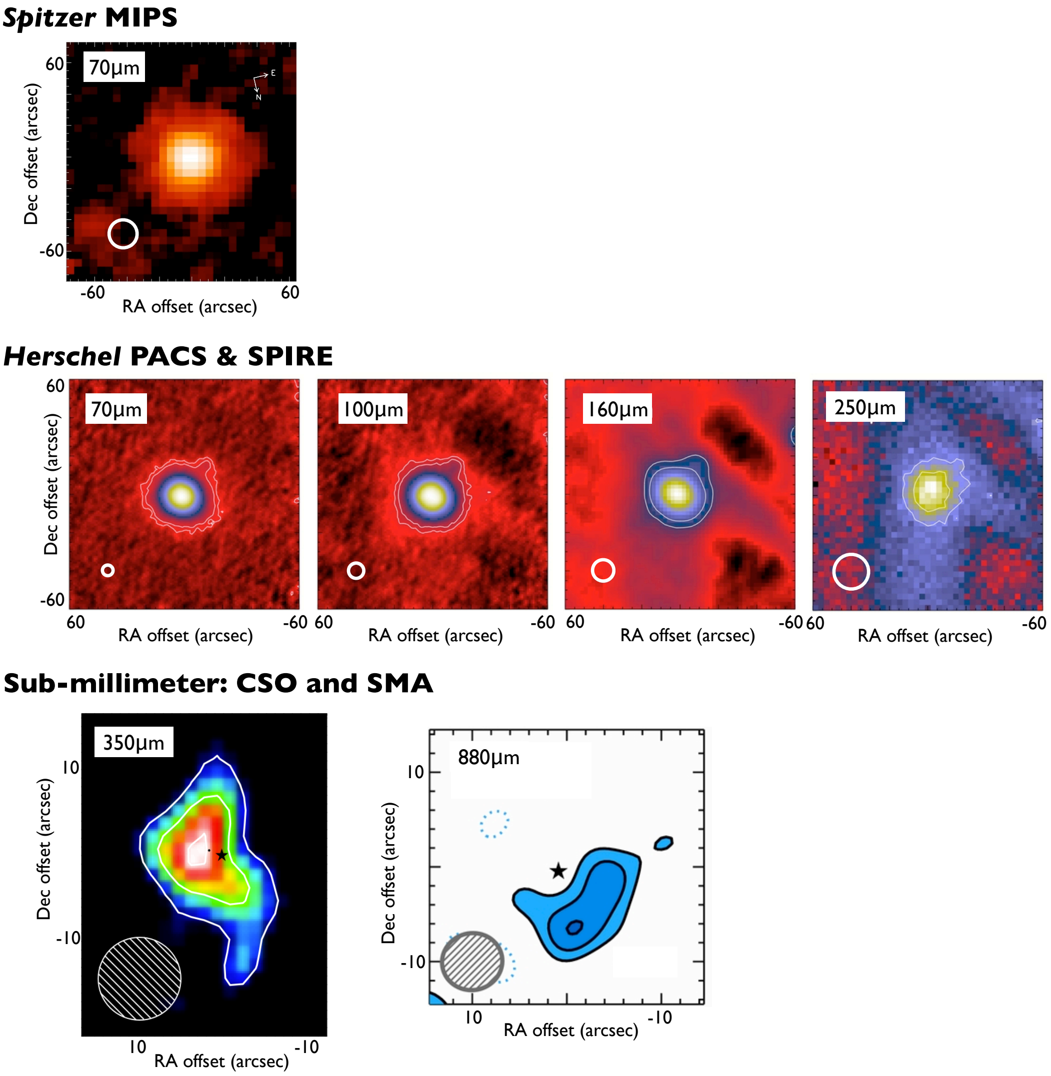

FIGURE 5.5: Resolved images of the HR 8799 debris disk obtained in the far-IR with *Spitzer* MIPS at 70 μm (**top image**; Su et al., 2009), and *Herschel* PACS and SPIRE at 70 μm, 100 μm, 160 μm, and 250 μm (**middle panel**; Matthews et al., 2013). Marginally resolved images obtained in the sub-mm are shown in the bottom panel, with the CSO at 350 μm (**bottom left**; presented here), and the SMA at 880 μm (**bottom right**; Hughes et al., 2011). The beam size at each observed wavelength is represented by the circle shown in the bottom left-hand corner of each image.

observations are consistent with numerical models in which the planetesimals are trapped in resonances (e.g., Wyatt, 2006).

Figure 5.5 also shows the interferometric map of the HR 8799 disk observed at 880 μm with the Submillimeter Array (SMA; Hughes et al., 2011). Asymmetric emission is witnessed in the morphology of the map and the emission peak position is offset compared to that seen the CSO 350 μm data. These results are consistent with the simulations of the surface density distribution from the N-body numerical models shown in Figure 5.6.

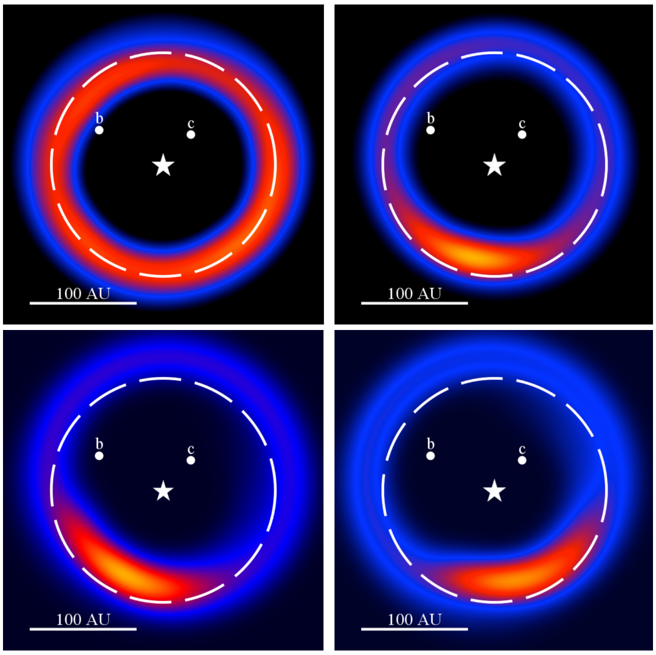

Figure 5.6: Simulations of surface density from the N-body numerical model at four wavelengths, increasing from (top) left to right: 24 μm, and 70 μm, and (bottom) from left to right: 350 μm, and 850 μm. The dynamic range is a factor of 10, and the simulation is smoothed to a resolution of $1''.5$, matching the capability of ALMA. All figures are contemporaneous in the evolution.

However, Hughes et al. (2011) attribute the asymmetry witnessed in the 880 μm map to noise features in low S/N data. ALMA observations of HR 8799 will have significantly higher sensitivity to improve the measurement of the disk structure, and will be ideal to pursue deeper, high fidelity maps for further insights into the planet formation process in this benchmark system.

Chapter 6

Future directions

Through the combination of observations with theory, pursuits in the study of circumstellar disks is being made to understand the physical processes that occur within them such as; irradiation by the central star, dispersion mechanism and planetary formation. However many questions about the structure and evolution of circumstellar disks still remain open.

This thesis has addressed disk properties that can be directly inferred from observations at the sub-millimeter wavelengths (i.e., disk mass) across a range of evolutionary stages and environmental conditions. Finally, through radiative transfer modelling procedures, the work in the thesis has addressed constraints on disk geometry such; as inclination, disk scale height, and flaring, by using diagnostic observations at far-IR wavelengths, from the first complete census of a low-mass star-forming region. The targets within this census, presented in Chapter 2 of the Taurus star-forming region, span stellar masses ranging from low-mass stars to brown dwarfs, and only a limited number possess observations at sub-millimeter wavelengths. Since the viability for planet formation depends upon key parameters, such as disk mass – of which estimations can be made through sub-millimeter observations as demonstrated in Chapters 3 and 4 – the natural questions that arise are whether the disks around these low-mass stars and brown dwarfs are capable of forming planets, and if so are the planet forming mechanisms the same across the stellar/sub-stellar boundary? Under the favoured core accretion scenario, the formation of a giant planet requires building a core of $\approx$10 $M_\oplus$ before it is able to accrete a gaseous envelope (Pollack et al., 1996). At the time of writing, the Atacama Large Millimeter/sub-millimeter Array (ALMA) will commence operations in full scientific mode, consisting of 66 antennas distributed in configurations that span separations of ∼0.001-16 km. ALMA provides over an order of magnitude improvement in sensitivity than existing instruments, and with observations at 850 μm is capable of reaching dust mass sensitivities $<M_\oplus$ at the distance of Taurus. ALMA observations of the low-mass population in Taurus will be complementary to the *Herschel* PACS far-IR data presented here, and will provide full coverage of the SEDs. ALMA observations will further enhance interpretation of *Herschel* data as the wavelength coverage (∼350 μm - mm wavelengths) probes SEDs in the Rayleigh-Jeans regime, and is sensitive to emission from larger dust grains. The physical parameters of disk properties can be investigated by radiative transfer modelling (e.g., through codes such as MCFOST; Pinte et al., 2006 – as used in Chapters 2 and 5), by fitting a large range of models to the empirical SED and obtaining probability distributions of the best-fit parameters.

Furthermore ALMA also provides dramatic improvement in both spatial angular resolution and spectral resolution, providing the capacity to detect both dust and gas emission, sensitive to the outer regions of protoplanetary disks. The mechanisms by which disks disperse material remains unknown e.g. via photoevaporation (Alexander et al., 2006), dust coagulation (Dullemond & Dominik, 2004a) or dynamical clearing (Lubow et al., 1999). Thus far, most studies that have investigated dispersion mechanisms have been limited to the inner regions of protoplanetary disks (<10 AU), and *Spitzer* surveys of near-by star-forming regions have estimated disk life times of $\lesssim$1-10 Myr (Mamajek, 2009). Analogous estimates of outer disk clearing mechanisms and timescales can be achieved through protoplanetary disk studies with ALMA. Chapter 3 presented the first sub-millimeter census of an association of T-Tauri stars in the Aquila star-forming region. Follow-up ALMA observations of this association will provide greater sensitivity limits, with higher angular resolution to further investigate the outer disk properties of these targets.

Finally, the sub-millimeter observations of the warm and cold debris disk candidates presented in Chapter 4 and the HR 8799 debris disk system presented in Chapter 5 were subject to limitations in both angular resolution and sensitivity from existing surveys and the capabilities of existing instrumentation. With the *Herschel* Space Observatory having now completed its mission and ALMA entering into full science operations, information about debris disk evolution from far-IR photometry reaching unprecedented sensitivity and angular resolution levels can be complemented by that from imaging at wavelengths from the sub-millimeter to millimeter. This broad range of wavelength coverage will revolutionise studies of debris disks providing further insight into the formation and evolution of planets and the architecture of planetary systems.

Appendix A

TBOSS survey I: extended material

Figures A.1-A.7 present the *Herschel* PACS maps of the detected targets observed under the OTC_patience_1 program, and are displayed in order of spectral evolutionary class, and spectral type. In each map the black star indicates the 2MASS position of the target. The 2MASS positions of known multiple companions are indicted by yellow triangles in the blue channel (70 μm) maps, and green triangles in the red channel (160 μm) maps. The PACS beam size is represented by the blue circle in the lower, right corner of each map.

The SEDs of the TBOSS Class I objects, multiple Class I and II systems are show in Figures A.8 and A.9 respectively. The remaining Class II objects that were not presented in Chapter 2 are shown in Figures A.10-A.11. The SEDs of the TBOSS Class II objects that were undetected in the far-IR are shown in Figure A.12. The SEDs of the TBOSS Class III objects that were undetected in the far-IR are shown in Figures A.13-A.16.

Table A.1: Observing log for the TBOSS sample observed under this program (OT1_jpatienc_1), ordered by target R.A..

2MASS	Other name	Scan ID	Cross scan ID	UT date	Tot. duration (s)	$T_{\rm int}$ on-source (s)
J04034997+2620382	XEST 06-006	1342241458	1342241459	2012 Mar 15	904	180
J04141188+2811535	...	1342241918	1342241919	2012 Mar 19	904	180
J04141458+2827580	FN Tau	1342241920	1342241921	2012 Mar 19	1129	240
J04141760+2806096	CIDA 1	1342228441	1342228442	2011 Sep 07	1129	240
J04144730+2646264	FP Tau	1342241884	1342241885	2012 Mar 19	904	180
J04144739+2803055	XEST 20-066	1342241916	1342241917	2012 Mar 19	904	180
J04151471+2800096	KPNO 1	1342241914	1342241915	2012 Mar 19	904	180
J04152409+2910434	...	1342241924	1342241925	2012 Mar 19	904	180
J04155799+2746175	...	1342241646	1342241645	2012 Mar 17	904	240
J04161210+2756385	...	1342241912	1342241913	2012 Mar 19	904	180
J04161885+2752155	...	1342241910	1342241911	2012 Mar 19	904	180
J04162725+2053091	...	1342241880	1342241881	2012 Mar 19	1129	240
J04163048+3037053	...	1342241641	1342241642	2012 Mar 17	904	180
J04163911+2858491	...	1342241922	1342241923	2012 Mar 19	904	180
J04174955+2813318	KPNO 10	1342241908	1342241909	2012 Mar 19	904	180
J04174965+2829362	V410 X-ray 1	1342241906	1342241907	2012 Mar 19	904	180
J04180796+2826036	V410 X-ray 3	1342241904	1342241905	2012 Mar 19	904	180
J04181710+2828419	V410 Anon 13	1342241902	1342241903	2012 Mar 19	904	180
J04183030+2743208	KPNO 11	1342241886	1342241887	2012 Mar 19	904	180
J04184023+2824245	V410 X-ray 4	1342241900	1342241901	2012 Mar 19	904	180

Table A.1: continued.

2MASS	Other name	Scan ID	Cross scan ID	UT date	Tot. duration (s)	T_{int} on-source (s)
J04185115+2814332	KPNO 2	1342241893	1342241892	2012 Mar 19	904	180
J04185813+2812234	IRAS 04158+2805	1342241890	1342241891	2012 Mar 19	904	180
J04190110+2819420	V410 X-ray 6	1342241894	1342241895	2012 Mar 19	904	180
J04190126+2802487	KPNO 12	1342241888	1342241889	2012 Mar 19	904	180
J04190197+2822332	V410 X-ray 5a	1342241896	1342241897	2012 Mar 19	904	180
J04193545+2827218	FR Tau	1342241898	1342241899	2012 Mar 19	904	180
J04194657+2712552	[GKH94] 41	1342242045	1342242046	2012 Mar 20	904	180
J04201611+2821325	...	1342242056	1342242057	2012 Mar 20	904	180
J04202555+2700355	...	1342242041	1342242042	2012 Mar 20	904	180
J04202583+2819237	IRAS 04173+2812	1342242054	1342242055	2012 Mar 20	904	180
J04203918+2717317	XEST 16-045	1342242043	1342242044	2012 Mar 20	904	180
J04205273+1746415	J2-157	1342241876	1342241877	2012 Mar 19	904	180
J04210795+2702204	CFHT 19	1342242039	1342242040	2012 Mar 20	904	180
J04210934+2750368	...	1342242048	1342242049	2012 Mar 20	904	180
J04213459+2701388	...	1342242037	1342242038	2012 Mar 20	904	180
J04214013+2814224	XEST 21-026	1342242052	1342242053	2012 Mar 20	904	180
J04214631+2659296	CFHT 10	1342242035	1342242036	2012 Mar 20	904	180
J04215450+2652315	...	1342242033	1342242034	2012 Mar 20	904	180
J04220007+1530248	IRAS 04191+1523 B	1342241874	1342241875	2012 Mar 19	904	180
J04221332+1934392	...	1342241878	1342241879	2012 Mar 19	904	180
J04221644+2549118	CFHT 14	1342242025	1342242026	2012 Mar 20	904	180
J04222404+2646258	XEST 11-087	1342242031	1342242032	2012 Mar 20	904	180
J04230607+2801194	...	1342242051	1342242050	2012 Mar 20	904	180
J04242090+2630511	...	1342242027	1342242028	2012 Mar 20	904	180
J04244506+2701447	J1-4423	1342242029	1342242030	2012 Mar 20	904	180
J04262939+2624137	KPNO 3	1342242060	1342242061	2012 Mar 20	904	180
J04263055+2443558	...	1342242023	1342242024	2012 Mar 20	904	180
J04265732+2606284	KPNO 13	1342242062	1342242063	2012 Mar 20	904	180
J04270739+2215037	...	1342242005	1342242006	2012 Mar 20	904	180
J04272799+2612052	KPNO 4	1342242065	1342242064	2012 Mar 20	904	180
J04274538+2357243	CFHT 15	1342242021	1342242022	2012 Mar 20	904	180
J04275730+2619183	IRAS 04248+2612	1342242066	1342242067	2012 Mar 20	904	180
...	L1521F-IRS	1342241643	1342241644	2012 Mar 17	1129	240
J04284263+2714039	...	1342243068	1342243069	2012 Mar 21	904	180
J04290068+2755033	...	1342243066	1342243067	2012 Mar 21	904	180
J04292165+2701259	IRAS 04263+2654	1342243070	1342243071	2012 Mar 21	904	180
J04294568+2630468	KPNO 5	1342243074	1342243075	2012 Mar 21	904	180
J04295422+1754041	...	1342241961	1342241962	2012 Mar 20	904	180
J04295950+2433078	CFHT 20	1342242019	1342242020	2012 Mar 20	904	180
J04302365+2359129	CFHT 16	1342242009	1342242010	2012 Mar 20	904	180
J04305171+2441475	ZZ Tau IRS	1342242017	1342242018	2012 Mar 20	904	180
J04311578+1820072	MHO 9	1342241967	1342241968	2012 Mar 20	904	180
J04311907+2335047	...	1342242007	1342242008	2012 Mar 20	904	180
J04312405+1800215	MHO 4	1342241963	1342241964	2012 Mar 20	904	180
J04312669+2703188	CFHT 13	1342243072	1342243073	2012 Mar 21	904	180
J04320329+2528078	...	1342243082	1342243083	2012 Mar 21	904	180
J04321606+1812464	MHO 5	1342241965	1342241966	2012 Mar 20	904	180
J04322210+1827426	MHO 6	1342241969	1342241970	2012 Mar 20	904	180
J04322329+2403013	...	1342242011	1342242012	2012 Mar 20	904	180
J04322415+2251083	...	1342242003	1342242004	2012 Mar 20	904	180
J04322627+1827521	MHO 7	1342243094	1342243095	2012 Mar 21	904	180
J04324938+2253082	JH 112 B	1342242001	1342242002	2012 Mar 20	904	180
J04325026+2422115	...	1342242015	1342242016	2012 Mar 20	904	180
J04325119+1730092	LH 0429+17	1342241957	1342241958	2012 Mar 20	904	180
J04330197+2421000	MHO 8	1342242013	1342242014	2012 Mar 20	904	180
J04330781+2616066	KPNO 14	1342243076	1342243077	2012 Mar 21	904	180
J04332621+2245293	XEST 17-036	1342241999	1342242000	2012 Mar 20	904	180
J04334171+1750402	...	1342241959	1342241960	2012 Mar 20	904	180
J04334291+2526470	...	1342243084	1342243085	2012 Mar 21	904	180
J04334465+2615005	...	1342243078	1342243079	2012 Mar 21	904	180
J04335245+2612548	...	1342243081	1342243080	2012 Mar 21	904	180
J04335252+2256269	XEST 17-059	1342241997	1342241998	2012 Mar 20	904	180
J04341527+2250309	CFHT 1	1342241995	1342241996	2012 Mar 20	904	180
J04344544+2308027	...	1342241992	1342241991	2012 Mar 20	904	180
J04350850+2311398	CFHT 11	1342241993	1342241994	2012 Mar 20	904	180
J04354183+2234115	KPNO 8	1342241977	1342241978	2012 Mar 20	904	180
J04354203+2252226	XEST 08-033	1342241983	1342241984	2012 Mar 20	904	180
J04354526+2737130	...	1342243466	1342243467	2012 Mar 24	904	180
J04355143+2249119	KPNO 9	1342241979	1342241980	2012 Mar 20	904	180
J04355209+2255039	XEST 08-047	1342241989	1342241990	2012 Mar 20	904	180
J04355286+2250585	XEST 08-049	1342241981	1342241982	2012 Mar 20	904	180
J04361030+2159364	...	1342241975	1342241976	2012 Mar 20	904	180
J04361038+2259560	CFHT 2	1342241987	1342241988	2012 Mar 20	904	180
J04362151+2351165	...	1342242072	1342242073	2012 Mar 20	904	180

Table A.1: continued.

2MASS	Other name	Scan ID	Cross scan ID	UT date	Tot. duration (s)	T_{int} on-source (s)
J04363893+2258119	CFHT 3	1342241985	1342241986	2012 Mar 20	904	180
J04373705+2331080	...	1342243088	1342243089	2012 Mar 21	904	180
J04380083+2558572	ITG 2	1342243458	1342243459	2012 Mar 24	904	180
J04381486+2611399	...	1342243462	1342243463	2012 Mar 24	904	180
J04381630+2326402	...	1342243090	1342243091	2012 Mar 21	904	180
J04382134+2609137	GM Tau	1342243460	1342243461	2012 Mar 24	904	180
J04385859+2336351	...	1342243434	1342243435	2012 Mar 24	904	180
J04385871+2323595	...	1342243092	1342243093	2012 Mar 21	904	180
J04390163+2336029	...	1342243086	1342243087	2012 Mar 21	904	180
J04390396+2544264	CFHT 6	1342243456	1342243457	2012 Mar 24	904	180
J04390637+2334179	...	1342243432	1342243433	2012 Mar 24	904	180
J04393364+2359212	...	1342243438	1342243439	2012 Mar 24	904	180
J04394488+2601527	ITG 15	1342243453	1342243452	2012 Mar 24	904	180
J04394748+2601407	CFHT 4	1342243454	1342243455	2012 Mar 24	904	180
J04400067+2358211	...	1342243436	1342243437	2012 Mar 24	904	180
J04400174+2556292	...	1342243450	1342243451	2012 Mar 24	904	180
J04403979+2519061	...	1342243442	1342243443	2012 Mar 24	904	180
J04410424+2557561	Haro 6-32	1342243449	1342243448	2012 Mar 24	904	180
J04411078+2555116	ITG 34	1342243446	1342243447	2012 Mar 24	904	180
J04414489+2301513	...	1342240750	1342240751	2012 Mar 07	904	180
J04414565+2301580	...	1342243430	1342243431	2012 Mar 24	904	180
J04414825+2534304	...	1342243444	1342243445	2012 Mar 24	904	180
J04422101+2520343	CIDA 7	1342243440	1342243441	2012 Mar 24	904	180
J04432023+2940060	CIDA 14	1342243472	1342243473	2012 Mar 24	904	180
J04464260+2459034	RXJ 04467+2459	1342228864	1342228865	2011 Sep 18	904	180
J04484189+1703374	...	1342243428	1342243429	2012 Mar 24	904	180
J04520668+3047175	IRAS 04489+3042	1342243492	1342243493	2012 Mar 24	904	180
J04552333+3027366	...	1342243484	1342243485	2012 Mar 24	904	180
J04554046+3039057	...	1342243488	1342243489	2012 Mar 24	904	180
J04554535+3019389	...	1342250330	1342250331	2012 Aug 26	904	180
J04554757+3028077	...	1342242762	1342242763	2012 Mar 30	1129	240
J04554801+3028050	...	1342243482	1342243483	2012 Mar 24	904	180
J04554969+3019400	...	1342243480	1342243481	2012 Mar 24	904	180
J04555288+3006523	...	1342243477	1342243476	2012 Mar 24	904	180
J04555605+3036209	XEST 26-062	1342243486	1342243487	2012 Mar 24	904	180
J04555636+3049374	...	1342243490	1342243491	2012 Mar 24	904	180
J04574903+3015195	...	1342243478	1342243479	2012 Mar 24	904	180
J05061674+2446102	CIDA 10	1342242686	1342242687	2012 Mar 29	904	180
J05064662+2104296	...	1342242684	1342242685	2012 Mar 29	904	180
J05075496+2500156	CIDA 12	1342242688	1342242689	2012 Mar 29	904	180

TABLE A.2: Observing log for the TBOSS sample observed with *Herschel* PACS under other programs. Targets are ordered by target R.A..

2MASS	Other name	Scan ID	Cross scan ID	UT date	Tot. duration (s)	Program ID
J04131414+2819108	LkCa 1	1342216513	1342216514	2011 Mar 21	552	KPOT_bdent_1
		(1342216515)	(1342216516)	2011 Mar 21	552	KPOT_bdent_1
J04150515+2808462	CIDA 2	1342216529	1342216530	2011 Mar 21	552	KPOT_bdent_1
		(1342216531)	(1342216532)	2011 Mar 21	552	KPOT_bdent_1
J04233539+2503026	FU Tau A	(1342227304)	(1342227305)	2011 Aug 24	21222	KPGT_pandre_1
J04233573+2502596	FU Tau B	(1342227304)	(1342227305)	2011 Aug 24	21222	KPGT_pandre_1
J04242646+2649503	CFHT 9	1342227059	1342227060	2011 Aug 21	2690	GT1_pharve01_2
J04292071+2633406	J1-507	1342227979	1342227980	2011 Sep 04	552	KPOT_bdent_1
		(1342227981)	(1342227982)	2011 Sep 04	552	KPOT_bdent_1
J04292971+2616532	FW Tau A+B+C	1342227987	1342227988	2011 Sep 04	552	KPOT_bdent_1
		(1342227989)	(1342227990)	2011 Sep 04	552	KPOT_bdent_1
J04300724+2608207	KPNO 6	1342227012	1342227013	2011 Aug 21	3140	GT1_pharve01_2
J04305718+2556394	KPNO 7	1342227999	1342228000	2011 Sep 04	3140	GT1_pharve01_2
J04312382+2410529	V927 Tau A+B	1342227055	1342227056	2011 Aug 21	552	KPOT_bdent_1
		(1342227057)	(1342227058)	2011 Aug 21	552	KPOT_bdent_1
J04313613+1813432	LkHa 358	1342228928	1342228929	2011 Sep 19	552	KPOT_bdent_1
		(1342228930)	(1342228931)	2011 Sep 19	552	KPOT_bdent_1
J04315844+2543299	J1-665	1342228001	1342228002	2011 Sep 04	552	KPOT_bdent_1
		(1342228003)	(1342228004)	2011 Sep 04	552	KPOT_bdent_1
J04321786+2422149	CFHT 7	(1342228005)	(1342228006)	2011 Sep 04	39224	KPGT_pandre_1
J04323028+1731303	GG Tau Ba+Bb	1342228940	1342228941	2011 Sep 19	552	KPOT_bdent_1
		(1342228942)	(1342228943)	2011 Sep 19	552	KPOT_bdent_1
J04330945+2246487	CFHT 12	1342227013	1342227014	2011 Aug 21	3140	GT1_pharve01_2
J04353536+2408266	IRAS 04325+2402 C	(1342228005)	(1342228006)	2011 Sep 04	39224	KPGT_pandre_1

Notes. The observations listed were performed with the PACS photometer Blue1 channel (70 μm) and the Red channel (160 μm). For the scan ID numbers within parenthesis, observations were performed with the PACS photometer Blue2 channel (100 μm) and the Red channel (160 μm).

Table A.3: Best-fit disk parameters of the transition disk targets

	Zone 1								Zone 2							
Target	$R_{\rm in}$ (AU)	$R_{\rm out}$ (AU)	H_0 (AU)	β	p	$a_{\rm min}$ (μm)	$a_{\rm max}$ (μm)	$M_{\rm disk}$ ($M_\odot$)	$R_{\rm in}$ (AU)	$R_{\rm out}$ (AU)	H_0 (AU)	β	p	$a_{\rm min}$ (μm)	$a_{\rm max}$ (μm)	$M_{\rm disk}$ ($M_\odot$)
FP Tau	0.04	50	5	1.30	-1.0	0.03	3000	7E-08	100	200	10	1.30	-1.0	10.00	3000	7E-06
V410 X-ray 6	2.00	10	8	1.35	-1.0	0.03	50	2E-09	50	200	1	1.35	-1	0.03	1000	1E-05
J04210934+2750368	0.50	10	1	1.35	-1.0	0.03	1	2E-09	15	200	15	1.35	-1	0.50	2000	2E-06
J04284263+2714039	0.03	10	1	1.35	-1.0	0.03	1	2E-09	30	200	10	1.35	-1	0.50	2000	2E-06
J04403979+2519061	3.00	10	5	1.35	-1.0	0.03	10	2E-09	15	200	15	1.35	-1	0.50	2000	2E-06
FW Tau	80.00	100	1	1.00	-1.0	0.03	1	3E-08	150	200	1.0	1.00	-1.0	0.03	1000	3E-06
J04161210+2756385	2.00	10	3	1.35	-1.0	0.03	100	2E-09	100	200	3	1.35	-1	0.03	1000	1E-05
MHO 6	2.00	30	4	1.35	-1.0	0.03	1000	3E-08	100	200	3	1.35	-1	0.03	1000	3E-05
J04202555+2700355	0.10	5	10	1.35	-1.0	0.03	10	2E-09	15	200	15	1.35	-1	0.50	1000	2E-05
J04213459+2701388	0.50	10	1	1.35	-1.0	0.03	1	2E-09	15	200	15	1.35	-1	0.50	2000	2E-06
J04295422+1754041	0.50	50	5	1.30	-1.0	0.03	3000	3E-08	100	200	10	1.30	-1.0	0.03	100	8E-07
XEST 17-036	50.00	100	10	1.13	-1.0	0.10	1000	8E-09	150	200	1	1.13	-1	0.03	1000	8E-07
XEST 08-033	100.00	120	1	1.13	-1.0	0.10	1000	8E-09	150	200	1	1.13	-1	0.03	1000	8E-07

Table A.4: TBOSS flux density compilation: optical - mid-IR wavelengths.

2MASS	Other name	R_C	I_C	J	H	K	W1	[3.6]	Ref
J04034997+2620382	XEST 06-006			7.8 ± 0.1	8.8 ± 0.2	7.7 ± 0.1	4.4 ± 0.1		
J04131414+2819108	LkCa 1	28.9 ± 1.8		222 ± 4	291 ± 6	237 ± 5	116 ± 2	112 ± 2	9, 1
J04141188+2811535	...			8.7 ± 0.2	12 ± 0.2	14.7 ± 0.3	13.6 ± 0.2	12.1 ± 0.2	1
J04141458+2827580	FN Tau	3.9 ± 0.2		260 ± 5	349 ± 7	353 ± 7	316 ± 5	280 ± 4	9, 1
J04141760+2806096	CIDA 1		4.7 ± 0.1	32.5 ± 0.6	60 ± 1	75 ± 1	75 ± 1	106 ± 2	4, 1
J04144730+2646264	FP Tau	25.2 ± 1.6	75 ± 2	175 ± 3	219 ± 4	188 ± 4	138 ± 2	138 ± 2	9, 1
J04144739+2803055	XEST 20-066			77 ± 1	88 ± 2	72 ± 1	38.5 ± 0.6	37.2 ± 0.5	1
J04150515+2808462	CIDA 2			144 ± 3	175 ± 3	154 ± 3	82 ± 1	83 ± 1	1
J04151471+2800096	KPNO 1		0.123 ± 0.002	1.45 ± 0.03	2.05 ± 0.04	2.07 ± 0.04	1.25 ± 0.02	1.49 ± 0.02	2, 5, 1
J04152409+2910434	...			5.4 ± 0.1	7.2 ± 0.1	7.6 ± 0.1	4.6 ± 0.1	5.2 ± 0.1	1
J04155799+2746175	...			32 ± 0.6	41.3 ± 0.8	41.1 ± 0.8	35.9 ± 0.5	36.7 ± 0.5	1
J04161210+2756385	...			19.7 ± 0.3	36.8 ± 0.7	49 ± 0.9	50.6 ± 0.8	51.1 ± 0.8	1
J04161885+2752155	...			15.3 ± 0.3	19.9 ± 0.4	19.2 ± 0.4	11.9 ± 0.2	12 ± 0.2	1
J04162725+2053091	...			24.1 ± 0.4	26.3 ± 0.5	23.9 ± 0.5	13.1 ± 0.2	13.8 ± 0.2	1
J04163048+3037053	...			5.7 ± 0.1	6.6 ± 0.1	6 ± 0.1	3.24 ± 0.05	3.4 ± 0.1	1
J04163911+2858491	...			13.1 ± 0.2	18.9 ± 0.4	20.5 ± 0.4	17.5 ± 0.3	18.4 ± 0.3	1
J04174955+2813318	KPNO 10		6.3 ± 0.1	28 ± 0.5	35.8 ± 0.7	32.1 ± 0.6	8.8 ± 0.1	13.6 ± 0.2	2, 4, 1
J04174965+2829362	V410 X-ray 1	1.8 ± 0.1	7.8 ± 0.2	62 ± 1	131 ± 3	155 ± 3	133 ± 2	136 ± 2	7, 4, 1
J04180796+2826036	V410 X-ray 3	0.81 ± 0.04	6.1 ± 0.1	38.4 ± 0.7	48.3 ± 0.9	44.2 ± 0.8	25.7 ± 0.4	28.3 ± 0.4	7, 5, 1
J04181710+2828419	V410 Anon 13	0.057 ± 0.002	0.62 ± 0.01	10.5 ± 0.2	22.2 ± 0.4	27.6 ± 0.5	19.5 ± 0.3	22.9 ± 0.3	6, 7, 5, 1
J04183030+2743208	KPNO 11		8.3 ± 0.2	28.1 ± 0.5	31.8 ± 0.6	26.4 ± 0.5	14.9 ± 0.2	15.3 ± 0.2	4, 1
J04184023+2824245	V410 X-ray 4		0.0277 ± 0.0004	5.6 ± 0.1	42.2 ± 0.8	89 ± 2	64 ± 1	82 ± 1	4, 1
J04185115+2814332	KPNO 2		0.64 ± 0.01	4.3 ± 0.1	5.2 ± 0.1	5.3 ± 0.1	3.4 ± 0.1	3.7 ± 0.1	2, 5, 1
J04185813+2812234	IRAS 04158+2805	0.115 ± 0.005	0.68 ± 0.01	4.9 ± 0.1	11.8 ± 0.2	22.6 ± 0.4	51 ± 0.8	56.8 ± 0.8	7, 4, 1
J04190110+2819420	V410 X-ray 6	1.8 ± 0.1	10.3 ± 0.2	98 ± 2	148 ± 3	149 ± 3	79 ± 1	86 ± 1	7, 4, 1
J04190126+2802487	KPNO 12		0.0339 ± 0.0005	0.48 ± 0.01	0.66 ± 0.01	0.71 ± 0.01	0.61 ± 0.01	0.75 ± 0.01	4, 1
J04190197+2822332	V410 X-ray 5a	0.22 ± 0.01	1.81 ± 0.04	25.5 ± 0.4	50 ± 1	58 ± 1	35.2 ± 0.5	39 ± 0.6	7, 4, 1
J04193545+2827218	FR Tau			66 ± 1	73 ± 1	68 ± 1	47.6 ± 0.7	48.4 ± 0.7	1
J04194657+2712552	[GKH94] 41			<0.1	2.5 ± 0.05	11.7 ± 0.2	15 ± 0.2	27.3 ± 0.4	1
J04201611+2821325	...			4.9 ± 0.1	5.8 ± 0.1	6.4 ± 0.1	4.9 ± 0.1	5.3 ± 0.1	1
J04202555+2700355	...			11.4 ± 0.2	16.1 ± 0.3	16.6 ± 0.3	10.4 ± 0.2	11.8 ± 0.2	1
J04202583+2819237	IRAS 04173+2812			1.18 ± 0.02	4.4 ± 0.1	13.7 ± 0.3	50.8 ± 0.8	59.8 ± 0.9	1
J04203918+2717317	XEST 16-045			101 ± 2	116 ± 2	100 ± 2	56 ± 0.8	49.7 ± 0.7	1
J04205273+1746415	J2-157			35.9 ± 0.6	39.3 ± 0.8	32.6 ± 0.6	18.2 ± 0.3	18.7 ± 0.3	1
J04210795+2702204	CFHT 19		0.62 ± 0.01	4.6 ± 0.1	15.3 ± 0.3	40.4 ± 0.8	194 ± 3	205 ± 3	2, 1

Table A.4: continued.

2MASS	Other name	R_C	I_C	J	H	K	W1	[3.6]	Ref
J04210934+2750368	...			51.4 ± 0.9	56 ± 1	47.9 ± 0.9	30.9 ± 0.5	28.1 ± 0.4	1
J04213459+2701388	...			27.8 ± 0.5	42.1 ± 0.8	44.6 ± 0.8	29.4 ± 0.4	30.5 ± 0.4	1
J04214013+2814224	XEST 21-026			27 ± 0.5	29.9 ± 0.6	25.8 ± 0.5	14.6 ± 0.2	15.7 ± 0.2	1
J04214631+2659296	...		0.46 ± 0.01	4.7 ± 0.1	8.3 ± 0.2	9.3 ± 0.2	6.2 ± 0.1	6.9 ± 0.1	2, 1
J04215450+2652315	...			0.97 ± 0.02	1.62 ± 0.03	1.83 ± 0.03	1.21 ± 0.02	1.52 ± 0.02	1
J04220007+1530248	IRAS 04191+1523 B			0.37 ± 0.01^a	11.7 ± 0.2^a	20.9 ± 0.4^a	3.7 ± 0.1	3.8 ± 0.1	1
J04221332+1934392	...			11.4 ± 0.2	15.4 ± 0.3	16.4 ± 0.3	9.7 ± 0.1	11 ± 0.2	1
J04221644+2549118	...		1.44 ± 0.03	9.5 ± 0.2	11.6 ± 0.2	11.2 ± 0.2	6.8 ± 0.1	7.5 ± 0.1	2, 1
J04222404+2646258	XEST 11-087			59 ± 1	86 ± 2	82 ± 2	43.7 ± 0.7	46.6 ± 0.7	1
J04230607+2801194	...			20.2 ± 0.4	23.2 ± 0.5	22 ± 0.4	14.8 ± 0.2	16.3 ± 0.2	1
J04233539+2503026	FU Tau A			78 ± 1	108 ± 2	124 ± 2	111 ± 2	130 ± 2	1
J04233573+2502596	FU Tau B			1.54 ± 0.03	2.8 ± 0.1	3.1 ± 0.1	111 ± 2	2.71 ± 0.05	1
J04242090+2630511	...			6.4 ± 0.1	7.7 ± 0.2	7.1 ± 0.1	4.9 ± 0.1	5.4 ± 0.1	1
J04242646+2649503	CFHT 9		1.85 ± 0.04	11.2 ± 0.2	13.6 ± 0.3	13.1 ± 0.2	8.7 ± 0.1	10.1 ± 0.1	2, 1
J04244506+2701447	J1-4423			46.4 ± 0.8	53 ± 1	43.7 ± 0.8	23.5 ± 0.4	23.8 ± 0.3	1
J04262939+2624137	KPNO 3		1.25 ± 0.02	7.5 ± 0.1	10.2 ± 0.2	9.8 ± 0.2	7.4 ± 0.1	7.9 ± 0.1	5, 1
J04263055+2443558	...			2.17 ± 0.04	2.7 ± 0.1	2.9 ± 0.1	2.2 ± 0.03	2.63 ± 0.04	1
J04265732+2606284	KPNO 13		8.4 ± 0.2	49 ± 0.9	87 ± 2	98 ± 2	83 ± 1	94 ± 1	4, 1
J04270739+2215037	...			19.6 ± 0.3	22.4 ± 0.4	20.2 ± 0.4	11.6 ± 0.2	12.3 ± 0.2	1
J04272799+2612052	KPNO 4	0.019 ± 0.001	0.081 ± 0.001	1.6 ± 0.03	2.51 ± 0.05	3.2 ± 0.1	2.35 ± 0.04	2.68 ± 0.04	1, 2, 5, 1
J04274538+2357243	...		0.17 ± 0.003	1.7 ± 0.03	2.07 ± 0.04	2.23 ± 0.04	1.3 ± 0.02	1.47 ± 0.02	2, 1
J04275730+2619183	IRAS 04248+2612			35.9 ± 0.6^a	75 ± 1^a	85 ± 2^a	36.7 ± 0.5	64 ± 1	1
...	L1521F-IRS			<0.05	<0.4	0.74 ± 0.02	0.205 ± 0.003	0.66 ± 0.01	1
J04284263+2714039	...			22.9 ± 0.4	38.3 ± 0.7	43.8 ± 0.8	37.8 ± 0.6	37.4 ± 0.6	1
J04290068+2755033	...			3.9 ± 0.1	4.8 ± 0.1	4.8 ± 0.1	3.14 ± 0.05	3.5 ± 0.1	1
J04292071+2633406	J1-507			188 ± 3	237 ± 5	203 ± 4	109 ± 2	109 ± 2	1
J04292165+2701259	IRAS 04263+2654		3.6 ± 0.1	76 ± 1	163 ± 3	216 ± 4	153 ± 2	166 ± 2	2, 1
J04292971+2616532	FW Tau A+B+C			117 ± 2	138 ± 3	117 ± 2	65 ± 1	67 ± 1	1
J04294568+2630468	KPNO 5	0.071 ± 0.003	2.37 ± 0.05	14 ± 0.2	17.5 ± 0.3	16.2 ± 0.3	10 ± 0.1	10.7 ± 0.2	1, 5, 1
J04295422+1754041	...			13.9 ± 0.2	21.2 ± 0.4	26 ± 0.5	28.3 ± 0.4		
J04295950+2433078	CFHT 20		2.33 ± 0.05	33.8 ± 0.6	63 ± 1	79 ± 2	73 ± 1	69 ± 1	2, 1
J04300724+2608207	KPNO 6	0.018 ± 0.001	0.185 ± 0.003	1.6 ± 0.03	2.15 ± 0.04	2.23 ± 0.04	1.48 ± 0.02	1.64 ± 0.02	1, 2, 5, 1
J04302365+2359129	...		0.175 ± 0.003	1.65 ± 0.03	2.05 ± 0.04	2.21 ± 0.04	1.24 ± 0.02	1.46 ± 0.02	2, 1
J04305171+2441475	ZZ Tau IRS		1.06 ± 0.02	11.6 ± 0.2	27.3 ± 0.5	50 ± 1	78 ± 1	161 ± 2	2, 1
J04305718+2556394	KPNO 7		0.35 ± 0.01	2.48 ± 0.04	3 ± 0.1	3.3 ± 0.1	2.27 ± 0.03	2.59 ± 0.04	5, 1

Table A.4: continued.

2MASS	Other name	R_C	I_C	J	H	K	W1	[3.6]	Ref
J04311578+1820072	MHO 9	3 ± 0.2	16.8 ± 0.4	52.3 ± 0.9	62 ± 1	50 ± 1	26.7 ± 0.4	27.1 ± 0.4	7, 4, 1
J04311907+2335047	...			6.3 ± 0.1	8.4 ± 0.2	8.8 ± 0.2	5.5 ± 0.1	6.1 ± 0.1	1
J04312382+2410529	V927 Tau A+B	14.2 ± 0.9	66 ± 2	205 ± 4	243 ± 5	207 ± 4	109 ± 2	110 ± 2	9, 1
J04312405+1800215	MHO 4	0.66 ± 0.03	4.8 ± 0.1	34.8 ± 0.6	43.8 ± 0.9	39.5 ± 0.8	22.4 ± 0.3	25.2 ± 0.4	7, 4, 1
J04312669+2703188	...		0.176 ± 0.003	1.87 ± 0.03	2.7 ± 0.1	2.8 ± 0.1	1.86 ± 0.03	2.01 ± 0.03	2, 1
J04315844+2543299	J1-665			93 ± 2	120 ± 2	100 ± 2	51.3 ± 0.8	53 ± 0.8	1
J04320329+2528078	...			32.8 ± 0.6	36.9 ± 0.7	34.3 ± 0.7	20.1 ± 0.3	21.9 ± 0.3	1
J04321606+1812464	MHO 5	1.3 ± 0.1	8.3 ± 0.2	59 ± 1	71 ± 1	63 ± 1	45.2 ± 0.7	53.5 ± 0.8	7, 4, 1
J04321786+2422149	CFHT 7	0.69 ± 0.03	5.7 ± 0.1	38.6 ± 0.7	49 ± 1	46.9 ± 0.9	27.4 ± 0.4	29.8 ± 0.4	1, 2, 1
J04322210+1827426	MHO 6	1.5 ± 0.1	7.7 ± 0.2	33 ± 0.6	40.1 ± 0.8	36.7 ± 0.7	25.7 ± 0.4	26.7 ± 0.4	7, 4, 1
J04322329+2403013	...			18.6 ± 0.3	21.6 ± 0.4	19.6 ± 0.4	12 ± 0.2	12 ± 0.2	1
J04322415+2251083	...			36 ± 0.6	47.8 ± 0.9	40.9 ± 0.8	26.8 ± 0.4	28.1 ± 0.4	1
J04322627+1827521	MHO 7	2.9 ± 0.2	13.6 ± 0.3	57 ± 1	73 ± 1	57 ± 1	30.5 ± 0.5	31.7 ± 0.5	7, 4, 1
J04323028+1731303	GG Tau Ba+Bb			60 ± 1	71 ± 1	68 ± 1	775 ± 12	58.7 ± 0.9	1
J04324938+2253082	JH112 B			58 ± 1	122 ± 2	140 ± 3	104 ± 2	113 ± 2	1
J04325026+2422115	...		0.078 ± 0.001	4.2 ± 0.1	13.2 ± 0.3	20.5 ± 0.4	14.3 ± 0.2	19.1 ± 0.3	2, 1
J04325119+1730092	LH 0429+17			2.12 ± 0.04	2.6 ± 0.1	2.52 ± 0.05	1.55 ± 0.02		
J04330197+2421000	MHO 8	1.6 ± 0.1	9 ± 0.2	72 ± 1	90 ± 2	86 ± 2	49.6 ± 0.7	53.5 ± 0.8	7, 4, 1
J04330781+2616066	KPNO 14		2.6 ± 0.1	27.5 ± 0.5	49 ± 1	52 ± 1	31.1 ± 0.5	35.4 ± 0.5	4, 1
J04330945+2246487	CFHT 12		0.8 ± 0.01	8.7 ± 0.2	14.2 ± 0.3	16.1 ± 0.3	12.2 ± 0.2	13.7 ± 0.2	2, 1
J04332621+2245293	XEST 17-036			30.3 ± 0.5	65 ± 1	72 ± 1	42.2 ± 0.6	43.1 ± 0.6	1
J04334171+1750402	...			49.3 ± 0.9	57 ± 1	50 ± 0.9	29.3 ± 0.4	28.9 ± 0.4	1
J04334291+2526470	...			2.22 ± 0.04	3 ± 0.1	3.1 ± 0.1	1.96 ± 0.03	2.36 ± 0.03	1
J04334465+2615005	...			35.2 ± 0.6	72 ± 1	84 ± 2	66 ± 1	90 ± 1	1
J04335245+2612548	...			0.76 ± 0.01	1.49 ± 0.03	1.69 ± 0.03	1.27 ± 0.02	1.57 ± 0.02	1
J04335252+2256269	XEST 17-059			128 ± 2	167 ± 3	151 ± 3	83 ± 1	86 ± 1	1
J04341527+2250309	CFHT 1	0.019 ± 0.001	0.279 ± 0.005	5.1 ± 0.1	9.9 ± 0.2	12.1 ± 0.2	7.8 ± 0.1	9.3 ± 0.1	6, 1
J04344544+2308027	...			12 ± 0.2	15.9 ± 0.3	13.9 ± 0.3	8.3 ± 0.1	9 ± 0.1	1
J04350850+2311398	...		2.8 ± 0.1	15.5 ± 0.3	17.2 ± 0.3	15.4 ± 0.3	9.1 ± 0.1	9.4 ± 0.1	2, 1
J04353536+2408266	IRAS 04325+2402 C			0.57 ± 0.01	25.6 ± 0.5	78 ± 1	36.4 ± 0.5	1.12 ± 0.02	1
J04354183+2234115	KPNO 8		2.33 ± 0.05	10.6 ± 0.2	11.6 ± 0.2	10.7 ± 0.2	6.1 ± 0.1	6.4 ± 0.1	5, 1
J04354203+2252226	XEST 08-033			50.3 ± 0.9	71 ± 1	67 ± 1		38.8 ± 0.6	1
J04354526+2737130	...			1.57 ± 0.03	2.06 ± 0.04	2.18 ± 0.04	1.3 ± 0.02	1.59 ± 0.02	1
J04355143+2249119	KPNO 9		0.08 ± 0.001	1.03 ± 0.02	1.4 ± 0.03	1.41 ± 0.03	0.87 ± 0.01	1.01 ± 0.01	5, 1
J04355209+2255039	XEST 08-047			47.7 ± 0.8	83 ± 2	79 ± 2	42.2 ± 0.6	43.3 ± 0.6	1

Table A.4: continued.

2MASS	Other name	R_C	I_C	J	H	K	W1	[3.6]	Ref
J04355286+2250585	XEST 08-049			64 ± 1	92 ± 2	84 ± 2	47.9 ± 0.7	47.9 ± 0.7	1
J04361030+2159364	...			1.81 ± 0.03	2.32 ± 0.05	2.32 ± 0.04	1.47 ± 0.02	1.81 ± 0.03	1
J04361038+2259560	CFHT 2	0.035 ± 0.001	0.48 ± 0.01	5 ± 0.1	8 ± 0.2	9 ± 0.2	6 ± 0.1	6.5 ± 0.1	6, 5, 1
J04362151+2351165	...			8.6 ± 0.2	9.9 ± 0.2	8.4 ± 0.2	5.1 ± 0.1	5 ± 0.1	1
J04363893+2258119	CFHT 3	0.032 ± 0.001	0.45 ± 0.01	5.2 ± 0.1	7.3 ± 0.1	7.5 ± 0.1	4.9 ± 0.1	5.5 ± 0.1	6, 5, 1
J04373705+2331080	...			0.177 ± 0.004	0.36 ± 0.01	0.45 ± 0.01	0.5 ± 0.01	0.61 ± 0.01	1
J04380083+2558572	ITG 2	0.025 ± 0.001	3.3 ± 0.1	38.6 ± 0.7	58 ± 1	61 ± 1	38.2 ± 0.6	41.7 ± 0.6	1, 3, 1
J04381486+2611399	...	0.023 ± 0.001	0.186 ± 0.003	1.36 ± 0.02	2.29 ± 0.05	4.3 ± 0.1	11.4 ± 0.2	13.6 ± 0.2	1, 3, 1
J04381630+2326402	...			30.2 ± 0.5	32.7 ± 0.6	27.5 ± 0.5	15.1 ± 0.2		
J04382134+2609137	GM Tau	1.8 ± 0.1	2.46 ± 0.05	12 ± 0.2	23.8 ± 0.5	37.3 ± 0.7	48.7 ± 0.7	51.8 ± 0.8	9, 3, 1
J04385859+2336351	...			25.9 ± 0.5	29.2 ± 0.6	25.7 ± 0.5	16.2 ± 0.2	17.9 ± 0.3	1
J04385871+2323595	...			16.1 ± 0.3	17.2 ± 0.3	15.3 ± 0.3	8.8 ± 0.1		
J04390163+2336029	...			46.6 ± 0.8	59 ± 1	56 ± 1	34.8 ± 0.5	36.4 ± 0.5	1
J04390396+2544264	...	0.13 ± 0.01	1.59 ± 0.03	13.9 ± 0.2	18.8 ± 0.4	18.9 ± 0.4	12.6 ± 0.2	13.7 ± 0.2	1, 2, 3, 1
J04390637+2334179	...			23.2 ± 0.4	25 ± 0.5	22.2 ± 0.4	13.7 ± 0.2	13.6 ± 0.2	1
J04393364+2359212	...			37.6 ± 0.7	49 ± 1	52 ± 1	38.2 ± 0.6	40.2 ± 0.6	1
J04394488+2601527	ITG 15			88 ± 2	160 ± 3	175 ± 3	135 ± 2	119 ± 2	1
J04394748+2601407	CFHT 4	0.098 ± 0.004	1.25 ± 0.02	21.6 ± 0.4	40.5 ± 0.8	49.1 ± 0.9	36.6 ± 0.5	44.9 ± 0.7	6, 3, 1
J04400067+2358211	...			17 ± 0.3	18.3 ± 0.4	17 ± 0.3	10.6 ± 0.2	12.3 ± 0.2	1
J04400174+2556292	CFHT 17		0.228 ± 0.004	8.2 ± 0.1	22.6 ± 0.4	33 ± 0.6	21 ± 0.3	25.6 ± 0.4	2, 1
J04403979+2519061	...		3.1 ± 0.1	29.8 ± 0.5	49 ± 1	54 ± 1	30.8 ± 0.5	34.1 ± 0.5	3, 1
J04410424+2557561	Haro 6-32		15.9 ± 0.4	67 ± 1	80 ± 2	70 ± 1	39.3 ± 0.6	41.4 ± 0.6	3, 1
J04411078+2555116	ITG 34	0.06 ± 0.002	0.75 ± 0.01	8.4 ± 0.1	14.5 ± 0.3	17.6 ± 0.3	12.4 ± 0.2	14.1 ± 0.2	1, 2, 3, 1
J04414489+2301513	...			2.72 ± 0.05	3.3 ± 0.1	3.6 ± 0.1	41.7 ± 0.6	3.5 ± 0.1	1
J04414565+2301580	...			81 ± 1	94 ± 2	76 ± 1	41.7 ± 0.6		
J04414825+2534304	...		0.39 ± 0.01	5.1 ± 0.1	7.8 ± 0.2	8.6 ± 0.2	7.1 ± 0.1	7.9 ± 0.1	3, 1
J04422101+2520343	CIDA 7		9.7 ± 0.2	44 ± 0.8	60 ± 1	57 ± 1	41.9 ± 0.6	43.9 ± 0.6	3, 1
J04432023+2940060	CIDA 14	6.2 ± 0.3	32.4 ± 0.8	110 ± 2	131 ± 3	115 ± 2	71 ± 1	76 ± 1	8, 1
J04442713+2512164	IRAS 04414+2506			21.1 ± 0.4	29.3 ± 0.6	33.1 ± 0.6	29.7 ± 0.4	39.3 ± 0.6	1
J04464260+2459034	RXJ 04467+2459	2.7 ± 0.1	14.5 ± 0.3	49.9 ± 0.9	55 ± 1	48.8 ± 0.9	26.9 ± 0.4	27.5 ± 0.4	8, 1
J04484189+1703374	...			6.2 ± 0.1	6.9 ± 0.1	6.7 ± 0.1	4 ± 0.1	4.2 ± 0.1	1
J04520668+3047175	IRAS 04489+3042		0.18 ± 0.003	2.7 ± 0.05	15.9 ± 0.3	46.9 ± 0.9	91 ± 1	120 ± 2	3, 1
J04552333+3027366	...		1.54 ± 0.03	9.5 ± 0.2	11.4 ± 0.2	10.9 ± 0.2	6.5 ± 0.1	7 ± 0.1	3, 1
J04554046+3039057	...		3.3 ± 0.1	13.1 ± 0.2	15.2 ± 0.3	13 ± 0.2	7.3 ± 0.1	7.4 ± 0.1	3, 1
J04554535+3019389	...		13.5 ± 0.3	42.3 ± 0.7	50 ± 1	43.6 ± 0.8	26.6 ± 0.4	29.3 ± 0.4	3, 1

Table A.4: continued.

2MASS	Other name	R_C	I_C	J	H	K	W1	[3.6]	Ref
J04554757+3028077	...		15.9 ± 0.4	61 ± 1	77 ± 2	68 ± 1	38 ± 0.6	39.5 ± 0.6	3, 1
J04554801+3028050	...		2.12 ± 0.04	8.5 ± 0.1	9.4 ± 0.2	9.2 ± 0.2	6.3 ± 0.1	7.6 ± 0.1	3, 1
J04554820+3030160	XEST 26-052			27.9 ± 0.5	33.2 ± 0.7	27.8 ± 0.5	15 ± 0.2	15.4 ± 0.2	1
J04554969+3019400	...		2.5 ± 0.1	12 ± 0.2	13.1 ± 0.3	12 ± 0.2	7.4 ± 0.1	8 ± 0.1	3, 1
J04555288+3006523	...		8.4 ± 0.2	35 ± 0.6	39.5 ± 0.8	33.9 ± 0.6	18.7 ± 0.3	19.6 ± 0.3	3, 1
J04555605+3036209	XEST 26-062			103 ± 2	140 ± 3	131 ± 2	84 ± 1	94 ± 1	1
J04555636+3049374	...		7.4 ± 0.2	25.2 ± 0.4	28.3 ± 0.6	24.4 ± 0.5	13.8 ± 0.2	14.1 ± 0.2	3, 1
J04574903+3015195	...		0.051 ± 0.001	0.78 ± 0.01	0.91 ± 0.02	1.07 ± 0.02	0.61 ± 0.01	0.79 ± 0.01	3, 1
J05061674+2446102	CIDA 10			77 ± 1	94 ± 2	79 ± 2	42 ± 0.6	41 ± 0.6	1
J05064662+2104296	...			24.1 ± 0.4	28 ± 0.5	23.9 ± 0.5	13.7 ± 0.2	14.3 ± 0.2	1
J05075496+2500156	CIDA 12			43.3 ± 0.8	53 ± 1	46.1 ± 0.9	27 ± 0.4	26.6 ± 0.4	1

Notes. All fluxes are reported in mJy. The median flux value is given for the targets with multiple photometry observations at the same filter/band, that have been reported in the literature. J, H, K fluxes have been extracted from the 2MASS point source catalog (Cutri et al., 2003) or the 2MASS extended source catalog where indicated (Skrutskie et al., 2006). W1 (3.4 μm) WISE fluxes have been extracted from the WISE All-Sky Catalog (Wright et al., 2010).

References. Luhman et al. (2010); (2) Guieu et al. (2007); (3) Guieu et al. (2006); (4) Luhman (2004); (5) Luhman et al. (2003a); (6) Briceño et al. (2002); (7) Martín et al. (2001); (8) Luhman (2000); (9) Briceño et al. (1999); (10) Kenyon & Hartmann (1995).

Table A.5: TBOSS flux density compilation: mid-IR wavelengths, ordered by target RA.

2MASS	Other name	[4.5]	W2	[5.8]	[8.0]	W3	W4
J04034997+2620382	XEST 06-006		3.07 ± 0.05			0.42 ± 0.02	<2
J04131414+2819108	LkCa 1	74 ± 1	71 ± 1	50.4 ± 0.8	27.8 ± 0.4	13.4 ± 0.2	2.3 ± 0.1
J04141188+2811535	...	13.5 ± 0.2	15.4 ± 0.2	13.3 ± 0.2	17.2 ± 0.2	20.3 ± 0.3	30.3 ± 0.5
J04141458+2827580	FN Tau	275 ± 4	336 ± 5	267 ± 4	339 ± 5	716 ± 11	1422 ± 26
J04141760+2806096	CIDA 1	117 ± 2	93 ± 1	116 ± 2	156 ± 2	197 ± 3	326 ± 5
J04144730+2646264	FP Tau	112 ± 2	114 ± 2	94 ± 1	81 ± 1	81 ± 1	146 ± 2
J04144739+2803055	XEST 20-066	26.8 ± 0.4	26.4 ± 0.4	17.5 ± 0.3	10.1 ± 0.1	5.62 ± 0.08	<4
J04150515+2808462	CIDA 2	57.9 ± 0.8	55.4 ± 0.8	39 ± 0.6	21.5 ± 0.3	11.7 ± 0.2	<5
J04151471+2800096	KPNO 1	1.08 ± 0.02	0.93 ± 0.01	0.67 ± 0.01	0.43 ± 0.01	<0.5	<2
J04152409+2910434	...	3.7 ± 0.1	3.48 ± 0.05	2.55 ± 0.04	1.56 ± 0.02	0.5 ± 0.01	<2
J04155799+2746175	...	32.1 ± 0.5	31.8 ± 0.5	27.8 ± 0.4	29.4 ± 0.4	31.8 ± 0.5	38.8 ± 0.6
J04161210+2756385	...	45.6 ± 0.7	49.3 ± 0.7	38.4 ± 0.6	31.4 ± 0.5	26.1 ± 0.4	51.3 ± 0.8
J04161885+2752155	...	9.1 ± 0.1	8.7 ± 0.1	6.4 ± 0.1	3.47 ± 0.05	2.01 ± 0.03	2.5 ± 0.1
J04162725+2053091	...	9.7 ± 0.1	9.1 ± 0.1	6.3 ± 0.1	3.8 ± 0.1	2.04 ± 0.03	<2
J04163048+3037053	...	2.44 ± 0.04	2.32 ± 0.03	1.57 ± 0.02	0.83 ± 0.01	0.72 ± 0.02	<3
J04163911+2858491	...	16.8 ± 0.2	15.8 ± 0.2	13.6 ± 0.2	11.2 ± 0.2	8.6 ± 0.1	9.1 ± 0.2
J04174955+2813318	KPNO 10	13.6 ± 0.2	10.4 ± 0.2	13.3 ± 0.2	19.2 ± 0.3	19.7 ± 0.3	32.1 ± 0.5
J04174965+2829362	V410 X-ray 1	143 ± 2	136 ± 2	136 ± 2	175 ± 3	196 ± 3	253 ± 4
J04180796+2826036	V410 X-ray 3	20.1 ± 0.3	19.2 ± 0.3	13.1 ± 0.2	7.7 ± 0.1	4.29 ± 0.06	<3
J04181710+2828419	V410 Anon 13	20.3 ± 0.3	20.1 ± 0.3	18.8 ± 0.3	19.5 ± 0.3	20.5 ± 0.3	30.6 ± 0.5
J04183030+2743208	KPNO 11	10.9 ± 0.2	10.5 ± 0.2	6.9 ± 0.1	4.1 ± 0.1	2.29 ± 0.04	<3
J04184023+2824245	V410 X-ray 4	64.6 ± 0.9	61.6 ± 0.9	45.4 ± 0.7	28.1 ± 0.4	13.3 ± 0.2	7.8 ± 0.2
J04185115+2814332	KPNO 2	2.65 ± 0.04	2.54 ± 0.04	1.82 ± 0.03	1.14 ± 0.02	1.23 ± 0.03	2.7 ± 0.2
J04185813+2812234	IRAS 04158+2805	75 ± 1	81 ± 1	91 ± 1	115 ± 2	163 ± 2	551 ± 9
J04190110+2819420	V410 X-ray 6	66 ± 1	60.4 ± 0.9	45.4 ± 0.7	32.5 ± 0.5	40.8 ± 0.6	248 ± 4
J04190126+2802487	KPNO 12	0.71 ± 0.01	0.7 ± 0.01	0.66 ± 0.01	0.59 ± 0.01	1.22 ± 0.02	<3
J04190197+2822332	V410 X-ray 5a	27.5 ± 0.4	28.2 ± 0.4	19 ± 7	844 ± 12	6.08 ± 0.09	3 ± 0.1
J04193545+2827218	FR Tau	51.6 ± 0.8	53.2 ± 0.8	56.3 ± 0.8	81 ± 1	90 ± 1	95 ± 2
J04194657+2712552	[GKH94] 41	34.2 ± 0.5	30.9 ± 0.5	41.8 ± 0.6	37.5 ± 0.5	46.3 ± 0.7	196 ± 3
J04201611+2821325	...	4.9 ± 0.1	4.52 ± 0.07	4.1 ± 0.1	3.9 ± 0.1	4.05 ± 0.06	<3
J04202555+2700355	...	9.5 ± 0.1	9 ± 0.1	7.7 ± 0.1	8.2 ± 0.1	10.5 ± 0.2	26.7 ± 0.5
J04202583+2819237	IRAS 04173+2812	78 ± 1	76 ± 1	79 ± 1	91 ± 1	119 ± 2	205 ± 3
J04203918+2717317	XEST 16-045	30.1 ± 0.4	35.5 ± 0.5	21.5 ± 0.3	12.3 ± 0.2	6.8 ± 0.1	<4
J04205273+1746415	J2-157	13 ± 0.2	12.4 ± 0.2	8.6 ± 0.1	5 ± 0.1	3.59 ± 0.05	3.3 ± 0.1

Table A.5: continued.

2MASS	Other name	[4.5]	W2	[5.8]	[8.0]	W3	W4
J04210795+2702204	CFHT 19	302 ± 4	309 ± 5	343 ± 5	479 ± 7	624 ± 9	1539 ± 28
J04210934+2750368	...	23.3 ± 0.3	24.4 ± 0.4	16.9 ± 0.3	13.6 ± 0.2	11.9 ± 0.2	8.5 ± 0.3
J04213459+2701388	...	25.7 ± 0.4	24.8 ± 0.4	21.1 ± 0.3	16.6 ± 0.2	13.6 ± 0.2	9.3 ± 0.3
J04214013+2814224	XEST 21-026	10.5 ± 0.2	9.9 ± 0.1	7 ± 0.1	4 ± 0.1	2.23 ± 0.04	<8
J04214631+2659296	...	5.7 ± 0.1	5.5 ± 0.08	4.5 ± 0.1	4.1 ± 0.1	5.89 ± 0.09	7.1 ± 0.3
J04215450+2652315	...	1.07 ± 0.02	1.08 ± 0.02	0.75 ± 0.01	0.45 ± 0.01	0.64 ± 0.02	<5
J04220007+1530248	IRAS 04191+1523 B	6 ± 0.1	8.4 ± 0.1	6 ± 0.1	7.8 ± 0.1	42.8 ± 0.7	546 ± 12
J04221332+1934392	...	7.9 ± 0.1	7.6 ± 0.1	5.4 ± 0.1	3.8 ± 0.1	1.92 ± 0.03	5.3 ± 0.2
J04221644+2549118	...	5.5 ± 0.1	5.08 ± 0.08	3.7 ± 0.1	2.07 ± 0.03	0.91 ± 0.03	<3
J04222404+2646258	XEST 11-087	32.4 ± 0.5	31.5 ± 0.5	21.9 ± 0.3	12 ± 0.2	6.7 ± 0.1	<5
J04230607+2801194	...	14.7 ± 0.2	13.6 ± 0.2	12 ± 0.2	11.8 ± 0.2	11.9 ± 0.2	22.1 ± 0.7
J04233539+2503026	FU Tau A	139 ± 2	125 ± 2	134 ± 2	152 ± 2	117 ± 2	121 ± 2
J04233573+2502596	FU Tau B	3.08 ± 0.05	125 ± 2	3 ± 0.1	3.05 ± 0.05	117 ± 2	121 ± 2
J04242090+2630511	...	4.9 ± 0.1	4.4 ± 0.07	4.6 ± 0.1	4.6 ± 0.1		
J04242646+2649503	CFHT 9	8.6 ± 0.1	7.5 ± 0.1	7.4 ± 0.1	7.5 ± 0.1		
J04244506+2701447	J1-4423	16 ± 0.2	15.4 ± 0.2	11 ± 0.2	6.2 ± 0.1	3.88 ± 0.08	<7
J04262939+2624137	KPNO 3	7.5 ± 0.1	7.2 ± 0.1	7.4 ± 0.1	8.7 ± 0.1	9.8 ± 0.1	12.4 ± 0.3
J04263055+2443558	...	2.42 ± 0.04	2.37 ± 0.04	2.24 ± 0.03	2.44 ± 0.03	2.41 ± 0.07	<6
J04265732+2606284	KPNO 13	88 ± 1	85 ± 1	84 ± 1	85 ± 1	72 ± 1	95 ± 2
J04270739+2215037	...	8.8 ± 0.1	8.4 ± 0.1	5.8 ± 0.1	3.31 ± 0.05	1.87 ± 0.04	<3
J04272799+2612052	KPNO 4	2.09 ± 0.03	2.04 ± 0.03	1.47 ± 0.02	0.92 ± 0.01	1.04 ± 0.03	<3
J04274538+2357243	...	1.08 ± 0.02	1.07 ± 0.02	0.74 ± 0.01	0.41 ± 0.01	<0.9	<5
J04275730+2619183	IRAS 04248+2612	71 ± 1	54.9 ± 0.8	68 ± 1	105 ± 1	205 ± 3	1005 ± 16
...	L1521F-IRS	0.98 ± 0.01	0.79 ± 0.01	0.97 ± 0.02	0.91 ± 0.01	<0.8	20.7 ± 0.4
J04284263+2714039	...	29.8 ± 0.4	30.7 ± 0.5	24.2 ± 0.4	19.1 ± 0.3	18.4 ± 0.3	29.5 ± 0.5
J04290068+2755033	...	2.98 ± 0.04	2.92 ± 0.04	2.68 ± 0.04	2.68 ± 0.04	3.25 ± 0.05	<5
J04292071+2633406	J1-507	72 ± 1	70 ± 1	48.2 ± 0.7	27.3 ± 0.4	14.6 ± 0.2	5.71 ± 0.09
J04292165+2701259	IRAS 04263+2654	158 ± 2	154 ± 2	142 ± 2	143 ± 2	153 ± 2	339 ± 6
J04292971+2616532	FW Tau A+B+C	48.6 ± 0.7	45.8 ± 0.7	31.7 ± 0.5	18.4 ± 0.3	9.6 ± 0.1	4.95 ± 0.08
J04294568+2630468	KPNO 5	7.7 ± 0.1	7.3 ± 0.1	5.3 ± 0.1	2.98 ± 0.04	2.06 ± 0.04	<3
J04295422+1754041	...		29.1 ± 0.4			18.5 ± 0.3	25.4 ± 0.5
J04295950+2433078	CFHT 20	68 ± 1	72 ± 1	55.3 ± 0.8	49.2 ± 0.7	57 ± 0.8	93 ± 2
J04300724+2608207	KPNO 6	1.43 ± 0.02	1.36 ± 0.02	1.25 ± 0.02	1.38 ± 0.02	0.67 ± 0.03	<3
J04302365+2359129	...	1.02 ± 0.01	0.95 ± 0.01	0.71 ± 0.01	0.4 ± 0.01	0.42 ± 0.02	2.7 ± 0.2
J04305171+2441475	ZZ Tau IRS	209 ± 3	238 ± 4	248 ± 4	330 ± 5	529 ± 8	1436 ± 24

Table A.5: continued.

2MASS	Other name	[4.5]	W2	[5.8]	[8.0]	W3	W4
J04305718+2556394	KPNO 7	2.27 ± 0.03	2.2 ± 0.03	1.88 ± 0.03	2.04 ± 0.03	1.75 ± 0.03	3 ± 0.2
J04311578+1820072	MHO 9	18.9 ± 0.3	18.1 ± 0.3	13.1 ± 0.2	7.1 ± 0.1	4.85 ± 0.08	<6
J04311907+2335047	...	4.4 ± 0.1	4.34 ± 0.06	2.81 ± 0.04	1.68 ± 0.02	1.1 ± 0.02	<4
J04312382+2410529	V927 Tau A+B	77 ± 1	72 ± 1	50.7 ± 0.8	28.7 ± 0.4	15.4 ± 0.2	5.39 ± 0.09
J04312405+1800215	MHO 4	18.1 ± 0.3	16.4 ± 0.2	12.2 ± 0.2	6.9 ± 0.1	4.32 ± 0.07	<4
J04312669+2703188	...	1.51 ± 0.02	1.41 ± 0.02	0.95 ± 0.01	0.55 ± 0.01	<0.5	<3
J04315844+2543299	J1-665	36 ± 0.5	34.4 ± 0.5	23.5 ± 0.4	13.1 ± 0.2	5.98 ± 0.09	<5
J04320329+2528078	...	15.8 ± 0.2	14.7 ± 0.2	10.6 ± 0.2	6 ± 0.1	2.29 ± 0.04	<4
J04321606+1812464	MHO 5	47.3 ± 0.7	42.1 ± 0.6	43.3 ± 0.7	47 ± 0.7	49.7 ± 0.7	45.8 ± 0.9
J04321786+2422149	CFHT 7	21.6 ± 0.3	20.7 ± 0.3	14.7 ± 0.2	8.4 ± 0.1	4.6 ± 0.07	<6
J04322210+1827426	MHO 6	22.8 ± 0.3	21.9 ± 0.3	17.1 ± 0.3	15.4 ± 0.2	12.4 ± 0.2	19.1 ± 0.4
J04322329+2403013	...	8.8 ± 0.1	8.5 ± 0.1	5.3 ± 0.1	3.44 ± 0.05	1.7 ± 0.04	<4
J04322415+2251083	...	25 ± 0.4	24.4 ± 0.4	21.7 ± 0.3	26.6 ± 0.4	27.3 ± 0.4	28.2 ± 0.5
J04322627+1827521	MHO 7	21.8 ± 0.3	21.1 ± 0.3	14.3 ± 0.2	8.2 ± 0.1	4.69 ± 0.07	<5
J04323028+1731303	GG Tau Ba+Bb	54.3 ± 0.8	636 ± 9	50.2 ± 0.8	58.6 ± 0.8	736 ± 11	1364 ± 22
J04324938+2253082	JH112 B	96 ± 1	96 ± 1	91 ± 1	99 ± 1	88 ± 1	113 ± 3
J04325026+2422115	...	15.1 ± 0.2	13.8 ± 0.2	10.7 ± 0.2	6.2 ± 0.1	2.25 ± 0.05	<4
J04325119+1730092	LH 0429+17	1.24 ± 0.02	1.12 ± 0.02		0.52 ± 0.01	<0.5	<5
J04330197+2421000	MHO 8	39 ± 0.6	37.5 ± 0.6	25.9 ± 0.4	15.1 ± 0.2	8 ± 0.1	3 ± 0.2
J04330781+2616066	KPNO 14	25.5 ± 0.4	24.1 ± 0.4	16.8 ± 0.3	9.8 ± 0.1	4.75 ± 0.07	<3
J04330945+2246487	CFHT 12	10.9 ± 0.2	10.7 ± 0.2	8.6 ± 0.1	6.9 ± 0.1	5.72 ± 0.09	6.3 ± 0.2
J04332621+2245293	XEST 17-036	30.8 ± 0.4	30.1 ± 0.4	21.6 ± 0.3	12 ± 0.2	5.96 ± 0.09	3 ± 0.2
J04334171+1750402	...	21.8 ± 0.3	22 ± 0.3	17.2 ± 0.3	15.3 ± 0.2	14.3 ± 0.2	23.1 ± 0.4
J04334291+2526470	...	1.67 ± 0.02	1.52 ± 0.02	1.18 ± 0.02	0.65 ± 0.01	<0.5	<3
J04334465+2615005	...	91 ± 1	74 ± 1	88 ± 1	88 ± 1	70 ± 1	106 ± 2
J04335245+2612548	...	1.54 ± 0.02	1.49 ± 0.02	1.45 ± 0.02	1.65 ± 0.02	1.6 ± 0.03	<4
J04335252+2256269	XEST 17-059	63.2 ± 0.9	60.2 ± 0.9	41.8 ± 0.6	23.7 ± 0.3	12.6 ± 0.2	5.9 ± 0.2
J04341527+2250309	CFHT 1	6.8 ± 0.1	6.5 ± 0.1	4.8 ± 0.1	2.62 ± 0.04	1.14 ± 0.03	<4
J04344544+2308027	...	6 ± 0.1	5.99 ± 0.09	4.2 ± 0.1	2.4 ± 0.03	1.59 ± 0.03	<3
J04350850+2311398	...	6.8 ± 0.1	6.6 ± 0.1	4.5 ± 0.1	2.63 ± 0.04	2.16 ± 0.04	3 ± 0.2
J04353536+2408266	IRAS 04325+2402 C	1.24 ± 0.02	56.4 ± 0.8	1.05 ± 0.02	1.03 ± 0.02	84 ± 1	1893 ± 31
J04354183+2234115	KPNO 8	4.7 ± 0.1	4.3 ± 0.06	3.1 ± 0.05	1.75 ± 0.02	0.82 ± 0.02	<4
J04354203+2252226	XEST 08-033	29 ± 0.4	25.9 ± 0.4	18.8 ± 0.3	10.3 ± 0.1	5.78 ± 0.09	<7
J04354526+2737130	...	1.09 ± 0.02	1.01 ± 0.01	0.8 ± 0.01	0.39 ± 0.01	<0.3	<3
J04355143+2249119	KPNO 9	0.72 ± 0.01	0.69 ± 0.01	0.46 ± 0.01	0.279 ± 0.004	0.72 ± 0.02	6.2 ± 0.2

Table A.5: continued.

2MASS	Other name	[4.5]	W2	[5.8]	[8.0]	W3	W4
J04355209+2255039	XEST 08-047	30.2 ± 0.4	28.6 ± 0.4	20.4 ± 0.3	11.6 ± 0.2	6.22 ± 0.09	7.5 ± 0.2
J04355286+2250585	XEST 08-049	34.2 ± 0.5	31.8 ± 0.5	22.3 ± 0.3	12.6 ± 0.2	6.2 ± 0.09	6.4 ± 0.2
J04361030+2159364	...	1.52 ± 0.02	1.44 ± 0.02	1.31 ± 0.02	1.29 ± 0.02	0.96 ± 0.02	2.9 ± 0.2
J04361038+2259560	CFHT 2	5 ± 0.1	4.63 ± 0.07	3.26 ± 0.05	1.92 ± 0.03	0.95 ± 0.02	3.6 ± 0.2
J04362151+2351165	...	4.6 ± 0.1	4.48 ± 0.07	4.1 ± 0.1	3.9 ± 0.1	3.34 ± 0.05	4.2 ± 0.2
J04363893+2258119	CFHT 3	3.9 ± 0.1	3.82 ± 0.06	2.73 ± 0.04	1.57 ± 0.02	1.09 ± 0.02	<3
J04373705+2331080	...	0.5 ± 0.01	0.49 ± 0.01	0.42 ± 0.01	0.311 ± 0.005	0.35 ± 0.01	<2
J04380083+2558572	ITG 2	30.7 ± 0.4	29.8 ± 0.4	21.3 ± 0.3	11.9 ± 0.2	6.5 ± 0.1	<4
J04381486+2611399	...	15.8 ± 0.2	16.3 ± 0.2	16.5 ± 0.2	17.7 ± 0.3	21.9 ± 0.3	80 ± 1
J04381630+2326402	...		10.5 ± 0.2			2.63 ± 0.04	2.9 ± 0.1
J04382134+2609137	GM Tau	52.3 ± 0.8	51.1 ± 0.8	44.9 ± 0.7	44.9 ± 0.6	46.2 ± 0.7	63 ± 1
J04385859+2336351	...		14.4 ± 0.2	13.3 ± 0.2		14.8 ± 0.2	21.8 ± 0.4
J04385871+2323595	...		6.34 ± 0.09			2.26 ± 0.04	<4
J04390163+2336029	...		28 ± 0.4	24.7 ± 0.4		20.7 ± 0.3	25.6 ± 0.4
J04390396+2544264	...	12.8 ± 0.2	12.2 ± 0.2	11.2 ± 0.2	14.1 ± 0.2	14.6 ± 0.2	21 ± 0.4
J04390637+2334179	...		9.7 ± 0.1	6.1 ± 0.1		2.4 ± 0.04	<4
J04393364+2359212	...	39 ± 0.6	37.6 ± 0.6	34.1 ± 0.5	44.5 ± 0.6	51 ± 0.7	67 ± 1
J04394488+2601527	ITG 15	101 ± 1	134 ± 2	95 ± 1	94 ± 1	95 ± 1	195 ± 3
J04394748+2601407	CFHT 4	42.7 ± 0.6	44.3 ± 0.7	41.6 ± 0.6	48.1 ± 0.7	48 ± 0.7	73 ± 1
J04400067+2358211	...	10.2 ± 0.1	9.4 ± 0.1	8.3 ± 0.1	8.6 ± 0.1	8.9 ± 0.1	19.7 ± 0.4
J04400174+2556292	CFHT 17	19.5 ± 0.3	18.6 ± 0.3	13.5 ± 0.2	7.7 ± 0.1	3.42 ± 0.05	<4
J04403979+2519061	...	25.7 ± 0.4	23 ± 0.3	16.3 ± 0.2	9.6 ± 0.1	4.86 ± 0.07	8.9 ± 0.2
J04410424+2557561	Haro 6-32	28.7 ± 0.4	27.5 ± 0.4	18.7 ± 0.3	10.6 ± 0.1	8.1 ± 0.1	6.6 ± 0.2
J04411078+2555116	ITG 34	14.2 ± 0.2	13 ± 0.2	12.6 ± 0.2	13.9 ± 0.2	16 ± 0.2	19.9 ± 0.4
J04414489+2301513	...	3.18 ± 0.05	28.9 ± 0.4	2.81 ± 0.04	2.58 ± 0.04	8.4 ± 0.1	8.9 ± 0.2
J04414565+2301580	...	29 ± 0.4	28.9 ± 0.4	20.5 ± 0.3	13.3 ± 0.2	8.4 ± 0.1	8.9 ± 0.2
J04414825+2534304	...	8.1 ± 0.1	8.3 ± 0.1	7.5 ± 0.1	9.7 ± 0.1	11.8 ± 0.2	25.4 ± 0.5
J04422101+2520343	CIDA 7	39.5 ± 0.6	41.4 ± 0.6	40.1 ± 0.6	49.2 ± 0.7	57.4 ± 0.8	152 ± 2
J04432023+2940060	CIDA 14	64.1 ± 0.9	60.4 ± 0.9	55.8 ± 0.8	59.7 ± 0.8	55.3 ± 0.8	47.4 ± 0.8
J04442713+2512164	IRAS 04414+2506	39.3 ± 0.6	31.3 ± 0.5	41.8 ± 0.6	56 ± 0.8	62.7 ± 0.9	159 ± 3
J04464260+2459034	RXJ 04467+2459	19.3 ± 0.3	18.6 ± 0.3	12.4 ± 0.2	7.1 ± 0.1	4.24 ± 0.06	<3
J04484189+1703374	...	3.01 ± 0.04	2.91 ± 0.04	2.02 ± 0.03	1.15 ± 0.02	0.48 ± 0.02	<2
J04520668+3047175	IRAS 04489+3042	152 ± 2	164 ± 2	172 ± 3	221 ± 3	283 ± 4	861 ± 14
J04552333+3027366	...	5 ± 0.1	4.81 ± 0.07	3.35 ± 0.05	1.91 ± 0.03	1.56 ± 0.03	<4
J04554046+3039057	...	5.4 ± 0.1	5.1 ± 0.08	3.6 ± 0.1	2.09 ± 0.03	1.31 ± 0.03	2.9 ± 0.1

Table A.5: continued.

2MASS	Other name	[4.5]	W2	[5.8]	[8.0]	W3	W4
J04554535+3019389	...	25.5 ± 0.4	23.4 ± 0.3	21.3 ± 0.3	20.7 ± 0.3	18.1 ± 0.3	19.7 ± 0.4
J04554757+3028077	...	28.1 ± 0.4	26.2 ± 0.4	18.4 ± 0.3	10.8 ± 0.2	5.71 ± 0.09	<3
J04554801+3028050	...	6.9 ± 0.1	5.87 ± 0.09	5.8 ± 0.1	6.2 ± 0.1	6.9 ± 0.1	15.8 ± 0.3
J04554820+3030160	XEST 26-052	10.9 ± 0.2	10.2 ± 0.2	7 ± 0.1	4.3 ± 0.1	2.53 ± 0.04	8.1 ± 0.2
J04554969+3019400	...	6.2 ± 0.1	5.92 ± 0.09	4.8 ± 0.1	3.6 ± 0.1	3.2 ± 0.05	4.6 ± 0.2
J04555288+3006523	...	13.5 ± 0.2	12.7 ± 0.2	9.1 ± 0.1	5.2 ± 0.1	2.88 ± 0.05	<3
J04555605+3036209	XEST 26-062	81 ± 1	73 ± 1	73 ± 1	87 ± 1	119 ± 2	272 ± 4
J04555636+3049374	...	9.9 ± 0.1	9.5 ± 0.1	6.7 ± 0.1	3.8 ± 0.1	2.39 ± 0.04	<3
J04574903+3015195	...	0.56 ± 0.01	0.49 ± 0.01	0.4 ± 0.01	0.204 ± 0.003	<0.4	<2
J05061674+2446102	CIDA 10	29.8 ± 0.4	27.5 ± 0.4	19.3 ± 0.3	11.2 ± 0.2	6.18 ± 0.09	2.8 ± 0.1
J05064662+2104296	...	10 ± 0.1	9.4 ± 0.1	6.7 ± 0.1	3.8 ± 0.1	2.35 ± 0.04	2.1 ± 0.1
J05075496+2500156	CIDA 12	20.8 ± 0.3	21 ± 0.3	18.1 ± 0.3	21.1 ± 0.3	22.6 ± 0.3	34.8 ± 0.6

Notes. All fluxes are reported in mJy. The median flux value is given for the targets with multiple photometry observations at the same filter/band, that have been reported in the literature. *Spitzer* IRAC fluxes have been extracted from Luhman et al. (2010). W2, (4.6 μm), W3 (12 μm) and W4 (22 μm) WISE fluxes have been extracted from the WISE All-Sky Catalog (Wright et al., 2010).

Table A.6: TBOSS flux density compilation far-IR wavelengths, ordered by target RA.

2MASS	Other name	$[70]_{\mathrm{MIPS}}$	70_{PACS}	100_{PACS}	160_{PACS}	Ref.	Notes
J04034997+2620382	XEST 06-006		<5		<20	1	
J04131414+2819108	LkCa 1	<235	<9	<9	<21	3, 4	b
J04141188+2811535	...	<301	17 ± 5		<293	1, 4	
J04141458+2827580	FN Tau	979 ± 199	1755 ± 4		816 ± 16	1, 4	
J04141760+2806096	CIDA 1	239 ± 49	266 ± 2		212 ± 21	1, 4	
J04144730+2646264	FP Tau	253 ± 51	307 ± 3		351 ± 11	1, 4	
J04144739+2803055	XEST 20-066		<6		<67	1	
J04150515+2808462	CIDA 2	<233	<9	<9	<22	3, 4	b
J04151471+2800096	KPNO 1	<340	<3		<41	1, 4	
J04152409+2910434	...	<272	<7		<29	1, 4	
J04155799+2746175	...	<253	25 ± 3		<48	1, 4	
J04161210+2756385	...	187 ± 38	201 ± 3		228 ± 8	1, 4	
J04161885+2752155	...	<244	<6		<50	1, 4	
J04162725+2053091	...		<9		<39	1	
J04163048+3037053	...		<11		<28	1	
J04163911+2858491	...	<248	<9		<55	1, 4	
J04174955+2813318	KPNO 10	133 ± 27	160 ± 2		82 ± 26	1, 4	
J04174965+2829362	V410 X-ray 1	51 ± 10	36 ± 3		<122	1, 4	
J04180796+2826036	V410 X-ray 3	<150	<7		<86	1, 4	
J04181710+2828419	V410 Anon 13		35 ± 2		<113	1	
J04183030+2743208	KPNO 11	<203	<6		<55	1, 4	
J04184023+2824245	V410 X-ray 4	<178	<23		<88	1, 4	
J04185115+2814332	KPNO 2	<180	<7		<74	1, 4	
J04185813+2812234	IRAS 04158+2805	830 ± 169	1089 ± 3		2953 ± 25	1, 4	
J04190110+2819420	V410 X-ray 6	412 ± 84	445 ± 4		342 ± 36	1, 4	
J04190126+2802487	KPNO 12	<157	<6		<88	1, 4	
J04190197+2822332	V410 X-ray 5a	<180	<5		<75	1, 4	
J04193545+2827218	FR Tau	43 ± 9	46 ± 3		<33	1, 4	
J04194657+2712552	[GKH94] 41	<267	269 ± 5		279 ± 66	1, 4	
J04201611+2821325	...	<290	<7		<26	1, 4	
J04202555+2700355	...	79 ± 16	107 ± 3		100 ± 15	1, 4	
J04202583+2819237	IRAS 04173+2812	133 ± 27	172 ± 3		72 ± 6	1, 4	
J04203918+2717317	XEST 16-045	<195	<5		<45	1, 4	
J04205273+1746415	J2-157		<5		<27	1	
J04210795+2702204	CFHT 19	2307 ± 469	3277 ± 8		3076 ± 61	1, 4	
J04210934+2750368	...	<190	<13		<47	1, 4	
J04213459+2701388	...	<172	37 ± 2		101 ± 19	1, 4	
J04214013+2814224	XEST 21-026		<8		<31	1	
J04214631+2659296	CFHT 10	<205	<10		<84	1, 4	
J04215450+2652315	...	<169	<5		<35	1, 4	
J04220007+1530248	IRAS 04191+1523 B		(8358 ± 26)		(10033 ± 289)	1	d
J04221332+1934392	...		<5		<45	1	
J04221644+2549118	CFHT 14	<267	<5		<26	1, 4	
J04222404+2646258	XEST 11-087	<185	<6		<44	1, 4	
J04230607+2801194	...	<431	41 ± 3		38 ± 9	1, 4	
J04233539+2503026	FU Tau A	86 ± 17		<39	<247	1, 4	a
J04233573+2502596	FU Tau B			<39	<247	1	a
J04242090+2630511	...	<275	<9		<58	1, 4	
J04242646+2649503	CFHT 9	<383	10 ± 1		<6	2, 4	
J04244506+2701447	J1-4423	<296	<5		<41	1, 4	
J04251550+2829275	...	<369				4	
J04262939+2624137	KPNO 3	<285	23 ± 4		33 ± 12	1, 4	
J04263055+2443558	...	<285	<12		<51	1, 4	
J04265732+2606284	KPNO 13	<330	28 ± 4		<182	1, 4	
J04270739+2215037	...		<8		<27	1	
J04272799+2612052	KPNO 4	<296	<7		<21	1, 4	
J04274538+2357243	CFHT 15	<293	<6		<47	1, 4	
J04275730+2619183	IRAS 04248+2612	3155 ± 641	5208 ± 19		10675 ± 247	1, 4	
...	L1521F-IRS	460 ± 94	631 ± 1		4162 ± 75	1, 4	
J04284263+2714039	...	<346	20 ± 2		51 ± 12	1, 4	
J04290068+2755033	...	<346	<8		<36	1, 4	
J04292071+2633406	J1-507	<299	<8	<8	<21	3, 4	b
J04292165+2701259	IRAS 04263+2654	280 ± 57	329 ± 3		176 ± 14	1, 4	
J04292971+2616532	FW Tau A+B+C	<290	19 ± 0.01	2 ± 0	8 ± 0.01	3, 4	b
J04294568+2630468	KPNO 5	<340	<7		<37	1, 4	
J04295422+1754041	...		89 ± 3		86 ± 8	1	
J04295950+2433078	CFHT 20	117 ± 24	128 ± 4		91 ± 23	1, 4	
J04300724+2608207	KPNO 6	<307	2 ± 1		<5	2, 4	
J04302365+2359129	CFHT 16	<310	<6		<51	1, 4	
J04305171+2441475	ZZ Tau IRS	1936 ± 393	2901 ± 5		2922 ± 26	1, 4	
J04305718+2556394	KPNO 7	<251	4 ± 1		<7	2, 4	
J04311578+1820072	MHO 9		<8		<76	1	
J04311907+2335047	...	<352	<7		<24	1, 4	
J04312382+2410529	V927 Tau A+B	<336	<9	<9	<32	3, 4	b

Table A.6: continued.

2MASS	Other name	$[70]_{\mathrm{MIPS}}$	70_{PACS}	100_{PACS}	160_{PACS}	Ref.	Notes
J04312405+1800215	MHO 4		<11		<38	1	
J04312669+2703188	CFHT 13	<416	<8		<54	1, 4	
J04313613+1813432	LkHa 358		1440 ± 0.2	1310 ± 0.2	1500 ± 0.3	3	b
J04315844+2543299	J1-665	<288	<9	<9	<25	3, 4	b
J04320329+2528078	...	<301	<9		<33	1, 4	
J04321606+1812464	MHO 5		<11		<82	1	
J04321786+2422149	CFHT 7	<352		<39	<322	1, 4	a
J04322210+1827426	MHO 6		107 ± 2		188 ± 7	1	
J04322329+2403013	...	<336	<9		<35	1, 4	
J04322415+2251083	...	<208	<9		<77	1, 4	
J04322627+1827521	MHO 7		<8		<23	1	
J04323028+1731303	GG Tau Ba+Bb		<750	<665	(8431 ± 17)	1	b, c
J04324938+2253082	JH 112 B		<318		(284 ± 26)	1	c
J04325026+2422115	...	<267	<10		<82	1, 4	
J04325119+1730092	LH 0429+17		<7		<33	1	
J04330197+2421000	MHO 8	<346	<4		<48	1, 4	
J04330781+2616066	KPNO 14	<207	<6		<79	1, 4	
J04330945+2246487	CFHT 12	<267	2 ± 1		<8	2, 4	
J04332621+2245293	XEST 17-036	130 ± 26	108 ± 4		281 ± 55	1, 4	
J04334171+1750402	...		17 ± 3		<28	1	
J04334291+2526470	...	<208	<6		<32	1, 4	
J04334465+2615005	...	142 ± 29	149 ± 2		178 ± 22	1, 4	
J04335245+2612548	...	<290	<11		<47	1, 4	
J04335252+2256269	XEST 17-059	<212	<12		<27	1, 4	
J04341527+2250309	CFHT 1	<310	<7		<67	1, 4	
J04344544+2308027	...		<10		<48	1	
J04350850+2311398	CFHT 11	<553	<7		<56	1, 4	
J04353536+2408266	IRAS 04325+2402 C			(15340 ± 39)		1	a, d, f
J04354183+2234115	KPNO 8	<277	<3		<31	1, 4	
J04354203+2252226	XEST 08-033	<290	<16		104 ± 28	1, 4	
J04354526+2737130	...	<201	<8		<30	1, 4	
J04355143+2249119	KPNO 9	<352	<7		<102	1, 4	
J04355209+2255039	XEST 08-047	<491	<11		<1657	1, 4	
J04355286+2250585	XEST 08-049	<330	<6		<109	1, 4	
J04355760+2253574	...	<346				4	
J04361030+2159364	...	<290	<7		<22	1, 4	
J04361038+2259560	CFHT 2	<199	<7		<82	1, 4	
J04362151+2351165	...	<293	<15		<64	1, 4	
J04363893+2258119	CFHT 3	<277	<5		<50	1, 4	
J04373705+2331080	...		<5		<27	1	
J04380083+2558572	ITG 2	<321	<6		<69	1, 4	
J04381486+2611399	...	<372	95 ± 2		67 ± 24	1, 4	
J04381630+2326402	...		<6		<26	1	
J04382134+2609137	GM Tau	<318	36 ± 2		<35	1, 4	
J04385859+2336351	...	<356	38 ± 3		76 ± 13	1, 4	
J04385871+2323595	...		<4		<30	1	
J04390163+2336029	...	<94	15 ± 3		<24	1, 4	
J04390396+2544264	CFHT 6	<505	23 ± 3		<56	1, 4	
J04390637+2334179	...		<5		<44	1	
J04393364+2359212	...	<333	70 ± 1		44 ± 15	1, 4	
J04394488+2601527	ITG 15	231 ± 47	272 ± 3		114 ± 28	1, 4	
J04394748+2601407	CFHT 4	<336	109 ± 5		<150	1, 4	
J04400067+2358211	...	<379	55 ± 2		52 ± 5	1, 4	
J04400174+2556292	...	<394	<11		<159	1, 4	
J04403979+2519061	...	<310	72 ± 2		61 ± 20	1, 4	
J04410424+2557561	Haro 6-32	<408	<8		<48	1, 4	
J04411078+2555116	ITG 34	<394	21 ± 4		<38	1, 4	
J04414489+2301513	...		11 ± 2		<18	1	
J04414565+2301580	...		<5		<18	1	
J04414825+2534304	...	<304	37 ± 3		<122	1, 4	
J04422101+2520343	CIDA 7	275 ± 56	330 ± 2		342 ± 19	1, 4	
J04432023+2940060	CIDA 14		<13		<25	1	
J04442713+2512164	IRAS S04414+2506	154 ± 31				2, 4	
J04464260+2459034	RXJ 04467+2459	<321	<10		<35	1, 4	
J04484189+1703374	...		<6		<25	1	
J04520668+3047175	IRAS 04489+3042		2151 ± 5		2103 ± 34	1	
J04552333+3027366	...		<7		<34	1	
J04554046+3039057	...		<10		<73	1	
J04554535+3019389	...		22 ± 3		<30	1	
J04554757+3028077	...		<7		<63	1	
J04554801+3028050	...		11 ± 3		<63	1	
J04554820+3030160	XEST 26-052						e
J04554969+3019400	...		<5		<17	1	
J04555288+3006523	...		<7		<16	1	

Table A.6: continued.

2MASS	Other name	$[70]_{\mathrm{MIPS}}$	70_{PACS}	100_{PACS}	160_{PACS}	Ref.	Notes
J04555605+3036209	XEST 26-062		330 ± 4		639 ± 39	1	
J04555636+3049374	...		<5		<35	1	
J04574903+3015195	...		<9		<15	1	
J05061674+2446102	CIDA 10		<6		<42	1	
J05064662+2104296	...		<6		<22	1	
J05075496+2500156	CIDA 12		51 ± 3		44 ± 6	1	

Notes. All fluxes are reported in mJy. Upper limits are reported at a 3σ level. The errors listed are the 1σ statistical measurement errors. Uncertainties in the absolute flux calibration at 70 μm, 100 μm and 160 μm are 2.64%, 2.75% and 4.15% respectively. Unresolved system fluxes in indicated with values in parenthesis.

a. *Herschel* PACS fluxes measured from the level 2.5 processed maps observed under the program KPGT_pandre_1.

b. *Herschel* PACS observations carried out under the program KPOT_bdent_1.

c. Multiple system of which the target listed is resolved with *Herschel* PACS in the Blue1 and/or Blue2 channel(s) but unresolved from its companion in the Red channel.

d. Multiple system of which the target listed is the later type secondary. The *Herschel* PACS fluxes reported are contaminated from the primary companion.

e. No far-IR observation exists for this target.

e. IRAS 04325+2402 falls outside of the coverage region from the KPGT_pandre_1 processed map at 160 μm.

References. This work; (2) Harvey et al. (2012); (3) Howard et al. (2013); (4) Rebull et al. (2010).

Table A.7: TBOSS flux density compilation submm - mm wavelengths, ordered by target RA.

2MASS	Other name	350μm	450μm	850μm	880μm	1.2mm	1.3mm	2.6mm	Ref.	Notes.
J04034997+2620382	XEST 06-006									
J04131414+2819108	LkCa 1		<89	<8			<14		1, D	
J04141188+2811535	...						<2		H	
J04141458+2827580	FN Tau						<18	<5	G	
J04141760+2806096	CIDA 1						14 ± 3	<8	G	
J04144730+2646264	FP Tau						<9	<9	G	
J04144739+2803055	XEST 20-066									
J04150515+2808462	CIDA 2		<165	<14					1	
J04151471+2800096	KPNO 1						<2		H	
J04152409+2910434	...									
J04155799+2746175	...									
J04161210+2756385	...						<4		A	
J04161885+2752155	...									
J04162725+2053091	...									
J04163048+3037053	...									
J04163911+2858491	...									
J04174955+2813318	KPNO 10						8 ± 1		A	
J04174965+2829362	V410 X-ray 1		<94	<9					1	
J04180796+2826036	V410 X-ray 3									
J04181710+2828419	V410 Anon 13						<9	<7	G	
J04183030+2743208	KPNO 11									
J04184023+2824245	V410 X-ray 4									
J04185115+2814332	KPNO 2						1.8 ± 0.8		H	
J04185813+2812234	IRAS 04158+2805		1600 ± 400	440 ± 40			110 ± 5		2, C	
J04190110+2819420	V410 X-ray 6						<2		A	
J04190126+2802487	KPNO 12						<2		H	
J04190197+2822332	V410 X-ray 5a									
J04193545+2827218	FR Tau						<15		D	
J04194657+2712552	[GKH94] 41									
J04201611+2821325	...						<2		A	
J04202555+2700355	...						8 ± 1		A	
J04202583+2819237	IRAS 04173+2812						<2		A	
J04203918+2717317	XEST 16-045									
J04205273+1746415	J2-157						<14		D	

Table A.7: continued.

2MASS	Other name	350μm	450μm	850μm	880μm	1.2mm	1.3mm	2.6mm	Ref.	Notes.
J04210795+2702204	CFHT 19						<3		A	
J04210934+2750368	...						<2		A	
J04213459+2701388	...						<3		A	
J04214013+2814224	XEST 21-026									
J04214631+2659296	CFHT 10						<4		A	
J04215450+2652315	...									
J04220007+1530248	IRAS 04191+1523 B		1800 ± 220	440 ± 20			110 ± 7		5, C	a
J04221332+1934392	...									
J04221644+2549118	CFHT 14									
J04222404+2646258	XEST 11-087									
J04230607+2801194	...						5 ± 1		A	
J04233539+2503026	FU Tau A						<2		A	
J04233573+2502596	FU Tau B						<2		A	
J04242090+2630511	...						<1		A	
J04242646+2649503	CFHT 9						<3		A	
J04244506+2701447	J1-4423		<52	<8			<11		1, D	
J04251550+2829275	...									
J04262939+2624137	KPNO 3						6 ± 1		A	
J04263055+2443558	...									
J04265732+2606284	KPNO 13									
J04270739+2215037	...									
J04272799+2612052	KPNO 4						<3		H	
J04274538+2357243	CFHT 15									
J04275730+2619183	IRAS 04248+2612	1178 ± 30	2960 ± 1024	560 ± 178			60 ± 7		9, C	c
...	L1521F-IRS	4600 ± 700	7000 ± 1800	1500 ± 500		600 ± 150			3	b
J04284263+2714039	...									
J04290068+2755033	...						<2		A	
J04292071+2633406	J1-507		<52	<6			<14		1, D	
J04292165+2701259	IRAS 04263+2654						<4		A	
J04292971+2616532	FW Tau A+B+C		<35	5 ± 1			<15		1, B	
J04294568+2630468	KPNO 5						<2		H	
J04295422+1754041	...									
J04295950+2433078	CFHT 20						<3		A	
J04300724+2608207	KPNO 6						<2		H	
J04302365+2359129	CFHT 16									

Table A.7: continued.

2MASS	Other name	350μm	450μm	850μm	880μm	1.2mm	1.3mm	2.6mm	Ref.	Notes.
J04305171+2441475	ZZ Tau IRS						106 ± 2		A	
J04305718+2556394	KPNO 7						<3		H	
J04311578+1820072	MHO 9									
J04311907+2335047	...									
J04312382+2410529	V927 Tau A+B		<1030	<10			<20		1, B	
J04312405+1800215	MHO 4						<10	<8	G	
J04312669+2703188	CFHT 13									
J04313613+1813432	LkHa 358						17 ± 1	4 ± 0.6	D, G	
J04315844+2543299	J1-665									
J04320329+2528078	...									
J04321606+1812464	MHO 5						<9	<8	G	
J04321786+2422149	CFHT 7									
J04322210+1827426	MHO 6						14 ± 2		A	
J04322329+2403013	...									
J04322415+2251083	...						<6		A	
J04322627+1827521	MHO 7									
J04323028+1731303	GG Tau Ba+Bb						<5		6	
J04324938+2253082	JH 112 B									
J04325026+2422115	...									
J04325119+1730092	LH 0429+17									
J04330197+2421000	MHO 8									
J04330781+2616066	KPNO 14									
J04330945+2246487	CFHT 12			4 ± 1			<3		8, A	
J04332621+2245293	XEST 17-036									
J04334171+1750402	...						6 ± 2		A	
J04334291+2526470	...									
J04334465+2615005	...						18 ± 2		A	
J04335245+2612548	...									
J04335252+2256269	XEST 17-059									
J04341527+2250309	CFHT 1						<3		H	
J04344544+2308027	...									
J04350850+2311398	CFHT 11									
J04353536+2408266	IRAS 04325+2402 C		606 ± 185	186 ± 11			110 ± 7		1, C	a
J04354183+2234115	KPNO 8									
J04354203+2252226	XEST 08-033									

Table A.7: continued.

2MASS	Other name	350μm	450μm	850μm	880μm	1.2mm	1.3mm	2.6mm	Ref.	Notes.
J04354526+2737130	...									
J04355143+2249119	KPNO 9						<2		H	
J04355209+2255039	XEST 08-047									
J04355286+2250585	XEST 08-049									
J04355760+2253574	...									
J04361030+2159364	...									
J04361038+2259560	CFHT 2			<6			<2		7, H	
J04362151+2351165	...						<5		A	
J04363893+2258119	CFHT 3						<2		H	
J04373705+2331080	...									
J04380083+2558572	ITG 2									
J04381486+2611399	...						2.3 ± 0.8		H	
J04381630+2326402	...									
J04382134+2609137	GM Tau			<3			<5	<2	8, G	
J04385859+2336351	...						13 ± 2		A	
J04385871+2323595	...									
J04390163+2336029	...						<7		A	
J04390396+2544264	CFHT 6						2.4 ± 0.4		E	
J04390637+2334179	...									
J04393364+2359212	...						<6		A	
J04394488+2601527	ITG 15						<6		A	
J04394748+2601407	CFHT 4			11 ± 2			2.4 ± 0.8		7, H	
J04400067+2358211	...						<6		A	
J04400174+2556292	...									
J04403979+2519061	...						<2		A	
J04410424+2557561	Haro 6-32									
J04411078+2555116	ITG 34						<5		A	
J04414489+2301513	...				<24				6	
J04414565+2301580	...				<24				6	
J04414825+2534304	...						2.2 ± 0.4		E	
J04422101+2520343	CIDA 7		990 ± 330	38 ± 8			<19	<5	1, G	d
J04432023+2940060	CIDA 14						<5	<2	G	
J04442713+2512164	IRAS S04414+2506		36 ± 15	10 ± 1			5.2 ± 0.3		4, 8, F	
J04464260+2459034	RXJ 04467+2459						<5	<2	G	
J04484189+1703374	...									

Table A.7: continued.

2MASS	Other name	350μm	450μm	850μm	880μm	1.2mm	1.3mm	2.6mm	Ref.	Notes.
J04520668+3047175	IRAS 04489+3042						15 ± 4		C	
J04552333+3027366	...						<3		H	
J04554046+3039057	...									
J04554535+3019389	...						<5		A	
J04554757+3028077	...				<23				6	
J04554801+3028050	...				<23				6	
J04554820+3030160	XEST 26-052									
J04554969+3019400	...						<3		A	
J04555288+3006523	...									
J04555605+3036209	XEST 26-062						9 ± 2		A	
J04555636+3049374	...									
J04574903+3015195	...						<2		H	
J05061674+2446102	CIDA 10		<94	<11					1	
J05064662+2104296	...									
J05075496+2500156	CIDA 12		<88	<7			<5	<2	1, G	

Notes. All fluxes are reported in mJy. Upper limits are reported at a 3σ level. The errors listed are the 1σ statistical measurement errors. The typical quoted, absolute flux calibration uncertainties at 350 μm and 450 μm are ~25%; at 850 μm is ~10% and with SCUBA-2 at 850 μm is ~ 5% Mohanty et al. (2013). The reported calibration uncertainties at mm wavelengths are ~10-20%.

a. Multiple system, of which the flux densities are unresolved.

b. The listed submm and mm uncertainties include both the statistical measurement errors and uncertainties in the absolute calibration.

c. The 450 μm and 850 μm uncertainties include both the statistical measurement errors and uncertainties in the absolute calibration.

d. An anomalous continuum slope is reported in Andrews & Williams (2005) for this member.

References. The spectral types and uncertainties have been extracted from the following references: he following references are for observations at 350 - 1200 μm: (1) Andrews & Williams (2005); (2) Andrews et al. (2008); (3) Bourke et al. (2006); (4) Bouy et al. (2008); (5) Francesco et al. (2008); (6) Harris et al. (2012); (7)Klein et al. (2003); (8) Mohanty et al. (2013); (9) Young et al. (2003).

The following references are for observations at 1.3 mm and 2.6 mm: (A) Andrews et al. (2013); (B) Beckwith et al. (1990); (C) Motte & André (2001); (D) Osterloh & Beckwith (1995); (E) Phan-Bao et al. (2011); (F) Ricci et al. (2013); (G) Schaefer et al. (2009); (H) Scholz et al. (2006).

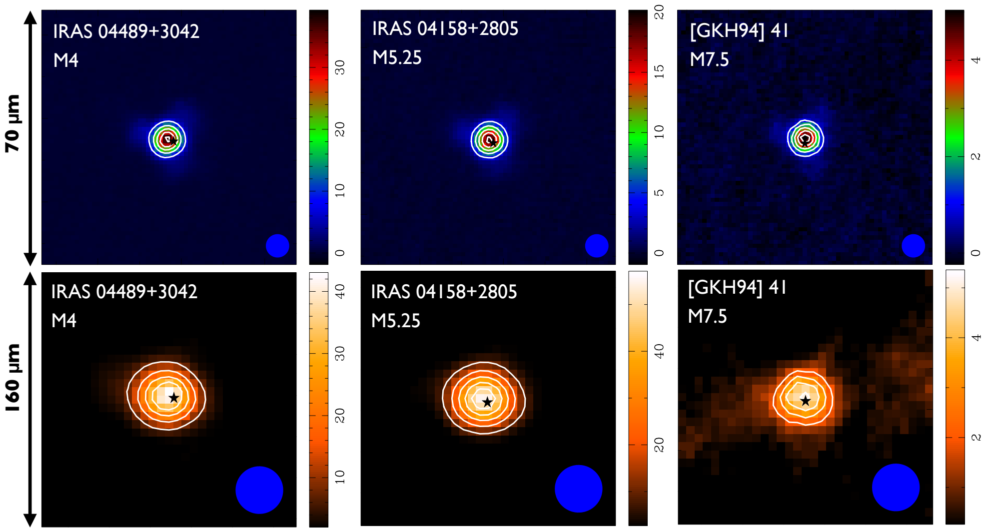

Figure A.1: Class I Blue & Red channel detections.

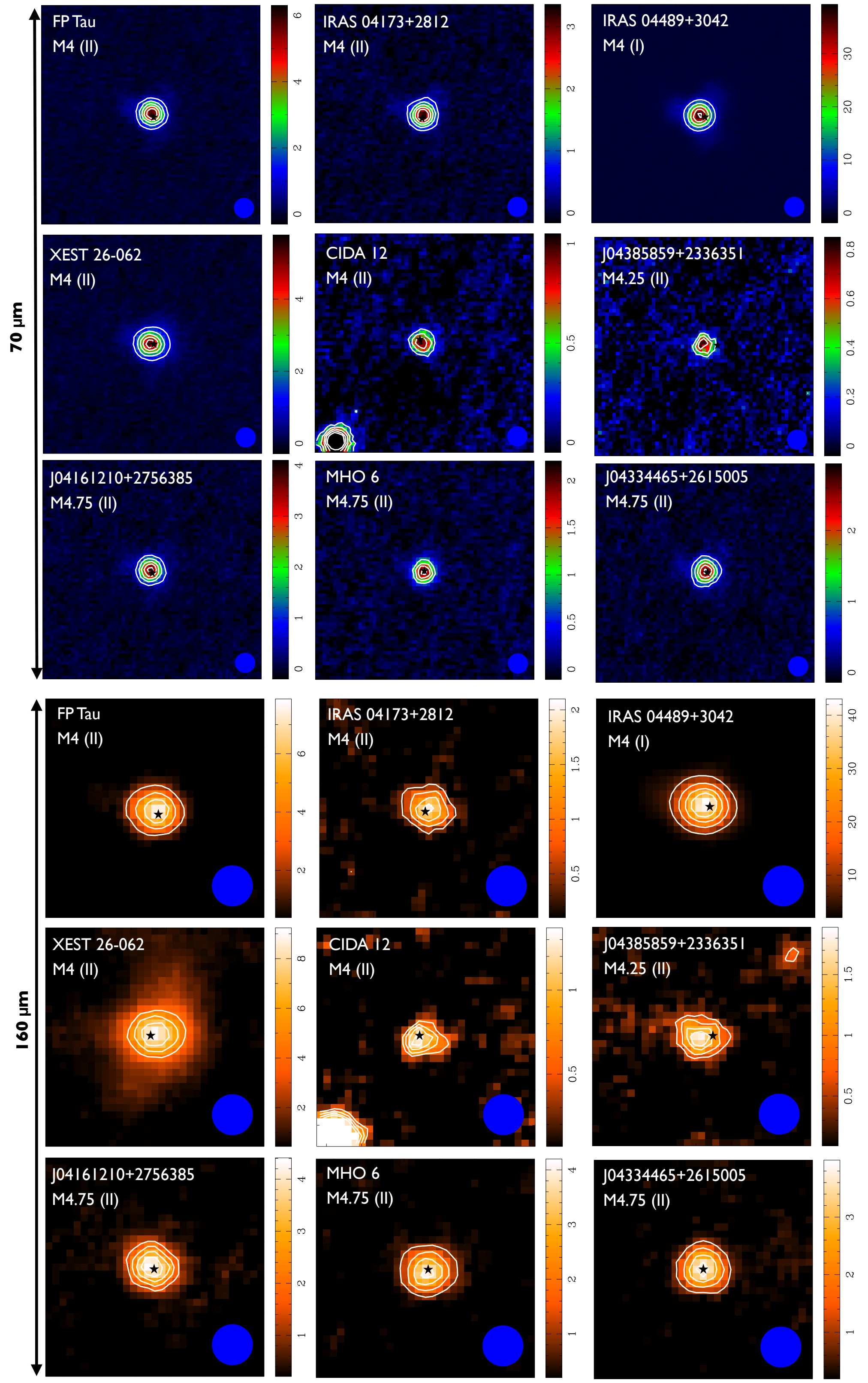

FIGURE A.2: Class II Blue & Red channel detections.

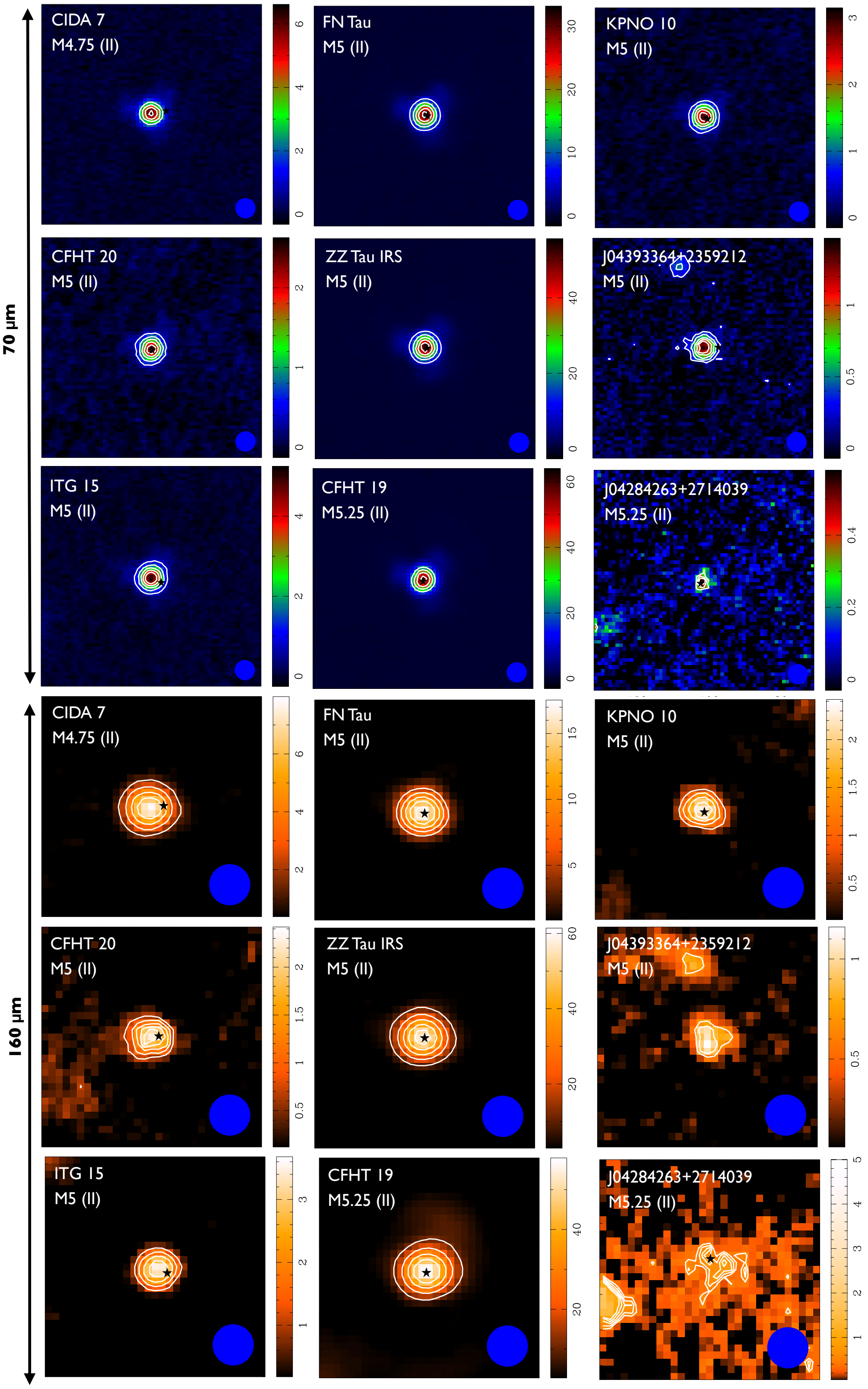

Figure A.3: Class II Blue & Red channel detections.

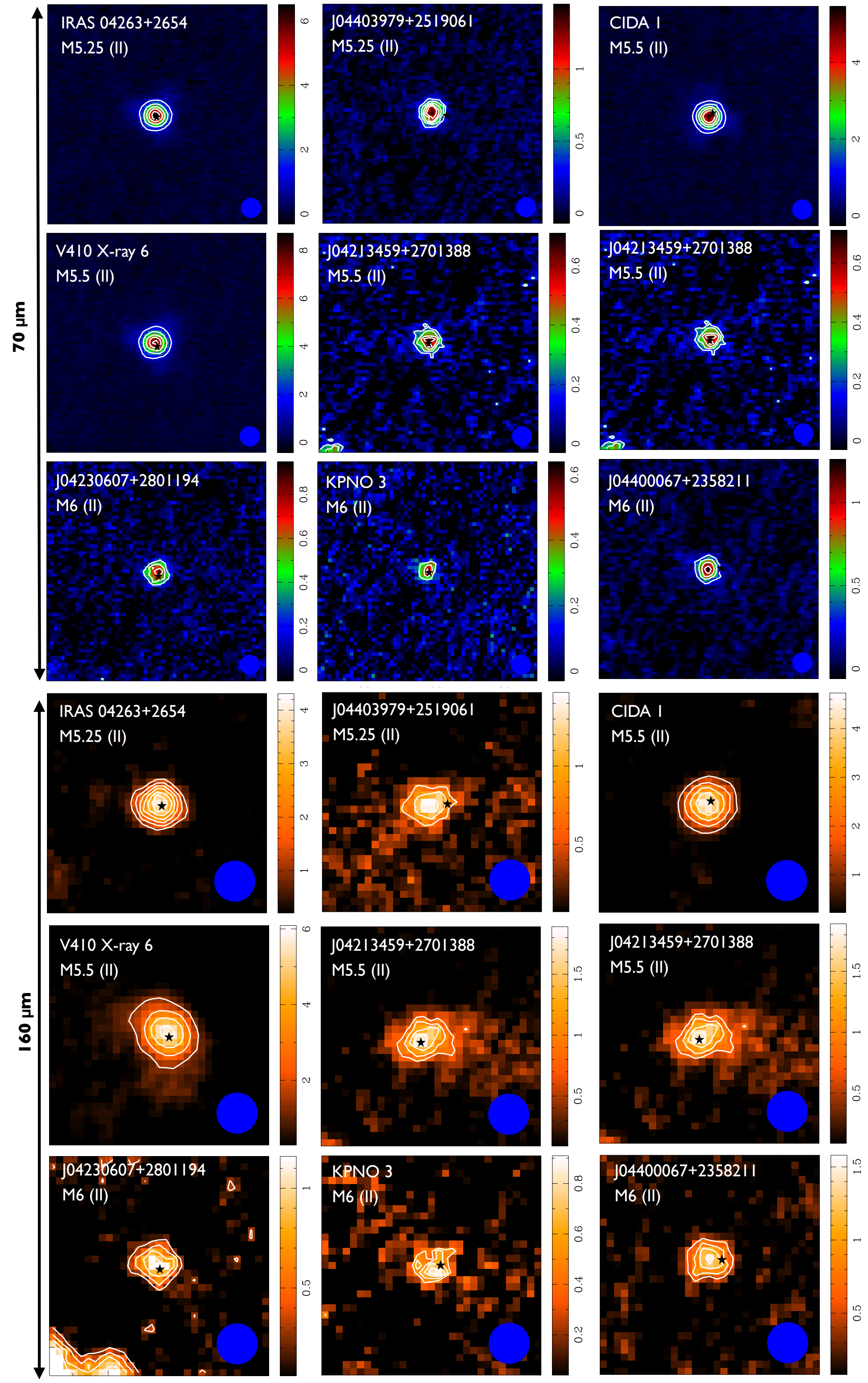

FIGURE A.4: Class II Blue & Red channel detections.

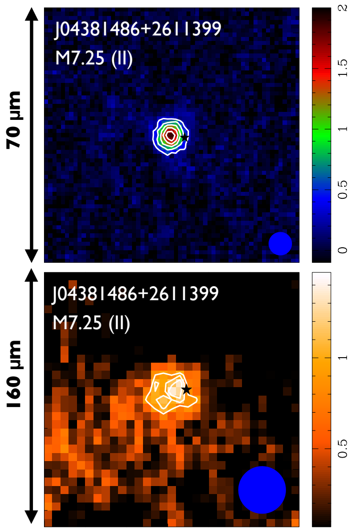

Figure A.5: Class II Blue & Red channel detections.

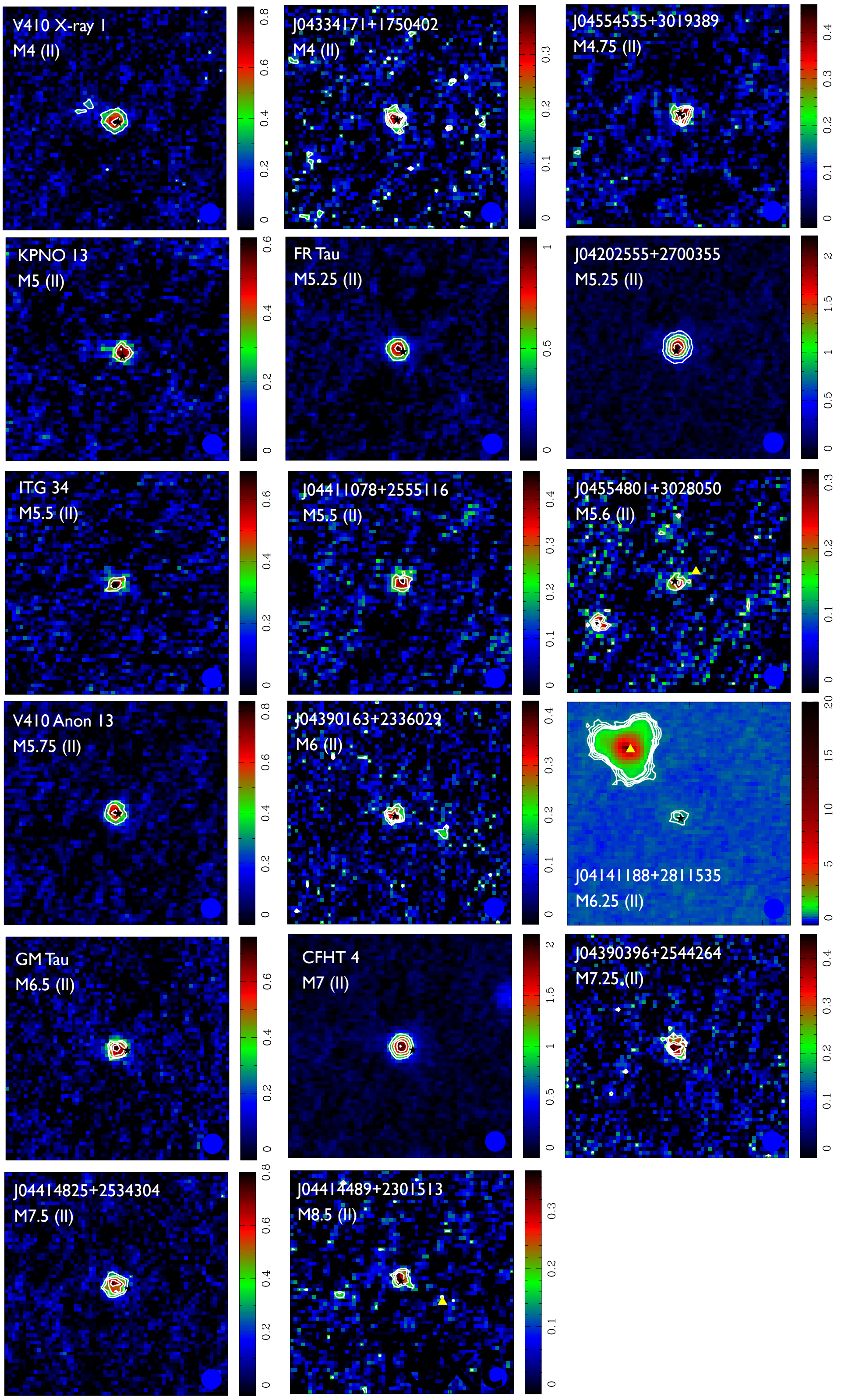

Figure A.6: Class II - Blue channel detections.

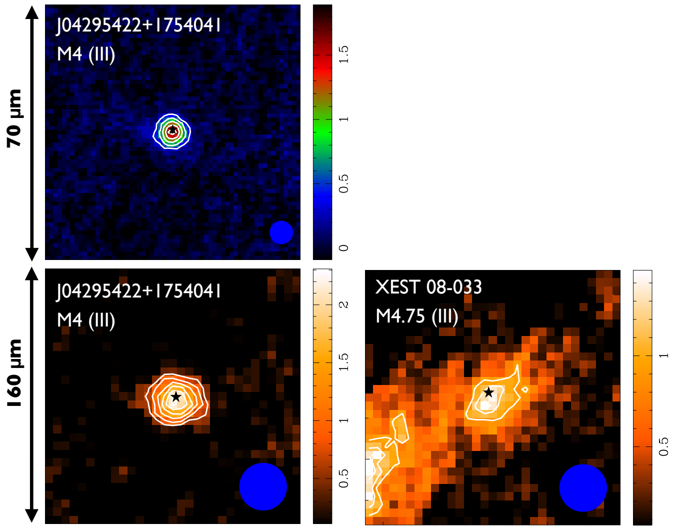

FIGURE A.7: Class III detections.

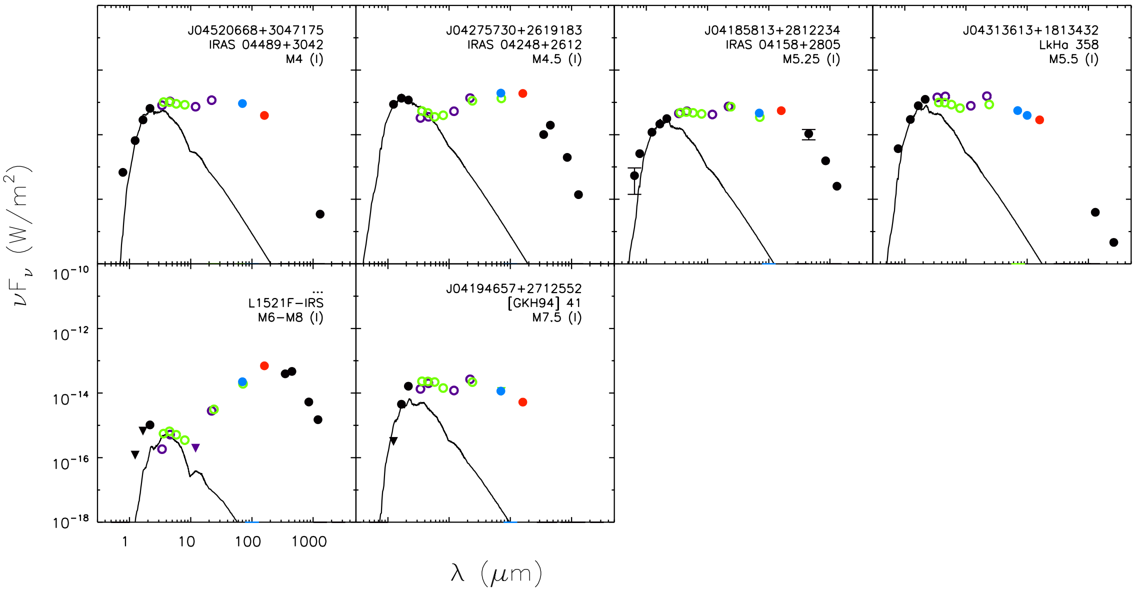

FIGURE A.8: Spectral energy distributions (SEDs) of the TBOSS of the Class I objects. The target name, spectral type, and spectral class are labelled in each SED. The observed broadband photometry is compiled from optical (R_C, I_C), and near-IR (2MASS; *JHK*) wavelengths (black points), the mid-IR (IRAC and *WISE*; green and purple open circles respectively), the far-IR (MIPS, PACS Blue and Red channels; green open circles, blue and red points respectively) and submm-mm wavelengths (black points). 3σ upper limits are represented by the downwards triangles. The best-fit atmospheric model are displayed for each target.

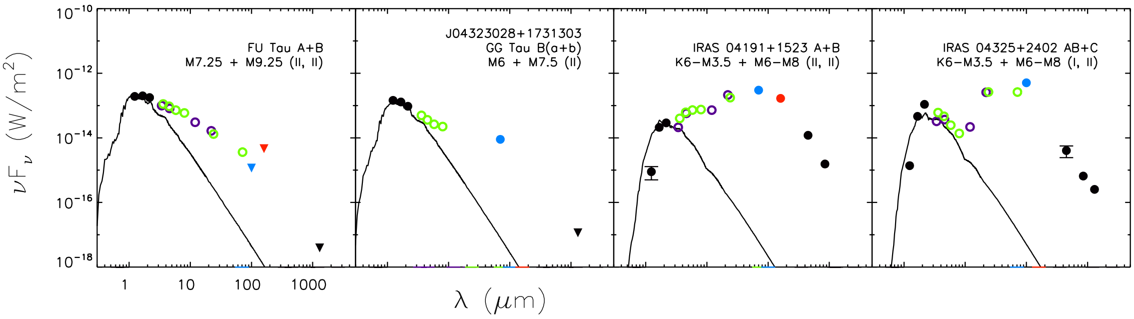

Figure A.9: SEDs for the four known TBOSS Class I and/or II multiple systems in which combined broadband photometry and atmospheric models of each of the system components was required. The system name, component spectral types, and spectral classes are labelled in each SED. The observed broadband photometry is compiled from optical (R_C, I_C), and near-IR (2MASS; *JHK*) wavelengths (black points), the mid-IR (IRAC and *WISE*; green and purple open circles respectively), the far-IR (MIPS, PACS Blue and Red channels; green open circles, blue and red points respectively) and submm-mm wavelengths (black points). 3σ upper limits are represented by the downwards triangles. The best-fit atmospheric model are displayed for each target.

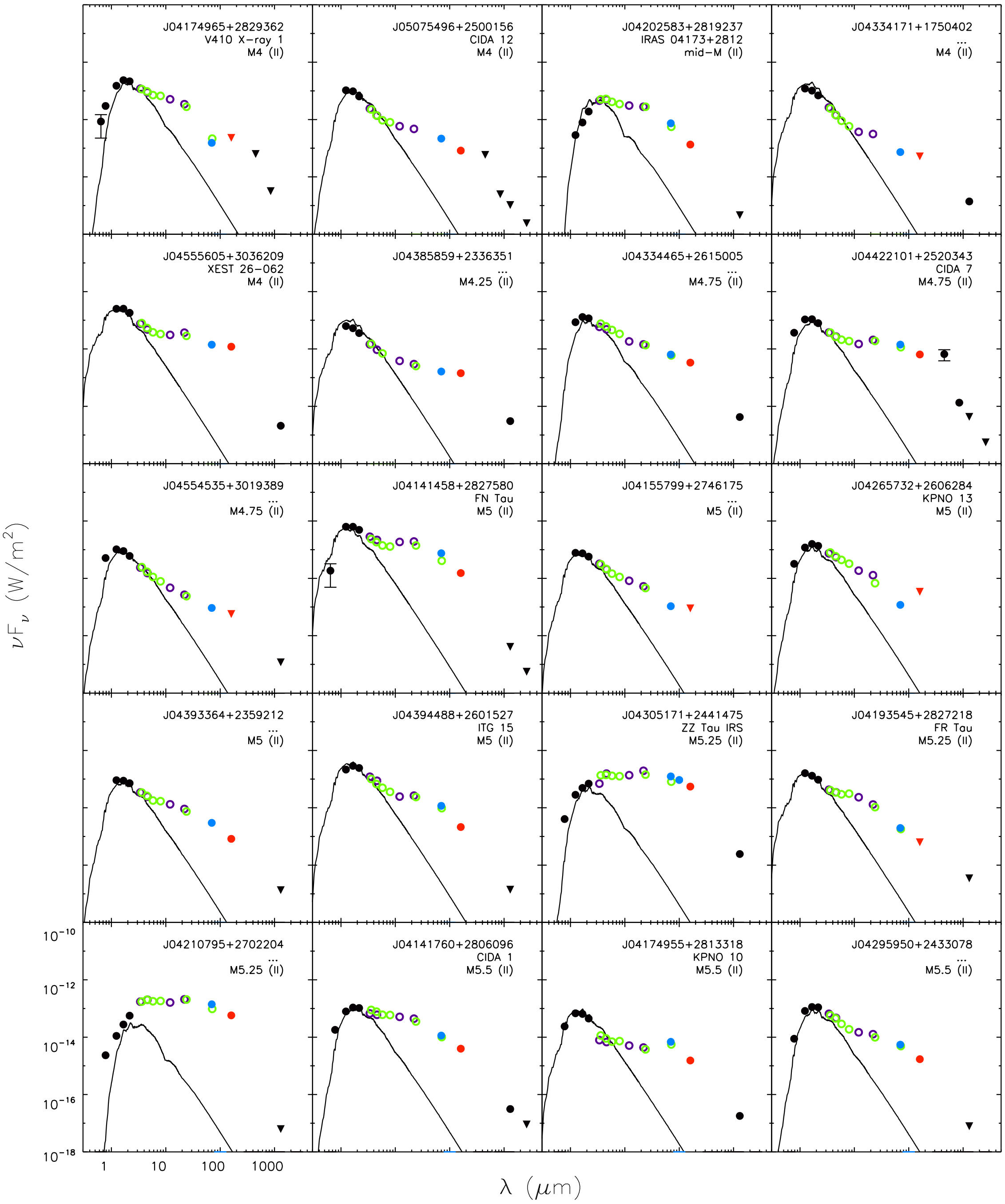

Figure A.10: SEDs of the detected Class II objects with spectral types M4-M5.5. The target name, spectral type, and spectral class are labelled in each SED. The observed broadband photometry is compiled from optical (R_C, I_C), and near-IR (2MASS; *JHK*) wavelengths (black points), the mid-IR (IRAC and *WISE*; green and purple open circles respectively), the far-IR (MIPS, PACS Blue and Red channels; green open circles, blue and red points respectively) and submm-mm wavelengths (black points). 3σ upper limits are represented by the downwards triangles. The best-fit atmospheric model are displayed for each target.

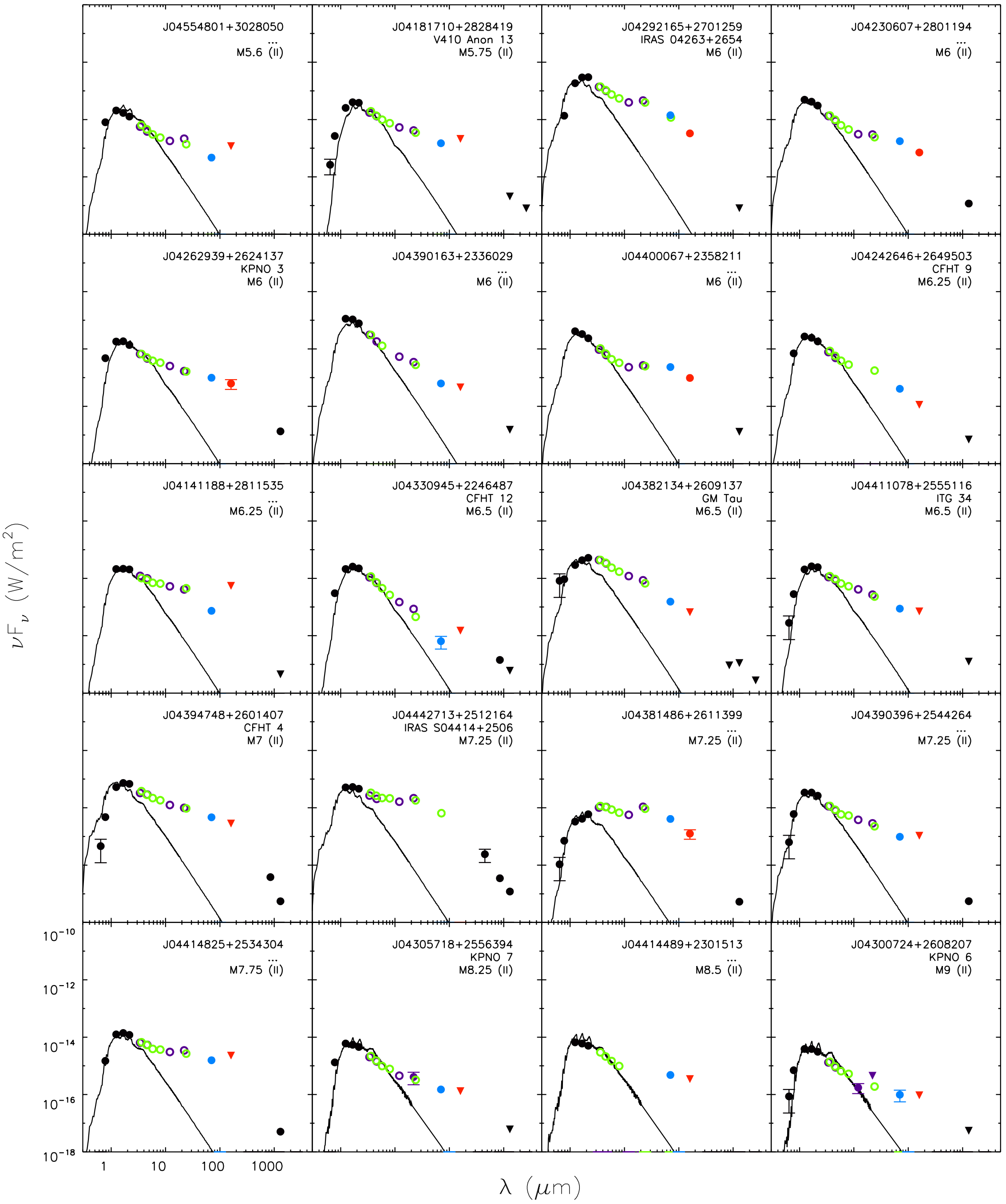

FIGURE A.11: SEDs of the detected Class II objects with spectral types M5.6-M9. The target name, spectral type, and spectral class are labelled in each SED. The observed broadband photometry is compiled from optical (R_C, I_C), and near-IR (2MASS; *JHK*) wavelengths (black points), the mid-IR (IRAC and *WISE*; green and purple open circles respectively), the far-IR (MIPS, PACS Blue and Red channels; green open circles, blue and red points respectively) and submm-mm wavelengths (black points). 3σ upper limits are represented by the downwards triangles. The best-fit atmospheric model are displayed for each target.

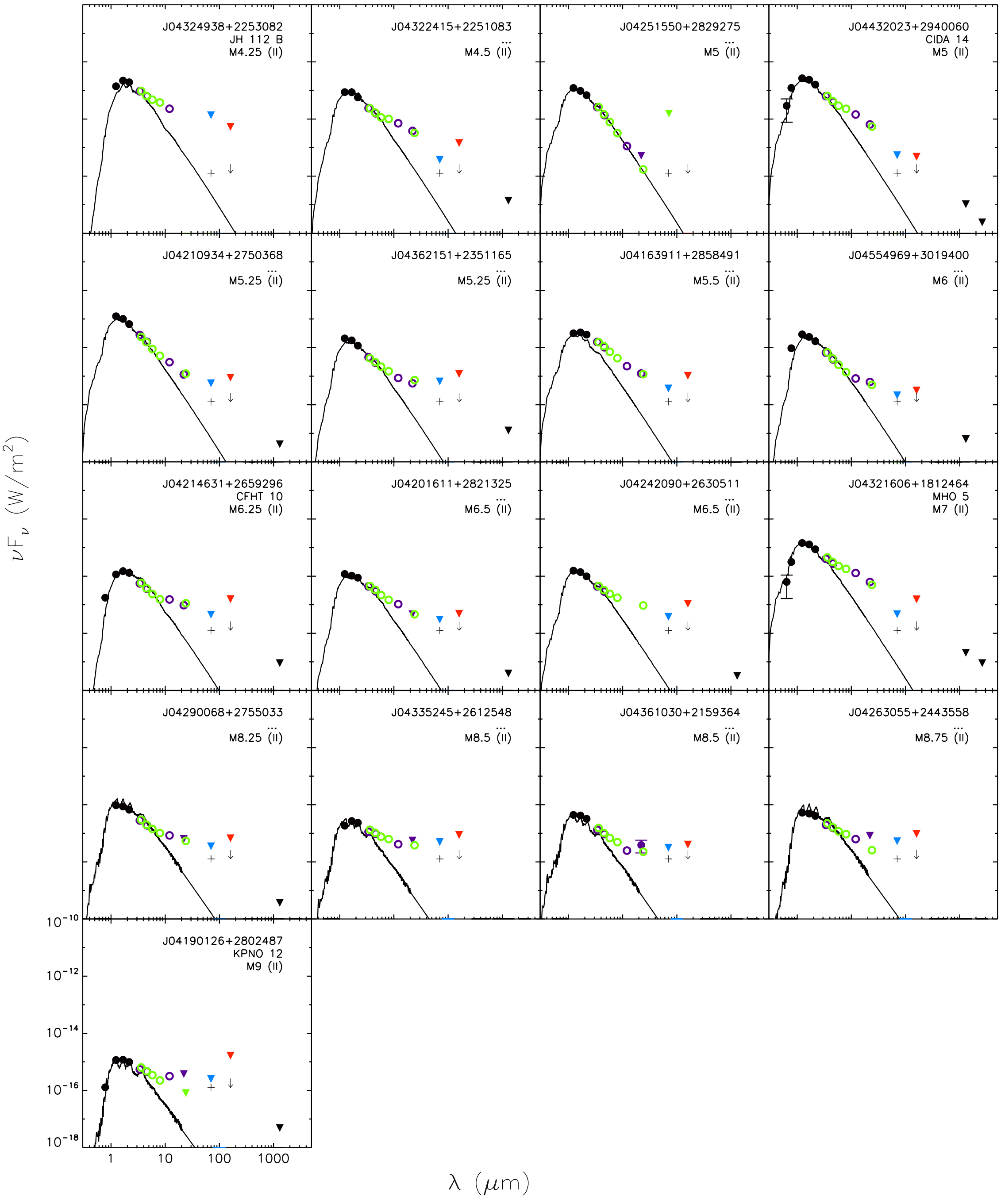

FIGURE A.12: SEDs of the undetected Class II objects with spectral types spanning M4.25-M9. The target name, spectral type, and spectral class are labelled in each SED. The observed broadband photometry is compiled from optical (R_C, I_C), and near-IR (2MASS; *JHK*) wavelengths (black points), the mid-IR (IRAC and *WISE*; green and purple open circles respectively), the far-IR (MIPS, PACS Blue and Red channels; green open circles, blue and red points respectively) and submm-mm wavelengths (black points). 3σ upper limits are represented by the downwards triangles. The best-fit atmospheric model are displayed for each target. The grey cross show level of the artificial detection generated from combined Class II upper limit maps.

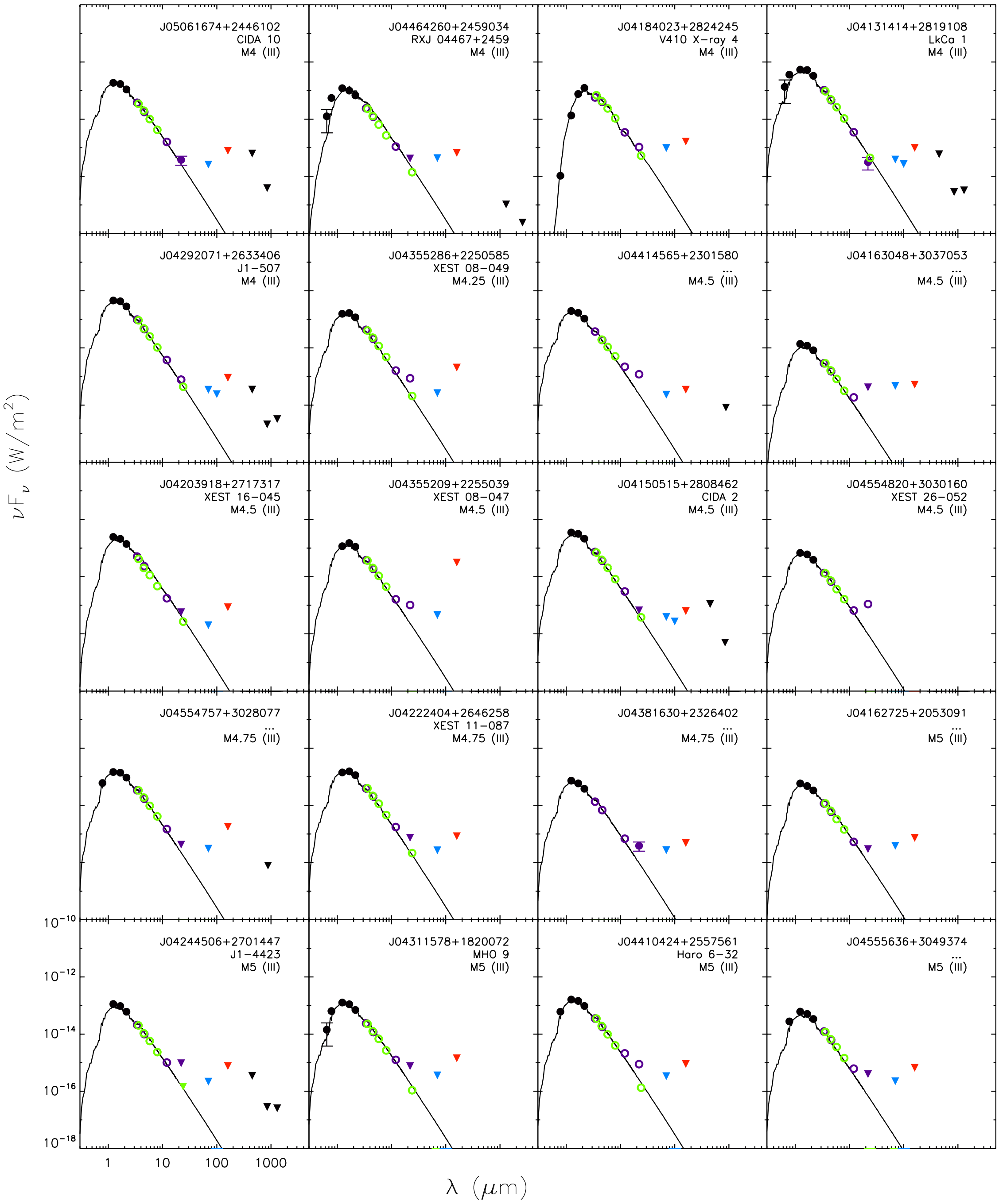

FIGURE A.13: SEDs of the undetected Class III objects with spectral types spanning M4-M5. The target name, spectral type, and spectral class are labelled in each SED. The observed broadband photometry is compiled from optical (R_C, I_C), and near-IR (2MASS; *JHK*) wavelengths (black points), the mid-IR (IRAC and *WISE*; green and purple open circles respectively), the far-IR (MIPS, PACS Blue and Red channels; green open circles, blue and red points respectively) and submm-mm wavelengths (black points). 3σ upper limits are represented by the downwards triangles. The best-fit atmospheric model are displayed for each target.

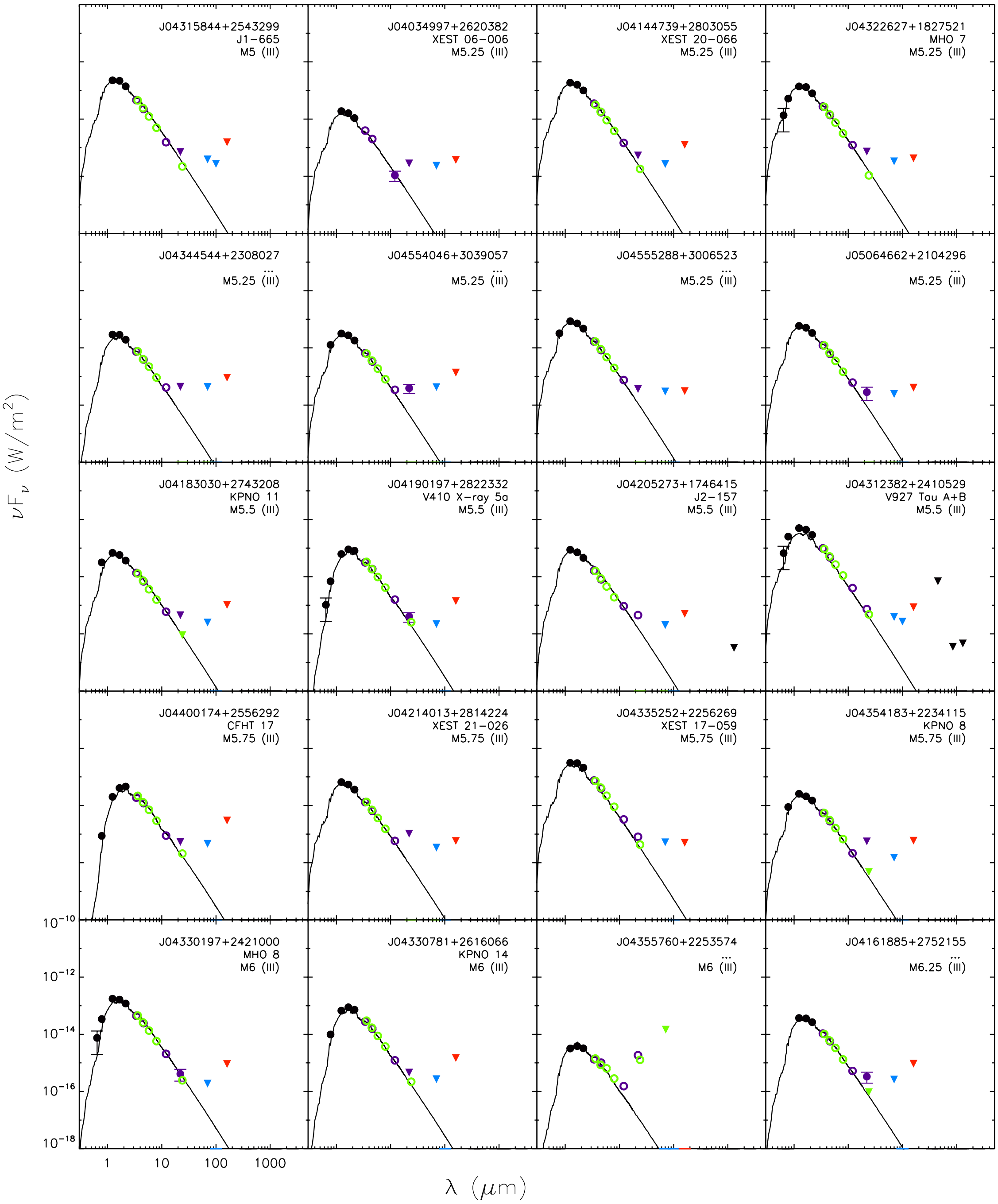

Figure A.14: SEDs of the undetected Class III objects with spectral types spanning M5-M6.25. The target name, spectral type, and spectral class are labelled in each SED. The observed broadband photometry is compiled from optical (R_C, I_C), and near-IR (2MASS; *JHK*) wavelengths (black points), the mid-IR (IRAC and *WISE*; green and purple open circles respectively), the far-IR (MIPS, PACS Blue and Red channels; green open circles, blue and red points respectively) and submm-mm wavelengths (black points). 3σ upper limits are represented by the downwards triangles. The best-fit atmospheric model are displayed for each target.

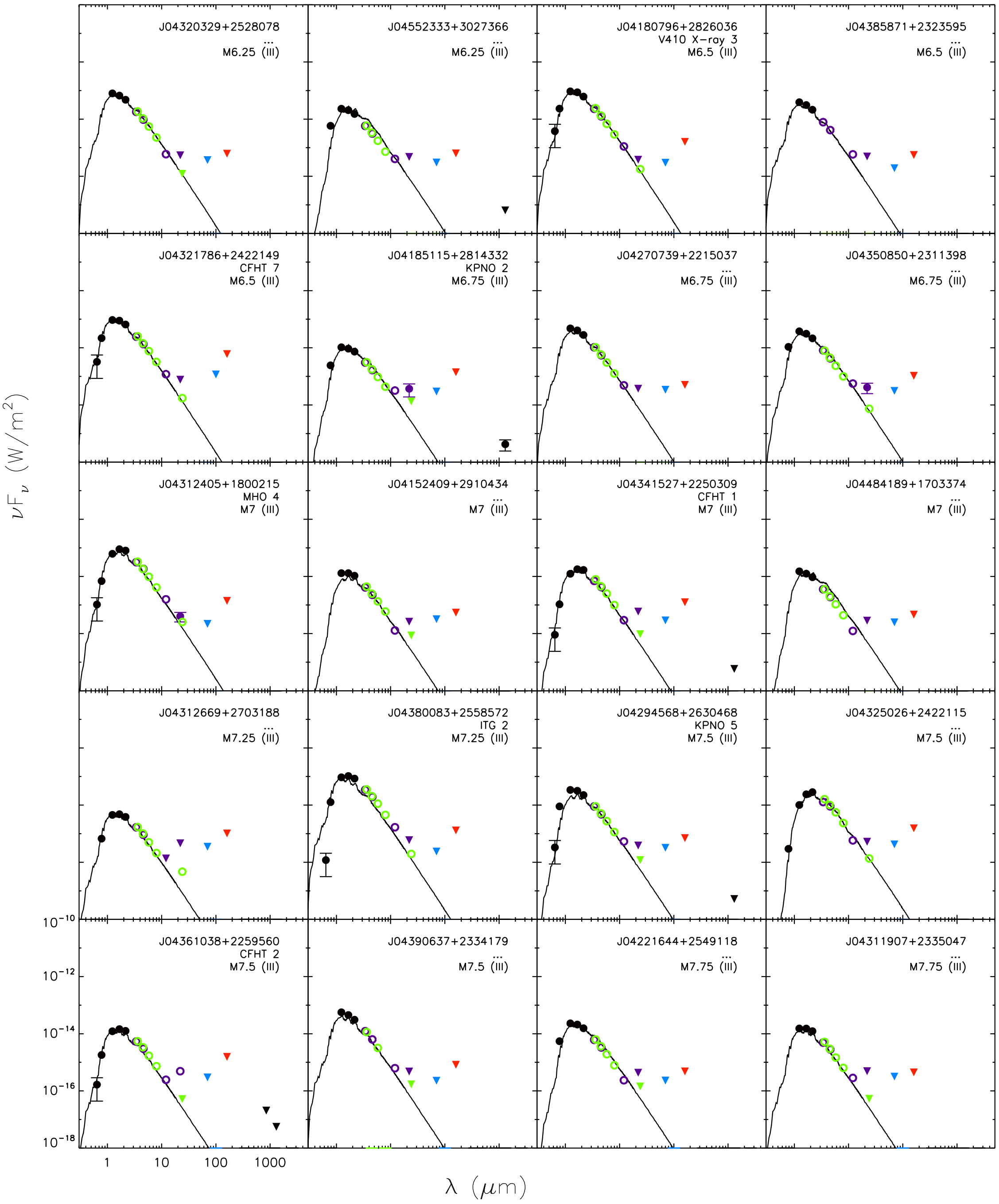

FIGURE A.15: SEDs of the undetected Class III objects with spectral types spanning M5-M6.25. The target name, spectral type, and spectral class are labelled in each SED. The observed broadband photometry is compiled from optical (R_C, I_C), and near-IR (2MASS; *JHK*) wavelengths (black points), the mid-IR (IRAC and *WISE*; green and purple open circles respectively), the far-IR (MIPS, PACS Blue and Red channels; green open circles, blue and red points respectively) and submm-mm wavelengths (black points). 3σ upper limits are represented by the downwards triangles. The best-fit atmospheric model are displayed for each target.

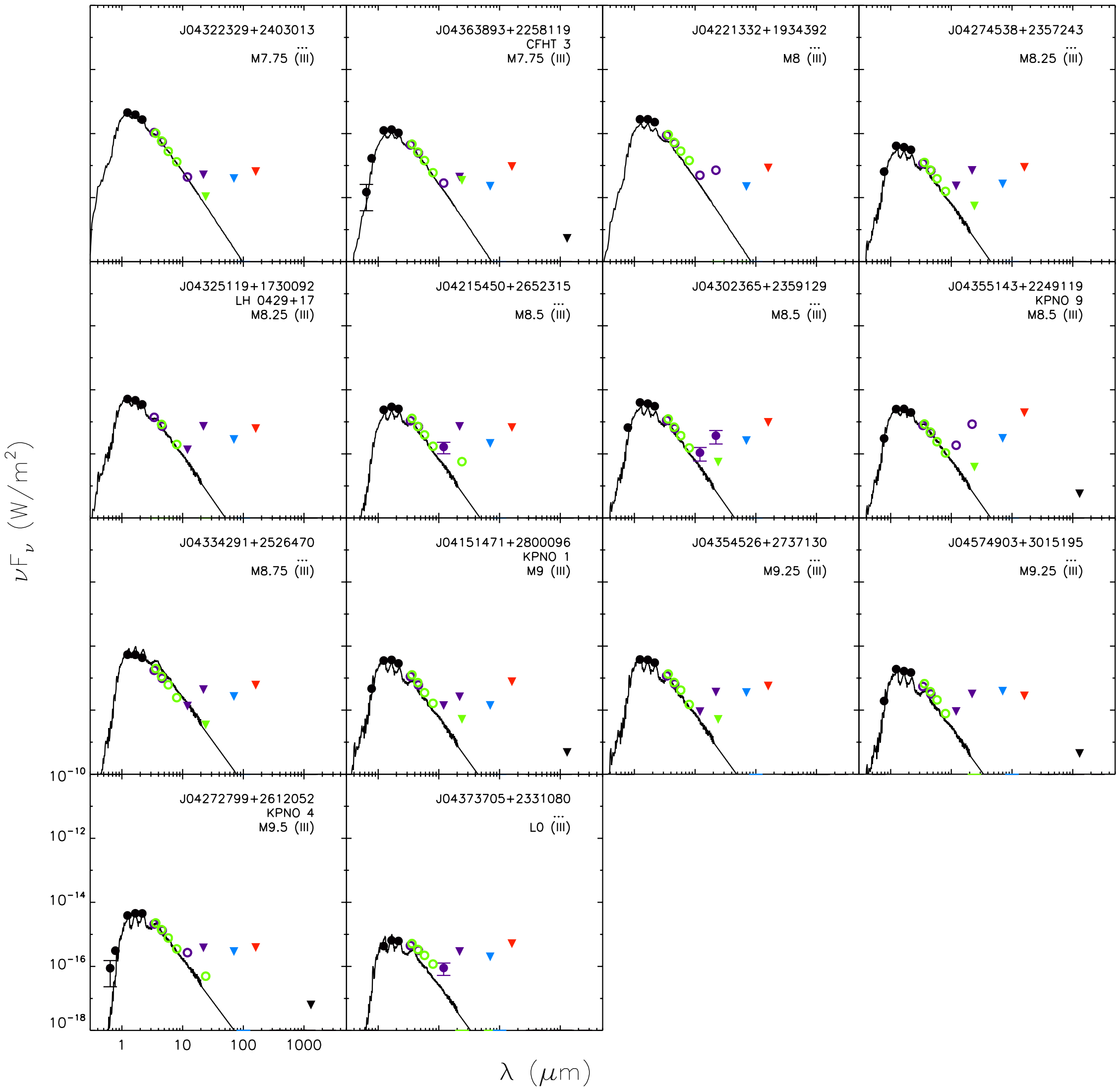

FIGURE A.16: SEDs of the undetected Class III objects with spectral types spanning M5-M6.25. The target name, spectral type, and spectral class are labelled in each SED. The observed broadband photometry is compiled from optical (R_C, I_C), and near-IR (2MASS; *JHK*) wavelengths (black points), the mid-IR (IRAC and *WISE*; green and purple open circles respectively), the far-IR (MIPS, PACS Blue and Red channels; green open circles, blue and red points respectively) and submm-mm wavelengths (black points). 3σ upper limits are represented by the downwards triangles. The best-fit atmospheric model are displayed for each target.

References

Adams, F. C., Lada, C. J., & Shu, F. H. 1987, Astrophysical Journal, 312, 788

Ageorges, N., Menard, F., Monin, J.-L., & Eckart, A. 1994, Astronomy and Astrophysics (ISSN 0004-6361), 283, L5

Alexander, R. D., Clarke, C. J., & Pringle, J. E. 2006, Monthly Notices of the Royal Astronomical Society, 369, 229

Ali, B., Sellgren, K., Depoy, D. L., et al. 1998, ASP Conf. Ser. 154, 154, 1663, iSBN: 1-886733-74-0

Allard, F., Guillot, T., Ludwig, H.-G., et al. 2003, Brown Dwarfs, 211, 325

Allard, F., Hauschildt, P. H., Alexander, D. R., Tamanai, A., & Schweitzer, A. 2001, The Astrophysical Journal, 556, 357

Allard, F., Homeier, D., & Freytag, B. 2011, 16th Cambridge Workshop on Cool Stars, 448, 91

Andre, P., Ward-Thompson, D., & Barsony, M. 1993, Astrophysical Journal, 406, 122

André, P., Ward-Thompson, D., & Greaves, J. 2012, Science, 337, 69, (c) 2012: Science

Andrews, S. M., Liu, M. C., Williams, J. P., & Allers, K. N. 2008, The Astrophysical Journal, 685, 1039

Andrews, S. M., Rosenfeld, K. A., Kraus, A. L., & Wilner, D. J. 2013, arXiv, astro-ph.SR

Andrews, S. M. & Williams, J. P. 2005, The Astrophysical Journal, 631, 1134

Andrews, S. M. & Williams, J. P. 2007, The Astrophysical Journal, 671, 1800

Andrews, S. M., Wilner, D. J., Espaillat, C., et al. 2011, The Astrophysical Journal, 732, 42

Artymowicz, P. & Lubow, S. H. 1994, Astrophysical Journal, 421, 651

Aumann, H. H., Beichman, C. A., Gillett, F. C., et al. 1984, Astrophysical Journal, 278, L23

Backman, D. E. & Paresce, F. 1993, In: Protostars and planets III (A93-42937 17-90), 1253

Baillié, K. & Charnoz, S. 2014, arXiv, astro-ph.EP

Balega, I. I., Balega, Y. Y., Maksimov, A. F., et al. 2007, Astrophysical Bulletin, 62, 339

Baraffe, I., Chabrier, G., Allard, F., & Hauschildt, P. H. 1998, Astronomy and Astrophysics, 337, 403

Basu, S. & Vorobyov, E. I. 2012, The Astrophysical Journal, 750, 30

Bate, M. R., Bonnell, I. A., & Bromm, V. 2003, Monthly Notice of the Royal Astronomical Society, 339, 577

Beckwith, S. V. W. & Sargent, A. I. 1991, Astrophysical Journal, 381, 250

Beckwith, S. V. W., Sargent, A. I., Chini, R. S., & Guesten, R. 1990, Astronomical Journal (ISSN 0004-6256), 99, 924

Behrend, R. & Maeder, A. 2001, Astronomy and Astrophysics, 373, 190

Beichman, C. A., Tanner, A., Bryden, G., et al. 2006, The Astrophysical Journal, 639, 1166

Berta, S., Magnelli, B., Nordon, R., et al. 2011, Astronomy & Astrophysics, 532, 49

Bertout, C., Robichon, N., & Arenou, F. 1999, Astronomy and Astrophysics, 352, 574

Bessell, M. S. 1979, Astronomical Society of the Pacific, 91, 589, a&AA ID. AAA026.113.045

Blanford, G. E. 1982, LUNAR AND PLANETARY SCIENCE XIII, 13, 47

Boden, A. F., Torres, G., Duchêne, G., et al. 2012, The Astrophysical Journal, 747, 17

Boden, A. F., Torres, G., Sargent, A. I., et al. 2007, The Astrophysical Journal, 670, 1214

Booth, M., Kennedy, G., Sibthorpe, B., et al. 2013, Monthly Notices of the Royal Astronomical Society, 428, 1263

Boss, A. P. 1997, Science, 276, 1836

Bourke, T. L., Myers, P. C., Evans, N. J., et al. 2006, The Astrophysical Journal, 649, L37

Bouy, H., Huélamo, N., Pinte, C., et al. 2008, Astronomy and Astrophysics, 486, 877

Briceño, C., Calvet, N., Kenyon, S., & Hartmann, L. 1999, The Astronomical Journal, 118, 1354

Briceño, C., Hartmann, L., Stauffer, J., & Martín, E. 1998, The Astronomical Journal, 115, 2074

Briceño, C., Luhman, K. L., Hartmann, L., Stauffer, J. R., & Kirkpatrick, J. D. 2002, The Astrophysical Journal, 580, 317

Brown, J. M., Blake, G. A., Dullemond, C. P., et al. 2007, The Astrophysical Journal, 664, L107

Bryden, G., Beichman, C. A., Trilling, D. E., et al. 2006, The Astrophysical Journal, 636, 1098

Burns, J. A., Lamy, P. L., & Soter, S. 1979, Icarus, 40, 1, a&AA ID. AAA026.106.016

Burrows, C. J., Stapelfeldt, K. R., Watson, A. M., et al. 1996, Astrophysical Journal v.473, 473, 437

Calvet, N., D'Alessio, P., Watson, D. M., et al. 2005, The Astrophysical Journal, 630, L185

Cameron, A. G. W. 1997, Icarus, 126, 126

Canup, R. M. 2007, 38th Lunar and Planetary Science Conference, 38, 2137

Carpenter, J. M. 2002, The Astronomical Journal, 124, 1593

Carpenter, J. M., Bouwman, J., Mamajek, E. E., et al. 2009, The Astrophysical Journal Supplement, 181, 197

Carpenter, J. M., Wolf, S., Schreyer, K., Launhardt, R., & Henning, T. 2005, The Astronomical Journal, 129, 1049

Chabrier, G., Baraffe, I., Allard, F., & Hauschildt, P. 2000, The Astrophysical Journal, 542, 464

Chambers, J. E. 2001, Icarus, 152, 205

Chauvin, G., Lagrange, A.-M., Dumas, C., et al. 2004, Astronomy and Astrophysics, 425, L29

Chen, C. H., Sargent, B. A., Bohac, C., et al. 2006, The Astrophysical Journal Supplement Series, 166, 351

Chiang, E. I. & Goldreich, P. 1997, Astrophysical Journal v.490, 490, 368

Cieza, L. A., Schreiber, M. R., Romero, G. A., et al. 2012, The Astrophysical Journal, 750, 157

Clarke, C. J. & Pringle, J. E. 1991, Monthly Notices of the Royal Astronomical Society (ISSN 0035-8711), 249, 588

Cohen, B. A., Swindle, T. D., & Kring, D. A. 2000, Science, 290, 1754

Cohen, M., Wheaton, W. A., & Megeath, S. T. 2003, The Astronomical Journal, 126, 1090

Currie, T., Burrows, A., Itoh, Y., et al. 2011, The Astrophysical Journal, 729, 128

Currie, T., Lada, C. J., Plavchan, P., et al. 2009, The Astrophysical Journal, 698, 1

Cutri, R. M. & et al. 2012, VizieR On-line Data Catalog, 2311, 0

Cutri, R. M., Skrutskie, M. F., van Dyk, S., et al. 2003, The IRSA 2MASS All-Sky Point Source Catalog

Daemgen, S., Correia, S., & Petr-Gotzens, M. G. 2012, Astronomy & Astrophysics, 540, 46

Dame, T. M., Hartmann, D., & Thaddeus, P. 2001, The Astrophysical Journal, 547, 792

de Oliveira, C. A., Ábrahám, P., Marton, G., et al. 2013, arXiv, astro-ph.GA, accepted for publication in A&A

Dent, W. R. F., Thi, W. F., Kamp, I., et al. 2013, Publications of the Astronomical Society of the Pacific, 125, 477

Dent, W. R. F., Walker, H. J., Holland, W. S., & Greaves, J. S. 2000, Monthly Notices of the Royal Astronomical Society, 314, 702

Dobashi, K., Uehara, H., Kandori, R., et al. 2005, Publications of the Astronomical Society of Japan, 57, 1

Dodson-Robinson, S. E., Veras, D., Ford, E. B., & Beichman, C. A. 2009, The Astrophysical Journal, 707, 79

Dowell, C. D., Allen, C. A., Babu, R. S., et al. 2003, Millimeter and Submillimeter Detectors for Astronomy. Edited by Phillips, 4855, 73

Duchêne, G., Bouvier, J., Bontemps, S., André, P., & Motte, F. 2004, Astronomy and Astrophysics, 427, 651

Dullemond, C. P. & Dominik, C. 2004a, Astronomy and Astrophysics, 421, 1075

Dullemond, C. P. & Dominik, C. 2004b, Astronomy and Astrophysics, 417, 159

Dullemond, C. P., Hollenbach, D., Kamp, I., & D'Alessio, P. 2006, arXiv, astro-ph, review chapter in "Protostars and Planets V"

Dunne, L. & Eales, S. A. 2001, Monthly Notices of the Royal Astronomical Society, 327, 697

Eisner, J. A. & Carpenter, J. M. 2003, The Astrophysical Journal, 598, 1341

Eisner, J. A., Plambeck, R. L., Carpenter, J. M., et al. 2008, The Astrophysical Journal, 683, 304

Elmegreen, B. G. & Lada, C. J. 1977, Astrophysical Journal, 214, 725, a&AA ID. AAA019.152.005

Engelbracht, C. W., Blaylock, M., Su, K. Y. L., et al. 2007, The Publications of the Astronomical Society of the Pacific, 119, 994

Espaillat, C., Furlan, E., D'Alessio, P., et al. 2011, The Astrophysical Journal, 728, 49

Fabrycky, D. C. & Murray-Clay, R. A. 2010, The Astrophysical Journal, 710, 1408

Fazio, G. G., Hora, J. L., Allen, L. E., et al. 2004, The Astrophysical Journal Supplement Series, 154, 10

Francesco, J. D., Johnstone, D., Kirk, H., MacKenzie, T., & Ledwosinska, E. 2008, The Astrophysical Journal Supplement Series, 175, 277

Friesen, R. K., Johnstone, D., Naylor, D. A., & Davis, G. R. 2005, Monthly Notices of the Royal Astronomical Society, 361, 460

Furlan, E., Luhman, K. L., Espaillat, C., et al. 2011, The Astrophysical Journal Supplement, 195, 3

Ghez, A. M., Neugebauer, G., & Matthews, K. 1993, Astronomical Journal (ISSN 0004-6256), 106, 2005

Goldsmith, P. F., Bergin, E. A., & Lis, D. C. 1997, Astrophysical Journal v.491, 491, 615

Gomes, R., Levison, H. F., Tsiganis, K., & Morbidelli, A. 2005, Nature, 435, 466

Gomez, M., Hartmann, L., Kenyon, S. J., & Hewett, R. 1993, Astronomical Journal (ISSN 0004-6256), 105, 1927

Goździewski, K. & Migaszewski, C. 2009, Monthly Notices of the Royal Astronomical Society: Letters, 397, L16

Greaves, J. S. 2005, Science, 307, 68

Greaves, J. S., Holland, W. S., Moriarty-Schieven, G., et al. 1998, The Astrophysical Journal, 506, L133

Greene, T. P. & Meyer, M. R. 1995, Astrophysical Journal v.450, 450, 233

Griffin, M. J. & Orton, G. S. 1993, Icarus, 105, 537

Guieu, S., Dougados, C., Monin, J.-L., Magnier, E., & Martín, E. L. 2006, Astronomy and Astrophysics, 446, 485

Guieu, S., Pinte, C., Monin, J.-L., et al. 2007, Astronomy and Astrophysics, 465, 855

Gullbring, E., Hartmann, L., Briceno, C., & Calvet, N. 1998, Astrophysical Journal v.492, 492, 323

Habing, H. J., Dominik, C., de Muizon, M. J., et al. 1999, Nature, 401, 456

Haisch, K. E., Barsony, M., & Tinney, C. 2010, The Astrophysical Journal Letters, 719, L90

Haisch, K. E., Lada, E. A., & Lada, C. J. 2001a, The Astronomical Journal, 121, 2065

Haisch, K. E., Lada, E. A., & Lada, C. J. 2001b, The Astrophysical Journal, 553, L153

Hambly, N. C., MacGillivray, H. T., Read, M. A., et al. 2001, Monthly Notices of the Royal Astronomical Society, 326, 1279

Harris, R. J., Andrews, S. M., Wilner, D. J., & Kraus, A. L. 2012, The Astrophysical Journal, 751, 115

Hartkopf, W. I. & Mason, B. D. 2009, The Astronomical Journal, 138, 813

Hartkopf, W. I. & McAlister, H. A. 1984, Astronomical Society of the Pacific, 96, 105

Hartmann, L. 1997, Herbig-Haro Flows and the Birth of Stars; IAU Symposium No. 182, 182, 391

Hartmann, L., Ballesteros-Paredes, J., & Bergin, E. A. 2001, The Astrophysical Journal, 562, 852

Hartmann, L., Calvet, N., Allen, L., Chen, H., & Jayawardhana, R. 1999, The Astronomical Journal, 118, 1784

Hartmann, W. K., Davis, D. R., Chapman, C. R., Soter, S., & Greenberg, R. 1975, International Astronomical Union, 25, 588, a&AA ID. AAA014.097.201

Harvey, P. M., Henning, T., Liu, Y., et al. 2012, The Astrophysical Journal, 755, 67

Hauschildt, P. H., Allard, F., & Baron, E. 1999, The Astrophysical Journal, 512, 377

Hennebelle, P. & Chabrier, G. 2008, The Astrophysical Journal, 684, 395

Henry, T. J. 1998, Brown dwarfs and extrasolar planets, 134, 28

Herbig, G. H. 1960, Astrophysical Journal Supplement, 4, 337

Hernández, J., Calvet, N., Briceño, C., et al. 2007, The Astrophysical Journal, 671, 1784

Hillenbrand, L. A. 1997, Astronomical Journal v.113, 113, 1733

Hillenbrand, L. A., Carpenter, J. M., Kim, J. S., et al. 2008, The Astrophysical Journal, 677, 630

Holland, W. S., Greaves, J. S., Zuckerman, B., et al. 1998, Nature, 392, 788

Hollenbach, D., Johnstone, D., Lizano, S., & Shu, F. 1994, The Astrophysical Journal, 428, 654

Hollenbach, D. J., Yorke, H. W., & Johnstone, D. 2000, Protostars and Planets IV (Book - Tucson: University of Arizona Press; eds Mannings, 401

Howard, A. W., Marcy, G. W., Bryson, S. T., et al. 2012, The Astrophysical Journal Supplement, 201, 15

Howard, C. D., Sandell, G., Vacca, W. D., et al. 2013, The Astrophysical Journal, 776, 21

Hughes, A. M., Wilner, D. J., Andrews, S. M., et al. 2011, The Astrophysical Journal, 740, 38

Hunter, T. R. 1998, The Publications of the Astronomical Society of the Pacific, 110, 634

Impey, C. D. & Neugebauer, G. 1988, Astronomical Journal (ISSN 0004-6256), 95, 307

Isella, A., Carpenter, J. M., & Sargent, A. I. 2010, The Astrophysical Journal, 714, 1746

Jayawardhana, R., Holland, W. S., Kalas, P., et al. 2002, The Astrophysical Journal, 570, L93

Jenness, T., Stevens, J. A., Archibald, E. N., et al. 2002, Monthly Notice of the Royal Astronomical Society, 336, 14

Jensen, E. L. N. & Akeson, R. L. 2003, The Astrophysical Journal, 584, 875

Jensen, E. L. N., Mathieu, R. D., & Fuller, G. A. 1994, The Astrophysical Journal, 429, L29

Johnson, J. A., Aller, K. M., Howard, A. W., & Crepp, J. R. 2010, Publications of the Astronomical Society of the Pacific, 122, 905

Joy, A. H. 1945, Astrophysical Journal, 102, 168

Kahn, F. D. 1974, Astronomy and Astrophysics, 37, 149, a&AA ID. AAA012.065.128

Kalas, P., Graham, J. R., Chiang, E., et al. 2008, Science, 322, 1345

Kenyon, S. J., Dobrzycka, D., & Hartmann, L. 1994, The Astronomical Journal (ISSN 0004-6256), 108, 1872

Kenyon, S. J. & Hartmann, L. 1987, Astrophysical Journal, 323, 714

Kenyon, S. J. & Hartmann, L. 1995, Astrophysical Journal Supplement v.101, 101, 117

Kim, K. H., Watson, D. M., Manoj, P., et al. 2013, The Astrophysical Journal, 769, 149

King, R. R., Parker, R. J., Patience, J., & Goodwin, S. P. 2012, Monthly Notices of the Royal Astronomical Society, 421, 2025

Kirsh, D. R., Duncan, M., Brasser, R., & Levison, H. F. 2009, , 199, 197

Kitamura, Y., Momose, M., Yokogawa, S., et al. 2002, The Astrophysical Journal, 581, 357

Klein, R., Apai, D., Pascucci, I., Henning, T., & Waters, L. B. F. M. 2003, The Astrophysical Journal, 593, L57

Kleine, T., Palme, H., Mezger, K., & Halliday, A. N. 2005, Science, 310, 1671

Koenigl, A. 1991, Astrophysical Journal, 370, L39

Kohler, R. & Leinert, C. 1998, Astronomy and Astrophysics, 331, 977

Konopacky, Q. M., Ghez, A. M., Rice, E. L., & Duchêne, G. 2007, The Astrophysical Journal, 663, 394

Könyves, V., André, P., Men'shchikov, A., et al. 2010, Astronomy and Astrophysics, 518, L106

Kovács, A. 2006, Proquest Dissertations And Theses 2006. Section 0036, 28

Kovács, A. 2008, Millimeter and Submillimeter Detectors and Instrumentation for Astronomy IV. Edited by Duncan, 7020, 45

Kraus, A. L. & Hillenbrand, L. A. 2009, The Astrophysical Journal, 703, 1511

Kraus, A. L., Ireland, M. J., Hillenbrand, L. A., & Martinache, F. 2012, The Astrophysical Journal, 745, 19

Kraus, A. L., Ireland, M. J., Martinache, F., & Hillenbrand, L. A. 2011, The Astrophysical Journal, 731, 8

Kuchner, M. J. & Holman, M. J. 2003, The Astrophysical Journal, 588, 1110

Lada, C. J. 1987, IN: Star forming regions; Proceedings of the Symposium, 115, 1

Lada, E. A. 1992, Astrophysical Journal, 393, L25

Lada, E. A., Depoy, D. L., Evans, N. J., & Gatley, I. 1991, Astrophysical Journal, 371, 171

Lafrenière, D., Marois, C., Doyon, R., & Barman, T. 2009, The Astrophysical Journal Letters, 694, L148

Lagrange, A.-M., Bonnefoy, M., Chauvin, G., et al. 2010, Science, 329, 57, (c) 2010: Science

Leinert, C., Zinnecker, H., Weitzel, N., et al. 1993, Astronomy and Astrophysics (ISSN 0004-6361), 278, 129

Leong, M., Peng, R., Houde, M., et al. 2006, Millimeter and Submillimeter Detectors and Instrumentation for Astronomy III. Edited by Zmuidzinas, 6275, 21

Lestrade, J.-F., Matthews, B. C., Sibthorpe, B., et al. 2012, Astronomy & Astrophysics, 548, 86

Lestrade, J.-F., Wyatt, M. C., Bertoldi, F., Dent, W. R. F., & Menten, K. M. 2006, Astronomy and Astrophysics, 460, 733

Liou, J.-C. & Zook, H. A. 1999, The Astronomical Journal, 118, 580

Lisse, C., Schultz, A., Fernandez, Y., et al. 2002, The Astrophysical Journal, 570, 779

Liu, M. C., Matthews, B. C., Williams, J. P., & Kalas, P. G. 2004, The Astrophysical Journal, 608, 526

Lubow, S. H., Seibert, M., & Artymowicz, P. 1999, The Astrophysical Journal, 526, 1001

Luhman, K. L. 2000, The Astrophysical Journal, 544, 1044

Luhman, K. L. 2004, The Astrophysical Journal, 617, 1216

Luhman, K. L. 2006, The Astrophysical Journal, 645, 676

Luhman, K. L., Adame, L., D'Alessio, P., et al. 2007, The Astrophysical Journal, 666, 1219

Luhman, K. L., Allen, P. R., Espaillat, C., Hartmann, L., & Calvet, N. 2010, The Astrophysical Journal Supplement, 186, 111

Luhman, K. L., Briceño, C., Stauffer, J. R., et al. 2003a, The Astrophysical Journal, 590, 348

Luhman, K. L., Hernández, J., Downes, J. J., Hartmann, L., & Briceño, C. 2008, The Astrophysical Journal, 688, 362

Luhman, K. L., Lada, C. J., Hartmann, L., et al. 2005, The Astrophysical Journal, 631, L69

Luhman, K. L., Mamajek, E. E., Allen, P. R., & Cruz, K. L. 2009a, The Astrophysical Journal, 703, 399

Luhman, K. L., Mamajek, E. E., Allen, P. R., Muench, A. A., & Finkbeiner, D. P. 2009b, The Astrophysical Journal, 691, 1265

Luhman, K. L. & Rieke, G. H. 1998, Astrophysical Journal v.497, 497, 354

Luhman, K. L., Stauffer, J. R., Muench, A. A., et al. 2003b, The Astrophysical Journal, 593, 1093

Luhman, K. L., Whitney, B. A., Meade, M. R., et al. 2006, The Astrophysical Journal, 647, 1180

Lynden-Bell, D. & Pringle, J. E. 1974, Monthly Notices of the Royal Astronomical Society, 168, 603, a&AA ID. AAA012.065.020

MacGregor, M. A., Wilner, D. J., Rosenfeld, K. A., et al. 2013, The Astrophysical Journal Letters, 762, L21

Malhotra, R. 1993, American Astronomical Society, 25, 1137

Mamajek, E. E. 2009, EXOPLANETS AND DISKS: THEIR FORMATION AND DIVERSITY: Proceedings of the International Conference. AIP Conference Proceedings, 1158, 3

Mannings, V. & Barlow, M. J. 1998, Astrophysical Journal v.497, 497, 330

Marois, C., Macintosh, B., Barman, T., et al. 2008, Science, 322, 1348

Marois, C., Zuckerman, B., Konopacky, Q. M., Macintosh, B., & Barman, T. 2010, Nature, 468, 1080, (c) 2010: Nature

Martín, E. L., Dougados, C., Magnier, E., et al. 2001, The Astrophysical Journal, 561, L195

Mathieu, R. D., Ghez, A. M., Jensen, E. L. N., & Simon, M. 2000, Protostars and Planets IV (Book - Tucson: University of Arizona Press; eds Mannings, 703

Mathis, J. S. 1990, IN: Annual review of astronomy and astrophysics. Vol. 28 (A91-28201 10-90). Palo Alto, 28, 37

Mathis, J. S., Rumpl, W., & Nordsieck, K. H. 1977, Astrophysical Journal, 217, 425, a&AA ID. AAA020.131.074

Matthews, B. C., Kennedy, G., Sibthorpe, B., et al. 2013, arXiv, astro-ph.SR

Mayne, N. J., Harries, T. J., Rowe, J., & Acreman, D. M. 2012, Monthly Notices of the Royal Astronomical Society, 423, 1775

McCarthy, D. W., Ge, J., Hinz, J. L., et al. 1998, American Astronomical Society, 193, 1265

McKee, C. F. & Ostriker, E. C. 2007, Annual Review of Astronomy & Astrophysics, 45, 565

Melis, C., Zuckerman, B., Rhee, J. H., et al. 2012, Nature, 487, 74

Miura, N., Iribe, T., Kubo, T., Baba, N., & Isobe, S. 1995, Publications of the National Astronomical Observatory of Japan, 4, 67

Mohanty, S., Greaves, J., Mortlock, D., et al. 2013, arXiv, astro-ph.SR, apJ, accepted (in press)

Monin, J.-L., Clarke, C. J., Prato, L., & McCabe, C. 2007, Protostars and Planets V, 395

Moór, A., Ábrahám, P., Derekas, A., et al. 2006, The Astrophysical Journal, 644, 525

Moór, A., Pascucci, I., Kóspál, Á., et al. 2011, The Astrophysical Journal Supplement, 193, 4

Moro-Martín, A., Rieke, G. H., & Su, K. Y. L. 2010, The Astrophysical Journal Letters, 721, L199

Moshir, M., Kopman, G., & Conrow, T. A. O. 1992, Pasadena: Infrared Processing and Analysis Center

Motte, F. & André, P. 2001, Astronomy and Astrophysics, 365, 440

Mouillet, D., Larwood, J. D., Papaloizou, J. C. B., & Lagrange, A. M. 1997, Royal Astronomical Society, 292, 896

Mulders, G. D. & Dominik, C. 2012, Astronomy & Astrophysics, 539, 9

Muzerolle, J., Allen, L. E., Megeath, S. T., Hernández, J., & Gutermuth, R. A. 2010, The Astrophysical Journal, 708, 1107

Najita, J. & Williams, J. P. 2005, The Astrophysical Journal, 635, 625

Natta, A., Testi, L., Calvet, N., et al. 2007, Protostars and Planets V, 767

Okamoto, Y. K., Kataza, H., Honda, M., et al. 2009, The Astrophysical Journal, 706, 665

Osterloh, M. & Beckwith, S. V. W. 1995, Astrophysical Journal, 439, 288

Ott, S. 2010, Astronomical Data Analysis Software and Systems XIX. Proceedings of a conference held October 4-8, 434, 139

Padgett, D. L., Brandner, W., Stapelfeldt, K. R., et al. 1999, The Astronomical Journal, 117, 1490

Padoan, P., Kritsuk, A., Michael, Norman, L., & Nordlund, Å. 2005, Memorie della Società Astronomica Italiana, 76, 187

Palla, F. & Stahler, S. W. 1999, The Astrophysical Journal, 525, 772

Pascucci, I., Laughlin, G., Gaudi, B. S., et al. 2011, 16th Cambridge Workshop on Cool Stars, 448, 469

Patience, J., Akeson, R. L., & Jensen, E. L. N. 2008, The Astrophysical Journal, 677, 616

Patience, J., Bulger, J., King, R. R., et al. 2011, Astronomy & Astrophysics, 531, L17

Perryman, M. A. C. & ESA. 1997, The Hipparcos and Tycho catalogues. Astrometric and photometric star catalogues derived from the ESA Hipparcos Space Astrometry Mission, 1200, iSBN: 9290923997

Phan-Bao, N., Lee, C.-F., Ho, P. T. P., & Tang, Y.-W. 2011, The Astrophysical Journal, 735, 14

Pilbratt, G. L., Riedinger, J. R., Passvogel, T., et al. 2010, Astronomy and Astrophysics, 518, L1

Pinte, C., Harries, T. J., Min, M., et al. 2009, Astronomy and Astrophysics, 498, 967

Pinte, C., Ménard, F., Duchêne, G., & Bastien, P. 2006, Astronomy and Astrophysics, 459, 797

Poglitsch, A., Waelkens, C., Geis, N., et al. 2010, Astronomy and Astrophysics, 518, L2

Pollack, J. B., Hollenbach, D., Beckwith, S., et al. 1994, Astrophysical Journal, 421, 615

Pollack, J. B., Hubickyj, O., Bodenheimer, P., et al. 1996, Icarus, 124, 62

Pound, M. W. & Blitz, L. 1993, Astrophysical Journal v.418, 418, 328

Quillen, A. C. & Faber, P. 2006, Monthly Notices of the Royal Astronomical Society, 373, 1245

Ratzka, T., Leinert, C., Henning, T., et al. 2007, Astronomy and Astrophysics, 471, 173

Reach, W. T., Megeath, S. T., Cohen, M., et al. 2005, The Publications of the Astronomical Society of the Pacific, 117, 978

Rebull, L. M., Padgett, D. L., McCabe, C.-E., et al. 2010, The Astrophysical Journal Supplement, 186, 259

Reche, R., Beust, H., Augereau, J.-C., & Absil, O. 2008, Astronomy and Astrophysics, 480, 551

Reid, I. N. & Gizis, J. E. 1997, Astronomical Journal v.113, 113, 2246

Reidemeister, M., Krivov, A. V., Schmidt, T. O. B., et al. 2009, Astronomy and Astrophysics, 503, 247

Reipurth, B. & Clarke, C. 2001, The Astronomical Journal, 122, 432

Rhee, J. H., Song, I., Zuckerman, B., & McElwain, M. 2007, The Astrophysical Journal, 660, 1556

Ricci, L., Isella, A., Carpenter, J. M., & Testi, L. 2013, The Astrophysical Journal Letters, 764, L27

Rice, E. L., Prato, L., & McLean, I. S. 2006, The Astrophysical Journal, 647, 432

Rieke, G. H., Su, K. Y. L., Stansberry, J. A., et al. 2005, The Astrophysical Journal, 620, 1010

Rieke, G. H., Young, E. T., Engelbracht, C. W., et al. 2004, The Astrophysical Journal Supplement Series, 154, 25

Robitaille, T. P., Whitney, B. A., Indebetouw, R., & Wood, K. 2007, The Astrophysical Journal Supplement Series, 169, 328

Robitaille, T. P., Whitney, B. A., Indebetouw, R., Wood, K., & Denzmore, P. 2006, The Astrophysical Journal Supplement Series, 167, 256

Roeser, S., Demleitner, M., & Schilbach, E. 2010, The Astronomical Journal, 139, 2440

Sandell, G. 2003, 'The calibration legacy of the ISO Mission', 481, 439

Sault, R. J., Teuben, P. J., & Wright, M. C. H. 1995, Astronomical Data Analysis Software and Systems IV, 77, 433

Scally, A. & Clarke, C. 2001, Monthly Notices of the Royal Astronomical Society, 325, 449

Schaefer, G. H., Dutrey, A., Guilloteau, S., Simon, M., & White, R. J. 2009, The Astrophysical Journal, 701, 698

Scholz, A. & Jayawardhana, R. 2008, The Astrophysical Journal, 672, L49

Scholz, A., Jayawardhana, R., & Wood, K. 2006, The Astrophysical Journal, 645, 1498

Scholz, A., Jayawardhana, R., Wood, K., et al. 2007, The Astrophysical Journal, 660, 1517

Shaya, E. J. & Olling, R. P. 2011, The Astrophysical Journal Supplement, 192, 2

Sheret, I., Dent, W. R. F., & Wyatt, M. C. 2004, Monthly Notices of the Royal Astronomical Society, 348, 1282

Shu, F., Najita, J., Galli, D., Ostriker, E., & Lizano, S. 1993, In: Protostars and planets III (A93-42937 17-90), 3

Shu, F., Najita, J., Ostriker, E., et al. 1994, The Astrophysical Journal, 429, 781

Shu, F. H., Adams, F. C., & Lizano, S. 1987, IN: Annual review of astronomy and astrophysics. Volume 25 (A88-13240 03-90). Palo Alto, 25, 23

Silverstone, M. D. 2000, Thesis (PhD). UNIVERSITY OF CALIFORNIA, 17

Skrutskie, M. F., Cutri, R. M., Stiening, R., et al. 2006, The Astronomical Journal, 131, 1163

Slesnick, C. L., Carpenter, J. M., Hillenbrand, L. A., & Mamajek, E. E. 2006, The Astronomical Journal, 132, 2665

Smith, B. A. & Terrile, R. J. 1984, Science (ISSN 0036-8075), 226, 1421

Song, I., Schneider, G., Zuckerman, B., et al. 2006, The Astrophysical Journal, 652, 724

Song, I., Weinberger, A. J., Becklin, E. E., Zuckerman, B., & Chen, C. 2002, The Astronomical Journal, 124, 514

Stamatellos, D. & Whitworth, A. 2011, Computational Star Formation, 270, 223

Stamatellos, D. & Whitworth, A. P. 2009, Monthly Notices of the Royal Astronomical Society, 392, 413

Stern, S. A. 1996, Astronomy and Astrophysics, 310, 999

Strom, K. M. & Strom, S. E. 1994, Astrophysical Journal, 424, 237

Strom, S. E. 1972, Publications of the Astronomical Society of the Pacific, 84, 745, a&AA ID. AAA008.064.065

Strom, S. E., Strom, K. M., & Grasdalen, G. L. 1975, In: Annual review of astronomy and astrophysics. Volume 13. (A76-10076 01-88) Palo Alto, 13, 187, a&AA ID. AAA014.065.118

Su, K. Y. L., Rieke, G. H., Stansberry, J. A., et al. 2006, The Astrophysical Journal, 653, 675

Su, K. Y. L., Rieke, G. H., Stapelfeldt, K. R., et al. 2009, The Astrophysical Journal, 705, 314

Sylvester, R. J., Dunkin, S. K., & Barlow, M. J. 2001, Monthly Notices of the Royal Astronomical Society, 327, 133

Szűcs, L., Apai, D., Pascucci, I., & Dullemond, C. P. 2010, The Astrophysical Journal, 720, 1668

Terebey, S., Shu, F. H., & Cassen, P. 1984, Astrophysical Journal, 286, 529

Thies, I. & Kroupa, P. 2007, The Astrophysical Journal, 671, 767

Thompson, R. I., Rieke, M., Schneider, G., Hines, D. C., & Corbin, M. R. 1998, Astrophysical Journal Letters v.492, 492, L95

Torres, R. M., Loinard, L., Mioduszewski, A. J., & Rodríguez, L. F. 2009, The Astrophysical Journal, 698, 242

van Belle, G. T. 2010, The Interferometric View on Hot Stars (Eds. Th. Rivinius & M. Curé) Revista Mexicana de Astronomía y Astrofísica (Serie de Conferencias) Vol. 38, 38, 119

van Belle, G. T., van Belle, G., Creech-Eakman, M. J., et al. 2008, The Astrophysical Journal Supplement Series, 176, 276

van Leeuwen, F. 2007, Astronomy and Astrophysics, 474, 653

Ward-Thompson, D., André, P., Crutcher, R., et al. 2007, Protostars and Planets V, 33

Weidenschilling, S. J. 1977, Astrophysics and Space Science, 51, 153, a&AA ID. AAA020.107.033

White, R. J. & Basri, G. 2003, The Astrophysical Journal, 582, 1109

White, R. J. & Ghez, A. M. 2001, The Astrophysical Journal, 556, 265

White, R. J. & Hillenbrand, L. A. 2004, The Astrophysical Journal, 616, 998

Whitney, B. A., Kenyon, S. J., & Gomez, M. 1997, Astrophysical Journal v.485, 485, 703

Whitworth, A. P. & Zinnecker, H. 2004, Astronomy and Astrophysics, 427, 299

Wilking, B. A. 1989, Astronomical Society of the Pacific, 101, 229

Williams, J. P. & Andrews, S. M. 2006, The Astrophysical Journal, 653, 1480

Williams, J. P., Blitz, L., & McKee, C. F. 2000, Protostars and Planets IV (Book - Tucson: University of Arizona Press; eds Mannings, 97

Williams, J. P. & Cieza, L. A. 2011, Annual Review of Astronomy and Astrophysics, 49, 67

Woitke, P., Riaz, B., Duchêne, G., et al. 2011, Astronomy & Astrophysics, 534, 44

Wood, K., Lada, C. J., Bjorkman, J. E., et al. 2002, The Astrophysical Journal, 567, 1183

Wright, E. L., Eisenhardt, P. R. M., Mainzer, A. K., et al. 2010, The Astronomical Journal, 140, 1868

Wyatt, M. C. 2006, The Astrophysical Journal, 639, 1153

Wyatt, M. C. 2008, Annual Review of Astronomy & Astrophysics, 46, 339

Wyatt, M. C., Dent, W. R. F., & Greaves, J. S. 2003, Monthly Notice of the Royal Astronomical Society, 342, 876

Young, C. H., Shirley, Y. L., Evans, N. J., & Rawlings, J. M. C. 2003, The Astrophysical Journal Supplement Series, 145, 111

Zacharias, N., Finch, C. T., Girard, T. M., et al. 2012, VizieR On-line Data Catalog, 1322, 0

Zuckerman, B. 2001, Annual Review of Astronomy and Astrophysics, 39, 549

Zuckerman, B. & Becklin, E. E. 1993, Astrophysical Journal, 414, 793

Zuckerman, B., Rhee, J. H., Song, I., & Bessell, M. S. 2011, The Astrophysical Journal, 732, 61, accepted for publication in ApJ

Zuckerman, B. & Song, I. 2004, The Astrophysical Journal, 603, 738